

DEVELOPMENT OF ELECTROCHEMICAL CO₂
REDUCTION TO GAS AND LIQUID FUELS IN
AQUEOUS MEDIA WITH SCALE-UP
POTENTIAL

by

Hang Xiang

A thesis presented for the degree of

Doctor of Philosophy



School of Engineering
Newcastle University, UK

October 2019

Abstract

Electrochemical CO₂ reduction reaction (eCO₂RR) in CO₂ utilization field attracts large interests as it only consumes water and electricity as the inputs to build valuable carbonaceous fuels and chemicals (i.e., CO, formate, low-carbon oxygen-contained and oxygen-free hydrocarbons). However, in aqueous media, hydrogen evolution reaction (HER) competes with eCO₂RR and theoretically much easier to be carried out resulting in low Faradaic efficiency (FE) towards eCO₂RR. Aiming at developing eCO₂RR system with suppressed HER, this study enhanced CO₂ mass transfer and reaction kinetics through cell configuration and electrolyte engineering, and developed the FE of valuable carbonaceous products by catalysts design. eCO₂RR has been generally carried out by a two-chamber (2C) cell using CO₂-saturated electrolyte, mass transfer is challenged by the CO₂ solubility. This study constructed a gas diffusion electrode (GDE) cell that CO₂ could be directly supplied to reaction interface with less resistance from the electrolyte, which greatly enhanced the overall FE for carbonaceous products compared with the 2C cell. The use of high alkalinity catholytes in GDE cell improved reaction kinetics and further increased FE of carbonaceous products, especially for C₂ (ethanol and ethylene). C₂ FE achieved 40% and current density reached -234 mA cm⁻² at -1.17 V (RHE) with using 2.0 M KOH. Targeting to enhance the selectivity of CO, a simple synthesis procedure for Cu-In catalyst was developed by electrochemical spontaneous precipitation (ESP) method. The material possessed a hybrid structure of amorphous In(OH)₃ nano-layer capping on polycrystalline Cu_xO, which structurally facilitated Cu-In interaction. CO production using Cu-In catalyst reached ~90% FE and -200 mA cm⁻² current density at -1.17 V (RHE). Syngas with tunable CO/H₂ ratio could be also produced by changing the ESP condition. Carbon supported SnO₂ catalyst was studied for selective formate production (>80% FE). High concentration (0.5 M) of formate solution was produced within 1-hour CO₂ reduction, which was utilized for a direct formate fuel cell (DFFC). The DFFC used Pd-CeO₂/C anode and

FeCo/C cathode, producing 92 mW cm^{-2} peak power density at 30% energy efficiency. A close loop of “electricity-formate-electricity” was realized, illustrating the important potential of synthetic liquid fuels from CO_2 for energy storage and transportation applications.

Acknowledgements

Undertaking this PhD study has been the most challenging but rewarding experience so far for me and it would not have been possible to do without the support and guidance that I received from many people.

First of all, I would like to express my very great appreciation to my supervisor Dr Eileen Yu for giving me the opportunity to do this project, and for the continues support of my PhD research with her motivation, enthusiasm, and immense expertise.

I gratefully acknowledge the Doctor Training Awards from Faculty of Science, Agriculture and Engineering of Newcastle University that supported my 4-year PhD study. Financial support from EPSRC LifesCO2R project (EP/N009746/1) for supporting this research work is very appreciated. My sincere thanks also go to Prof Keith Scott for his academic support and supervisory role and also Dr Shahid Rasul and Dr Henriette Christensen for their valuable inputs. Many thanks to Dr Hamish Andrew Miller from ICCOM-CNR (Italy) for the collaborative work on formate fuel cell test, the result is shown in Section 6.3.3 of this thesis.

My time at Newcastle was made enjoyable in large part due to many friends and groups that became a part of my life. I am grateful for time spent with my adorable friends for all the hardship and joy we've been through together in the last four years. Thank all my colleagues, technicians, and research fellows in the Chemical Engineering Department who gave me support during this work.

I don't think I'm able to pay back what I owe my parents who are always there for me with wise counsel and sympathetic ear, helping me work through the emotional quandaries. Thanks to Mengmeng whose faithful support during the most part of this Ph.D. journey is so appreciated.

Table of Contents

Abstract	i
Acknowledgements	iii
Table of Contents	v
List of Publications and Conferences	ix
List of Figures	x
List of Tables	xvi
Nomenclature	xviii
Chapter 1 Introduction	1
1.1 CO₂ issue and research opportunities	1
1.2 Approaches of CO₂ conversion	4
1.2.1 <i>CO₂ thermal hydrogenation</i>	4
1.2.2 <i>CO₂ electrochemical reduction</i>	5
1.2.3 <i>CO₂ photocatalytic reduction</i>	6
1.3 Challenges for CO₂ electrochemical reduction	7
1.4 Aim and objectives of this project	7
1.4.1 <i>Aim</i>	7
1.4.2 <i>Objectives</i>	8
1.5 Thesis Structure	8
Chapter 2 Electrochemical CO₂ Reduction in Aqueous Media – State-of-the-Art Review	10
2.1 Reaction mechanism of electrochemical CO₂ reduction	10
2.2 Conquering the CO₂ mass transfer problem	12
2.2.1 <i>CO₂ mass transfer from the macroscopic view – external diffusion</i>	12
2.2.1.1 <i>CO₂ purging into electrolyte</i>	13
2.2.1.2 <i>CO₂ diffusion from gas diffusion electrode</i>	17
2.2.2 <i>CO₂ mass transfer from the microscopic view – internal diffusion</i>	19
2.3 Electro-catalysts for CO₂ reduction reaction	20
2.3.1 <i>Design principle of the inorganic heterogeneous catalyst</i>	21
2.3.2 <i>Heterogeneous catalysts for CO production</i>	25
2.3.3 <i>Heterogeneous catalyst for formate production</i>	30
2.3.4 <i>Heterogeneous catalyst for (oxygenated) hydrocarbons</i>	33
2.4 Chapter summary	39
Chapter 3 Methodology	41

3.1	Process flow diagram of operating electrochemical CO₂ reduction reaction	41
3.2	Reactor design and fabrication	42
3.2.1	<i>Gas diffusion electrode (GDE)-holder used in an existing H-type cell</i>	42
3.2.2	<i>3D-printed compact cells</i>	42
3.3	Catalyst synthesis and cathode preparation	46
3.3.1	<i>Painting commercial Cu₂O on gas diffusion electrode (GDE)</i>	46
3.3.2	<i>Synthesizing Cu_xO catalyst and applying it to gas diffusion electrode (GDE)</i> ..	46
3.3.3	<i>Synthesizing Cu-In catalysts on gas diffusion electrode (GDE) by spontaneous precipitation</i>	46
3.3.4	<i>Fabricating C-supported SnO₂ bonded gas diffusion electrode (GDE)</i>	47
3.4	eCO₂RR system set-up and electrochemical measurement	48
3.4.1	<i>eCO₂RR system set-up</i>	48
3.4.2	<i>Electrochemical measurement</i>	49
3.4.2.1	<i>Cyclic Voltammetry (CV)</i>	49
3.4.2.2	<i>Electrochemical impedance spectroscopy (EIS)</i>	49
3.5	Methods for analysing CO₂ reduction products and catalyst materials	50
3.5.1	<i>Product analysis</i>	50
3.5.2	<i>Characterization of catalyst materials</i>	50
Chapter 4	Enhanced Selectivity of Carbonaceous Products from Electrochemical Reduction of CO₂ in Aqueous Media	52
4.1	Introduction	52
4.2	Experimental	53
4.2.1	<i>Initial application of gas diffusion electrode (GDE) – the feasibility test</i>	53
4.2.2	<i>CO₂ electro-reduction in compact cells</i>	54
4.3	Results and Discussion	55
4.3.1	<i>Initial application of gas diffusion electrode (GDE) – the feasibility test</i>	55
4.3.2	<i>The application of compact cells in CO₂ electro-reduction</i>	57
4.3.2.1	<i>Catalyst characterisations and the measurement of electrode actual surface area</i>	57
4.3.2.2	<i>The effect of CO₂ supply method</i>	60
4.3.2.3	<i>The effect of catholyte alkalinity</i>	67
4.4	Chapter summary	77
Chapter 5	A Scalable Process for Cu-In Catalyst Synthesis for Highly Selective CO and Tunable Syngas Production from CO₂ Electrochemical Reduction	79
5.1	Introduction	79
5.2	Experimental	80

5.2.1	<i>Preparation of Cu-In catalysts on gas diffusion electrode by two spontaneous precipitation methods</i>	80
5.2.2	<i>Catalyst characterisations</i>	81
5.2.3	<i>Catalyst evaluation by CO₂ electro-reduction</i>	81
5.3	Results and discussion	82
5.3.1	<i>Cu-In prepared by spontaneous precipitation (SP)</i>	82
5.3.1.1	<i>Catalyst characterisation and synthesis mechanism</i>	82
5.3.1.2	<i>eCO₂RR activities of CuIn-SP</i>	87
5.3.2	<i>Cu-In prepared by electrochemical spontaneous precipitation (ESP)</i>	89
5.3.2.1	<i>Catalyst characterisation and synthesis mechanism</i>	89
5.3.2.2	<i>eCO₂RR activities of CuIn-ESP</i>	97
5.3.2.3	<i>The structural Cu-In interaction</i>	98
5.3.2.4	<i>Production of highly selective CO and tunable Syngas using Cu-In catalyst</i>	101
5.4	Chapter summary	103
Chapter 6	Production of Formate from CO₂ Reduction and Its Application in Energy Storage	104
6.1	Introduction	104
6.2	Experimental	105
6.2.1	<i>Fabricating SnO₂/C bonded gas diffusion electrode (GDE)</i>	105
6.2.2	<i>Catalyst characterization</i>	105
6.2.3	<i>CO₂ reduction system and electrochemical analysis</i>	105
6.2.4	<i>Analysis of products from CO₂ reduction</i>	106
6.2.5	<i>Test of direct formate fuel cell (DFFC)</i>	106
6.3	Results and discussion	107
6.3.1	<i>Catalyst Characterization</i>	107
6.3.2	<i>Catalyst performance on electrochemical CO₂ reduction reaction</i>	109
6.3.2.1	<i>Effect of carbon support</i>	109
6.3.2.2	<i>Controllable formate production</i>	115
6.3.3	<i>Performance with direct formate fuel cell (DFFC) using formate from eCO₂RR</i>	117
6.4	Chapter summary	121
Chapter 7	Conclusions and future directions	122
7.1	Conclusions	122
7.2	Future Directions	124
Appendix I	Literature Research in Terms of Different Heterogeneous Catalysts Used for Electrochemical CO₂ Reduction	126

Appendix II Product Analysis and The Calculation of Faradaic Efficiency	138
Appendix III Design of the compact cell	144
Appendix IV Supplementary Information of Chapter 4, 5, and 6	149
References	164

List of Publications and Conferences

Publications

- **H. Xiang**, S. Rasul, K. Scott, J. Portoles, P. Cumpson, E. H. Yu. Enhanced selectivity of carbonaceous products from electrochemical reduction of CO₂ in aqueous media. *Journal of CO₂ Utilization*. 2019, 30, 214-221.
- S. Rasul, A. Pugniant, **H. Xiang**, J. Fontmorin, E. H. Yu. Low cost and efficient alloy electrocatalysts for CO₂ reduction to formate. *Journal of CO₂ Utilization*. 2019, 32, 1-10.
- **H. Xiang**, S. Rasul, H. Bo, J. Portoles, P. Cumpson. E. H. Yu. Copper-indium binary catalyst for high-performance CO₂ electrochemical reduction with record CO production efficiency. *ACS Applied Materials & Interfaces*. 2019, under revision.
- **H. Xiang**, H. A. Miller, M. Bellini, H. Christensen, K. Scott, S. Rasul, E. H. Yu. Production of formate from CO₂ electrochemical reduction and its application in energy storage. *Sustainable Energy & Fuels*. 2019, accepted.
- **H. Xiang**, Y. Wang, X. Liu, et al. Heterogeneous CO₂ electrochemical reduction in aqueous media – a review on the effect of CO₂ mass transfer. *Nano-micro Lett.* invited review, 2019, in process.

Selected Conference Presentations

- **H. Xiang**, S. Rasul, E. H. Yu. Strategies to develop electrochemical CO₂ reduction reaction with aqueous electrolyte - from system to catalyst. Oral presentation at Electrochem 2018 – 25th Annual Conference, 16th-18th September 2018, Lancaster, UK.
- **H. Xiang**, S. Rasul, K. Scott, E. H. Yu. Enhanced electrochemical production of carbonaceous products from CO₂ in aqueous electrolytes. Poster presentation at 69th Annual Meeting of the International Society of Electrochemistry, 2nd-7th September 2018, Bologna, Italy.
- **H. Xiang**, S. Rasul, E. H. Yu. Strategies to develop electrochemical CO₂ reduction reaction-from system to catalyst. Oral presentation at SCI Electrochemistry Postgraduate Conference 2018, 31st May 2018, Glasgow, UK.
- **H. Xiang**, H. Christensen, E. H. Yu. Characterization of electrochemical catalysts for CO₂ reduction. Poster presentation at International Summer School on CO₂ Conversion, 29th August -2nd September, Geneva, Switzerland.

List of Figures

- Figure 1-1** a) The average variation of global surface temperatures in 1960 (left) and 2018 (right). Dark blue indicates areas cooler than average. Dark red indicates areas warmer than average¹. b) The Keeling Curve showed accelerating increases in annual average carbon dioxide concentration in the atmosphere². 2
- Figure 1-2** A comparison in world energy structure between nowadays and the year 2070 by Shell analysis ⁶. 3
- Figure 2-1** Schematics of the two general reactors – 2C cell and GDE cell to achieve the CO₂ supply method of “purging into electrolyte” and “diffusion from GDE” respectively³⁶. 12
- Figure 2-2** Mass transfer of CO₂ and competitive charge transfer in the aqueous eCO₂RR system with applying the CO₂ supply method of “purging into electrolyte”. 13
- Figure 2-3** Scheme of the eCO₂RR reactor with the MEA configuration. The difference in ion transfer of using a) proton exchange membrane (PEM), and b) alkaline anion exchange membrane (AAEM). Reproduced from Ref.⁵⁸ with permission from the Journal of CO₂ Utilization Owner Societies. 19
- Figure 2-4** Grouping the transition metals in terms of selectivity towards HCOO⁻, CO, (oxygenated) hydrocarbons, and H₂ from eCO₂RR in aqueous electrolyte..... 21
- Figure 2-5** Possible reaction pathways for eCO₂RR on different groups of transition metals. 22
- Figure 2-6** a) Volcano plot using *COOH binding energy as a descriptor for CO partial current density at -0.9 V vs. RHE. b) Volcano plot using *OCHO binding energy as a descriptor for formate partial current density at - 0.9 V vs. RHE. Reprinted with permission from Ref.⁷². Copyright (2017) American Chemical Society. 23
- Figure 2-7** Limiting potentials (U_L) for elementary proton-transfer steps as a function of CO* binding energy (E_B[CO]). Competitive pathways are shown as lines of the same colour, and the more favourable route is shown as a solid line, while the less favourable route is shown dotted. The equilibrium potential for the overall electrochemical reduction of CO₂ to CH₄ is +0.17 V (vs. RHE), indicated as the horizontal dash line. Reprinted with permission from Ref.⁷³. Copyright (2012) American Chemical Society..... 24
- Figure 2-8** Catalytic performances of reported heterogeneous catalysts for eCO₂RR to CO in recent publications, with the solid round symbol representing the noble-metal based

catalysts and hollow square symbol for non-noble-metal based catalysts. An overview of a) CO Faradaic efficiency and b) CO partial current density as a function of applied cathodic potential.	29
Figure 2-9 Catalytic performances of reported heterogeneous catalysts for eCO ₂ RR to formate, with the solid round symbol representing the results in 2C cell and hollow square symbol for GDE cell system. An overview of a) formate Faradaic efficiency and b) formate partial current density as a function of cathodic potential.....	32
Figure 2-10 The performance of eCO ₂ RR on polycrystalline Cu. a) Current/Faradaic efficiency and b) partial current density as a function of cathodic potential for all the products. Reproduced from Ref. ¹¹⁸ by permission of The Royal Society of Chemistry.....	35
Figure 3-1 Process flow diagram of operating the electrochemical CO ₂ reduction reaction. .	41
Figure 3-2 a) Design drawing of the GDE-holder. b) H-type cell fitted with GDE-holder	42
Figure 3-3 Schematic diagrams of aqueous eCO ₂ RR system using a) 2C cell and b) GDE cell.	43
Figure 3-4 3D drawings of a) 2C cell and b) GDE cell compared in this work	44
Figure 4-1 Photo and schematic diagrams of immersed GDL and GDE-holder with two CO ₂ flow paths used in an H-type cell.	53
Figure 4-2 CV measurements of a) immersed GDL and b) GDE-holder under N ₂ and CO ₂ atmosphere in the H-type cell with the scan rate 50 mV s ⁻¹ . Scan cycles: 3, all those diagrams were taken from the 3rd cycle. c) CA results of eCO ₂ RR for 1.5 hours at -2.0 V (vs. Ag/AgCl) in the H-type cell.	56
Figure 4-3 SEM images of self.Cu _x O catalyst a) before reaction and b) after reaction, point EDX diagrams of self.Cu _x O catalyst c) before reaction and d) after reaction.	58
Figure 4-4 Determination of double-layer capacitance for a smooth stainless-steel sheet and the self.Cu _x O-GDE with the same geometric surface area. a) and b) CVs taken over a range of scan rates in a potential window where only double-layer charging and discharging is relevant for stainless-steel and self.Cu _x O-GDE respectively. c) and d) Current due to double-layer charge/discharge plotted against CV scan rate for stainless-steel and self.Cu _x O-GDE respectively.	59
Figure 4-5 CV measurements under N ₂ and CO ₂ atmosphere in 2C cell and GDE cell with KHCO ₃ catholytes using fresh self.Cu _x O catalyst. Scan rate: 50 mV s ⁻¹ , scan circles: 3, all	

those diagrams were taken from the 2 nd or 3 rd cycle of scan.	61
Figure 4-6 CA results of eCO ₂ RR in 2C cell and GDE cell with KHCO ₃ catholytes using Cu _x O catalyst. Each run was driven under certain cathodic potential (-0.17 (only in GDE cell), -0.37, -0.57, -0.77, -0.97 and -1.17 V vs. RHE) for 1800 s.	62
Figure 4-7 eCO ₂ RRs catalysed by self.Cu _x O catalyst at a wide range of applied potentials in a) 2C cell with different concentrations of KHCO ₃ and b) GDE cell with different concentrations of KHCO ₃	64
Figure 4-8 Schematics of (a)the cathode including 3 layers, (b) CO ₂ mass transfer in 2C cell and (c) GDE cell.	66
Figure 4-9 Cyclic voltammetry (CV) measurements under N ₂ and CO ₂ atmosphere in GDE cell with KOH catholyte using fresh self.Cu _x O catalyst. Scan rate: 50 mV s ⁻¹ , scan circles: 3, all those diagrams were taken from the 2 nd or 3 rd cycle of scan.	68
Figure 4-10 Chronoamperometry (CA) of eCO ₂ RR in GDE cell with KOH catholytes using Cu _x O catalyst. Each run was driven under certain cathodic potential (-0.17, -0.37, -0.57, -0.77, -0.97 and -1.17 V vs. RHE) for 1800s.	68
Figure 4-11 eCO ₂ RRs catalysed by self.Cu _x O catalyst at a wide range of applied potentials in GDE cell with different concentrations of KOH.	69
Figure 4-12 Tafel plots of the partial current density of CO ₂ reduced to CO versus overpotential for CO formation in GDE cell with different catholytes.	70
Figure 4-13 a) Nyquist plots of GDE cell using KOH catholyte with different concentrations at OCV and -0.77 V (vs. RHE) cathodic potential. b) The enlarged views of Nyquist plots obtained under OCV and -0.77 V cathode potential sorted by KOH concentrations.	72
Figure 4-14 a) XRD patterns and b) XPS spectra of Cu ₂ P and the peak-differentiating of Cu ₂ P _{3/2} for the Cu _x O-GDE before eCO ₂ RR and after 3 hours eCO ₂ RR in 1.0 M KOH and 1.0 M KHCO ₃	75
Figure 4-15 Stability test of eCO ₂ RR at -0.97 V (vs. RHE) using self.Cu _x O catalyst and 1 M KOH catholyte in GDE cell.	77
Figure 5-1 Experiment set-up schematic and process observation for 1 hour of a) electrochemical spontaneous precipitation (ESP) and b) spontaneous precipitation (SP).	81
Figure 5-2 Photographic images of com.Cu ₂ O-GDE (0 min) and CuIn-SP by 5 min to 2 h SP	

time.....	82
Figure 5-3 a) SEM images of com.Cu ₂ O. SEM images, elemental mapping, and quantitative EDX analysis of b) CuIn-SP25min and c) CuIn-SP2h.	84
Figure 5-4 a) XRD profiles of com.Cu ₂ O, CuIn-SP25min and CuIn-SP2h. b) High-resolution XPS spectrum of O1s, Cu2p, and In3d of com.Cu ₂ O (top), CuIn-SP25min (middle), and CuIn-SP2h (bottom).	86
Figure 5-5 Normalized FE of all the products and current density (j) of eCO ₂ RRs at -0.77 V (vs. RHE) catalysed by blank GDL, com.Cu ₂ O, and CuIn prepared by SP with different precipitation time.....	88
Figure 5-6 Photographic images of com.Cu ₂ O-GDE (0 min) and CuIn-ESP GDEs with 5 min to 2 h precipitation time.	89
Figure 5-7 SEM images, elemental mapping, and quantitative EDX analysis of a) CuIn-ESP25min and b) CuIn-ESP2h.	91
Figure 5-8 a) XRD profiles of com.Cu ₂ O, CuIn-ESP25min and CuIn-ESP2h. b) High-resolution XPS spectrum of O1s, Cu2p, and In3d of com.Cu ₂ O (top), CuIn-ESP25min (middle), and CuIn-ESP2h (bottom). c) Quantification analysis on XPS survey spectrum of CuIn-ESP15min, CuIn-ESP25min, and CuIn-ESP2h.....	92
Figure 5-9 a) Open circuit voltage (OCV) between fresh In foil and Cu ₂ O-GDL immersed in 0.4 M citric acid mixed 0.05 M In ₂ (SO ₄) ₃ solution (pH = 2.5), measured for an hour. b) Current recording during ESP process. c) The calculated charge density over ESP time.	95
Figure 5-10 Photographic images and schematic illustration of the electrode surface reconstruction over ESP time from 0 to 2 hours. Within 5 min: the bottomed CuO/Cu ₂ O were firstly reduced, with the outmost Cu oxides etching simultaneously. The initial In(OH) ₃ precipitation site was where the Cu oxides etched. From 5~25 min: with reduction of CuO/Cu ₂ O on going, protons consumed causing local pH increasing, resulting in In(OH) ₃ precipitation. The surface mass ratio of In/Cu increased during this period as more In(OH) ₃ precipitated. After 25min: particle size of CuO/Cu ₂ O shrank after reduction so that outer Cu particles were gradually free of the bond of Nafion and collaterally took away the precipitated In(OH) ₃ . With the exposure of the nether Cu without precipitated indium, the surface In/Cu ratio decreased.	96
Figure 5-11 eCO ₂ RR activities of CuIn-ESP catalysts with different precipitation time at a) -	

0.17 V, b) -0.37 V, c) -0.57 V, d) -0.77 V, e) -0.97 V, f) -1.17 V (vs. RHE).....	97
Figure 5-12 a) SEM, b) HAADF STEM image and element mapping, c) TEM, d) HRTEM, and e) SAED of CuIn-ESP25min.	99
Figure 5-13 a) CO yield and CO ₂ conversion of eCO ₂ RR catalysed by CuIn-ESP25min at a wide range of applied potentials. b) A comparison of CO yield from eCO ₂ RR between this work and other published related studies in recent years. c) Syngas production at -1.17 V from eCO ₂ RR catalysed by Cu ₂ O, CuIn-ESP5min, CuIn-ESP15min, CuIn-ESP25min, CuIn-ESP35min and CuIn-ESP2h.....	102
Figure 5-14 Stability test of CuIn-ESP25min catalysed eCO ₂ RR at -0.77 V (vs. RHE).....	102
Figure 6-1 SEM images of a) Vulcan XC-72 carbon black, b) SnO ₂ /C(3.5) catalyst before eCO ₂ RR, c) SnO ₂ /C(3.5) catalyst after 6 hours' eCO ₂ RR at -1.2 V.	108
Figure 6-2 XRD spectra of SnO ₂ /C(3.5) catalyst before eCO ₂ RR (blue) and after 6 hours' eCO ₂ RR at -1.2 V (orange).....	108
Figure 6-3 Cyclic voltammetry (CV) measurements under N ₂ (blue) and CO ₂ (orange) atmosphere using SnO ₂ /C(3.5) catalyst. Scan rate: 10 mV s ⁻¹ , scan circles: 3, both diagrams were taken from the 3 rd cycle of scan.	109
Figure 6-4 Results of eCO ₂ RRs catalysed by SnO ₂ /C mixtures and individual SnO ₂ and carbon at a wide range of applied potentials.	110
Figure 6-5 Determination of double-layer capacitance for a smooth stainless-steel sheet and the SnO ₂ /C-GDEs with various SnO ₂ /C mass ratio. a) CVs taken over a range of scan rates in a potential window where only double-layer charging and discharging is relevant for stainless-steel and SnO ₂ /C-GDEs. b) Current due to double-layer charge/discharge plotted against CV scan rate for stainless-steel and SnO ₂ /C-GDEs.	113
Figure 6-6 a) The yield of formate and overall CO ₂ conversion rate of eCO ₂ RRs catalysed by SnO ₂ /C(3.5) at specific applied potentials. b) A comparison with related studies published in recent 5 years in terms of formate yield per milliliter CO ₂ feedstock on every 1 cm ² working electrode (WE).	116
Figure 6-7 a) Formate concentration, average Faradaic efficiency (FE) and energy efficiency (EE) with 1-hour electrolysis at specific applied potentials -0.47 ~ -1.27 V. b) Energy efficiencies of all the products from eCO ₂ RR and the time consumed for producing 0.5 M formate at specific applied potentials -0.47 ~ -1.27V with static catholyte	117

Figure 6-8 The performances of DFFC using the model fuel and renewable fuel: a) polarization curves at 25 °C and 60 °C, b) power density curves at 25 °C and 60 °C, c) galvanostatic curves at 25 mA cm ⁻² (60 °C) by circulating 25 ml fuel, and d) discharge energy curves at 25 mA cm ⁻² (60 °C) by circulating 25 ml fuel.	118
Figure AII-1 GC data acquisition in gas mode of a) the standard gas and b) a sample gas..	139
Figure AIII-1 3D drawing of all the 3D printouts (yellow) to constitute a GDE cell.....	144
Figure AIII-2 The design drawing of the gas chamber with dimensions.....	145
Figure AIII-3 The design drawing of the GDE-window plate with dimensions.	146
Figure AIII-4 The design drawing of the cathode chamber with dimensions.	147
Figure AIII-5 The design drawing of the anode chamber with dimensions.	148
Figure AIV-1 Multi-point quantification analysis on XPS survey spectrum of a) CuIn-ESP15min, b) CuIn-ESP25min, and c) CuIn-ESP2h.....	156
Figure AIV-2 Partial current densities to produce H ₂ , CO, and format from eCO ₂ RR as a function of the applied potential for different catalysts: a) C, b) SnO ₂ /C(0.5), c) SnO ₂ /C(1.5), d) SnO ₂ /C(3.5), e) SnO ₂	161
Figure AIV-3 Schematic of pore conditions in the catalyst layer. (a) Flooded pore: pore volume filled with electrolyte. (b) Wetted pore: a thin layer of electrolyte covers the pore walls. (c) Dry pore: catalyst inactive due to lack of an ionic pathway. Reproduced from Ref. ¹⁹⁸ with permission from the PCCP Owner Societies.....	162

List of Tables

Table 2-1 Representative eCO ₂ RRs and HER in aqueous solution, the rate-determine-steps (RDS) and the corresponding standard potentials.	10
Table 2-2 CO ₂ mass transfer steps and the corresponding rates	14
Table 4-1 Composition of tail gas produced by eCO ₂ RR for 1.5 hours at -2.0 V (vs. Ag/AgCl) in the H-type cell.	56
Table 4-2 Calculations for the actual surface area of self.Cu _x O-GDE.....	60
Table 4-3 Tafel parameters obtained from the Tafel plots (Figure 3b), b represents the Tafel slope for the lower overpotential region.	71
Table 4-4 The electrical conductivities ¹⁵⁹ at 20°C and ambient pressure, and the fitted R _s , R _{ad} and R _{ct} values of eCO ₂ RR at -0.77 V(RHE) cathodic potential varied by KOH catholyte concentration.....	73
Table 6-1 Double layer capacitances and relative area of electrode/electrolyte interface of SnO ₂ /C-GDEs with various SnO ₂ /C mass ratio, C-GDE, and SnO ₂ -GDE in contrast with a smooth stainless-steel (SS) foil.....	113
Table 6-2 Fuel composition.....	117
Table 6-3 Parameters of DFFC performance using the model fuel and renewable fuel at 60 °C.	119
Table 6-4 Calculations of OH ⁻ concentration in the residual catholyte after eCO ₂ RR producing 0.5 M formate.	120
Table AI-1 An overview of heterogeneous catalysts for selective CO production from eCO ₂ RR in two-chamber (2C) cell system.....	127
Table AI-2 An overview of heterogeneous catalysts for selective CO production from eCO ₂ RR in GDE cell system	132
Table AI-3 An overview of heterogeneous catalysts for selective formate/formic acid production from eCO ₂ RR in 2C cell system.....	133
Table AI-4 An overview of heterogeneous catalysts for selective formate/formic acid production from eCO ₂ RR in GDE cell system	135
Table AI-5 An overview of modified Cu-based catalysts for (oxygenated) hydrocarbon	

production from eCO ₂ RR.....	136
Table AII-1 Detecting conditions of GC for analysing gas.....	138
Table AII-2 Peak areas of the standard gas and sample gas	139
Table AII-3 Detecting conditions of GC for analysing alcoholic liquid.....	141
Table AII-4 Detecting conditions of IC for analysing fatty acid	142
Table AII-5 An example of the actual calculated FE values of all the products from eCO ₂ RR.	142
Table AIV-1 The a) absolute Faradaic efficiencies (FEs) and b) normalized FEs of all the products and average current density (j) of eCO ₂ RRs in two-chamber (2C) cell and gas diffusion electrode (GDE) cell with various catholytes, at wide range of cathodic potentials (V vs. RHE). Random error is shown in brackets.....	149
Table AIV-2 Calculations on half-cell reduction potentials (in reduction form) involved in ESP process at standard state. Gibbs–Helmholtz equation, Nernst equation were used based on the database from Outokumpu HSC Chemistry 6.0 software.	157
Table AIV-3 The practical production amounts of all the gas and liquid products of eCO ₂ RR catalysed by Cu ₂ O, CuIn-ESP5min, CuIn-ESP15min, CuIn-ESP25min, CuIn-ESP35min and CuIn-ESP2h.....	158
Table AIV-4 Normalized Faradaic efficiencies (FEs) of all the products and current density (j) of eCO ₂ RRs using different catalysts in gas diffusion electrode (GDE) cell with 1 M KOH catholyte, at wide range of cathodic potentials (V vs. RHE). Random error is shown in brackets.....	159
Table AIV-5 Calculations on half-cell reduction potentials (in reduction form) involved in formate fuel cell when formate concentration is 0.5 M at pH=14, 60 °C. Gibbs–Helmholtz equation, Nernst equation were used based on the database from Outokumpu HSC Chemistry 6.0 software.	163

Nomenclature

Symbols

a	Specific gas/liquid surface area ($\text{m}^2 \text{m}^{-3}$)
$a_{\text{Ox}}/a_{\text{Red}}$	Chemical activity of the oxidized/reduced form, for solid or pure phase, $a=1$; for ions in solution, a can be related to ion concentration.
b	Tafel slope (mV dec^{-1})
C	Molar concentration (M or mol L^{-1})
$C_{\text{O}}(0,t)/C_{\text{R}}(0,t)$	The surface concentration of oxidant/reduced product at time t
$C_{\text{O}}^*/C_{\text{R}}^*$	The bulk concentration of oxidant/reduced product
D	Diffusion coefficient ($\text{m}^2 \text{s}^{-1}$)
E	Potential (V)
F	Faradaic constant (96485 C mol^{-1})
f	A constant ($=F/RT$)
h_{L}	Liquid hold-up
I:	Current (A or mA)
j	Current density (A m^{-2} or mA cm^{-2})
j_0	Exchange current density (A m^{-2})
k_-	Rate constant of backward reaction (s^{-1})
k_+	Rate constant of forward reaction (s^{-1})
K_0	Equilibrium constant
$k_{\text{G/L}}$	Mass transfer coefficient (m s^{-1}),
n	Molar mass (mol)
p_{CO_2}	CO_2 partial pressure(kPa)
Q	Quantity of electric charge (C)
R	Gas constant, = 8.314
R_{ad}	Gas adsorption resistance (Ω)
R_{ct}	Charge transfer resistance(Ω)
R_{ET}	Electron transfer rate
R_{MT}	Mass transfer rate

R_s	Internal resistance (Ω)
S_{geo}	Geometric surface area (cm^2)
T	Temperature (K)
t	Time (s)
V	Volume (L or mL)
x	Diffusion distance (m)
z	Number of electron transfer
ΔG_r^\ominus	Change in the Gibbs free energy at standard state (KJ)
ΔH_r^\ominus	Change in enthalpy at standard state(KJ)
ΔS_r^\ominus	Change in entropy at standard state (J K^{-1})

Greek letters

α	Transfer coefficient ($0 \leq \alpha \leq 1$)
η	Overpotential (V)
λ	Wavelength of X-ray (nm)
ε	Voidage of 3D cathode

List of main abbreviations

2C cell	Two-chambers cell
AEM	Anion exchange membrane
CA	Chronoamperometry
CEM	Cation exchange membrane
CN	Coordination number
CV	Cyclic voltammetry
Com.Cu ₂ O	Commercial Cu ₂ O
Conc.	Concentration
DFFC	Direct formate fuel cell
eCO ₂ RR	Electrochemical CO ₂ reduction reaction
ECSA	Electrochemical surface area
EIS	Electrochemical impedance spectroscopy

ESP	Electrochemical spontaneous precipitation
FE	Faradaic efficiency
GC	Gas chromatography
GCE	Glassy carbon electrode
GDE	Gas diffusion electrode
GDE cell	Gas diffusion cell
GDL	Gas diffusion layer
HER	Hydrogen evolution reaction
IC	Ion chromatography
IEM	Ion exchange membrane
LSV	Linear sweep voltammetry
NHE	Normal hydrogen electrode
NP	Nanoparticle
NW	Nanowire
OCV	Open circuit voltage
OER	Oxygen evolution reaction
RDS	Rate determining step
Ref.	Reference
RHE	Reversible hydrogen electrode
SCE	Saturated calomel electrode
Self.Cu _x O	Self-synthesized Cu _x O
SHE	Standard hydrogen electrode
SP	Spontaneous precipitation

Chapter 1 Introduction

1.1 CO₂ issue and research opportunities

From the global temperature change reported by NASA in 2018, the climatic anomaly is increasing annually relative to 1951-1980 average temperatures and 18 of the 19 warmest years all have occurred since 2001¹. As shown in Figure 1-1 a, the comparison of the global temperature distribution between the year 1960 and 2018 indicates the fact of global warming. The increasing concentrations of atmospheric carbon dioxide (CO₂) and other greenhouse gases are regarded as the main reason to this climate problem. Observed by Mauna Loa Observatory in Hawaii, the atmospheric CO₂ concentration has sharply increased from 315ppm in the year 1960 to 414.96 ppm in 2019 as illustrated in Figure 1-1 b², which is the consequence of overexploiting and massive combusting fossil fuels by humans on the increasing demand of energy.

In the year 2016, Paris Agreement was signed in New York, which is a legally binding deal targeting to limit the increase in global average temperature to 1.5 °C³. Governments around the world are taking actions to reach the agreement's emission targets, such as setting up plans to limit the use and sale of petrol and diesel vehicles⁴, ban the use of coal to produce electricity⁵, and raise the proportion of clean energy in the world's energy industry, etc., which offers important implications for academic research. The Europe's biggest oil company Shell proposed "Sky Scenario" which envisions a world that achieves net-zero carbon emissions by 2070 with a significant adjustment of energy structure, as shown in Figure 1-2⁶.

From Shell's assumption, the clean energy (with zero CO₂ emission, such as nuclear, solar, wind, and others) will occupy 64% in the world power generation industry by 2070. While the 36% rest "unclean" energy with the discharge of CO₂ will be treated by CO₂ capture and storage (CCS), the captured CO₂ will be stored underground eventually. It was evaluated that from

2070 forward, Shell will bury around 11 gigatons of CO₂ a year, equivalent to 1.7 times the current total emissions from the United States⁷. The large scale of CO₂ burying aroused widespread scepticism as how the buried CO₂ affects the deep subsurface is not explicit currently⁸.

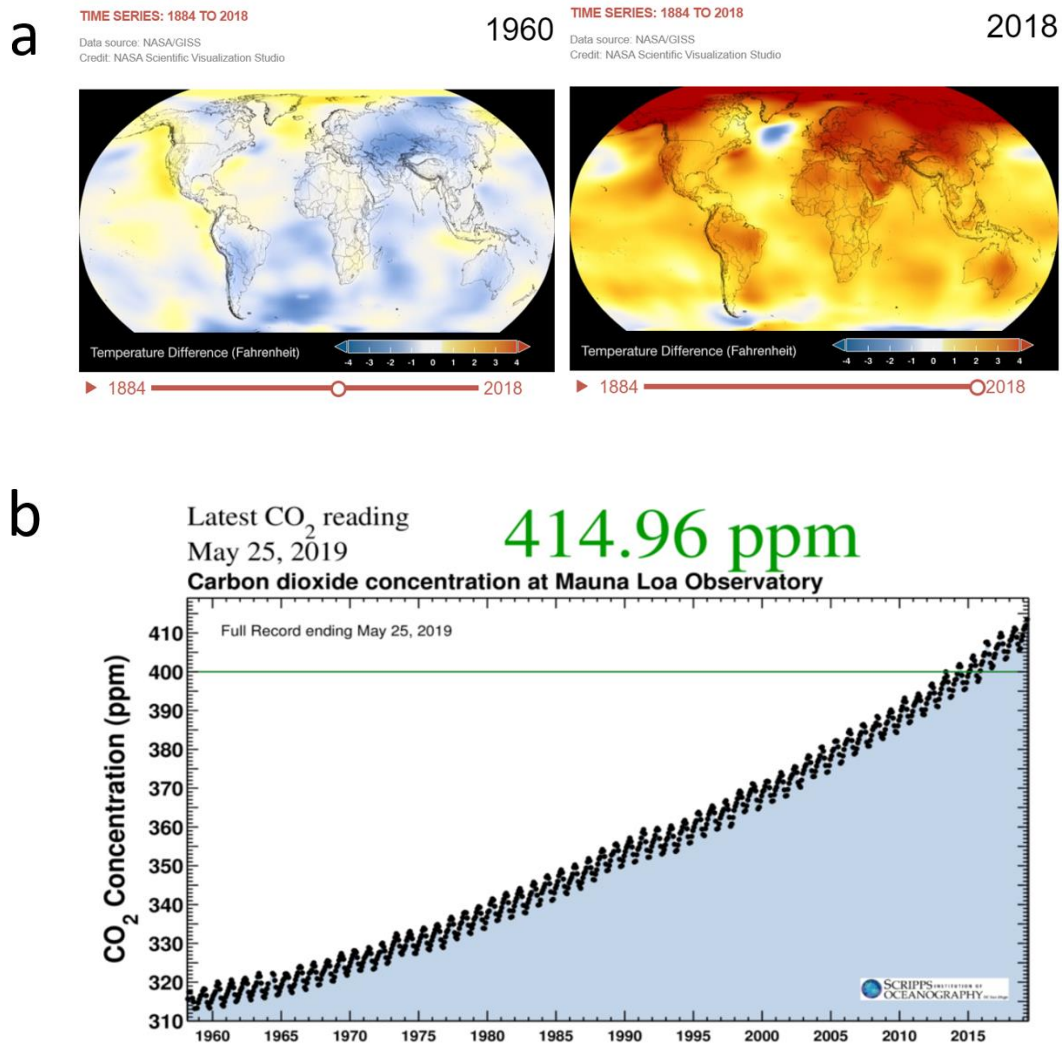


Figure 1-1 a) The average variation of global surface temperatures in 1960 (left) and 2018 (right). Dark blue indicates areas cooler than average. Dark red indicates areas warmer than average¹. b) The Keeling Curve showed accelerating increases in annual average carbon dioxide concentration in the atmosphere².

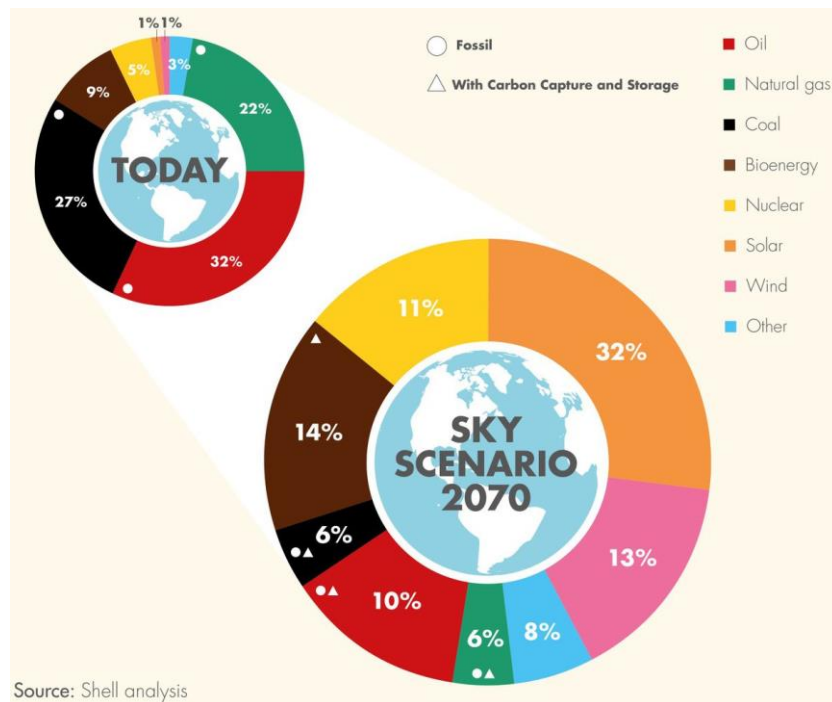


Figure 1-2 A comparison in world energy structure between nowadays and the year 2070 by Shell analysis ⁶.

Almost all materials surround us in our daily lives are carbon-based. As the most abundant carbon resource in the atmosphere, CO₂ has great potential to transit from “debt” to “asset” by producing those carbonaceous chemicals and fuels. However, those chemical conversions started with the inert CO₂ are thermodynamically energy-uphill processes so that large amount of energy will be needed as the input⁹. Additionally, CO₂ conversion routes are various, and the techniques of CO₂ conversion are still at early-stage, its potential economic profit is unlikely to be quantified currently¹⁰. Thus, compare to CO₂ storage, CO₂ utilization is more challenged by the market in view of present policies.

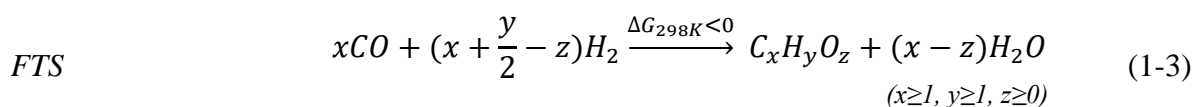
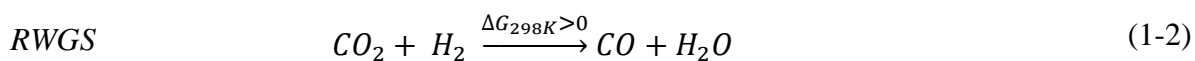
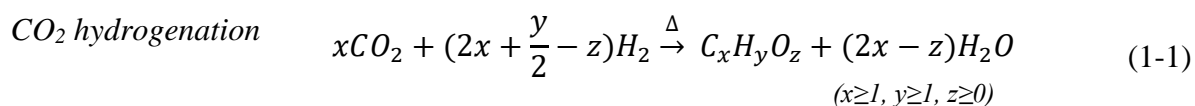
However, with the reducing cost of renewable energy and the improving policies (such as carbon tax and pricing the CO₂-derived products¹¹) in the near future, CO₂ utilisation and conversion to value-added carbonaceous chemicals and fuels is still promising to be deployed on a commercial-scale. This will mostly rely on technologies to make the conversion more efficient and cost-effective.

1.2 Approaches of CO₂ conversion

Converting the thermodynamically-stable CO₂ molecule needs energy input and the attendance of catalysts, the reaction pathways are numerous. CO₂ can be used as building blocks to promote the growth of carbon-chain for the formation of multi-carbon compounds and polymers, such as reacting with propylene oxide to produce cyclic carbonates and polycarbonates, reacting with methanol to synthesize dimethyl carbonate¹², reacting with terminal alkyne to synthesize propiolic acid, carboxylating by oxazole to form oxazole 2-carboxylic acid¹³, producing oxazolidinones, quinazolines, carbamates, isocyanates, and polyurethanes by C-N bonding¹⁴. CO₂ can also react with small carbonaceous molecule to adjust the molecular structure, such as CO₂ reforming of CH₄ to produce Syngas. Among those CO₂ conversion approaches, using CO₂ as the exclusive carbon source to produce value-added carbonaceous products has been most-popularly interested by the scientific community in recent decades, including CO₂ thermal hydrogenation, CO₂ electrochemical reduction, and CO₂ photocatalytic reduction.

1.2.1 CO₂ thermal hydrogenation

CO₂ thermal hydrogenation reaction can be expressed as Equation (1-1), with oxygen-free or oxygen-contained hydrocarbons as the products. It is normally regarded as a combination of reversed water-gas shift (RWGS) reaction and Fischer-Tropsch synthesis (FTS) as illustrated in Equation (1-2) and Equation (1-3) respectively.

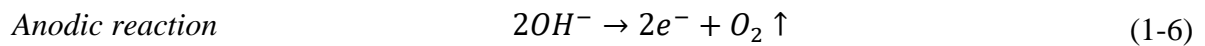
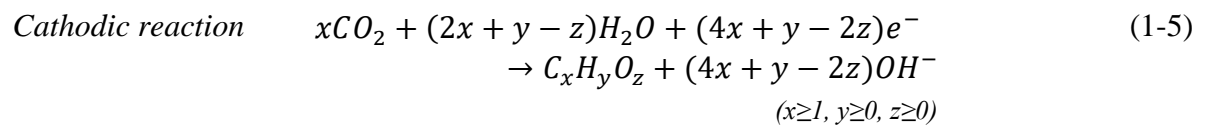
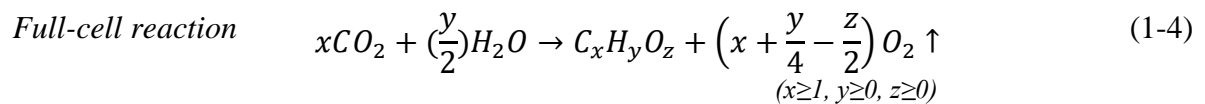


RWGS is an endothermic reaction while FTS is exothermic, thus the operation temperature of

CO₂ hydrogenation is compromised at a suitable range, specifically within 520-770 K. For the synthesis of C_{>2} products (i.e., $x > 2$ in Equation (1-1)), high reaction pressure is kinetically necessary to promote the forward reaction as the number of moles of gas is decreased. Higher than 3 MPa is normally applied for the formation of C₂ ~ C₄¹⁵. C_{>5} (oxygen-contained) hydrocarbons could be produced from the best documented so far in related literature, with the selectivity remained to be improved¹⁶. Additionally, the stringent reaction condition of high temperature and pressure, and the large consumption of H₂ bring more economic challenges to this reaction.

1.2.2 CO₂ electrochemical reduction

Compared to CO₂ thermal hydrogenation, electrochemical CO₂ reduction reaction (eCO₂RR) which is a half-cell cathodic reaction has been much-less economically constrained by the reaction conditions and reductant. eCO₂RR is normally operated under ambient temperature and pressure with consuming only water and electricity as the proton and electron donor, as shown in Equation (1-5). Also, pure O₂ can be produced as a by-product on the anodic side as illustrated in Equation (1-6)¹⁷.



Different from the gas-solid 2-phase reaction - CO₂ thermal hydrogenation, eCO₂RR involves gaseous CO₂, liquid electrolyte, and solid electrode, which takes place on the gas-solid-liquid three-phase interface. The low efficiency of mass transfer of CO₂ is the main concern which constrains the large-scale development of this operational-friendly reaction¹⁸. Moreover, the

residence time of CO₂ molecules on the 3-phase interface is not comparable to the case of CO₂ hydrogenation with gas-solid reaction, due to the fast conversion of CO₂ to CO₃²⁻/HCO₃⁻ in aqueous electrolyte. This would cause insufficient CO₂ reactants “holding” on the active sites of catalyst for deeper carbon chain-growth reaction¹⁹, which might be a reason that products from eCO₂RR are rarely go up to C_{>2}.

1.2.3 CO₂ photocatalytic reduction

CO₂ photocatalytic reduction shares the same macroscopic reaction with eCO₂RR, but with different charge transfer mechanism that electrons are excited from the valence band (VB) to the conduction band (CB) of a light-activated semiconductor. VB is the highest energy band occupied by electrons and CB is the lowest energy band without electron at the ground state, these electron-hole pairs are the charge carriers²⁰. Thus, semiconductor photocatalysts with specific CB and VB potentials, bandgap energies, and adsorption properties for the key intermediates have been mostly relied for reaching an efficient CO₂ photocatalytic reduction reaction. Although related studies have started decades ago²¹, the research progress of overall reaction efficiency has been lagged by the limited option of photocatalysts, existing works were mostly focused on TiO₂-based materials and other types of metal oxide and mixed metal oxide semiconductors, including ZrO₂, Ga₂O₃, Ta₂O₅, CaFe₂O₄, NaNbO₃, and ZnGa₂O₄, etc.²² Compared to eCO₂RR, the current rate of average productivity in photocatalytic reduction of CO₂ is considerably low due to great constraints by low photocatalytic efficiency, low response to sunlight, inefficient electron transport and so on²⁰. Additionally, deeper reduction of CO₂ is hardly to be achieved by photocatalysis, C_{>1} products have been rarely reported from this process in related literature.

Among the above three approaches of CO₂ chemical conversion, the nowadays technology makes eCO₂RR possess both economic and scalable potential, but development works are still

needed to accelerate its scale-up process.

1.3 Challenges for CO₂ electrochemical reduction

(1) The inertness of CO₂ poses great challenges to its adsorption and activation so that a high overpotential is fundamentally required which need to be conquered.

(2) To realize the 3-phase reaction, CO₂ was normally dissolved into the aqueous electrolyte, however with a very low solubility. Consequently, the CO₂ mass transfer to the reaction interface is normally low-efficient.

(3) Hydrogen evolution reaction (HER) is inevitable in aqueous electrolyte under the reduction potential, which is competitive to eCO₂RR and constrains a high current efficiency achievement of eCO₂RR.

(4) Selectively and directly producing one specific product is always difficult due to the diversity of electron and proton transfer routes.

(5) The existing fundamental research, such as reaction mechanism and key intermediates, is not sufficient enough to guide the research direction.

1.4 Aim and objectives of this project

1.4.1 Aim

The aim of this project currently is to ameliorate the aqueous eCO₂RR system and to develop the selectivity, yield, and efficiency for the formation of target products with scale-up potential.

1.4.2 Objectives

(1) Efficient CO₂ mass transfer enables high reaction efficiency, but it is challenged by the low solubility of CO₂ in aqueous electrolyte. To enhance the CO₂ mass transfer, a high-performance electrolysis reactor with reduced mass transfer resistance is necessary to be studied and applied.

(2) Other reaction parameters, such as electrolyte, applied potential, and so on, have impacts on the overall reaction kinetics and efficiency, but the effects are unclear from existing studies.

The reaction system should be studied and optimized.

(3) Electrocatalysts also have impacts on reaction efficiency and play important role in product selectivity. Targeting different carbonaceous products, such as CO, HCOOH, and C₂ with high selectivity and production rate, cost-effective and multifunctional electrocatalysts should be designed, synthesized, and optimized.

(4) To develop the sustainability of CO₂ utilisation, it will be useful to explore the direct application approaches of the downstream products from eCO₂RR.

1.5 Thesis Structure

Chapter 1. Introduction				
Chapter 2. eCO ₂ RR in Aqueous Media – State-of-the-Art Review				
Reaction mechanism of eCO ₂ RR	Conquering the CO ₂ mass transfer problem	Electro-catalysts of eCO ₂ RR for producing CO, formate, and (oxygenated) hydrocarbons	Chapter summary	
Chapter 3. Methodology				
Process flow diagram	Reactor design and fabrication	Catalyst synthesis and cathode preparation	eCO ₂ RR system set-up and electrochemical measurement	Methods for analysing CO ₂ reduction products and catalyst materials

Chapter 4-6. Experimental results

<p>Chapter 4. Enhanced Selectivity of Carbonaceous Products from eCO₂RR in Aqueous Media</p>	<p>Chapter 5. A Scalable Process for Cu-In Catalyst Synthesis for Highly Selective CO and Tuneable Syngas Production from eCO₂RR</p>	<p>Chapter 6. Production of Formate from eCO₂RR and Its Application in Energy Storage</p>
<p>Introduction</p>	<p>Introduction</p>	<p>Introduction</p>
<p>Experimental</p>	<p>Experimental</p>	<p>Experimental</p>
<p>Result and discussion</p>	<p>Result and discussion</p>	<p>Result and discussion</p>
<ul style="list-style-type: none"> Initial application of GDE - the feasibility test The application of compact cells <ul style="list-style-type: none"> Catalyst characterisations and the measurement of electrode actual surface area The effect of CO₂ supply method The effect of catholyte alkalinity 	<ul style="list-style-type: none"> Cu-In prepared by spontaneous precipitation (SP) <ul style="list-style-type: none"> Catalyst characterisation and synthesis mechanism eCO₂RR activities of CuIn-SP Cu-In prepared by electrochemical spontaneous precipitation (ESP) <ul style="list-style-type: none"> Catalyst characterisation and synthesis mechanism eCO₂RR activities of CuIn-ESP The structural Cu-In interaction Production of highly selective CO and tuneable Syngas using Cu-In catalyst 	<ul style="list-style-type: none"> Catalyst Characterization Catalyst performance on electrochemical CO₂ reduction reaction <ul style="list-style-type: none"> Effect of carbon support Controllable formate production Performance with direct formate fuel cell (DFFC) using formate from eCO₂RR
<p>Chapter summary</p>	<p>Chapter summary</p>	<p>Chapter summary</p>
<p>Chapter 7. Conclusions and future directions</p>		
<p>Appendix I, II, III, IV</p>		
<p>References</p>		

Chapter 2 Electrochemical CO₂ Reduction in Aqueous Media – State-of-the-Art Review

2.1 Reaction mechanism of electrochemical CO₂ reduction

The electrochemical CO₂ reduction reaction (eCO₂RR) in aqueous media is a half-cell reaction driven by electrons from the cathode and protonated by the liquid electrolyte. Various carbonaceous products could be produced as displayed in Equation (2-1) – (2-6) in Table 2-1²³⁻²⁵, with small thermodynamic potential differences. However, the hydrogen evolution reaction (HER) takes place simultaneously in aqueous media as illustrated in Equation (2-8). Although the standard potential of HER is close to those of eCO₂RR, H₂ is much easier to be produced since the initial rate-determining step (RDS) of eCO₂RR needs much more energy than that of HER. The initial RDS of eCO₂RR is the generation of radical CO₂^{•-} which is the key intermediate for the proton-coupled multiple electron transfer reactions afterwards^{23-24, 26}. As presented in Equation (2-7), the formation of radical CO₂^{•-} anion is carried out by bending the linear CO₂ molecule²⁴. Armand et al.²⁷ firstly reported the energy needed for CO₂/CO₂^{•-} in anhydrous DMF should be as high as -2.21 V vs. SCE (about -1.9 V vs. NHE) at a scan rate of 4400 V s⁻¹.

Table 2-1 Representative eCO₂RRs and HER in aqueous solution, the rate-determine-steps (RDS) and the corresponding standard potentials.

Acidic electrolyte	Neutral or Alkaline electrolyte	E ⁰ (V vs. RHE)	No.
CO ₂ + 2H ⁺ + 2e ⁻ → HCOOH	CO ₂ + H ₂ O + 2e ⁻ → HCOOH + 2OH ⁻	-0.03	(2-1)
CO ₂ + 2H ⁺ + 2e ⁻ → CO + H ₂ O	CO ₂ + H ₂ O + 2e ⁻ → CO + 2OH ⁻	-0.11	(2-2)
CO ₂ + 6H ⁺ + 6e ⁻ → CH ₃ OH + H ₂ O	CO ₂ + 5H ₂ O + 6e ⁻ → CH ₃ OH + 6OH ⁻	0.03	(2-3)
CO ₂ + 8H ⁺ + 8e ⁻ → CH ₄ + H ₂ O	CO ₂ + 6H ₂ O + 8e ⁻ → CH ₄ + 8OH ⁻	0.17	(2-4)
2CO ₂ + 12H ⁺ + 12e ⁻ → C ₂ H ₄ + 4H ₂ O	2CO ₂ + 8H ₂ O + 12e ⁻ → C ₂ H ₄ + 12OH ⁻	0.08	(2-5)
2CO ₂ + 12H ⁺ + 12e ⁻ → C ₂ H ₅ OH + 3H ₂ O	2CO ₂ + 9H ₂ O + 12e ⁻ → C ₂ H ₅ OH + 12OH ⁻	0.09	(2-6)
RDS: CO ₂ + e ⁻ → CO ₂ ^{•-}			(2-7)
2H ⁺ + 2e ⁻ → H ₂	2H ₂ O + 2e ⁻ → H ₂ + 2OH ⁻	0.00	(2-8)
RDS: H ⁺ + e ⁻ → H [•]	H ₂ O + e ⁻ → H [•] + OH ⁻		(2-9)

HER is competitive to eCO₂RRs in terms of electron acceptance. The electron transfer rate (R_{ET}) of the one-electron reversible electrode process is generally defined in Equation (2-10)²⁸, based on the Current-overpotential Equation.

$$R_{ET} = \frac{j}{nF} = \frac{j_0 \left[\frac{C_O(0,t)}{C_O^*} e^{-\alpha f \eta} - \frac{C_R(0,t)}{C_R^*} e^{(1-\alpha) f \eta} \right]}{nF} \quad (2-10)$$

Where: j : local current density (A m⁻²)

n : number of electron transfer, here it is 1

F : Faradaic constant (96485 C mol⁻¹)

j_0 : exchange current density (A m⁻²)

$C_O(0,t)/C_R(0,t)$: the surface concentration of oxidant/reduced product at time t

C_O^*/C_R^* : the bulk concentration of oxidant/reduced product

α : transfer coefficient ($0 \leq \alpha \leq 1$)

f : a constant ($=F/RT$)

η : overpotential (V)

The initial rate of either eCO₂RR or HER accords with this equation, mainly determined by the exchange current density j_0 , the surface concentration of reactant, and overpotential. The j_0 is primarily related to the adsorption energy of the active species (CO₂⁻ or H^{*}) on the electrode material²⁹. A suitable catalyst³⁰ can alter the adsorption energy to those species, intending to control the selectivity between carbonaceous products and H₂.

In the aqueous eCO₂RR system, the inherent competitive advantage for HER is mass transfer, in other words, the surface concentration of H₂O (or H⁺) is always sufficient. However, the mass transfer of the heterogeneous CO₂ gas to the gas-solid-liquid 3-phase interface is more complicated, resulting in a high percentage of electron allocated to HER and low current efficiency towards eCO₂RR. To develop the reaction rate of aqueous eCO₂RR, the CO₂ mass transfer problem should be conquered primarily to suppress the H₂ production.

2.2 Conquering the CO₂ mass transfer problem

2.2.1 CO₂ mass transfer from the macroscopic view – external diffusion

Pure CO₂ is applied as the feedstock in nearly all the existing studies, since the research progress is still at an early stage. The CO₂ mass transfer from a macroscopic view is CO₂ transport from its pure phase to the adjacent region of reaction interface, depends on the CO₂ supply method to a great extent. As shown in Figure 2-1, “CO₂ purging into electrolyte” and “CO₂ diffusion from gas diffusion electrode (GDE)”, carried out by a two-chamber (2C) cell and a GDE cell respectively, are the two general CO₂ supply methods applied in published works³¹. Song et al.¹⁸ used liquid-phase and gas-phase system to define and distinguish these two CO₂ supply methods in their review paper. Promising reaction performance with high selective production of CO, formate, and C₂₋₂ hydrocarbons or their oxygenates has been achieved by both two CO₂ supply methods^{23-24, 32}, but the GDE system generally reached a high geometric current density³³⁻³⁵. For the further development of CO₂ reduction, it is imperative to investigate the CO₂ mass transfer process and the corresponding influence factors in these two popular systems.

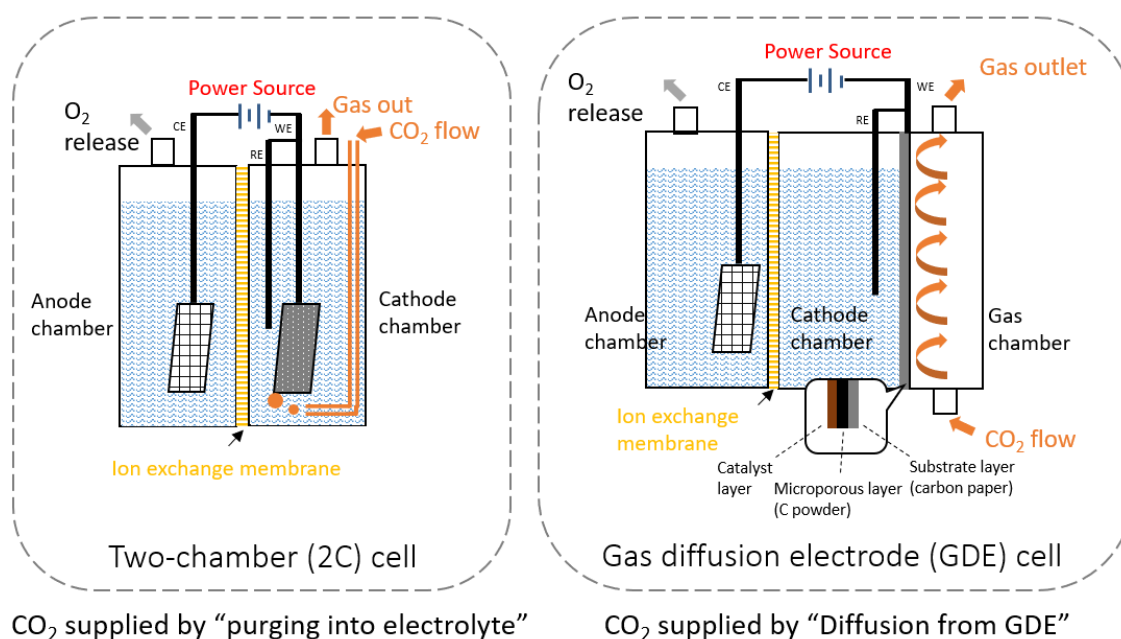


Figure 2-1 Schematics of the two general reactors – 2C cell and GDE cell to achieve the CO₂ supply method of “purging into electrolyte” and “diffusion from GDE” respectively³⁶.

2.2.1.1 CO₂ purging into electrolyte

The pre-bubbling of CO₂ is necessary before the reaction to reach the saturation solubility of CO₂ into the catholyte. It has been widely accepted that the real reactant in the eCO₂RR system is the dissolved CO₂ (generally written as CO₂(aq) or CO₂•(H₂O)_x), rather than ionic HCO₃⁻ and CO₃²⁻³⁷⁻³⁹. As shown in Figure 2-2, the process of CO₂ mass transfer in aqueous media is composed of two major steps: Step 1. CO₂ gas dissolution and equilibrium to produce the reactant CO₂(aq), Step 2. CO₂(aq) diffusion from bulk catholyte to local reaction sites. The rate of each step and the corresponding influence factors are summarised in Table 2-2.

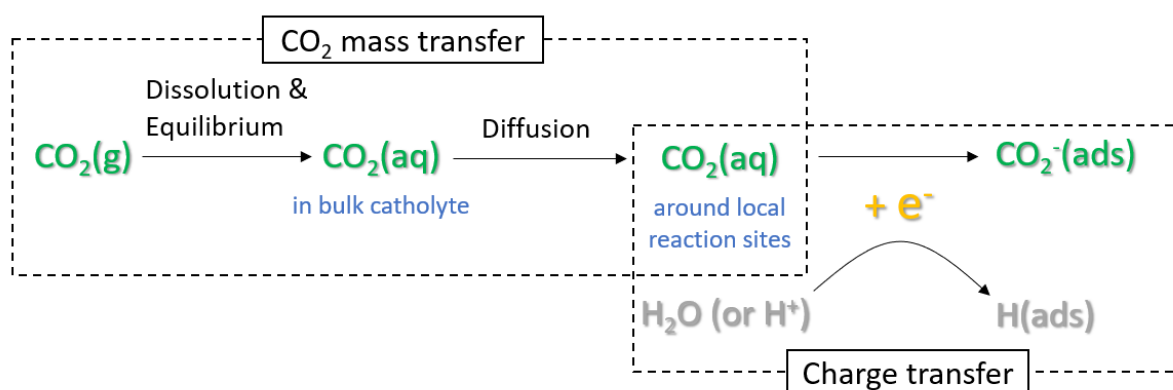


Figure 2-2 Mass transfer of CO₂ and competitive charge transfer in the aqueous eCO₂RR system with applying the CO₂ supply method of “purging into electrolyte”.

As presented in Table 2-2, Step 1 primarily consists of a physical mass transfer process as illustrated in Equation (2-11), and chemical reaction (2-13) or (2-15) (depends on the solution pH value), positively providing and negatively consuming the reactant CO₂(aq) respectively.

Table 2-2 CO₂ mass transfer steps and the corresponding rates

	Positive process	Negative process	Rate of the process
Step 1 Dissolution and Equilibrium	Physical mass transfer: $CO_2(g) + H_2O(l) \xrightleftharpoons{K_0} CO_2(aq)$ $+ x H_2O(l)$ $\equiv CO_2 \cdot (H_2O)_x$ (2-11)		$R_{MT} = k_{G/L} a p_{CO_2} K_0$ (2-12) R_{MT} : mass transfer rate (M s ⁻¹) $k_{G/L}$: mass transfer coefficient (m s ⁻¹), a : specific gas/liquid surface area (m ² m ⁻³), p_{CO_2} : CO ₂ partial pressure(kPa) K_0 : equilibrium constant, = $1 \times 10^{18} T^{-8.7051}$ (M kPa ⁻¹)
		Chemical reaction: pH < 8 $CO_2(aq) + H_2O(l) \xrightleftharpoons[k_{-0}]{k_{+0}} H_2CO_3 \rightleftharpoons H^+ + HCO_3^-$ (2-13)	$-\frac{d[CO_2(aq)]}{t} = k_{+0} h_L \varepsilon [CO_2(aq)]$ (2-14) k_{+0} : rate constant, = 3×10^{-2} (s ⁻¹); k_{-0} : rate constant, = 23.7 (s ⁻¹) h_L : liquid hold-up ε : voidage of 3D cathode $[CO_2(aq)]$: concentration of dissolved CO ₂ in bulk electrolyte (M)
		pH > 10 $CO_2(aq) + OH^- \xrightleftharpoons[k_{-1}]{k_{+1}} HCO_3^-$ (2-15)	$-\frac{d[CO_2(aq)]}{t} = k_{+1} h_L \varepsilon [CO_2(aq)] [OH^-]$ (2-16) k_{+1} : rate constant, = 8.5×10^3 (s ⁻¹); k_{-1} : rate constant, = 2.3×10^{-4} (s ⁻¹)
		8 < pH < 10, (2-13) and (2-15) both take place	$-\frac{d[CO_2(aq)]}{t} = (k_{+0} + k_{+1} [OH^-]) h_L \varepsilon [CO_2(aq)]$ (2-17)
Step 2 Diffusion	CO ₂ (aq) diffusion from the bulk electrolyte to local active sites		Fick's second Law $\frac{\partial C}{\partial t} = -D \frac{\partial^2 C}{\partial x^2}$ (2-18) C : concentration of CO ₂ (aq) (M) x : diffusion distance (m) D : diffusion coefficient of CO ₂ (aq) in water (m ² s ⁻¹) t : time (s)

The rate of CO₂(aq) generation via the physical mass transfer process was described in Equation (2-12), which is a function of the gas/liquid mass transfer coefficient $k_{G/L}$, specific gas/liquid surface area a , CO₂ partial pressure p_{CO_2} , and the equilibrium constant K_0 . The eCO₂RR reaction rate could be developed through optimizing this process. Hori et al.⁴⁰ found the partial current density of CO production on the gold electrode presented a linearly rising trend with the CO₂ partial pressure p_{CO_2} within the range from 0.25 to 1.0 atm. In order to enhance the specific gas/liquid surface area a , Peter et al.⁴¹ applied a glass frit bubbler to produce microbubbles with less than 0.2 mm radius. The CO₂ microbubbles contributed to higher hydrocarbon/H₂ ratio in the products of eCO₂RR, in comparison with bigger CO₂ bubbles (~0.5 mm radius) provided by a capillary tube bubbler. The equilibrium constant K_0 is a temperature-dependent constant, decreased with higher temperature. Thus, the R_{MT} is inversely correlated with the temperature, which is the reason for a declined CO₂ solubility in aqueous solution with increasing temperature.

However, the chemical reaction (2-13) or (2-15) consumes the formed CO₂(aq) immediately. When the solution pH is less than 8, reaction (2-13) dominates the whole chemical step which is a very slow step with forwarding reaction rate ($k_{+0}=3.0\times 10^{-2} \text{ s}^{-1}$) much smaller than the backward reaction rate ($k_{-0}=23.7 \text{ s}^{-1}$). Based on this, some studies⁴²⁻⁴³ used acidic catholyte to ease the CO₂(aq) consuming process. When electrolyte pH is over 10, reaction (2-15) dominates the whole chemical process which is a very fast step with the forward reaction rate ($k_{+1}=8.5\times 10^3 \text{ s}^{-1}$) much bigger than the backward reaction rate ($k_{-1}=2.3\times 10^{-4} \text{ s}^{-1}$). Therefore, when purging CO₂ gas into the alkaline electrolyte, the bulk solution turned to be neutral quickly. Overall, according to the two dynamic processes of CO₂(aq) providing and consumption simultaneously, how much CO₂(aq) (or CO₂·(H₂O)_x) could be the balanced eventually is one of the most important principles of catholyte selection. Heng et al.³⁹ calculated the CO₂·(H₂O)_x equilibrium concentrations after CO₂ bubbling into some popular catholytes, among which, KHCO₃

solution is selected to be the optimal catholyte since it can balance the higher concentration of $\text{CO}_2\cdot(\text{H}_2\text{O})_x$. 0.1 M, 0.5 M and 1.5 M KHCO_3 solutions balanced 33 mM, 37 mM and 45 mM $\text{CO}_2\cdot(\text{H}_2\text{O})_x$ respectively after adequate CO_2 bubbling, which means KHCO_3 with higher concentration has slightly more dissolved CO_2 reactant.

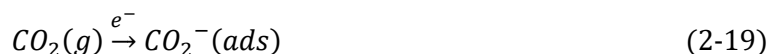
Unfortunately, Step 2 will further reduce the concentration of $\text{CO}_2(\text{aq})$ by the diffusion distance and time, which is a physical diffusion process that could be understood by Fick's Second Law²⁵. The diffusion coefficient D is a complex function of the intrinsic physical properties of electrolyte and environmental conditions. Due to the smaller liquid viscosity of more dilute solution under higher temperature, D_{CO_2} in aqueous solution is positively correlated to temperature but negatively correlated to the salt concentration⁴⁴. Thus, KHCO_3 solution with higher concentration more strongly constrains $\text{CO}_2(\text{aq})$ diffusion in this step, even though it can balance more $\text{CO}_2(\text{aq})$ after Step 1. Moreover, under the reduction potential, diffusion of $\text{CO}_2(\text{aq})$ adjacent to the double layer is actually more complex due to the adsorption of cations. Joaquin et al.⁴⁵ found that although the alkali metal cations wouldn't be reduced under the potential of eCO_2RR , they would be hydrated and absorbed around the outer Helmholtz layer of the cathode and create a dipole electric field ($1 \text{ V } \text{\AA}^{-1}$), whose stabilization decreases the energy for *CO_2 adsorption. Accordingly, the higher salt concentration of the catholyte could not facilitate the $\text{CO}_2(\text{aq})$ diffusion in this step because of the lower diffusion coefficient and larger coverage of cations around the reaction sites. This diffusion problem along with the high concentration catholyte was observed by Hori et al.³⁷ and Xiang et al.³⁶ that with the CO_2 supply method of "purging into electrolyte", the ratio of carbonaceous products/ H_2 from eCO_2RR decreased with the increasing catholyte salt concentration.

Summarily, when applying "purging into electrolyte" method to supply CO_2 , CO_2 mass transfer is mainly constrained by the low solubility and inefficient diffusion from the bulk electrolyte to the local reaction sites, resulting in incomparable competitiveness of eCO_2RR against HER

and reduced current efficiency of carbonaceous products.

2.2.1.2 CO₂ diffusion from gas diffusion electrode

An increasing number of GDE-related works have been published in recent years for the sake of enhancing the CO₂ mass transfer, as CO₂ gas could be feed directly to the reaction sites with an efficient gas-liquid-solid three-phase boundary. This gas supply method has been applied in hydrogen-oxygen fuel cells for a long time⁴⁶, the direct gas adsorption has been accepted as the mass transfer mechanism of the gas reactants H₂ and O₂⁴⁷⁻⁴⁹. In a similar way, the reactant of eCO₂RR by applying CO₂ “diffusion from GDE” was perceived to be gaseous CO₂⁵⁰⁻⁵¹ rather than the hydrated CO₂(aq) as discussed in the previous Section 2.2.1.1. Therefore, CO₂ gas could be directly adsorbed and activated by a less-restricted pathway without going through catholyte media, as illustrated in Equation (2-19).



The most outstanding achievement of applying GDE in eCO₂RR is the remarkable current density (j) which is normally over hundreds of mA cm⁻², bring the industrial potential to this currently bench-scale reaction¹⁸. In fact, it was found that electrolyte engineering played the predominant role in the high current density achievement rather than the effect of CO₂ supply way³⁶. Strong alkali with a high concentration of OH⁻ enabled low resistance in both of the cell internal and charge transfer was certificated to be the optimum aqueous electrolyte for eCO₂RR⁵². The use of strong alkaline media as the catholyte could be only enabled by the unique configuration of the GDE reactor since the CO₂ dissolving could be largely alleviated.

CO₂ mass transfer enhanced with a big step when transiting the CO₂ supply method from “purging into electrolyte” to “diffusion from GDE”. To the author’s best knowledge, apart from the development of electrode material/catalyst, there seems to have no much reported-work

about further enhancing the CO₂ mass transfer in the GDE system in a macroscopic view like cell configuration and reaction conditions. Only few studies⁵³⁻⁵⁶ were carried out on the effect of cell pressure. Gabardo et al.¹⁷ studied the pressurization effects on eCO₂RR selectivity and efficiency in the GDE cell, the FE of CO enhanced about 40% when rising the cell pressure from 1 to 7 atm. The reason for the selectivity shift was assumed to be the increased CO₂ surface coverage.

It is worth mentioning that the GDE system applying liquid catholyte commonly suffers the flooding problem. Poor reaction stability of fewer than 10 hours was observed accordingly, since the hydrophobic layers within GDE can be degraded during electrolysis, especially in alkaline media²⁰. The infiltration of liquid catholyte into the CO₂ gas phase alters the CO₂ supply method from “diffusion from GDE” back to “purging into electrolyte”, CO₂ mass transfer reduced by this degradation. A novel electrode architecture was then delivered by Dinh et al.⁵², to create an abrupt interface with graphite/carbon nanoparticles/Cu catalyst/PTFE layer to overcome the liquid electrolyte flooding issue. The reaction could be maintained with 70% Faradaic efficiency towards C₂H₄ for 150 hours. Apart from constructing a robust GDE to avoid flooding, some studies⁵⁷ abandoned the liquid electrolyte and adopted the polymer electrolyte membrane to fabricate a membrane electrode assembly (MEA) in compressed reactors. Protons can be supplied by vapor co-streamed with the CO₂ gas or ion migration from the anodic side via a proton exchange membrane (PEM) as illustrated in Figure 2-3⁵⁸. Lee et al.⁵⁰ applied the Sn-GDE (cathode), Nafion membrane, and Pt-GDE (anode) to fabricate the MEA for formate production from eCO₂RR, a high Faradaic efficiency about 90% was maintained for 50 hours. Kutz et al.⁵⁹ developed a robust membrane with using imidazolium-functionalized styrene and vinylbenzyl chloride polymer for eCO₂RR with an MEA configuration, showing remarkable durability of around 6 months for producing CO with 90% Faradaic efficiency and 50 mA cm⁻² current density.

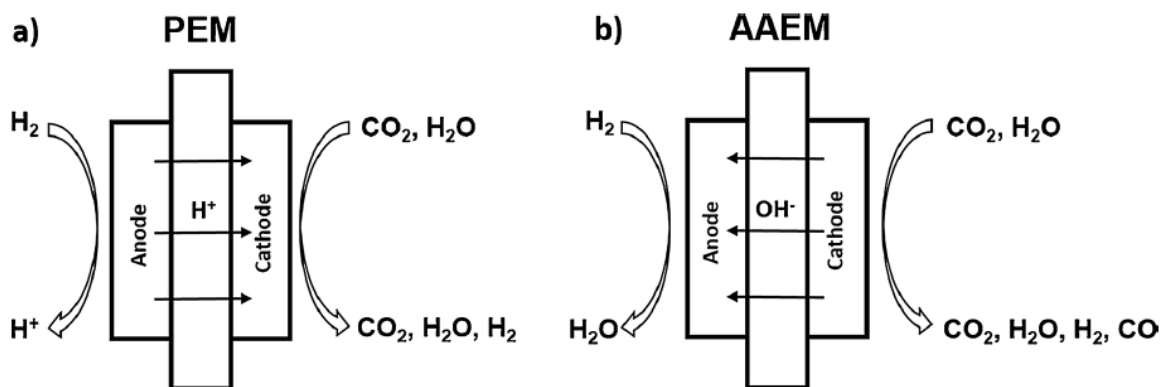


Figure 2-3 Scheme of the eCO₂RR reactor with the MEA configuration. The difference in ion transfer of using a) proton exchange membrane (PEM), and b) alkaline anion exchange membrane (AAEM). Reproduced from Ref.⁵⁸ with permission from the Journal of CO₂ Utilization Owner Societies.

Overall, the liquid-phase system of applying “purging into electrolyte” method to supply CO₂ is simple and handy to construct but constrains CO₂ mass transfer. Applying “diffusion from GDE” in the gas-phase system is a promising transit to perform a highly-efficient mass transfer and developed current efficiency towards CO₂ reduction, but the flooding problem will lead to poor durability which can be alleviated by adopting polymer electrolyte membrane. The development of CO₂ mass transfer from a macroscopic view can be approached by improving the reactor configuration and optimising the reaction conditions, contributes to higher CO₂ coverage around the cathode.

2.2.2 CO₂ mass transfer from the microscopic view – internal diffusion

The CO₂ mass transfer from a microscopic view is the internal diffusion of CO₂ from cathode adjacency to the reaction active sites, which is a physical adsorption process mostly relies on the cathode or catalyst material. To develop physical adsorption of CO₂ molecules by solid materials, enlarging the surface area of the adsorbent⁶⁰ is a promising approach which has been normally implemented by increasing the surface roughness of the solid electrode⁶¹⁻⁶² or using porous supporters⁶³. Since the activation function of the electrode/catalyst, the physical

adsorption of CO₂ has been always studied along with its chemical adsorption. As far as the author knows, the individual effect of CO₂ physical adsorption on electrode/catalyst on eCO₂RR was rarely reported. The following section will focus on the solid cathode/catalyst material applied in eCO₂RR in terms of the adsorption effect and the selectivity towards different carbonaceous products.

2.3 Electro-catalysts for CO₂ reduction reaction

As mentioned in Section 2.1, high activation energy is required to activate the inert CO₂ molecules. An appropriate catalyst can reduce the reaction energy barrier and lead the reaction route to a desired direction. Catalysts that have been used in eCO₂RR can be classified as homogeneous and heterogeneous catalysts.

The homogeneous catalysts are molecularly defined compounds which play the role as a shuttle between electrode and CO₂ to drive indirect electrolysis⁶⁴, generally containing organometallic complexes and metal-free organocatalysts⁶⁵. Due to their targeted facilitation and highly efficient electron transport, low overpotential of eCO₂RR and better controllable selectivity for some carbonaceous products (usually CO, formate and oxalic acid) could be achieved. However, the high cost, toxicity and difficult separation of liquid products (when using ionic liquid) bring their own sustainability issues.

Transition metals with an incomplete *d* sub-shell are capable to catalytic activate CO₂. The inorganic pure metals, metal alloys, and metal oxides/chalcogenides have been mostly applied as the heterogeneous catalyst for eCO₂RR with many advantages like low cost, facile synthesis, high stability, and so on, enabling great potential for the scale-up and industrial application. This review section and the research of this thesis will emphasize the development of inorganic heterogeneous catalysts in eCO₂RR.

2.3.1 Design principle of the inorganic heterogeneous catalyst

The bulk metal electrodes were primarily studied. It should be most mentionable that Hori and his co-workers^{37, 66-68} pioneeringly used different transition metals for catalysing CO₂ reduction to investigate their intrinsic properties. In terms of the product selectivity, the active metals have been divided into four groups, as displayed in Figure 2-4 and Figure 2-5. The first group of metals (Cd, In, Sn, Hg, Tl, etc.) can activate CO₂ to mainly produce formate or formic acid (HCOO⁻) owing to its weak binding energy of CO₂⁻ intermediates. The second group (Ag, Au, Sb, Bi, etc.) has high bind energy of *COOH for further reduction but weakly bind CO* to the metal surface, where * refers to a catalytic site at which a species can adsorb, thus CO would be desorbed easily as a primary product. The fourth group (Ti, Fe, Ni, Pt, etc.) has low hydrogen evolution overpotential so that H₂ is much easier to be produced. Cu, classified as the 3rd group, should be the most special one which has unique ability to generate C_{≥1} hydrocarbons and their oxygenates. CO* was always recognized as a key intermediate for the formation pathway of multi-carbon products⁶⁹⁻⁷⁰.

1st Group: HCOO⁻
 2nd Group: CO
 3rd Group: (oxygenated) hydrocarbons
 4th Group: H₂

22 Ti 47.88	23 V 50.942	24 Cr 51.996	25 Mn 54.938	26 Fe 55.845	27 Co 58.933	28 Ni 58.693	29 Cu 63.546	30 Zn 65.39	31 Ga 69.723	32 Ge 72.64	33 As 74.922
40 Zr 91.224	41 Nb 92.906	42 Mo 95.94	43 Tc 98.907	44 Ru 101.07	45 Rh 102.906	46 Pd 106.42	47 Ag 107.868	48 Cd 112.411	49 In 114.818	50 Sn 118.71	51 Sb 121.760
72 Hf 178.49	73 Ta 180.948	74 W 183.85	75 Re 186.207	76 Os 190.23	77 Ir 192.22	78 Pt 195.08	79 Au 196.967	80 Hg 200.59	81 Tl 204.383	82 Pb 207.2	83 Bi 208.980

Figure 2-4 Grouping the transition metals in terms of selectivity towards HCOO⁻, CO, (oxygenated) hydrocarbons, and H₂ from eCO₂RR in aqueous electrolyte.

The product selectivity mostly relies on the binding energy of the key intermediates on the electrode/catalyst surface. Computational investigations of eCO₂RR selectivity have largely applied the Sabatier principle⁷¹, which states that an optimal catalyst is one that binds key

intermediates neither too strongly nor too weakly. Density functional theory (DFT) has been popularly applied as a useful tool to calculate the theoretical binding energy of key adsorbates in CO₂ reduction on surface of different catalysts.

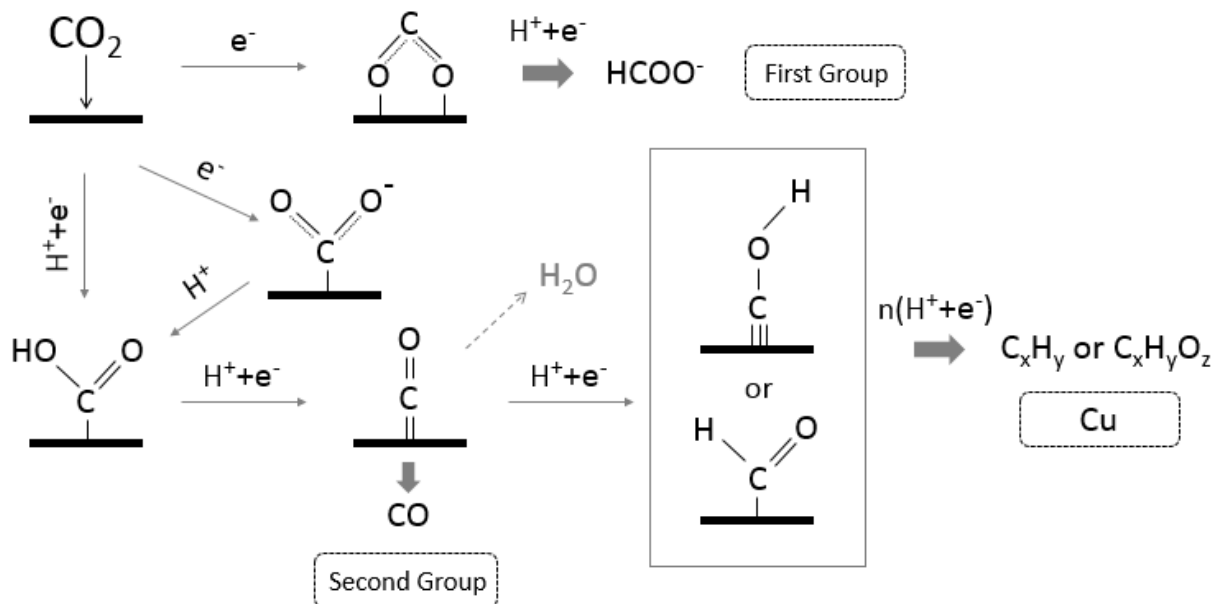


Figure 2-5 Possible reaction pathways for eCO₂RR on different groups of transition metals.

It has been accepted that *COOH and *OCHO are the key intermediates for CO and formate production respectively from eCO₂RR. Feaster et al.⁷² calculated the binding energies of *COOH and *OCHO on different metal surfaces, two volcano plots respectively described the relationship between *COOH binding energy and CO partial current density and that between *OCHO binding energy and formate partial current density are shown in Figure 2-6 a and b. Metals on the top of the volcano with high partial current density and moderate binding energy are commonly recognized as suitable catalysts for targeting products. Thus, Au and Sn here were speculated to be the optimum metal for CO and formate production respectively, which is in accordance with many experimental results.

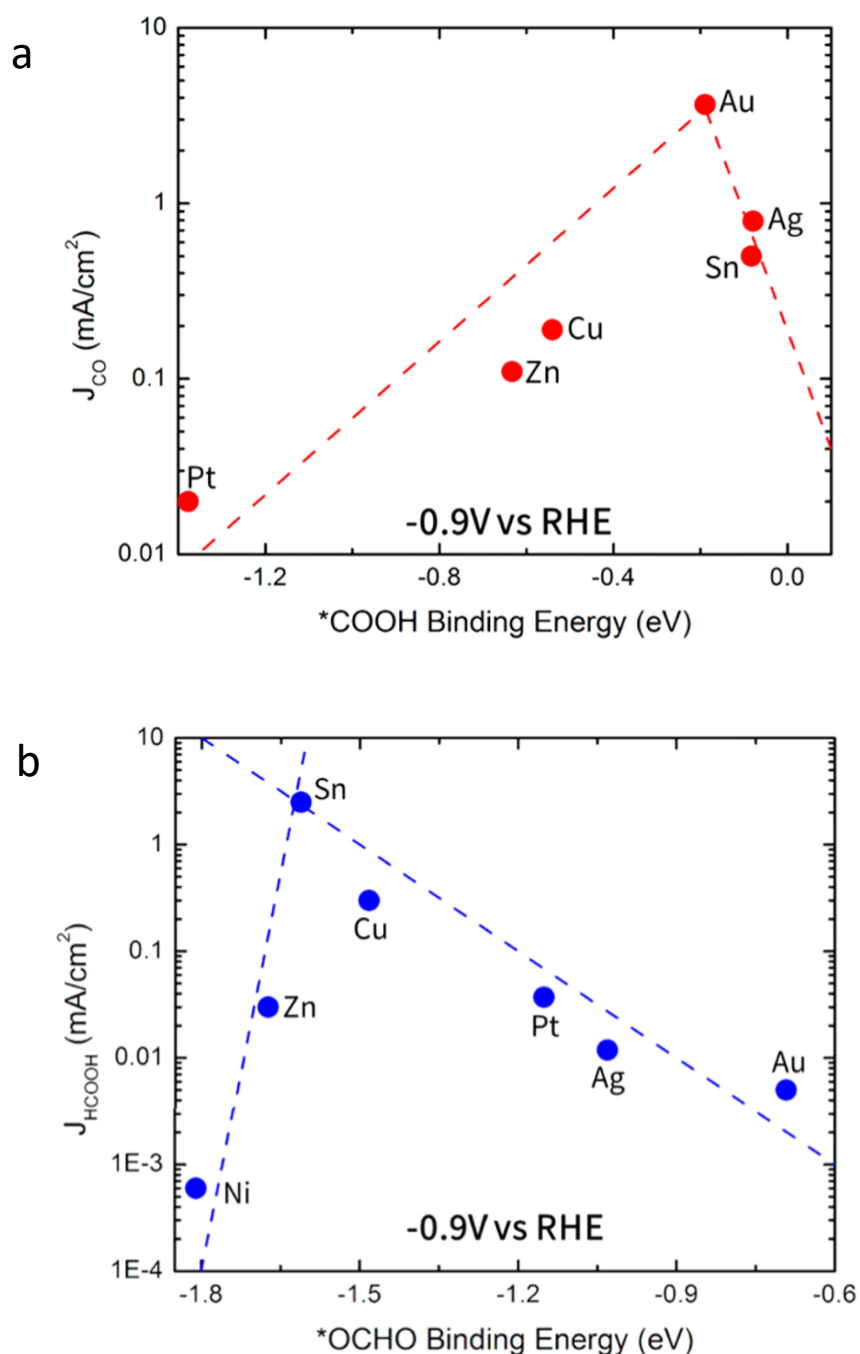


Figure 2-6 a) Volcano plot using *COOH binding energy as a descriptor for CO partial current density at -0.9 V vs. RHE. b) Volcano plot using *OCHO binding energy as a descriptor for formate partial current density at - 0.9 V vs. RHE. Reprinted with permission from Ref.⁷². Copyright (2017) American Chemical Society.

The formation of hydrocarbons and their oxygenates from CO₂ is much more complicated than CO and formate, as the transfer of more than two pairs of electron-proton is involved. Peterson et al.⁷³ carried out the DFT calculations to investigate the formation route of the simplest

hydrocarbon product CH₄ from CO₂ reduction. The protonation of absorbed CO* was investigated to be the most crucial step. Because as displayed in Figure 2-7 which presents the relationship between the CO binding energy and theoretical limiting potentials (U_L) for various protonation routes, CO* to CHO* with the most negative U_L determines the overpotential of CH₄ generation from CO₂. Cu, standing at the top of the volcano-like curve constructed by the two bottom-most lines, shows the smallest theoretical overpotential (the difference between the equilibrium and limiting potentials) and moderate binding energy of CO* which facilitates the further protonation to generate hydrocarbons.

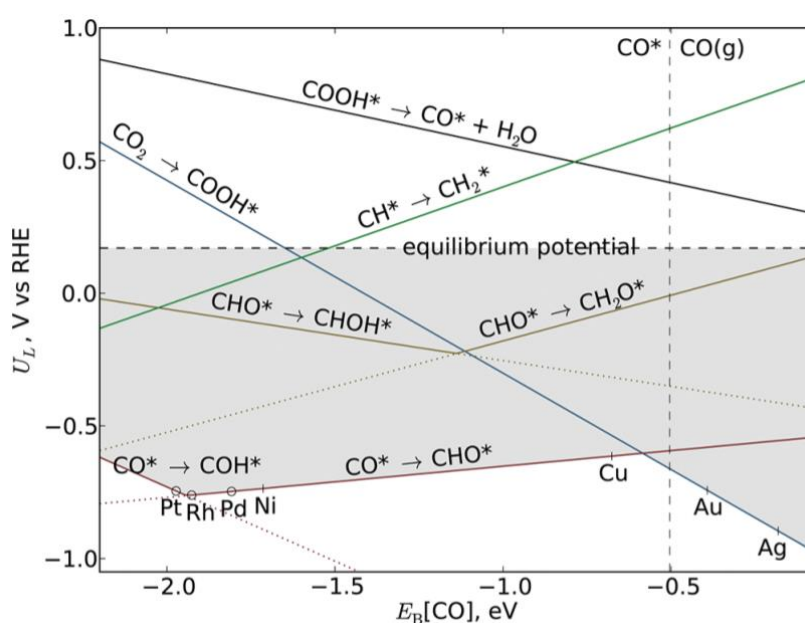


Figure 2-7 Limiting potentials (U_L) for elementary proton-transfer steps as a function of CO* binding energy ($E_B[\text{CO}]$). Competitive pathways are shown as lines of the same colour, and the more favourable route is shown as a solid line, while the less favourable route is shown dotted. The equilibrium potential for the overall electrochemical reduction of CO₂ to CH₄ is +0.17 V (vs. RHE), indicated as the horizontal dash line. Reprinted with permission from Ref.⁷³. Copyright (2012) American Chemical Society.

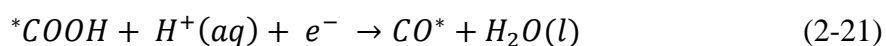
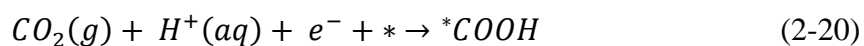
CO* is also the key intermediate for multi-carbon products such as ethylene and ethanol, instead of its direct protonation in the case of CH₄ production, dimerization of CO* has been mostly agreed as the rate determining step for the growth of carbon chain⁷⁴⁻⁷⁵. Products of eCO₂RR by using Cu catalysts always have a wide distribution. The binding energy of key

intermediates varied by different Cu crystal surfaces which is the key factor to alter the reaction selectivity. This structural dependence for the reduction of CO₂ on Cu has been reported by Hori and co-workers⁷⁶: C₂H₄ is produced more favourably on Cu(100) while CH₄ is more preferentially formed on Cu(111). From the DFT calculation of Kortlever et al.⁷⁰, the formation of CO dimer was most stable on square arrangements of 4 surface atoms, explaining the preferential formation of C₂H₄ on Cu(100). Liu et al.⁷⁷ also conducted DFT calculations to study the unique role of Cu in eCO₂RR. Different from most of the simulation studies which only considered the surface layer of atoms, the subsurface layer of Cu was also included. The interaction between surface Cu and carbon monomers which preferentially inserted into subsurface sites of Cu was demonstrated to play a crucial role in hydrocarbon formation.

The theoretical study which mostly built on DFT calculation is instructive and meaningful to the catalyst design for eCO₂RR. However, most DFT calculations were performed on a vacuum-metal surface or solid-liquid interface, the actual reaction situation is more complicated combined with the change of catalyst phase and morphology during reduction reaction, the competitive HER, the inefficient CO₂ mass transfer, etc. The following sections review heterogeneous catalysts in experimental studies for CO₂ reduction in aqueous media, classified by their selectivity towards CO, formate, and (oxygenated) hydrocarbons.

2.3.2 Heterogeneous catalysts for CO production

CO is a promising product from eCO₂RR, it has been maturely utilized in the chemical industry as a building block for the production of multi-carbon fuels and chemicals through Fischer-Tropsch synthesis⁷⁸⁻⁷⁹. Zhu et al.⁸⁰ studied the thermodynamic pathway of CO₂ reduction to CO, which is typically considered to consist of three elementary steps as described in Equation (2-20) to (2-22).



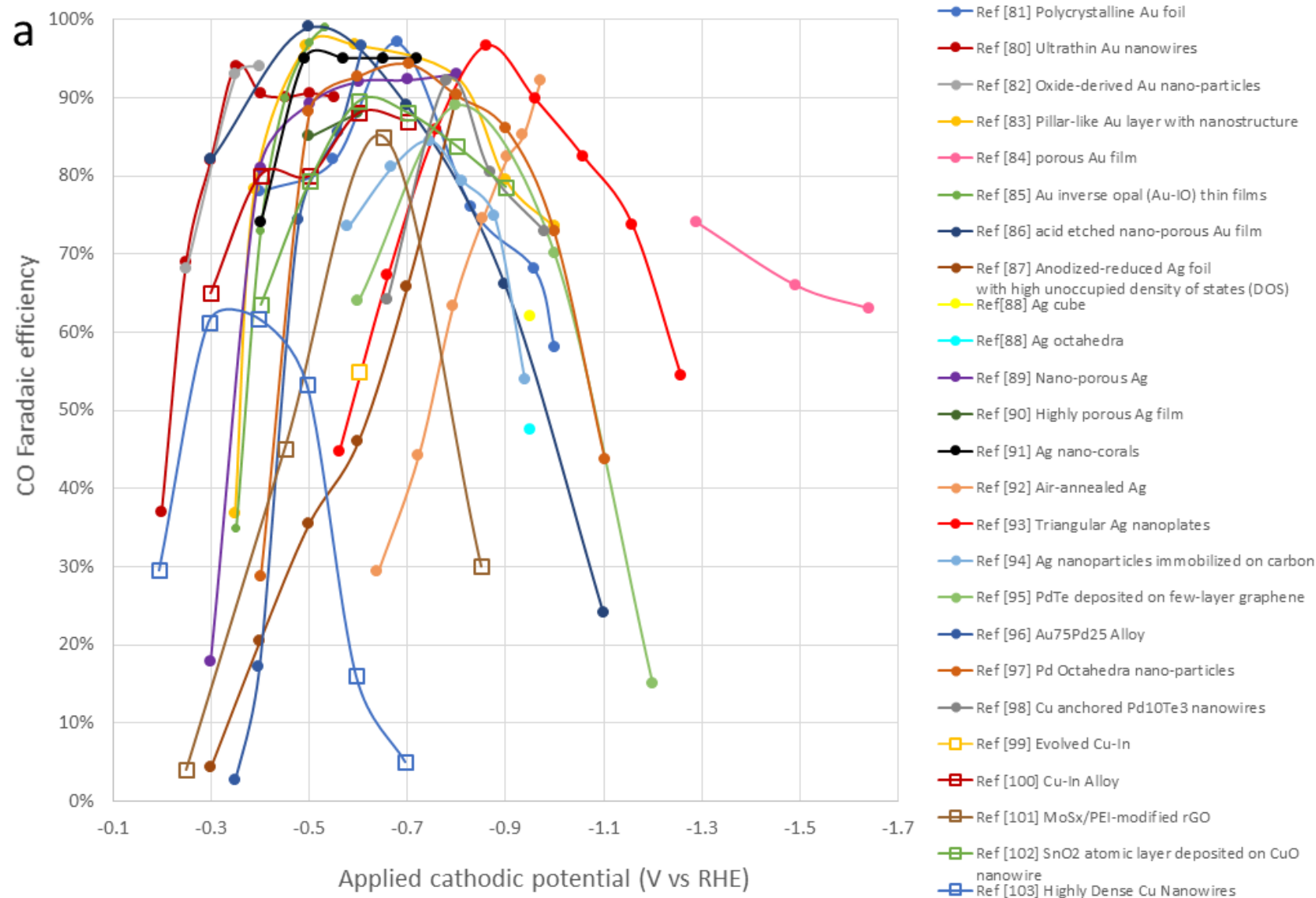


Thus, an ideal electrocatalyst for CO production from CO₂ reduction is expected to have a strong affinity to CO₂⁻⁵⁹, strong binding of *COOH, but weak CO* binding energy which has been widely agreed by related works. As stated above in Figure 2-6 a and Figure 2-7, noble metals such as Au, Ag, and Pd with this adsorption nature have been most-popularly selected. CO₂ supply method linked to CO₂ mass transfer has a great impact on eCO₂RR performance as discussed in Section 2.2.1, therefore the CO-selective catalysts will be reviewed respectively depends on which CO₂ supply method applied, i.e. using either two-chamber cell or GDE cell.

CO-selective catalysts in the two-chamber cell system

Most of the CO production works were operated in a two-chamber (2C) cell using noble-metal-based catalysts. Table AI-1 summarised the heterogeneous catalysts for CO production from eCO₂RR reported in recent years. The catalytic performance for CO production was generally weighed by CO Faradaic efficiency (FE) and partial current density (j_{CO}), which respectively relate to CO selectivity and production rate. Based on Table AI-1, CO FE and j_{CO} reported in related literature are respectively plotted in Figure 2-8 a and b, both showing a strong reliance on the applied potential. These two graphs overall indicate the applied potential to drive CO₂ reduction was mostly selected in the range of -0.2 ~ -1.3 V (vs. RHE), providing an experimental idea to the following lab work.

As shown in Figure 2-8 a, most of the reported materials⁸⁰⁻¹⁰³ reached higher than 90% CO FE in a moderate potential range, which are mostly noble-metal-based catalysts (solid round symbol). The non-noble-metal-based catalysts, drawn by hollow square symbol, generally perform < 90% CO FE. Figure 2-8 b presents an increasing trend of CO partial current density with the enhanced overpotential in most of the works, indicating the possibility to control CO production rate by energy input.



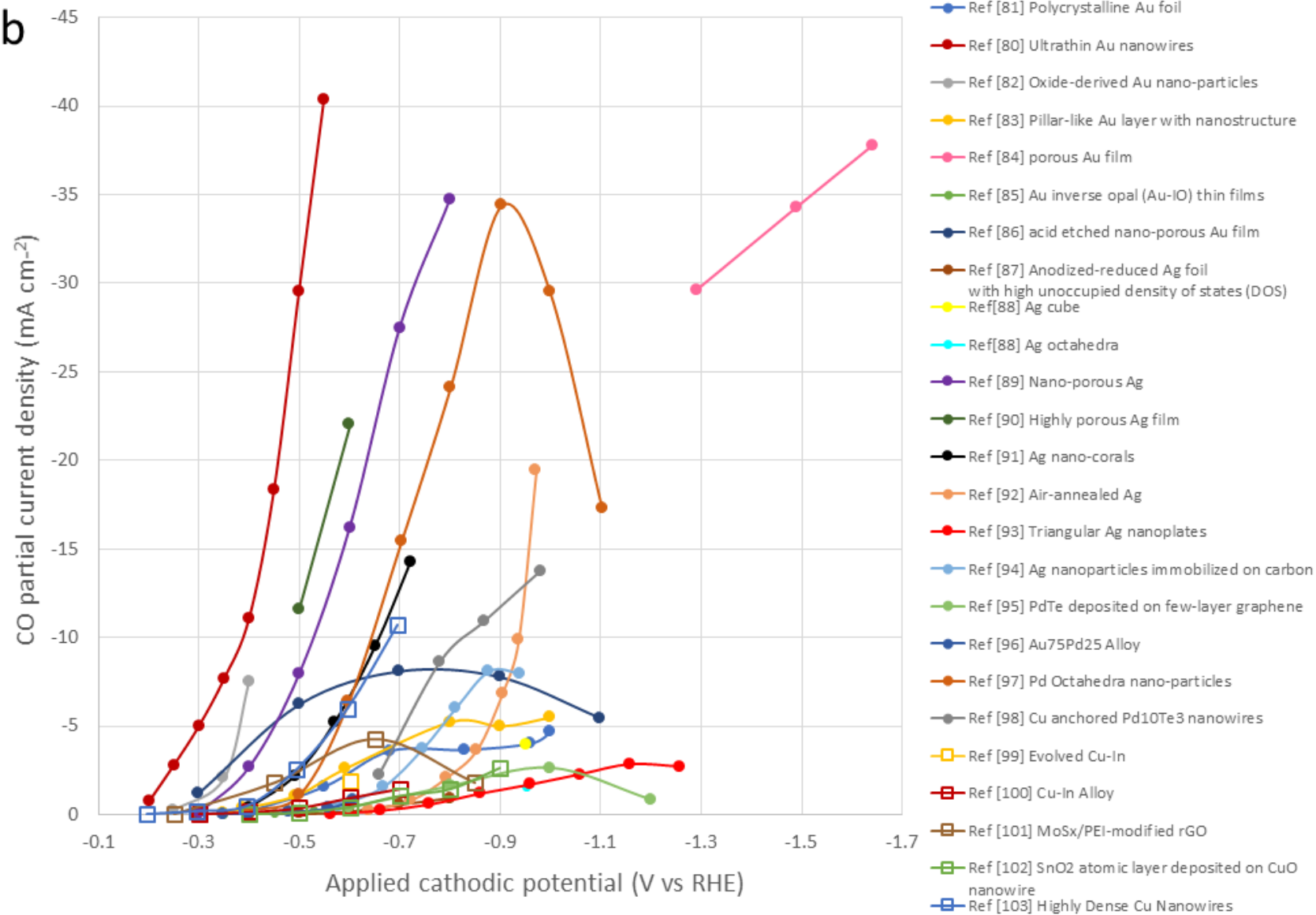
b

Figure 2-8 Catalytic performances of reported heterogeneous catalysts for eCO₂RR to CO in recent publications, with the solid round symbol representing the noble-metal based catalysts and hollow square symbol for non-noble-metal based catalysts. An overview of a) CO Faradaic efficiency and b) CO partial current density as a function of applied cathodic potential.

Since the pristine Au⁸¹, Ag⁸⁹ bulk metal electrodes have shown their capability to exclusively convert CO₂ to CO, however, high overpotential is always required⁸⁹. The catalyst modification to further develop CO production was mostly focused on constructing a rough surface to increase the electrochemical surface area (ECSA) as well as altering the surface atomic structure. Kim et al.⁸³ constructed two different Au nanostructure morphologies, nano-porous Au and Au nano-pillar, both exhibited significantly higher CO selectivity at a low overpotential than the untreated Au film. The reason was assumed to be the high density of grain boundaries which can assist with faster stabilization of the CO₂⁻. Stevens et al.⁸⁴ reached the same conclusion in their work on using Au porous film to selectively reduce CO₂ to CO. Zhu et al.⁸⁰ firstly developed a facile seed-mediated growth method to synthesize ultrathin (2 nm wide) Au nanowires (NWs) with dominant edge sites, showing enhancement on CO₂ reduction to CO with 94% FE. Their DFT calculations illustrated both *COOH and *CO preferred to be bond to the bridge site on the Au NW edge, with *COOH binding marginally (0.04 eV) stronger than that on the Au(211) edge, but *CO binding (0.23 eV) weaker than that on the Au₁₃ corner. This suggests that NW surface with maximal edge sites facilitates CO₂ activation to *COOH and the desorption of *CO. The applied modification approaches of Ag catalyst are similar to those of Au, with most of the works devoted to enhancing the catalyst surface roughness. For example, Lu et al.⁸⁹ found nano-porous Ag as an eCO₂RR electrocatalyst performed higher CO selectivity (92%) and lower overpotential (<0.50 V) than its polycrystalline counterpart. Hsieh et al.⁹¹ reported a high-surface-area Ag nano-coral catalyst for eCO₂RR, showing 95% CO FE at the low overpotential of 0.37 V and 32-fold enhancement in surface-area normalized activity compare to Ag foil. Another noble-metal Pd was normally modified by adding other metal

components, in order to alter the binding energy towards reaction intermediates by the synergistic effect. Tao et al.⁹⁵ found doping a small amount of Te on Pd can develop CO FE to higher than 90% at low overpotential. This mechanism was deduced by DFT calculations, indicating that Te adatoms preferentially bind at the terrace sites of Pd, thereby suppressing HER.

It has been mature to apply those noble metals in highly-selective CO production from eCO₂RR, even with the use of GDE cell.

CO-selective catalysts in the GDE cell system

As illustrated in Section 2.2.1.2, the use of the GDE system to a large extent develops CO₂ mass transfer and therefore increases the Faradaic efficiency towards carbonaceous products against H₂. Related works on highly-selective CO production in GDE cell system is concluded in Table AI-2. Nearly all carried out by using the noble Ag catalyst, reaching >90% CO FE and >100 mA cm⁻² CO partial current density when applied the potential less-negative than -1 V¹⁰⁴⁻¹⁰⁵.

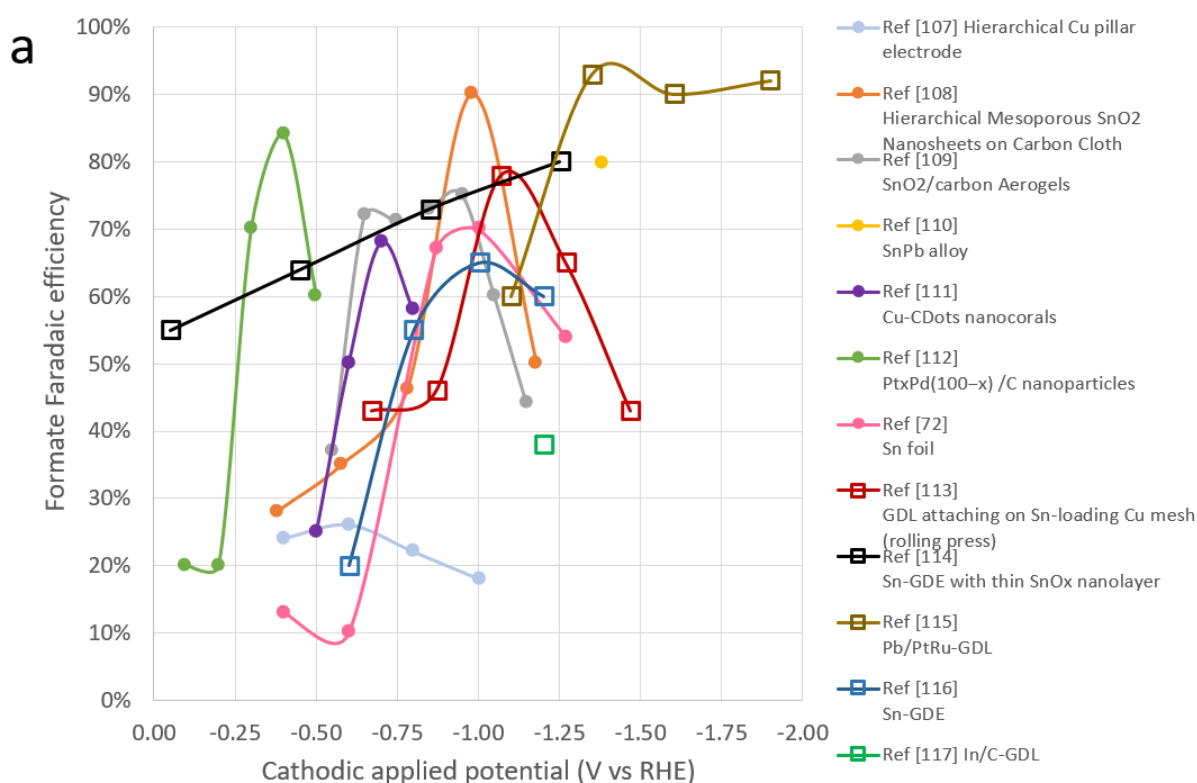
The use of noble-metals as the catalysts brings its own sustainability issues. In terms of catalyst development for the reaction scale-up, non-noble-metal materials should be more focused. But from the existed study⁹⁹⁻¹⁰³, high-level of both CO FE >90% and CO partial current density >100 mA cm⁻² are yet to be reached by the non-noble materials. To promote the industrialization of CO₂ reduction to CO, it still needs work on developing cheap catalysts with facile synthesis method and the combination with the GDE system.

2.3.3 Heterogeneous catalyst for formate production

Liquid products from eCO₂RR have obvious advantages in terms of transportation, storage, as well as handling. Formate (or formic acid) becomes the most common liquid product as the production route is simple with transferring only two pairs of electrons and protons. Compared

to the other two popular liquid products, methanol and ethanol, with higher energy density than formate, formate has its outstanding advantages to be a fuel for electrogenesis as it is non-flammable and non-toxic. In addition, when used in a fuel cell, it operates at a theoretical potential of 1.45V, which is 0.24 V, 0.31 V, and 0.22 V higher than the methanol, ethanol, and hydrogen fuel cells respectively¹⁰⁶.

As stated in Section 2.3.1, the bidentate *OCHO is assumed to be the key intermediate for the formation of formate. With this adsorption nature, Sn, Cu, Pb, and In were normally selected as the catalysts, among which Sn and Cu have been mostly studied due to the lower cost. The research on formate-selective catalysts can be also discussed respectively in different cells. Table AI-3 and AI-4 respectively summarises the formate-selective catalysts in two-chamber (2C) cell and GDE cell system. Their potential-dependent formate FE and partial current density are respectively plotted in Figure 2-9 a and b, with the solid round symbol representing the results in 2C cell and hollow square symbol for GDE cell system^{72, 107-117}.



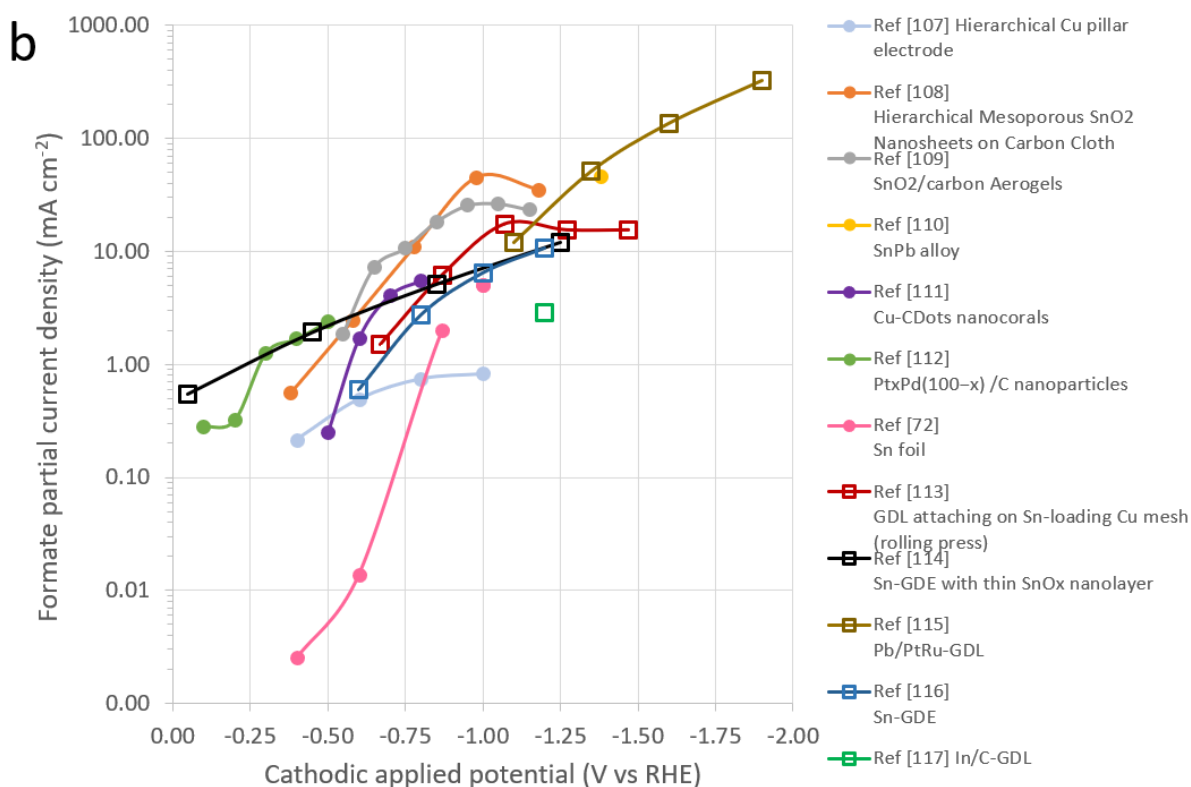


Figure 2-9 Catalytic performances of reported heterogeneous catalysts for eCO₂RR to formate, with the solid round symbol representing the results in 2C cell and hollow square symbol for GDE cell system. An overview of a) formate Faradaic efficiency and b) formate partial current density as a function of cathodic potential.

As shown in Figure 2-9 a, the reported catalysts averagely achieved higher than 50% FE for formate production, and few works surpassed 90%^{108, 115}. Similar to the CO FE presented in Figure 2-8 a, formate FE shows a strong reliance on the potential in majority of those works, which is boosted at a specific potential or a narrow potential range. It seems that, from the reported works, Sn is the most formate-selective metal to reach >50% FE in a single-component manner while Cu and Pb mostly cooperated with other active components to achieve high FE selectivity. From Figure 2-9 b, the partial current density of formate nearly, but not regularly, increased with the increasing overpotential, posing the potential of controlling formate production rate by the energy input.

Since those heterogeneous catalysts used for formate production were varied, and inconformity

of reaction conditions existed between different works, it is difficult to reach a conclusion of which catalyst material is optimum for formate production. However, some general ideas of constructing an active surface preferable for formate production could be still enlightened from the existed works.

As stated above, Sn could be used as a single-component catalyst for highly-selective formate production, thus approaches to further optimize Sn were normally focused on enlarging the specific surface area. Li et al.¹⁰⁸ suggested a 3D hierarchical structure composed of mesoporous SnO₂ nanosheets on carbon cloth to be a formate-selective catalytic material for eCO₂RR, which provided a large surface area and facilitates charge and mass transfer contributing to high formate partial current density of about 45 mA cm⁻² at a moderate overpotential (0.88 V) with formate FE about 87%. Yu et al.¹⁰⁹ demonstrated adding porous supporter into active Sn catalyst could also reach the aim of larger surface area and developed mass transfer. Highly-porous carbon aerogel was used as the support of SnO₂ in their work, which enabled higher electrode conductivity and achieved formate FE of ~76% and partial current density of ~26 mA cm⁻² at -0.96 V (vs. RHE). Choi et al.¹¹⁰ found alloying Sn with 22.7% Pb could develop the electrode conductivity and the performance of eCO₂RR to formate compared to pristine Sn, i.e., formate FE and partial current density respectively raised about 15% and 8 mA cm⁻² at -2.0 V (vs Ag/AgCl) in contrast with the pristine Sn electrode.

For scaling up formate production from eCO₂RR, a highly-efficient catalyst with low-cost is still to be developed. Also, it is necessary to construct a controllable and stable reaction system allowing formate yield to be controlled by the energy-input in general conditions.

2.3.4 *Heterogeneous catalyst for (oxygenated) hydrocarbons*

Hydrocarbons and oxygenated hydrocarbons, especially with multi-carbon, are the most challenging products from eCO₂RR, but attract most of the research interests due to their high

energy density and abundant hydrogen storage. Their current industrial production still largely relies on fossil fuels so that the direct one-step CO₂ conversion to (oxygenated) hydrocarbons was endowed with double significance in the environment and energy. However, the reaction route for the formation of (oxygenated) hydrocarbons is very complicated and yet to be figured out. Even for the simplest hydrocarbon CH₄, 8 pairs of electrons and protons transfer are involved. A very negative potential (< -0.8 V vs. RHE) is always necessary to conquer the activation barrier in the reaction pathway.

As stated in Section 2.3.1, only Cu in transition metal group shows catalytic activity to produce (oxygenated) hydrocarbons from eCO₂RR, but distribution of the products is quite wide. A guiding research from Kuhl et al.¹¹⁸ observed 16 different products from eCO₂RR catalysed by polycrystalline Cu in CO₂-saturated 0.1 M KHCO₃ catholyte, this representative result is attached as Figure 2-10.

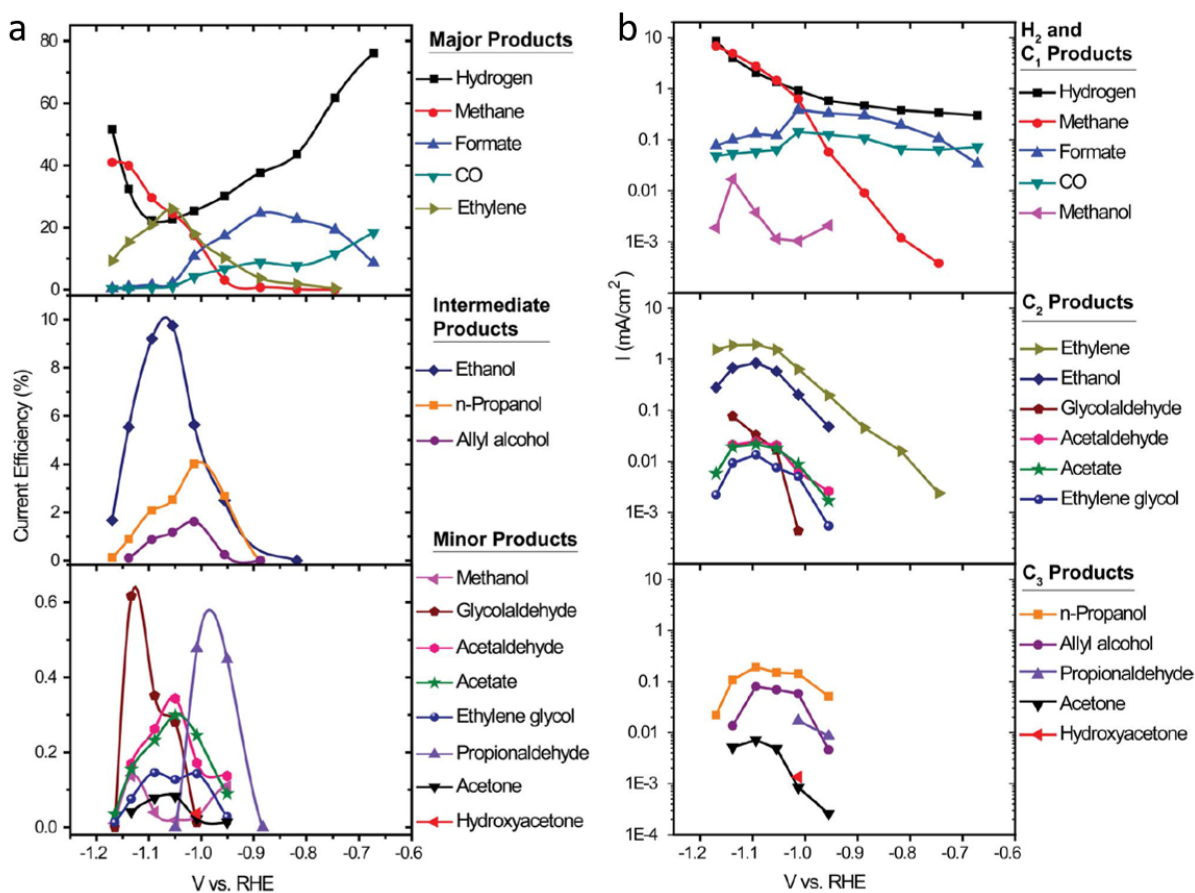


Figure 2-10 The performance of eCO₂RR on polycrystalline Cu. a) Current/Faradaic efficiency and b) partial current density as a function of cathodic potential for all the products. Reproduced from Ref.¹¹⁸ by permission of The Royal Society of Chemistry.

As shown in Figure 2-10, methane and ethylene are the two major hydrocarbon products with achieving more than 20% FE, ethanol also reached 10% FE as an intermediate product. Different from CO and formate that both reached > 90% selectivity from reported results, how to improve the selectivity towards certain hydrocarbon or oxygenated hydrocarbon is still a problem to be solved. From current related studies, only CH₄, C₂H₄, CH₃OH and C₂H₅OH have reached higher than 20% FE, mostly achieved by modifying Cu catalyst as summarized in Table AI-5. The modification works on Cu-based catalysts are generally in the following 4 aspects.

Altering the Lattice/crystal structure of pure Cu

Hori et al.³⁷ employed polycrystalline copper in eCO₂RR in 1989, the Faradaic efficiency of CH₄ and C₂H₄ were 29.4% and 30.1% respectively, in the ratio 1.0, similar to Kuhl's¹¹⁸ results mentioned before. Years later, Hori published another paper in 2002⁷⁶, using a series of single-crystal Cu electrodes to investigate the crystal-structural dependence of Cu electrode on eCO₂RR. All of the studies concluded that the product distribution of eCO₂RR varied greatly with the crystal lattice structure of the Cu electrode: Cu(111) is more inclined to generate CH₄, while Cu(100) gives preference to C_{≥2} products, majorly C₂H₄. A supporting research¹¹⁹ explained that the formation of adsorbed CO dimer (the rate determining step of C_{≥2}⁷⁰) occurs more easily and is most stable on the square arrangement of 4 surface atoms, i.e., (100) crystal plane.

It seems possible to regulate the product distribution by controlling the composition of the Cu crystal orientation. For example, Hori et al.¹²⁰ in 2003 tried some pure Cu electrode differing in crystal orientation, with the Cu(S)-[4(100)×(111)] composed of 4 atomic rows of (100) terrace and one atomic height of (111) step. It was shown to be a proper platform for ethylene formation

(the Faradaic efficiency going up to 50% with the ethylene/methane ratio around 13.5), which indicated that the stepped surface mixed with (100) and (111) is somehow more favourable for ethylene formation than a smooth surface mainly composed of low-index lattice surface.

Enhancing the surface roughness of Cu catalyst

Tang et al.⁶¹ utilized electrodeposition to generate a rough Cu overlayer on the electrode, resulting in a coverage which consisted of numerous nano-particles ranging from 50 to 100 nm. These nano-sized particles helped to achieve lower onset potential and higher C₂ product selectivity compared to smooth Cu foil. More specifically, the onset potential of nanoparticles coated Cu is -0.6 V vs. RHE which is 0.4 V more positive than that of smooth Cu. In addition, the Faradaic efficiency of the former one under -1.1 V (vs. RHE) is 22% higher than that of the latter one. Kanan's group attributed the effect of surface roughness to the grain boundaries¹²¹, and certificated the important role of grain-boundary surface terminations in developing eCO₂RR activity with unchanged HER performance¹²². Higher current efficiency and hydrocarbon selectivity were obtained by the rough Cu for two reasons: (1) rough Cu presents larger active surface area since it contains higher density of grain boundaries, such as steps, edges, and defects, which means more active sites can be exposed; (2) rough Cu can reduce the high energy barriers for the formation of intermediates of hydrocarbon products to some extent. An electrodeposition method was used by Goncalves et al.⁶² to gain a 7-fold larger active surface than that of smooth Cu. The proportional relationship between roughness and C₂ hydrocarbon selectivity was also confirmed. Based on these findings, this group further applied a more advanced ex-situ electrodeposition method¹²³ to form a Cu deposit with 3D honeycomb foam structure, which selectively produced C₂ hydrocarbons (C₂H₄ and C₂H₆), with suppressing CH₄. Apart from surface treatment on the bulk Cu electrode, a more controllable way to construct a highly-rough electrochemical surface is to prepare nano-size catalyst particles before attaching

them on a substrate electrode (normally carbon materials). Reske et al.¹²⁴ applied this approach to fabricate a rough electrode and discussed the influence of Cu particle size (ranging from 2 to 15 nm) on catalytic activity. When compared with the smooth Cu disc, Cu nanoparticles make positive change to the overall current density, especially for nanoparticles smaller than 5 nm. However, the production of hydrocarbons is restrained by decreasing nanoparticle size, with H₂ and CO gradually becoming the dominant products. Their DFT calculation suggests that when catalyst size is below 2 nm, the population of under-coordinated atoms is dramatically increased, resulting in stronger binding sites that accelerate hydrogen evolution and CO generation.

The shape of the nano-sized catalyst is another factor influencing the reaction. Xie¹²⁵ prepared a porous electrodeposited layer in a 3D flower-like structure. Compared to the Cu foil, these nano-flowers showed 400 mV lower overpotential for eCO₂RR and ~10 % higher FE for C₂H₄ production at -1.3 V. Moreover, the stability (9h) of this novel structured material is found to be much better than the raw Cu. Loiudice et al.¹²⁶ prepared tuneable Cu nano-cubes with different lengths using colloidal chemistry and compared their activities with Cu nano-sphere. The cubes performed better on both current density and C₂H₄ selectivity. It was speculated that the atoms on the edges of cubes benefit C-C coupling. Xie et al.¹²⁷ prepared Amine-functionalized Cu nano-wire for eCO₂RR, showing about 1 mA cm⁻² development on hydrocarbon partial current density at -1.9 V (vs. Ag/AgCl).

Oxide-derived Cu catalysts

In fact, the rough surface of Cu electrode prepared from electrodeposition in aqueous solution always presents an oxidized outer layer¹²⁸⁻¹³⁰. Thus, some researchers thought the special properties of the oxide-derived Cu layer made stronger influence than the surface roughness on the enhanced catalytic activity for CO₂ reduction¹³¹⁻¹³². Frese et al.¹³³ first demonstrated CH₃OH from eCO₂RR via an oxidized Cu electrode in 1991, but this only developed 1% of the

efficiency compared to the polycrystalline Cu¹¹⁸. There are two different oxidation states of Cu, the cuprous oxide (Cu₂O) is widely proposed to be the dominant species in methanol forming, due to its moderate binding energy with the methoxy adsorbates thus improving the stability of intermediates and altering selectivity towards CH₃OH¹³⁴. Some theoretical supports using DFT calculation from Zhang et al.¹³⁵ exposed that the intermediate CH₃O* can transform to CH₄ or CH₃OH depending on whether the interacting surface is metallic Cu or oxidized Cu, or on whether OH* or CO* is the predominant spectator. Hence, the selectivity of CH₃OH and the ratio of CH₃OH/CH₄ can be increased by introducing a moderate amount of O (in the form of oxide formations or hydroxyl spectator groups). However, there are some opposing views insisting that the active phase for eCO₂RR is metallic Cu^{73, 136-137} because the copper oxide is easily reduced under the eCO₂RR reaction conditions. For example, the reduction of Cu₂O to metallic Cu in pH=8 aqueous solution was observed at -0.57 V (vs. SCE)¹³⁸, which is a less negative potential than even HER. From Ren's research¹³⁹, the XRD diagram of the Cu₂O film after eCO₂RR, which only contains diffraction peaks of Cu⁰, also indicated that the bulk of Cu₂O films had reduced to metallic Cu during the process of eCO₂RR. Some studies in recent years announced the subsurface oxygen from the crystal lattice of Cu oxides can enhance the adsorption and rise the coverage of CO*¹⁴⁰⁻¹⁴¹. Also, this oxide-derived feature can be maintained during eCO₂R by the "protection" of OH groups from alkaline electrolyte^{36, 142}.

Adding other metal components to Cu catalysts

Adding other metal components to Cu catalysts is a good approach to reduce the reaction overpotential and adjust the product distribution, as the surface lattice strain that affecting the intermediates adsorption can be adjusted accordingly¹⁴³⁻¹⁴⁴. Hirunsit et al.¹⁴⁴ modelled eCO₂RR on Cu₃X alloy with the L12 crystal structure (X=Au, Ag, Pd, Pt, Ni, Co, Rh, Ir). Cu₃Pt, Cu₃Ni, Cu₃Co, Cu₃Rh in principle showed a preference for formic acid production, while Cu₃Pd and Cu₃Pt demonstrated efficient catalysis of methanol formation under a high overpotential around

0.7 V. Apart from Cu_3Pd and Cu_3Pt , Cu_3X catalysts mostly favoured the production of CH_4 than CH_3OH . Reske et al.¹⁴⁵ used Pt as the substrate to support Cu overlayers with different thicknesses (monolayer, 5nm, 15nm). The reaction activity and product selectivity showed a strong dependency on the thickness of Cu layer: with increased Cu layer thickness, the interactions between Pt and Cu declined, while partial current density of hydrocarbons developed with an increase in $\text{CH}_4/\text{C}_2\text{H}_4$ ratio. Varela's finding¹⁴⁶ helps explain the above phenomenon: during the electrolytic process, the morphology of the bulk Cu overlayer changed to be granular. The thinner the Cu-layer is, the more possible the Pt surface exposed, which was more favourable for HER. In the studies of CO production from eCO_2RR , examples of modifying catalysts by alloying are abundant^{100, 147-148}, but when it comes to hydrocarbons production, it is rarely to find any supportive study, which further reinforces the exclusive use of Cu in hydrocarbons production.

2.4 Chapter summary

This literature review represents the CO_2 mass transfer issue and the corresponding influence factors when using a traditional 2C cell for this electrolysis reaction. A detailed collection of published results shows applying GDE cell with CO_2 directly feeding to the electrode enhanced CO_2 mass transfer and further increased reaction rate. The review also shows the state-of-the-art studies on heterogeneous electrocatalysts for the high selectivity of valuable carbonaceous products, including CO, formate, and (oxygenated) hydrocarbons. For the scale-up purpose, there are still pending issues in electrochemical CO_2 reduction reaction (eCO_2RR) in aqueous media. The predominant one to be reformed is CO_2 mass transfer from its pure phase to the 3-phase reaction interface, otherwise, the preferable water reduction to H_2 could result in low current efficiency towards eCO_2RR which a waste of energy would be.

Within this literature review, several areas for future study have been identified. These focus

on both the further development on system engineering and catalytic science, aiming at ameliorating the aqueous eCO₂RR system with scale-up potential. Based on the gaps identified in this review, three research objectives are formulated and summarised below.

- I. GDE cell theoretically alleviates the CO₂ mass transfer resistance, which should be an ideal reactor for eCO₂RR. However, since there is a lack of direct comparison between the traditional 2C cell and GDE cell, the effect of CO₂ mass transfer on eCO₂RR performance has not been quantified. Electrolyte, applied potential, and other cell elements in GDE cell, which also have impacts on the overall reaction kinetics and efficiency, should be systematically studied and optimized.
- II. eCO₂RR has a wide distribution of products, converting CO₂ into a certain carbonaceous product with high efficiency and high selectivity is the common target of researchers in this area. Selective CO production from eCO₂RR is mostly performed on noble-metal catalysts, like Au, Ag, and Pd, bringing its own sustainability issues. For the sake of the reaction scale-up, it is necessary to develop a stable and non-noble catalyst which can be adaptable to GDE system to perform an efficient reaction, particularly to reach both CO FE >90% and CO partial current density >100 mA cm⁻² at moderate potentials.
- III. Regarding formate production, Sn is a cheap material and has been found to show high selectivity. Catalyst development work is still needed for Sn modification to further develop the formate selectivity and reduce the reaction onset potential. Additionally, to develop the sustainability of CO₂ utilisation, it will be useful to explore the direct utilisation of this liquid product. Thus, it is necessary to construct a facile system for easily-controlled formate yield or concentration.

Chapter 3 Methodology

3.1 Process flow diagram of operating electrochemical CO₂ reduction reaction

As shown in Figure 3-1, an electrolysis cell was used as the reactor for electrochemical CO₂ reduction reaction (eCO₂RR) which is normally composed with a cathodic chamber and an anodic chamber separated by an ion exchange membrane (IEM). An external power supply was connected to drive the reaction under constant voltage or current. The reduction reaction took place on the cathodic side. A reference electrode was used to set up a three-electrode system. Pure CO₂ was supplied to the cathodic side from a gas cylinder, with the flow rate regulated by a flow meter. Products from eCO₂RR were in gas and liquid phases. A gas sampling bag was used to collect the outlet gas for analysing the gaseous products by a gas chromatography (GC). The liquid products in catholyte after reaction was analysed by GC and ion chromatography (IC). Some experiments applied the flowed catholyte with the rate controlled by a flow meter.

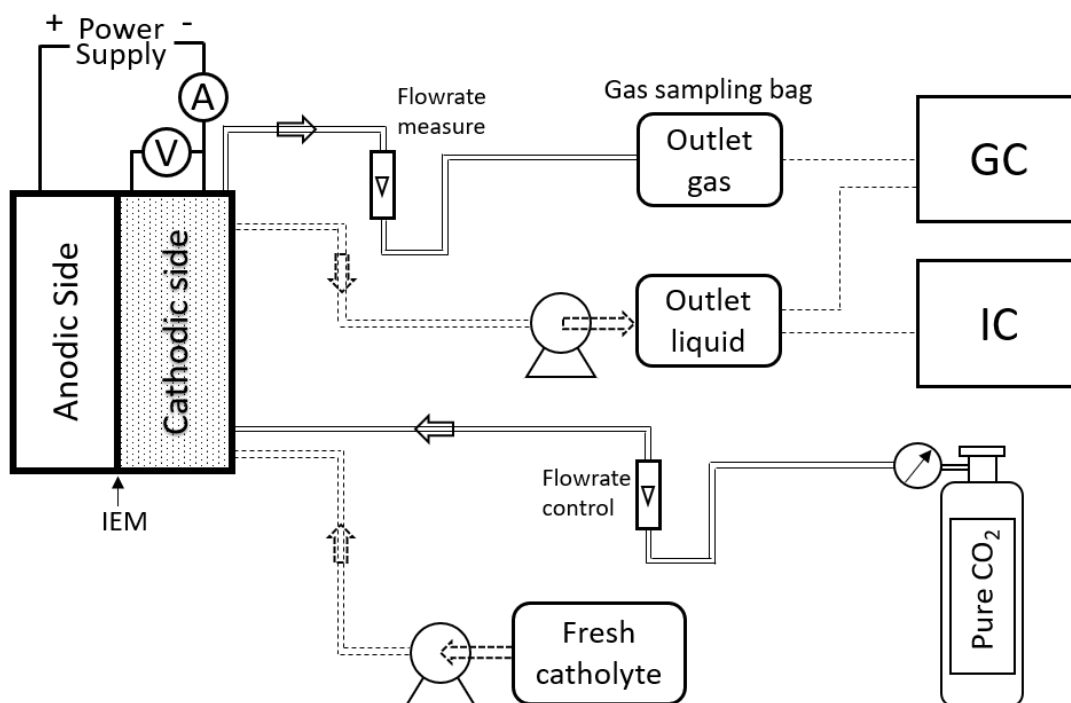


Figure 3-1 Process flow diagram of operating the electrochemical CO₂ reduction reaction.

3.2 Reactor design and fabrication

3.2.1 Gas diffusion electrode (GDE)-holder used in an existing H-type cell

In order to apply the gas diffusion electrode (GDE) in eCO₂RR system and initially explore the feasibility, a GDE-holder was designed and fabricated by polyvinyl chloride (PVC) material to fit an existing H-type cell. Figure 3-2 shows the design drawing of the GDE holder and a photo of the glass H-type cell. A coiled titanium (Ti) wire was used as the current collector, with a Ti mesh placed between the Ti wire and the gas diffusion layer (GDL) to enhance the conductivity.

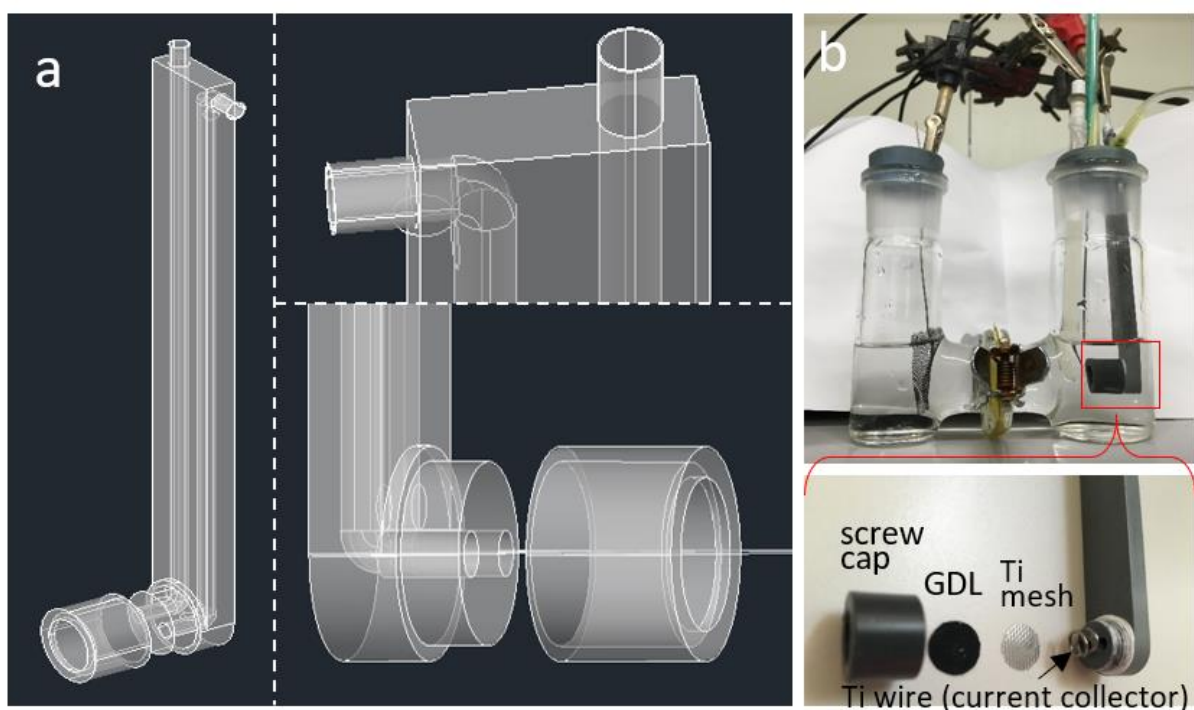


Figure 3-2 a) Design drawing of the GDE-holder. b) H-type cell fitted with GDE-holder

3.2.2 3D-printed compact cells

To minimize the internal resistance, the compact cell was utilized as the developed reactor for eCO₂RR. A two-chamber (2C) cell and a GDE cell were designed, using different CO₂ supply methods of “purging into electrolyte” and “diffusion from GDE” respectively. The schematics of the two cells are described in Figure 3-3 a and b.

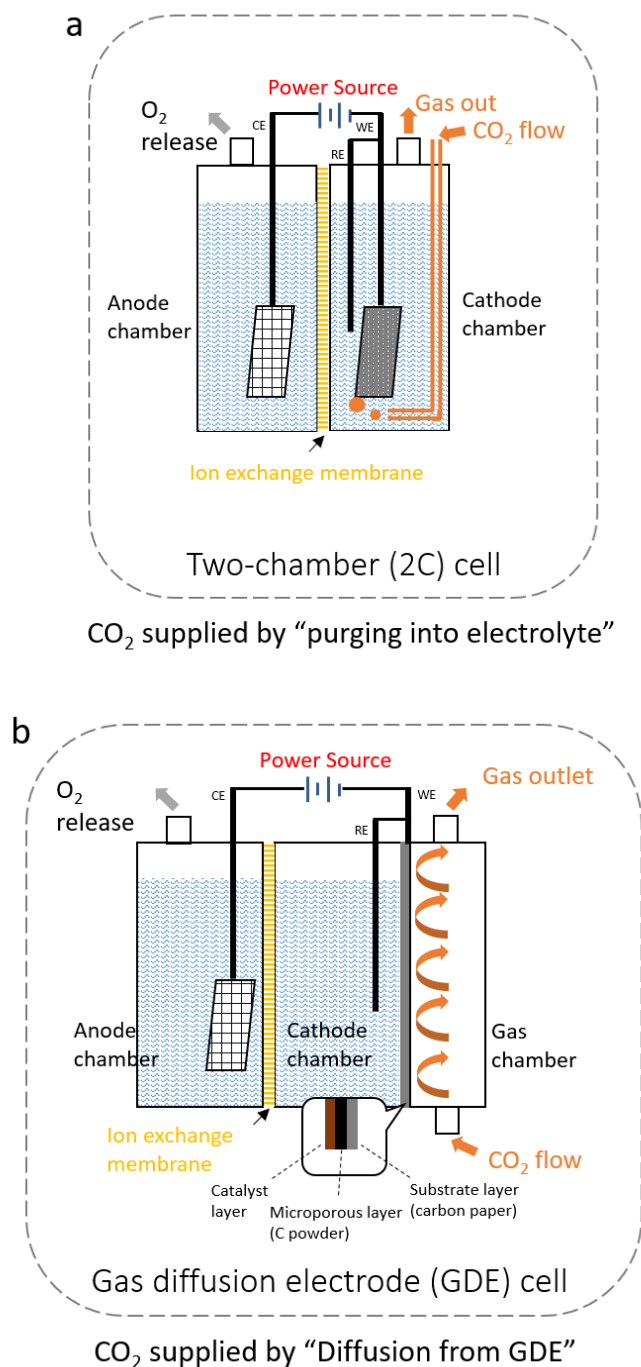


Figure 3-3 Schematic diagrams of aqueous eCO₂RR system using a) 2C cell and b) GDE cell.

A 3D printer (Form 2, Formlabs) combined with the photoreactive resin (Form 2 Clear Resin, Formlabs) was applied to fabricate the cells. The post-cured resin is semi-transparent and electrically insulated with a good resistance of strong acid and alkali that is in accordance with the conditions of eCO₂RR. Cell parts were screwed together using metal bolts. 3D drawings of the two cells set-up are shown in Figure 3-4 a and b. The design papers of each chamber with

specific dimensions are attached to Appendix III.

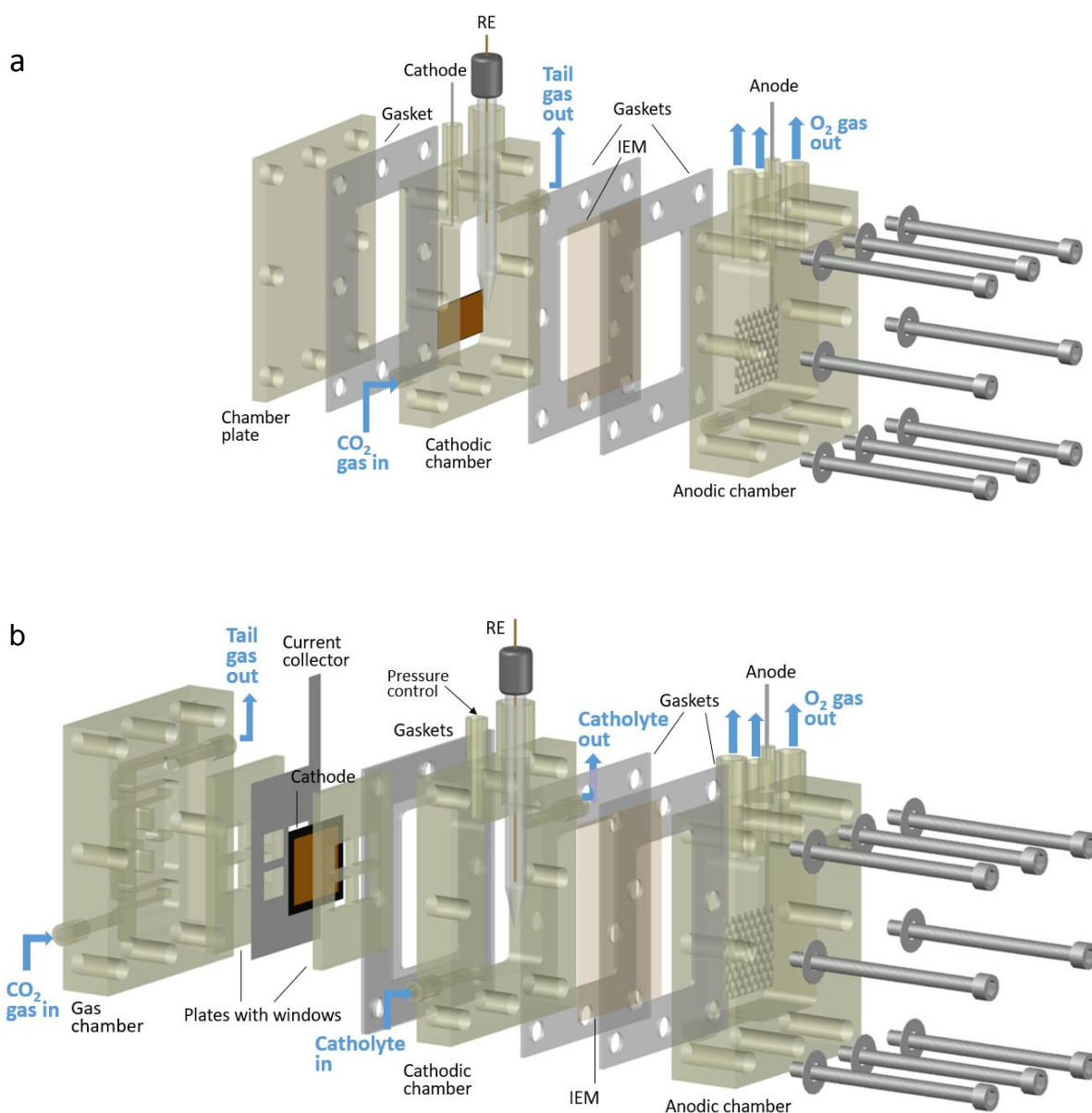


Figure 3-4 3D drawings of a) 2C cell and b) GDE cell compared in this work

The 2C cell (Figure 3-4 a) composed with cathodic and anodic chambers was separated by an ion exchange membrane. To guarantee the good gas and liquid tightness, the whole cell was bolted and sandwiched by thin rubber gaskets. The inter surfaces of the printed parts were manually sanded by a sandpaper and polished. CO₂ was bubbled through the bottom inlet and the tail gas was collected from the top outlet using gas sampling bags (20 ml, Deling (China)) for analyzing gas products. Open areas were designed on the top of the anodic chamber for

oxygen emission from the anodic reaction, to relieve the anolyte resistance growth and anode active surface area decline caused by undischarged O₂ bubbles^[149].

With the GDE cell (Figure 3-4 b), CO₂ and tail gas were flowed in and out from a gas chamber, and catholyte was also flowed through the cathodic chamber. The outlet on the top of the cathodic chamber was used to keep the gas pressure in headspace the same as gas chamber by tee-connection with the gas chamber outlet, allowing an unspoiled physical property of GDE. Gas and cathodic chambers were separated by the GDE cathode which was sandwiched by a stainless-steel foil (current collector) and two printed plates with totally 2 cm² open area (4 small square windows). The cathodic and anodic chambers were the same as the 2C cell, with the dimensions of 3.6 × 2.4 × 0.9 cm³ and 3.6 × 2.4 × 1.4 cm³ respectively.

The cathode used in both cells was catalyst-painted GDL with the geometric surface area 2 cm², but with different current collectors. The cathode was immersed into the catholyte in the 2C cell, a titanium wire was adhered to the back of the cathode (1 cm × 2 cm) by Silver conductive epoxy adhesive (Chemtronics). To prevent the effect of silver on electrode reactions, a dielectric epoxy adhesive (Araldite) was applied to cover the silver adhesive and to insulate the back of the cathode from the catholyte. Differently, the cathode current collector in GDE cell was a stainless-steel foil which attached to the back of the cathode by pressing the cells parts.

The anode used in all the experiments was Platinum plated Titanium mesh with a dimension of 4 cm². Before each eCO₂RR, the cell parts were soaked in 3 wt% HCl (Sigma-Aldrich) solution and cleaned by DI water.

3.3 Catalyst synthesis and cathode preparation

3.3.1 *Painting commercial Cu₂O on gas diffusion electrode (GDE)*

The commercial Cu₂O (Com.Cu₂O) catalyst was purchased from EPRUI Nanoparticles & Microspheres Co. Ltd. with the average particle size 100 nm. To fabricate a GDE with binder/catalyst=10 wt.%, the catalyst ink was prepared by dispersing 15 mg catalyst in 200 μ L isopropanol and 33 μ L Nafion binder (Nafion suspension, 5 wt.%, Sigma-Aldrich). The ink was sonicated for 20 minutes before painting onto the 2 cm² surface of gas diffusion layer (GDL) (H2315 I2 C6, Freudenberg). Drying (45 °C, 1 ~ 3 min) was applied between each layer. Painting, drying, and weighing were repeated until the desired Cu₂O catalyst loading of 4 ~ 5 mg cm⁻² was achieved.

3.3.2 *Synthesizing Cu_xO catalyst and applying it to gas diffusion electrode (GDE)*

The home-made Cu_xO catalyst (Self.Cu_xO) was synthesised using the hydrothermal method by reduction of Cu acetate (Sigma-Aldrich, 98%) in the solvent of water and ethanol (Sigma-Aldrich, > 99.8%) mixture reported previously^[150]. The volume ratio of water and ethanol was controlled as 1:7, i.e., 10 ml water and 70 ml ethanol. After washing with distilled water and ethanol, the catalyst was dried at 60 °C in an oven (Oven-30S, SciQuip) in air for 8 hours. The process of applying the Self.Cu_xO catalyst on the GDL substrate was in accordance with that of Com.Cu₂O-GDE.

3.3.3 *Synthesizing Cu-In catalysts on gas diffusion electrode (GDE) by spontaneous precipitation*

The Cu-In catalyst coated GDE was prepared by precipitation of indium species on the Com.Cu₂O-GDE. The first step was to prepare Com.Cu₂O-GDE with Nafion/catalyst = 20 wt.% as stated in 3.3.1.

To deposit indium species on the Com.Cu₂O-GDE, a pure indium foil (25 mm × 12.5 mm, 99.999%, ADVENT Research Materials Ltd.) and the Com.Cu₂O-GDE were placed face-to-face with a 1 cm distance in a 20 ml container. An external cable (2 Ω) was connected between Com.Cu₂O-GDE and In foil to facilitate the redox reaction. The synthesis process was electrochemical spontaneous precipitation (ESP), started from injecting the acidified In³⁺ solution (0.05 M In₂(SO₄)₃ and 0.4 M citric acid, pH = 2.5) into the container until immersing the two electrodes. The precipitation duration was controlled by discharging the In³⁺ solution. “CuIn-ESP” was used to denote the synthesized material by this method.

For comparison, a non-electrochemical spontaneous precipitation (SP) was carried out without connecting the external cable between In foil and Com.Cu₂O-GDE. Other conditions were kept unchanged. “CuIn-SP” was used to denote the synthesized material by this precipitation method. The precipitation time was also controlled by discharging the In³⁺ solution.

3.3.4 *Fabricating C-supported SnO₂ bonded gas diffusion electrode (GDE)*

The C-supported SnO₂ catalyst (SnO₂/C) was prepared by physical mixing SnO₂ (nano-powder, ≤ 100 nm, Sigma-Aldrich) and carbon black (Vulcan XC 72R, Cabot) particles with the desired mass ratio of 0.5, 1, and 3.5. The individual SnO₂ and C were also used for comparison. The process of applying the SnO₂/C catalyst on the GDL substrate was in accordance with that of Com.Cu₂O-GDE. Differently, the catalyst ink with highly-hydrophobic carbon black took much longer time of sonication (about 10 hours) before painting onto the surface of GDL using an air brush (Evolution AL plus, Harder & Steenbeck). Painting and drying were repeated until the desired catalyst loading of 3 ~ 4 mg cm⁻² was achieved.

3.4 eCO₂RR system set-up and electrochemical measurement

3.4.1 eCO₂RR system set-up

All the electrochemical reactions and measurements were carried out at ambient temperature and pressure using a potentiostat (Metrohm Autolab PGSTAT128N). eCO₂RR was carried out by chronoamperometry (CA) recording the current over time at a particular applied potential. The current density (j) was calculated based on the geometric surface area S_{geo} (2 cm²) of the cathode.

The flow rate of CO₂ (BOC 99.99%) was always controlled at 15 ml min⁻¹ by a gas flow meter (Cole-Parmer TMR1-010462). In Chapter 4, KHCO₃ (Alfa Aesar, 99%) and KOH (Emsure®, 85%) solution with different concentrations of 0.1 M, 0.5 M, 1.0 M, and 2.0 M (only in KOH) were used as the catholyte, and the comparison was carried out for system optimization. When using the 2C cell, CO₂ was purged into catholyte 1 hour before electrochemical tests, while no CO₂ pre-purging to the catholyte in the GDE cell set-up. Ag/AgCl (RE-5B, BASI, 3M NaCl, 0.197 V vs. SHE) was used as the reference electrode, and a luggin capillary was applied to prevent it from being damaged in alkaline electrolyte. In Chapter 6, an alkaline reference electrode (RE-61AP, BASI, 0.117 V vs. SHE) was used instead of Ag/AgCl. The applied potentials (vs. Ag/AgCl or vs. RE-61AP) in the three-electrode system were all converted to the reversible hydrogen electrode (RHE) according to Equation (3-1) and (3-2). The potentials stated in this study are referred to RHE unless otherwise stated. A commercial cation exchange membrane (CEM) (F-950, Fumapem) was applied due to its proper conductivity (11.3 mS cm⁻¹) in H₂O and efficient prevention of anion (formate and other anionic products from eCO₂RR) crossover. 5 M KOH solution was used as anolyte in most of the tests. All the electrolytes were pre-electrolysed chronopotentiometrically (constant current density 3.5 mA cm⁻²) for purification using Pt-mesh electrodes (10 cm²).

$$E (\text{vs. RHE}) = E (\text{vs. Ag/AgCl}) + 0.197 \text{ V} + 0.0591 \text{ V} \times \text{pH} \quad (3-1)$$

$$E (\text{vs. RHE}) = E (\text{vs. RE-61AP}) + 0.117 \text{ V} + 0.0591 \text{ V} \times \text{pH} \quad (3-2)$$

When using the GDE cell, a peristaltic pump (120U/DM2, Watson Marlow) was used to supply fresh catholyte to maintain the local pH and to remove the liquid product for reaction equilibrium. The flow rate was controlled at 0.25 ml min^{-1} under the applied potential $-0.17 \sim -0.77 \text{ V}$ and at 0.5 ml min^{-1} under the applied potential $-0.77 \sim -1.17 \text{ V}$.

3.4.2 *Electrochemical measurement*

3.4.2.1 Cyclic Voltammetry (CV)

CV is the most common electrochemical characterisation to initially explore the electrochemical behaviour, which was mostly carried out three cycles between a potential range with a particular scan rate, generally $5\text{-}100 \text{ mV s}^{-1}$. It was mostly applied before eCO₂RR to confirm the reaction onset potential and the redox properties of the electrocatalyst. In Chapter 4 and 6, CV was applied to determine the electrochemical surface area (ECSA) of different electrodes by measuring the double layer capacitance in 0.1 M HClO_4 ^[121].

3.4.2.2 Electrochemical impedance spectroscopy (EIS)

EIS is a useful tool to measure different resistances in a circuit, such as the internal resistance and charge transfer resistance. The FRA32M module on the Autolab potentiostat was operated for EIS measurement, which was recorded with an ac-amplitude of 10 mV over the frequency range from 10 kHz to 0.1 Hz either at open circuit voltage (OCV) or at a particular cathodic potential. The impedance spectra were analysed and fitted using NOVA 2.1 software.

3.5 Methods for analysing CO₂ reduction products and catalyst materials

3.5.1 Product analysis

A gas chromatography (Shimadzu Tracer GC-2010) equipped with Barrier Discharge Ionization (BID) detector was used to analyse gas products and alcoholic liquid products. The ShinCarbon ST micropacked column 80/100 (Restek) was used to quantitatively analyse permanent gases and light hydrocarbons, while the Zebron ZB-WAXplus capillary column (Phenomenex) was used for alcoholic liquids. An ion chromatography (Eco IC, Metrohm) equipped with the “METROHM 6.1005.200” column was used for quantifying volatile fatty acids (VFA) including formic acid. The gas products were quantified by internal standard method using a customized standard mixed gas (BOC) with the components of H₂ (1.000%), CO (1.000%), CH₄ (0.500%), CO₂ (96.000%), C₂H₄ (0.500%), C₂H₆ (0.500%), and C₃H₆ (0.500%). Liquid products were quantified by the external standard method with creating working curves. The Faradaic efficiency (FE) for each product was calculated based on Faraday's law (3-3)^[24], where z is the number of electrons transferred for per mole of reactant (e.g., $z = 2$ for reduction of CO₂ to CO), n is mass of the product from the electrode in moles, F is Faraday's constant (96485 C mol⁻¹), Q represents the total charge passed.

$$FE = \frac{z n F}{Q} \quad (3-3)$$

The detailed settings of GC and IC, sample calculations of the product contents, and FE normalization are given in Appendix II.

3.5.2 Characterization of catalyst materials

The crystal structure of the catalyst can be detected by X-ray diffraction (XRD) spectra which was obtained by a Philips X-ray diffractometer PW 1730 diffractometer equipped with a Cu X-ray tube (Cu-K α ; $\lambda = 0.154$ nm) operated at 40 kV and 40 mA.

To determine the elemental compositions and valence states of the electrode surface (~10 nm depth), X-ray photoelectron spectroscopy (XPS) was performed on a Kratos Axis Nova XPS spectrometer using a K-Alpha line X-Ray source (225W) over an area of approximately 300 × 700 microns.

To initially analyse the catalyst morphology in micro-scale, scanning electron microscopy (SEM, Hitachi SU-70) coupled with an energy dispersive X-ray detector (EDX, Bruker Quantax 400) were applied.

The micro- or nano- structures of the catalyst were further analysed by transmission electron microscope (TEM), HRTEM and SAED on a JEOL3000F at 300 kV. HAADF-STEM and XEDS elemental mapping was performed on a JEOL3000F with Be double-tilt analytical holder. SAED analysis was performed on JEOL-3000F at 300 kV and the camera length was 255.8 mm. All specimens were prepared by dispersing samples into ethanol and then drop-casted onto holy carbon supported Au grids.

Chapter 4 Enhanced Selectivity of Carbonaceous Products from Electrochemical Reduction of CO₂ in Aqueous Media

4.1 Introduction

As discussed in the Chapter 2, hydrogen evolution reaction (HER) is competitive to eCO₂RR in aqueous electrolyte. Improving CO₂ mass transfer to the reaction interface can develop the competitiveness of eCO₂RR and suppress HER, therefore, the selectivity of carbonaceous products can be developed. Using gas diffusion electrode (GDE) is a promising way, as it has been successful applied in the hydrogen-oxygen fuel cell to enhance the gas mass transfer to the 3-phase reaction interface¹⁵¹. To apply GDE in eCO₂RR, a well-designed reactor is normally needed to perform the gas diffusion function from the gas phase to the reaction interface without the interference by liquid electrolyte. In this chapter, the feasibility of GDE application was firstly studied in an existing H-type cell. To minimize the internal resistance, a compact GDE cell was then constructed. A compact two-chamber (2C) cell was also fabricated with the same dimension for a univariate comparison, to study the effect of CO₂ supply method on the performance of Cu_xO-catalyzed eCO₂RR in bicarbonate electrolyte system. The big difference of product distribution disclosed the crucial role of CO₂ mass transfer in the selectivity of carbonaceous products. Compared to the 2C cell, GDE cell with efficient CO₂ mass transfer showed more than 3-fold improvement of Faradaic efficiency for carbonaceous products. The unique structure of GDE cell alleviates CO₂ dissolution to a greater extend, allowing a wider selection range of catholyte including the alkaline hydroxide. The effect of catholyte alkalinity on selectivity of carbonaceous products (especially C₂) from eCO₂RR in GDE cell was also highlighted in this study.

4.2 Experimental

4.2.1 Initial application of gas diffusion electrode (GDE) – the feasibility test

The application of GDE was initially explored by using a GDE-holder in an existing H-type cell. The design and set-up of the GDE-holder are stated in Section 3.2.1. A commercial gas diffusion layer (GDL) without catalyst painting was used as the cathode. A GDL glued to a Titanium wire used as an immersed electrode was also studied in the H-type cell for comparison. Figure 4-1 shows the photo and schematic diagrams of the immersed GDL and GDE-holder with two CO₂ flow paths.

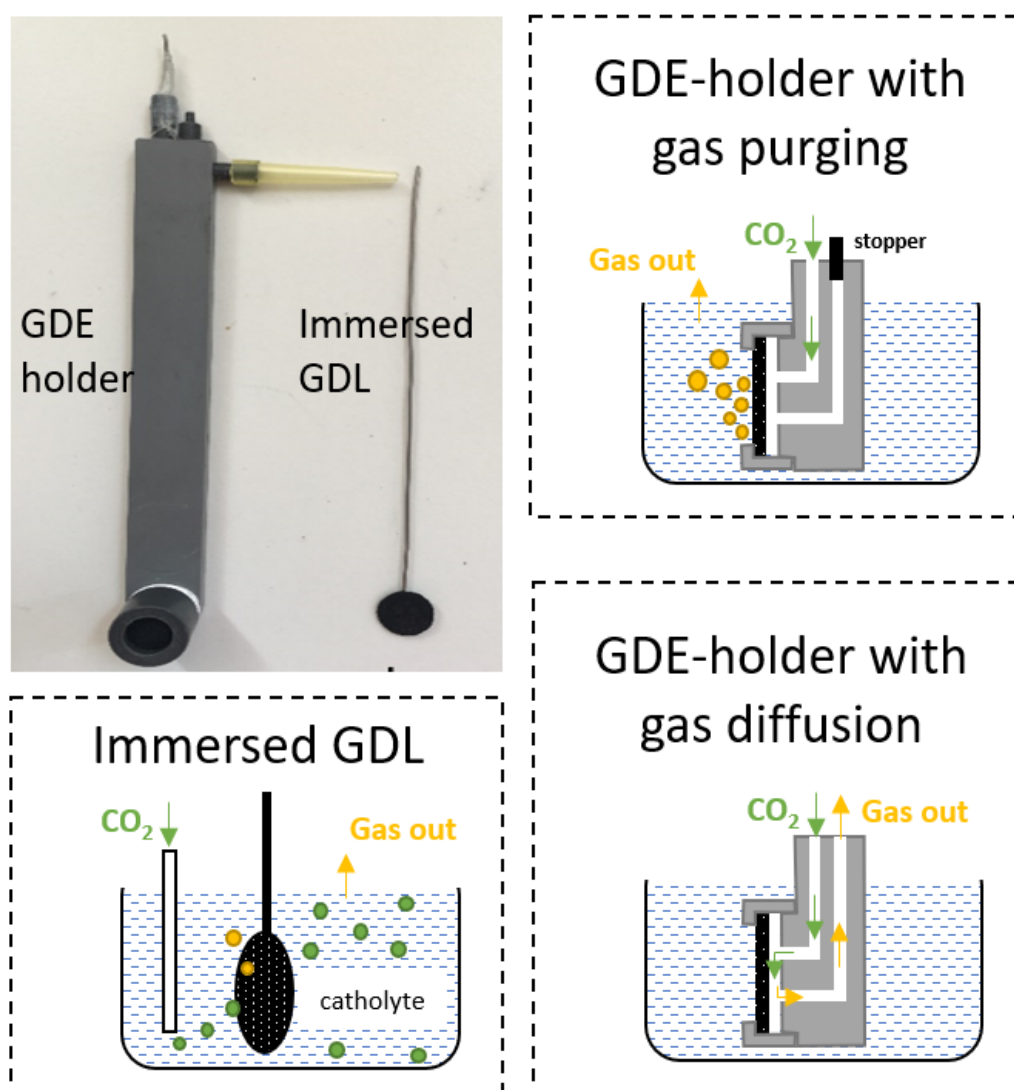


Figure 4-1 Photo and schematic diagrams of immersed GDL and GDE-holder with two CO₂ flow paths used in an H-type cell.

0.1 M KHCO_3 was used as the catholyte and anolyte separated by an anion exchange membrane (AEM). Ag/AgCl and a Ti mesh ($2 \times 2 \text{ cm}^2$) was used as the reference electrode and anode respectively. For the study of immersed GDL, catholyte was bubbled with CO_2 for 1 hour beforehand. To preliminarily evaluate the reaction behavior, Cyclic Voltammetry (CV) as stated in Section 3.4.2.1 was applied with the immersed GDL and GDE-holder under N_2 and CO_2 atmosphere respectively. CO_2 reduction reactions were carried out by chronoamperometry (CA) at -2.0 V (vs. Ag/AgCl) for 1.5 hours with CO_2 flow rate 25 ml min^{-1} . The tail gas of 1.5 hours reaction was analysed by gas chromatography (GC).

4.2.2 CO_2 electro-reduction in compact cells

To minimize the internal resistance, a compact gas diffusion electrode (GDE) cell fabricated by 3D-printing technology was utilized as the developed reactor for eCO_2RR . A two-chamber (2C) cell was also constructed with the same dimension for comparison to find out the effect of CO_2 supply method on the performance of eCO_2RR . The cell design and whole reactor set-up have been stated in Section 3.2.2. A home-made Cu_xO (denoted as self. Cu_xO) was used as the catalyst throughout this chapter, which was painted on the commercial GDL as stated in Section 3.3.2. The characterization of the catalyst before and after eCO_2RR was carried out by scanning electron microscopy (SEM), X-ray diffraction (XRD), and X-ray photoelectron spectroscopy (XPS) as presented in Section 3.5.2.

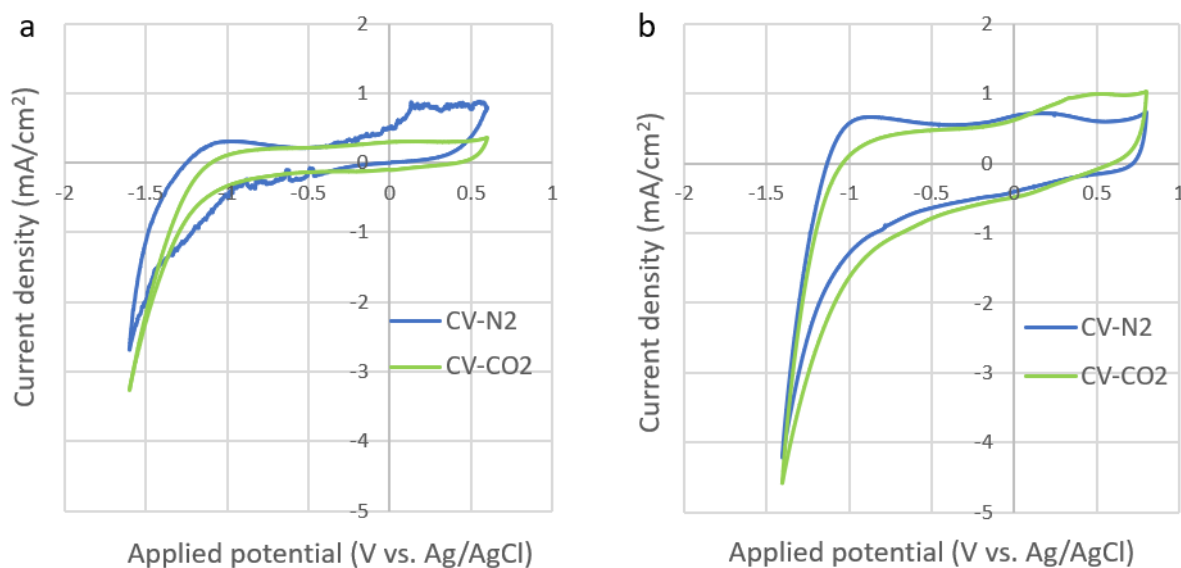
CV was carried out initially to explore the electrochemical behaviour in N_2 and CO_2 atmosphere respectively. Then, CA was operated to perform CO_2 electro-reduction at specific applied potentials: -0.17, -0.37, -0.57, -0.77, -0.97, -1.17 V (vs. RHE), running 30 min reaction time at each potential. 0.1 M, 0.5 M, 1.0 M KHCO_3 were used as the catholyte in both GDE cell and 2C cell. After determining the crucial role of GDE cell in the development of CO_2 mass transfer. 0.1 M, 0.5 M, 1.0 M, 2.0 M KOH solutions were compared in GDE cell to find out the effect of catholyte alkalinity. The reaction system of eCO_2RR is detailly illustrated in Section 3.4.1.

The products of eCO₂RR were analysed by gas chromatography (GC) and ion chromatography (IC) as expounded in Section 3.5.1.

4.3 Results and Discussion

4.3.1 Initial application of gas diffusion electrode (GDE) – the feasibility test

In the H-type cell, the immersed GDL and GDE-holder were tested by cyclic voltammetry (CV) at N₂ and CO₂ atmosphere respectively, with the scan rate 50 mV s⁻¹. The CV results are shown in Figure 4-2 a, b. Afterwards, eCO₂RR was carried out by chronoamperometry (CA) at -2.0 V (vs. Ag/AgCl) for 1.5 hours with immersed GDL and GDE-holder with two CO₂ flow paths. The CA results are combined in Figure 4-2 c. Table 4-1 displays the composition of the outlet gas after 1.5 hours eCO₂RR.



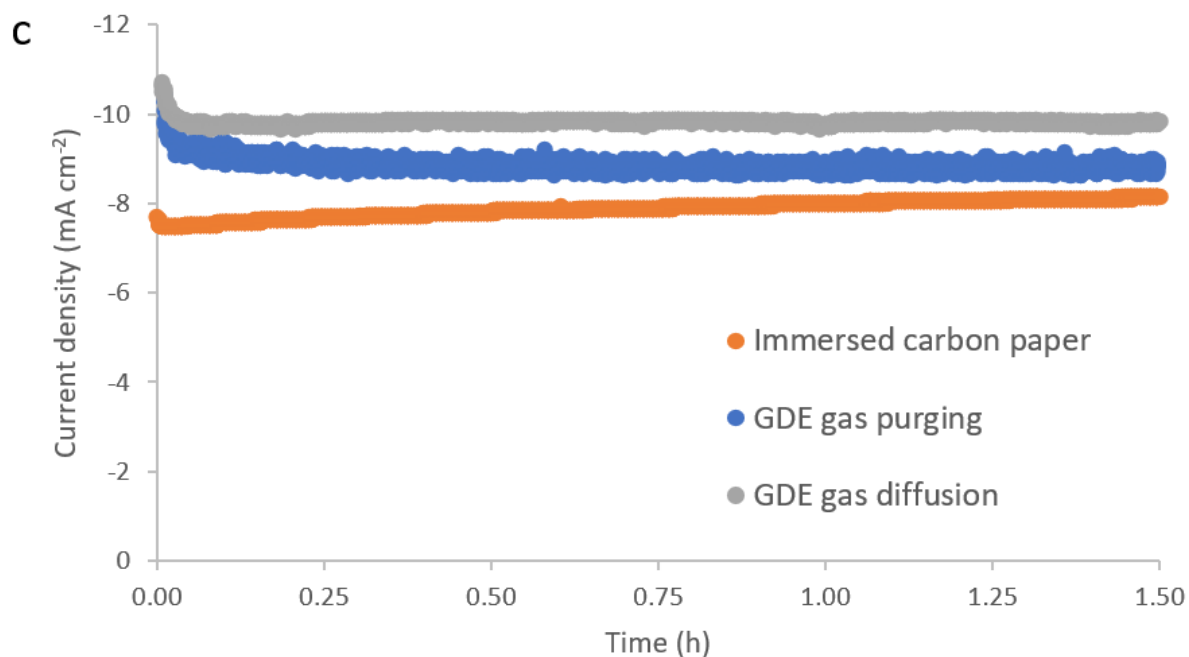


Figure 4-2 CV measurements of a) immersed GDL and b) GDE-holder under N₂ and CO₂ atmosphere in the H-type cell with the scan rate 50 mV s⁻¹. Scan cycles: 3, all those diagrams were taken from the 3rd cycle. c) CA results of eCO₂RR for 1.5 hours at -2.0 V (vs. Ag/AgCl) in the H-type cell.

Table 4-1 Composition of tail gas produced by eCO₂RR for 1.5 hours at -2.0 V (vs. Ag/AgCl) in the H-type cell.

	CO ₂	H ₂	CO
Immersed GDL	99.729%	0.271%	0.000%
GDE-holder (gas purging)	100.000%	0.000%	0.000%
GDE-holder (gas diffusion)	99.841%	0.126%	0.033%

As shown in Figure 4-2 a and b, no obvious redox peaks were found in the selected potential range due to the stability of carbon on the GDL surface. From the CV-CO₂ curves (green), the onset potential of the reduction reaction was observed to be -1.1 V of the immersed GDL and -0.75 V of the GDE-holder, indicating the less energy-input of the GDE-holder to drive the reduction reaction. HER shares a less-negative standard potential (0 V vs. RHE) than eCO₂RR, therefore the slope of reduction on CV-CO₂ curve more possibly represents HER. The CA

results (Figure 4-2 c) presents three similar current density values at -2.0 V vs. Ag/AgCl, with “GDE-holder gas diffusion” showing the highest current density of about -10 mA cm^{-1} . The *i-t* curve of “GDE-holder with gas purging” is more fluctuated than the other two, most-probably due to the interfere of gas bubbles on the electrode surface. From the tail-gas analysis results in Table 4-1, only the “GDE-holder gas diffusion” performs eCO₂RR capability with small amount of CO produced. The immersed GDL produced bit H₂ without CO formation. However, no product was found by “GDE-holder with gas purging”, probably because of the physical damage of the GDL by purging CO₂ flow.

The above results indicate the successful application of GDE in eCO₂RR by using a GDE-holder with gas diffusion method. Thus, the “gas diffusion” method of supplying CO₂ will be applied in the following works. However, the existing H-type cell has its intrinsic drawbacks: 1) the big distance (~6 cm) between the cathode and anode lengthens the ion transfer pathway which raises the internal resistance, 2) the large volume of the cathodic chamber (30 ml) diminishes the concentration of liquid products which brings problems for their qualitative and quantitative measurement, 3) the poor gas tightness of the cell leads to difficult tail-gas collection and analysis. Therefore, to overcome the above problems, a compact cell was fabricated with < 1 cm electrodes’ distance and small cathodic chamber with 7~12 ml for further study.

4.3.2 *The application of compact cells in CO₂ electro-reduction*

4.3.2.1 Catalyst characterisations and the measurement of electrode active surface area

The catalyst morphology of self.Cu_xO before and after 3 hours eCO₂RR in 1.0 M KHCO₃ was analysed by SEM and EDX as shown in Figure 4-3. The fresh catalyst consisted of spherical particles (100 ~ 1000 nm) which became finer after reaction. The EDX analysis indicated that self.Cu_xO catalyst was reduced during eCO₂RR since the atomic ratio of copper to oxygen

(Cu/O) was increased from 2.81 (before reaction) to 8.13 (after reaction).

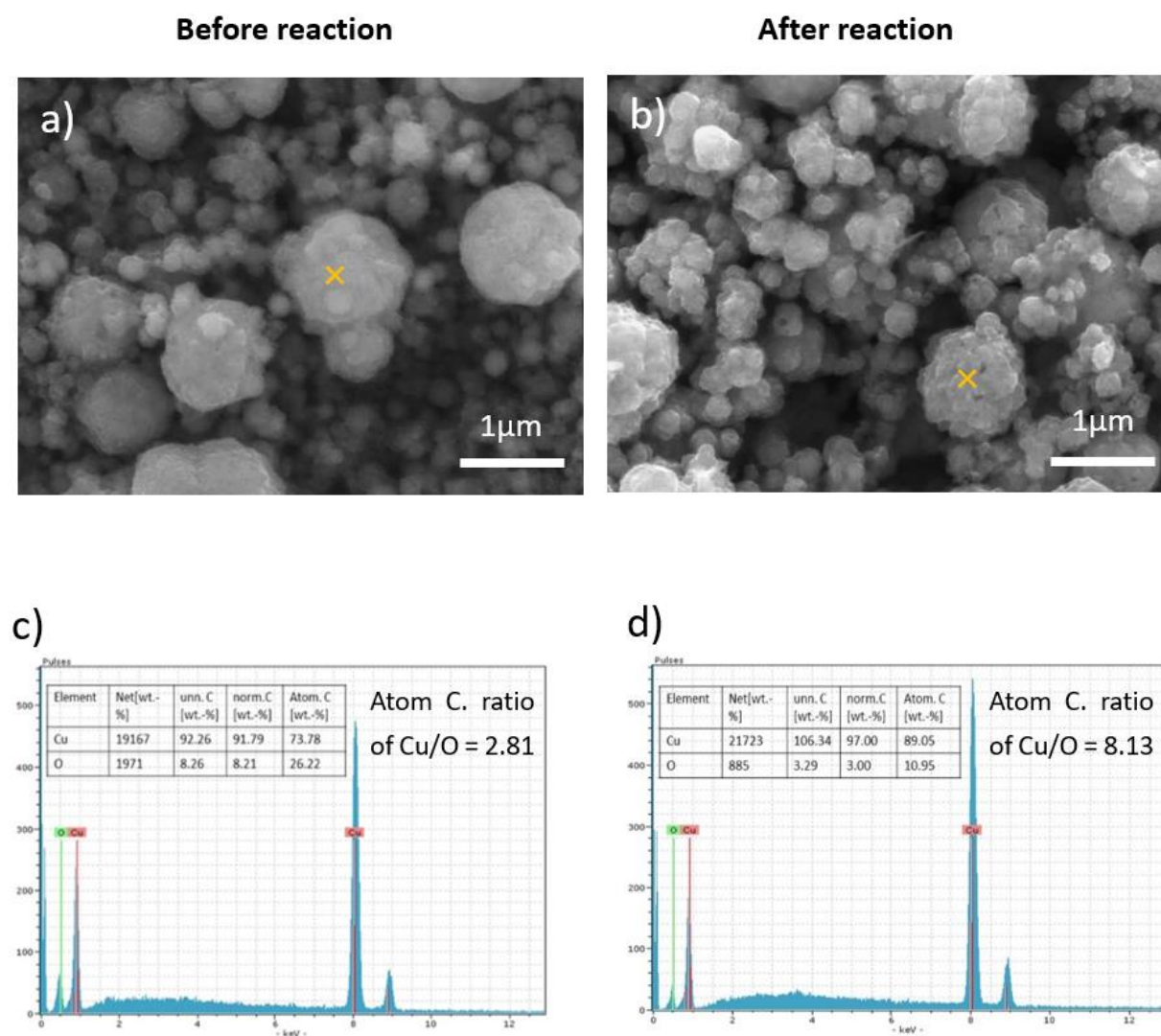


Figure 4-3 SEM images of self.Cu_xO catalyst a) before reaction and b) after reaction, point EDX diagrams of self.Cu_xO catalyst c) before reaction and d) after reaction.

The geometric surface area of the self.Cu_xO-GDE was always tailored to be 2 cm² in the compact cells. To determine its actual surface area, the double layer capacitance was measured in 0.1 M HClO₄ by CV at various scan rate¹²¹ as shown in Figure 4-4. A smooth stainless-steel (SS) foil was also tested as a reference with the roughness factor treated as 1. It is worth mentioning that there should have some differences in double-layer capacitance between two different materials with same surface roughness. But the effect of surface structure on the capacitance is much bigger than that of the material nature, as suggested by Gouy–Chapman–

Stern model¹⁵². From the comparison with the SS foil, the actual surface area of 2 cm² self.Cu_xO-GDE was calculated to be 108.6 cm² as displayed in Table 4-2.

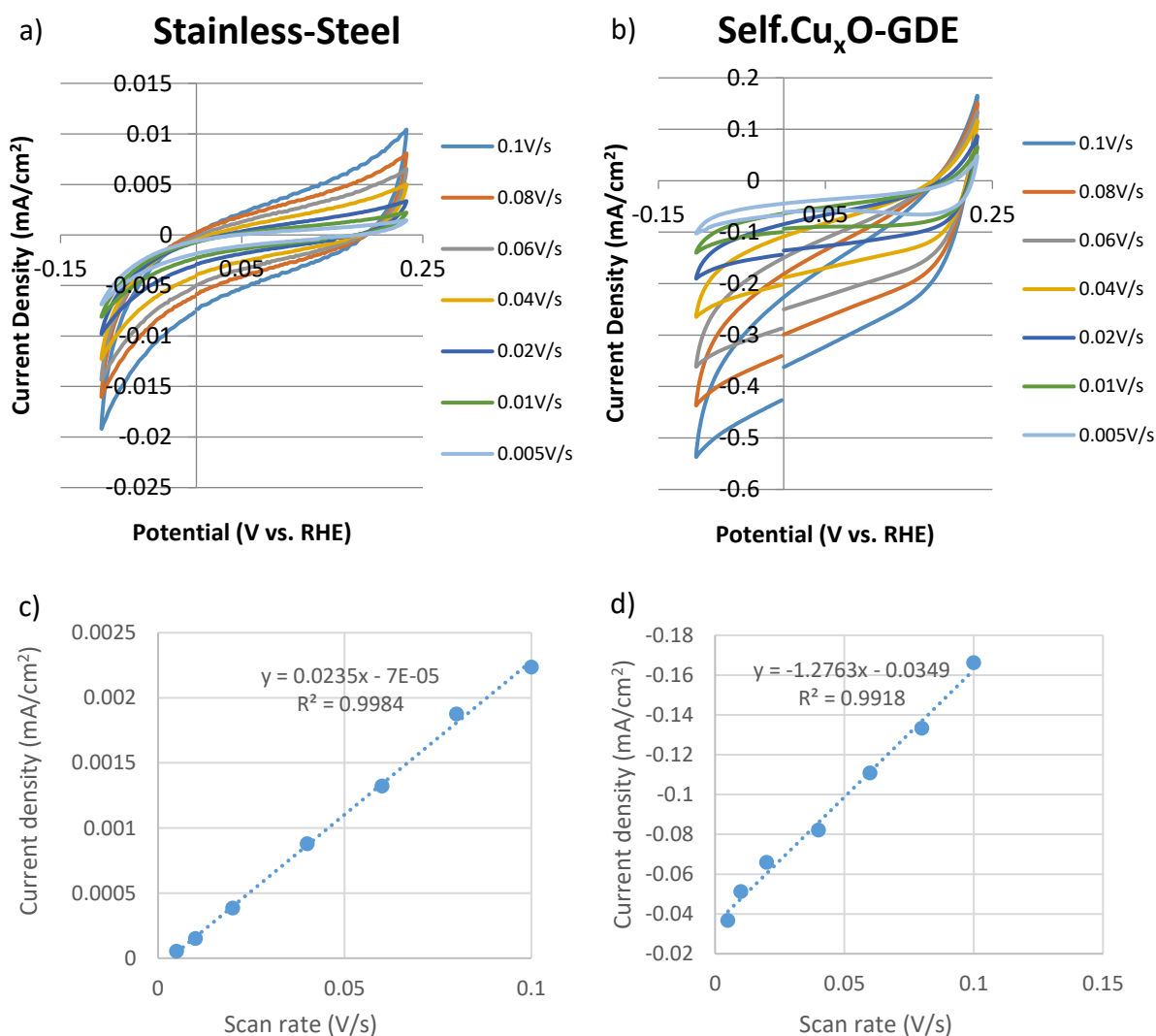


Figure 4-4 Determination of double-layer capacitance for a smooth stainless-steel sheet and the self.Cu_xO-GDE with the same geometric surface area. a) and b) CVs taken over a range of scan rates in a potential window where only double-layer charging and discharging is relevant for stainless-steel and self.Cu_xO-GDE respectively. c) and d) Current due to double-layer charge/discharge plotted against CV scan rate for stainless-steel and self.Cu_xO-GDE respectively.

Table 4-2 Calculations for the actual surface area of self.Cu_xO-GDE.

	Stainless-steel	Self.Cu _x O-GDE
Geometric surface area (cm ²)	2	2
Double layer capacitance (mF)	0.0235	1.2763
Roughness factor	1	54.3
Actual surface area (cm ²)	2	108.6

4.3.2.2 The effect of CO₂ supply method

Using the self.Cu_xO-GDE as the cathode and KHCO₃ solution with different concentration as the catholyte, the effect of CO₂ supply method (“purging into electrolyte” and “diffusion from GDE”) was studied by comparing the eCO₂RR performances in the 2C cell and GDE cell.

Since the substance composition and morphology of self.Cu_xO catalyst changed over the eCO₂RR duration, fresh self.Cu_xO catalyst was used in each eCO₂RR, with CV measurements in N₂ and CO₂ atmosphere respectively at the beginning. CV results which preliminarily evaluated the reaction behaviour are shown in Figure 4-5.

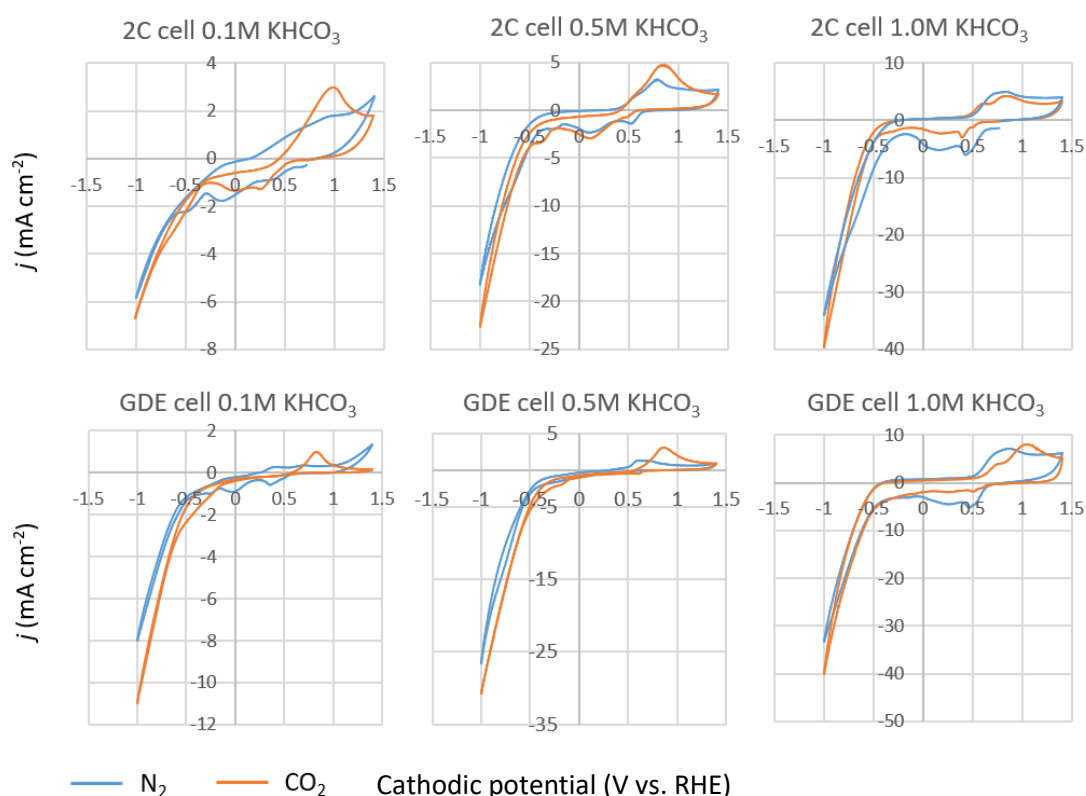


Figure 4-5 CV measurements under N₂ and CO₂ atmosphere in 2C cell and GDE cell with KHCO₃ catholytes using fresh self.Cu_xO catalyst. Scan rate: 50 mV s⁻¹, scan circles: 3, all those diagrams were taken from the 2nd or 3rd cycle of scan.

In General, each CV curve under N₂ atmosphere in Figure 4-5 shows two anodic peaks at around +0.5 V and +0.8 V, related to the oxidation process of Cu(0)/Cu(I) and Cu(I)/Cu(II). The corresponding cathodic peaks of Cu species reduction were at around 0 V and 0.5 V¹⁵³. Potentials of those redox reactions follow the Pourbaix diagrams of copper presented by Beverskog et al.¹⁵⁴ Positions of those peaks shifted with different degree in different catholyte, this is because the cathodic potentials (V vs. RHE) in this paper were all calculated from bulk pH of catholyte, but the real pH value on the reaction sites (local pH) is unmeasurable and has a deviation from the bulk owing to a big pH gradient inside the porous GDE. The pH deviation between the bulk and the local is affected by the type and concentration of the catholyte, also on the depth of catholyte infiltrated in GDE.

Under CO₂ atmosphere with using the 2C cell, the onset potential (where the current started to sharply increase in reduction area) shifted negatively with the increasing KHCO₃ concentration, indicating a declined eCO₂RR activity. But in GDE cell when using the same KHCO₃ catholyte, the onset potential of CO₂ ER was not affected by the KHCO₃ concentration and showed better eCO₂RR activity with any KHCO₃ concentration (less negative onset potential and bigger reduction slope in CO₂ than in N₂).

The CV results provided proofs of a suitable potential range for eCO₂RR which should be more negative than the onset potential (generally -0.2 V vs. RHE from the above results), and suggested the Cu_xO catalyst would be reduced to metallic Cu under the reaction potential of eCO₂RR. After CV, eCO₂RRs were carried out by CA at specific fixed potentials from -0.37 V to -1.17 V vs. RHE (30 min for each potential), the *j*-*t* curves of CA at different potentials are given in Figure 4-6.

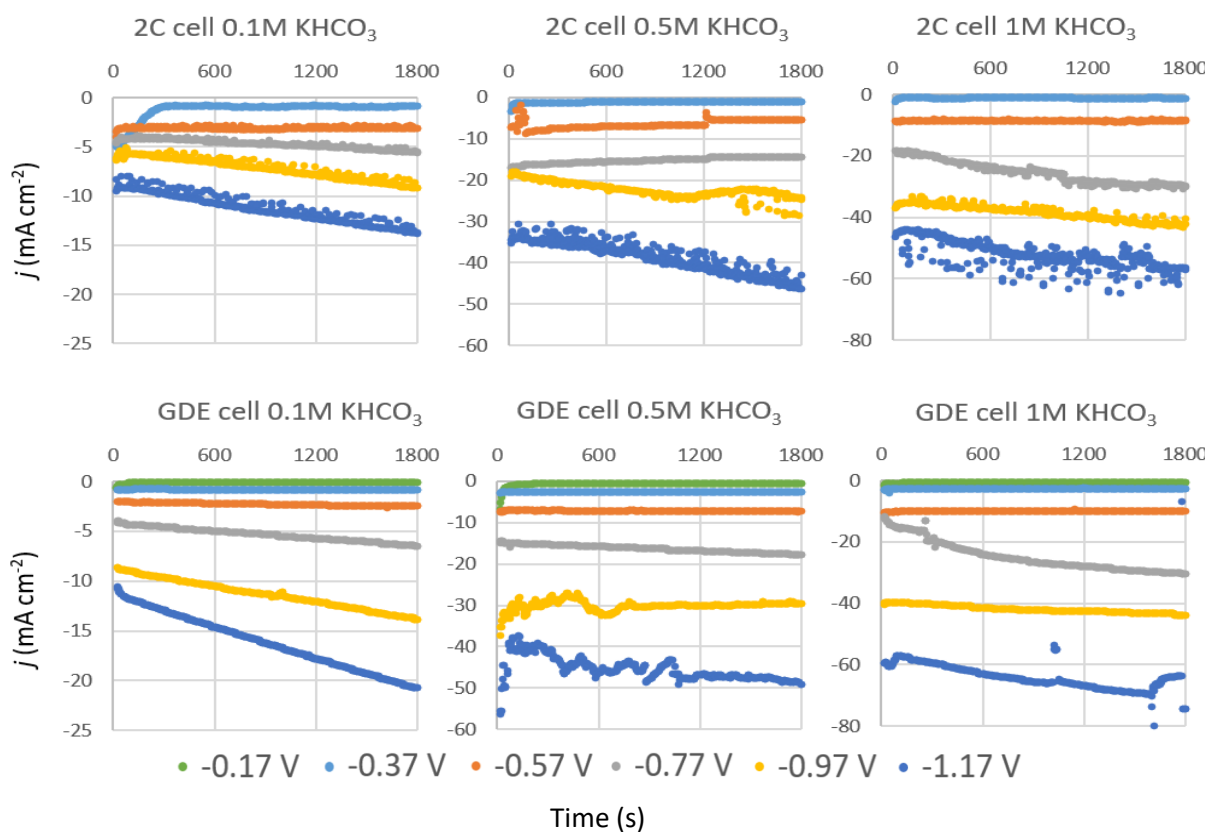
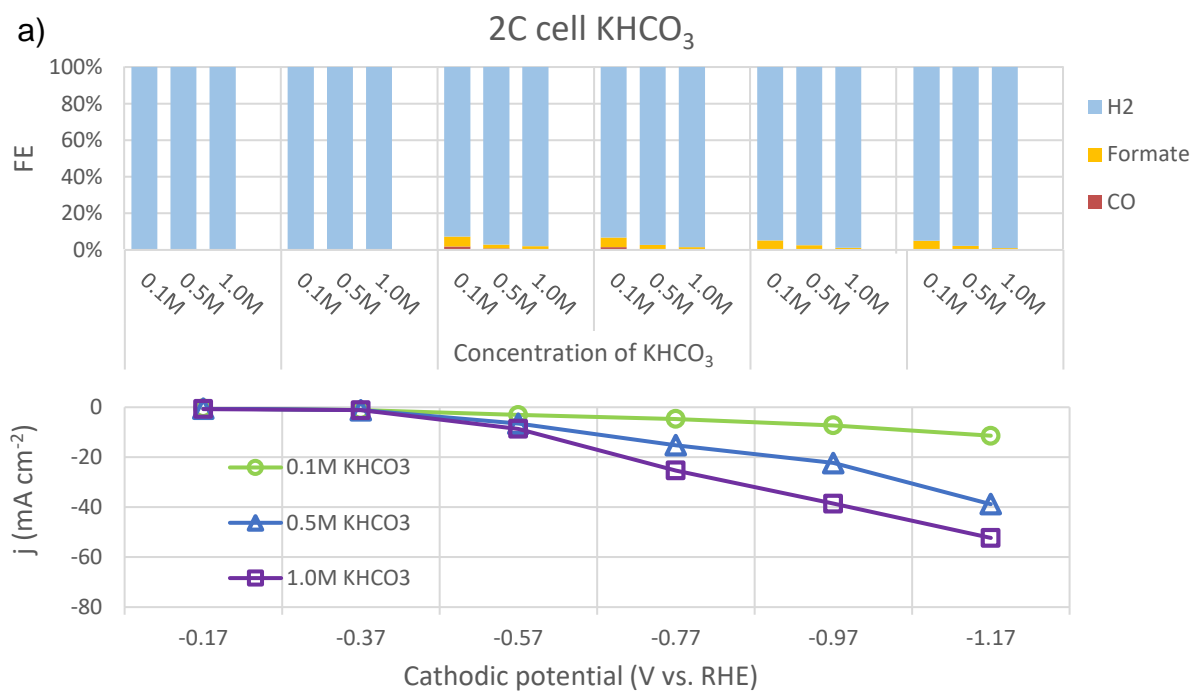


Figure 4-6 CA results of eCO₂RR in 2C cell and GDE cell with KHCO₃ catholytes using Cu_xO catalyst. Each run was driven under certain cathodic potential (-0.17 (only in GDE cell), -0.37, -0.57, -0.77, -0.97 and -1.17 V vs. RHE) for 1800 s.

From the CA results of the 2C cell and GDE cell shown in Figure 4-6, with the same catholyte, the current density (j) increased with applying more negative potential. With the same potential and catholyte, the average current density value of the 2C cell is close to that of GDE cell, but the j - t curves of 2C cell are more fluctuated due to the bubble interference. All those j - t curves present the tendency of increasing j with t , which most probably related to the gradual local pH decline caused by the dissolution of CO₂ and the production of formic acid on the electrode surface.

All the products of 30 min electrolysis were analysed, with the absolute FEs the average current density(j) of eCO₂RRs in the 2C and GDE cell presented in Table AIV-1 a of Appendix IV. Liquid products were accumulated continuously and collected for 30 min, the absolute FEs of liquid products represented average values. Differently, the gas products were collected during

a short period of time at the very last minutes of 30 min reaction, the absolute FEs of gas products represented instantaneous values. The catalyst Cu_xO (about 10 mg on each electrode) would be entirely reduced at the first few minutes of eCO_2RR when current density reached few tens of mA cm^{-2} , thus electrons should be overall used for eCO_2RR and HER afterwards. To present an average product distribution of 30 min reaction and achieve a more comparable dataset, the FE sum was normalized to 100% with fixing the liquid FEs and proportionally adjusting the gas FEs with the data presented in Table AIV-1 b of Appendix IV. The normalised FEs of carbonaceous products and H_2 and average j are presented in Figure 4-7 in a more illustrative way.



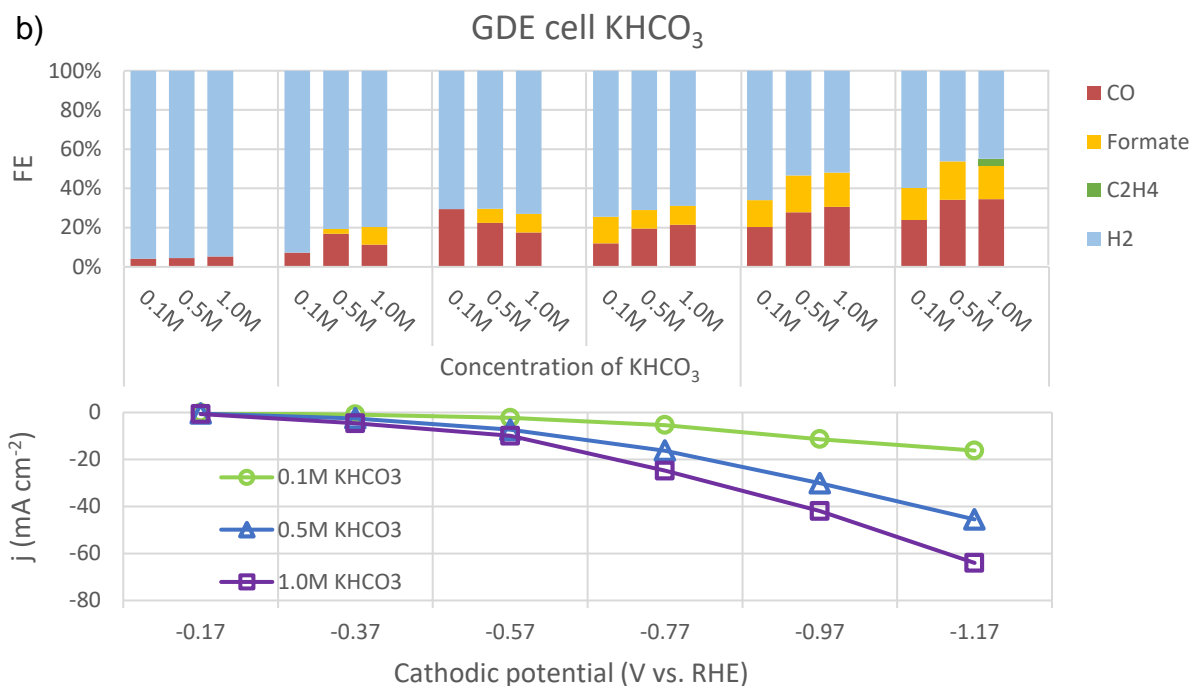


Figure 4-7 eCO₂RRs catalysed by self.Cu_xO catalyst at a wide range of applied potentials in a) 2C cell with different concentrations of KHCO₃ and b) GDE cell with different concentrations of KHCO₃.

It can be observed from the comparison between Figure 4-7 a and b that:

Within the potential range from -0.17 to -1.17 V, the GDE cell produced carbonaceous products with higher FE than the 2C cell. Although the current densities of the two cells were similar at the same catholyte and potential, the current in the 2C cell was mostly associated with HER. Only a small amount of formate and CO were produced when potentials were more negative than -0.37 V in the 2C cell, whereas CO was observed from -0.17 V in all KHCO₃ electrolytes from GDE cell. The FE of carbonaceous products in GDE cell increased with more negative potential, 5% at -0.17 V to 54% at -1.17 V.

The relationship between total FE of carbonaceous products and KHCO₃ catholyte concentration in 2C cell and GDE cell were opposite. In the 2C cell, FE of carbonaceous products decreased with an increase in KHCO₃ concentration (a similar result was reported by Hori³⁷). However, the GDE cell showed the carbonaceous FE increased with the increasing

KHCO₃ concentration.

Changing the CO₂ supply method has an impact on CO₂ mass transfer. As illustrated in Section 2.2.1.1 in Chapter 2, the process of CO₂ mass transfer in aqueous media is composed of two major steps: Step 1. CO₂ gas dissolution and equilibrium to produce the reactant CO₂(aq), Step 2. CO₂(aq) diffusion from bulk catholyte to local reaction sites. The rate of each step and the corresponding influence factors were summarised in Table 2-2 of Chapter 2. It indicated that KHCO₃ with higher concentration can balance slightly more CO₂(aq) in the bulk electrolyte³⁹ in Step 1, but constrains CO₂(aq) diffusion⁴⁴ in Step 2. Moreover, under reduction potential, the K⁺ of catholyte would be adsorbed around the double layer that further hinders CO₂(aq) diffusion⁴⁵, in favour of hydrogen evolution.

The cathode used in all the experiments is a porous GDE with a 3D structure as shown in Figure 4-8 a. The electrochemical reaction interface includes the electrode outside surface and more importantly interior surface that consisted of gaps between each agglomerates and pores inside agglomerates which are approachable for aqueous electrolyte^{28, 155}. When CO₂ supplied by “purging into electrolyte” in 2C cell (Figure 4-8 b), the CO₂(aq) distributed in bulk catholyte would go through a long-distance diffusion pathway reaching to the electrode surface. Additionally, some narrow channels in the porous electrode might prevent the diffusion of hydrous CO₂(aq) molecules to the interior reaction interface. Comparing different concentration of KHCO₃ catholyte in the 2C cell, KHCO₃ with higher concentration can balance more CO₂(aq), but would constrain the diffusion of CO₂(aq). This has been discussed in the previous Section 2.2.1.1. The diffusion limitation in 2C cell is probably the reason to the inverse correlation between the carbonaceous FE and KHCO₃ concentration presented in Figure 4-7 a. In other words, the reaction rate of eCO₂RR is diffusion-controlled in 2C cell.

When CO₂ supplied by “diffusion from GDE” in GDE cell as described by Figure 4-8 c, the carbonaceous FE positively correlated with the KHCO₃ concentration as presented in Figure 4-7 b. If CO₂(aq) was still the reactant in this case, this tendency indicates a negligible diffusion resistance from the concentrated KHCO₃ catholyte with high concentration. The main reason would be a largely shortened CO₂(aq) diffusion distance in GDE cell so that eCO₂RR most probably gets rid of the diffusion control. Another possibility is that “diffusion from GDE” approached another adsorption mechanism as shown in Equation 4-1 where CO₂ gas can be directly adsorbed on the reaction sites without going through dissolution in liquid phase. The gas adsorption mechanism in GDE was also reported in oxygen reduction reaction (ORR) related studies⁴⁹. With either mass transfer mechanism in GDE cell, sufficient CO₂ reactant could be provided around reaction sites, which develops the competitiveness of eCO₂RR against HER, resulting in greatly enhanced carbonaceous FE than 2C cell.

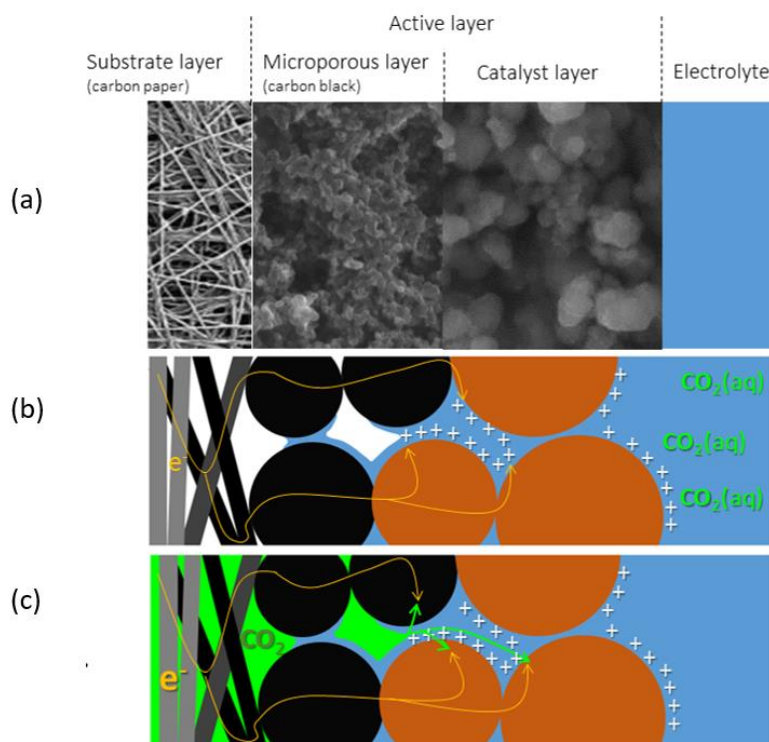


Figure 4-8 Schematics of (a) the cathode including 3 layers, (b) CO₂ mass transfer in 2C cell and (c) GDE cell.

In GDE cell, FE of carbonaceous products and current density both increased with the KHCO_3 concentration which was probably related to the alkalinity of catholyte. KOH with different concentrations were applied to further study the effect of alkaline catholyte in GDE cell, discussed in the following section.

4.3.2.3 The effect of catholyte alkalinity

Apart from the developed CO_2 mass transfer, the GDE cell has another advantage for eCO_2RR that more types of catholyte could be selected instead of CO_2 -saturated solution, so that strong alkali could be applied. KOH solution with 4 concentrations (0.1 M, 0.5 M, 1.0 M, 2.0 M) were studied as the catholyte in GDE cell. Same as the last section, fresh self- Cu_xO , 5 M KOH solution, and a Platinum-plated Titanium mesh were applied as the cathodic catalyst, anolyte, and anode. CV measurements (Figure 4-9) in N_2 and CO_2 atmosphere were respectively taken at the beginning, followed by eCO_2RR s carried out by CA at specific fixed potentials from -0.17 V to -1.17 V vs. RHE (30 min for each potential), the i-t curves of CA at different potentials are given in Figure 4-10.

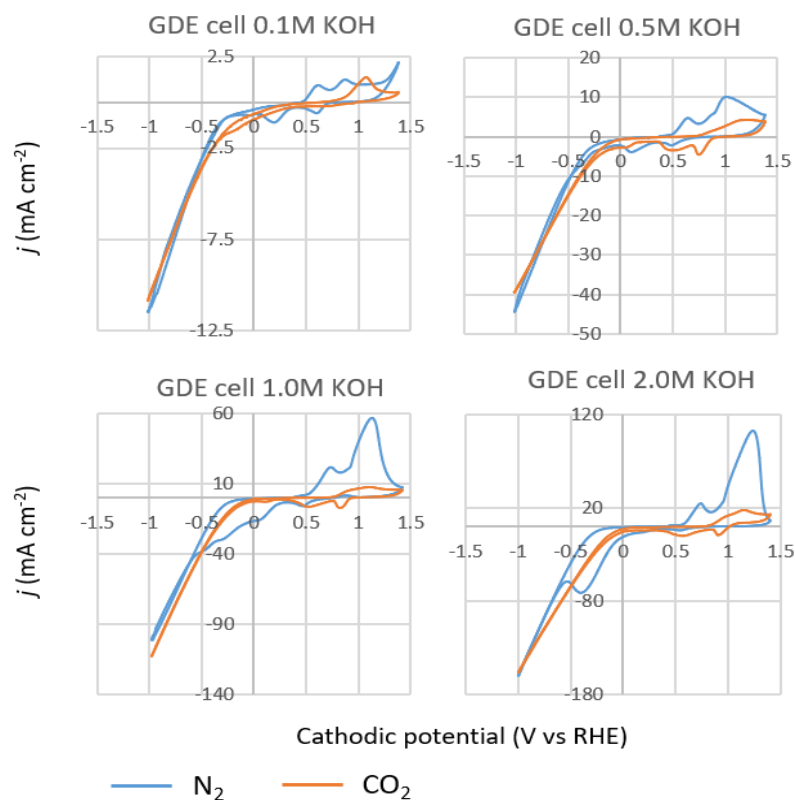


Figure 4-9 Cyclic voltammetry (CV) measurements under N₂ and CO₂ atmosphere in GDE cell with KOH catholyte using fresh self.Cu_xO catalyst. Scan rate: 50 mV s⁻¹, scan circles: 3, all those diagrams were taken from the 2nd or 3rd cycle of scan.

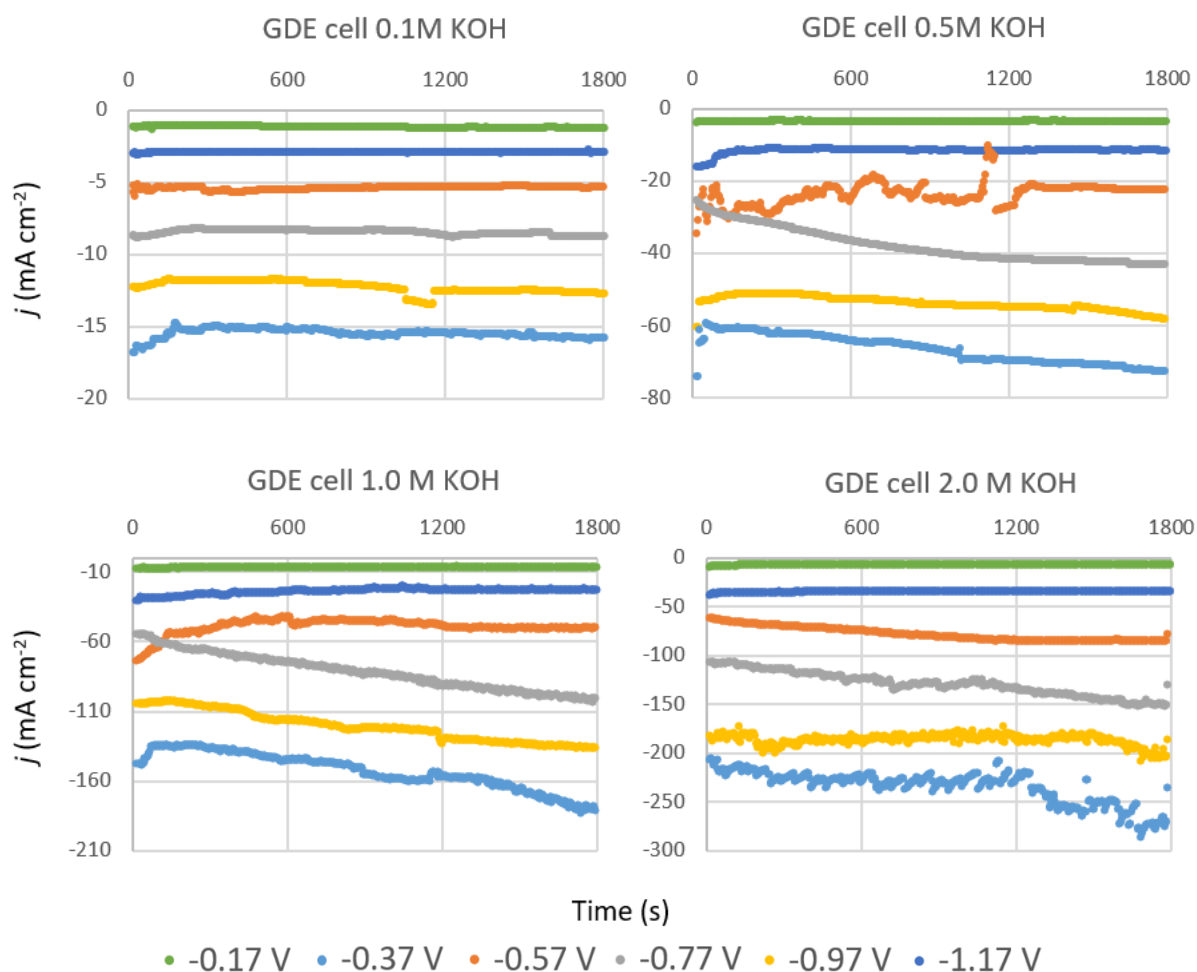


Figure 4-10 Chronoamperometry (CA) of eCO₂RR in GDE cell with KOH catholytes using Cu_xO catalyst. Each run was driven under certain cathodic potential (-0.17, -0.37, -0.57, -0.77, -0.97 and -1.17 V vs. RHE) for 1800s.

As shown in Figure 4-9, the N₂-CV curves of all the KOH concentrations present two anodic peaks at around +0.5 V and +0.8 V, linked to the oxidation process of Cu(0)/Cu(I) and Cu(I)/Cu(II), similar with the results of GDE cell using KHCO₃ shown in Figure 4-5. Differently, the N₂-CV curves in KOH ≥ 0.5 M showed a huge anodic peak between 0.9 to 1.4 V probably indicating the formation of Cu(OH)₂¹⁵⁶. Correspondingly, the reduction of Cu(II)/Cu(I) and Cu(I)/Cu(0) were observed by the two cathodic peaks at around +0.5 V and +0.1 V. As observed from the CV-CO₂ curves, the onset potential of the reduction reaction

shifted positively with the increasing KOH concentration, probably due to the enhanced reaction kinetics by stronger alkaline catholyte.

The CA results (Figure 4-10) show the current density enhanced with higher KOH concentrations and more negative potentials. The 2 M KOH even made around -250 mA cm^{-2} current density at -1.17 V . All the products of 30 min CA were analysed. The normalized FEs for carbonaceous products and H_2 , and the average current density of eCO_2RRs in the 2C and GDE cell were calculated and are attached to Table AIV-1 in Appendix IV, which are also presented in Figure 4-11.

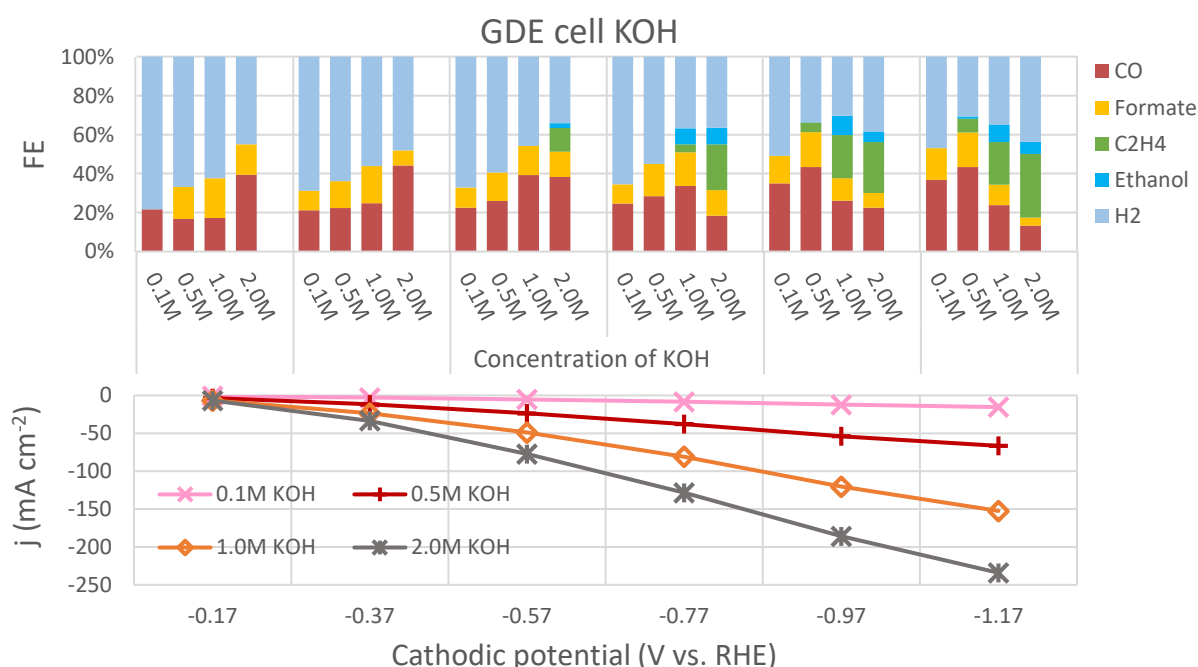


Figure 4-11 eCO_2RRs catalysed by self. Cu_xO catalyst at a wide range of applied potentials in GDE cell with different concentrations of KOH.

Comparing eCO_2RR in GDE cell with KHCO_3 catholyte (Figure 4-7 b) and KOH catholyte (Figure 4-11), the selectivity of the carbonaceous products is greater with KOH solution than with KHCO_3 solutions shown by higher FE in KOH at the same potentials. Also, in both KOH and KHCO_3 electrolytes, the carbonaceous FE was enhanced with increasing electrolyte concentrations. 1.0 and 2.0 M KOH at -0.17V had similar FE of carbonaceous products to

KHCO₃ at -1.17 V. This 1 V shift suggests lower energy required in catholyte with higher alkalinity. To assess the mechanistic pathway of eCO₂RR in GDE cell, Tafel plots of CO production from eCO₂RR in GDE cell with different catholyte are displayed in Figure 4-12 since CO was the common product for all the situations and the easiest to be generated at low overpotential. The Tafel slopes show the relationship of IR-corrected overpotential, to eliminate the effect of solution resistance. The partial current density here was using the actual electrode surface area 108.6 cm² determined in Figure 4-4 and Table 4-2. The Tafel parameters of different catholytes in GDE cell obtained from Figure 4-12 are displayed in Table 4-3.

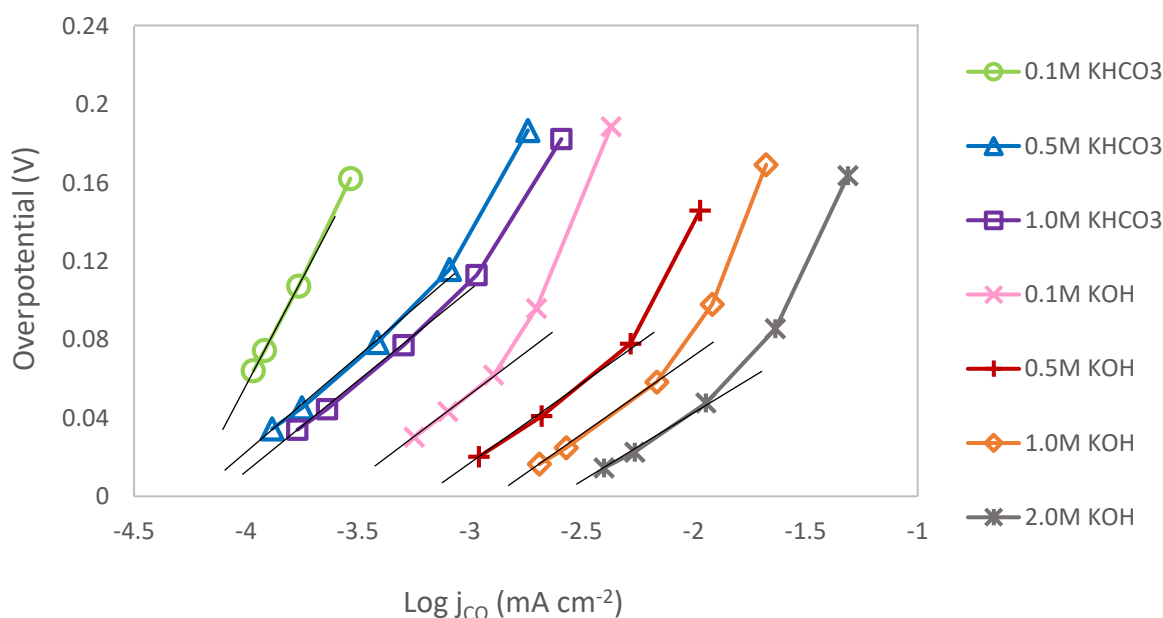


Figure 4-12 Tafel plots of the partial current density of CO₂ reduced to CO versus overpotential for CO formation in GDE cell with different catholytes.

Table 4-3 shows the Tafel parameters of different catholytes in GDE cell obtained from Figure 4-12. With the increasing catholyte pH, the Tafel slope decreased, and the exchange current density $j_0(\text{eCO}_2\text{RR})$ for CO production increased, indicating faster kinetics and higher activity of eCO₂RR with more alkaline catholyte. Apart from 0.1 M KHCO₃ with lowest [OH⁻], the difference between other Tafel slope values were small, decreased from 94.8 mV dec⁻¹ in 0.5 M KHCO₃ to 74 mV dec⁻¹ in 2.0 M KOH. This suggests the same mechanism for CO₂ reduction

to CO despite different $[\text{OH}^-]$ in the catholyte.

Table 4-3 Tafel parameters obtained from the Tafel plots (Figure 3b), b represents the Tafel slope for the lower overpotential region.

	KHCO ₃			KOH			
	0.1 M	0.5 M	1.0 M	0.1 M	0.5 M	1.0 M	2.0 M
pH	8.55	9.04	9.67	13.02	13.56	13.96	14.30
b (mV dec ⁻¹)	213	94.8	91.5	89.5	85.7	80.6	74
j_0 (mA cm ⁻²)	5.41 $\times 10^{-5}$	5.76 $\times 10^{-5}$	7.30 $\times 10^{-5}$	2.61 $\times 10^{-4}$	5.77 $\times 10^{-4}$	1.30 $\times 10^{-3}$	2.60 $\times 10^{-3}$

Back to Figure 4-11, C₂ products (ethylene and ethanol) were notably produced in KOH catholyte with the concentration higher than 0.5 M. At -1.17 V, the C₂ FE reached almost 40% in 2.0 M KOH. Within the potential range in this study, C₂ selectivity was increased with more negative potentials and higher KOH concentration. The current density (j) increased with increasing the overpotential and catholyte concentration. Under the same potential, the current density of KOH was much higher than KHCO₃ with the same concentration. EIS measurement with the CO₂ atmosphere was used to survey the effect of KOH concentration on resistances, with the results displaying in Figure 4-13.

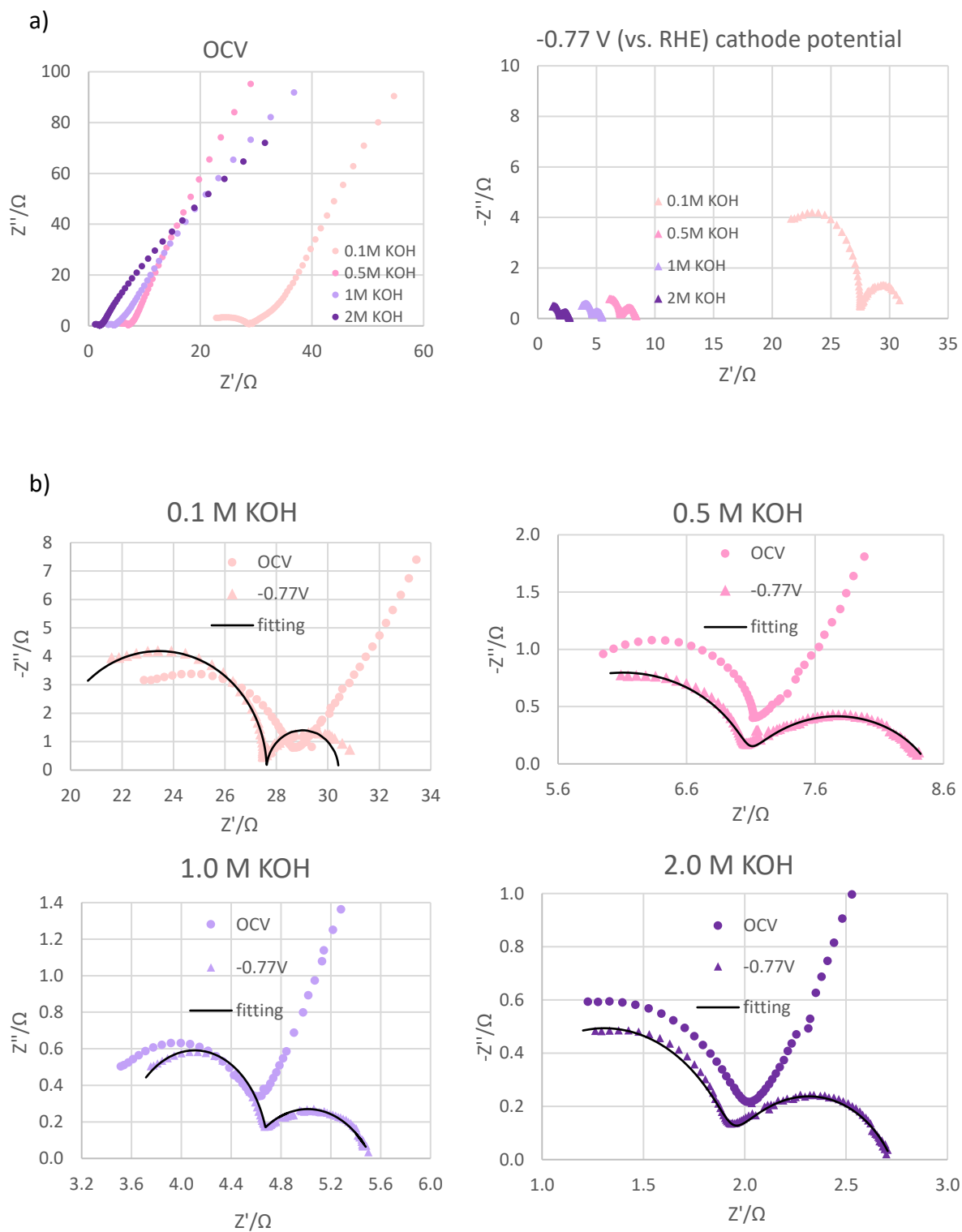


Figure 4-13 a) Nyquist plots of GDE cell using KOH catholyte with different concentrations at OCV and -0.77 V (vs. RHE) cathodic potential. b) The enlarged views of Nyquist plots obtained under OCV and -0.77 V cathode potential sorted by KOH concentrations.

In Figure 4-13 a, the two Nyquist diagrams were taken under open-circuit voltage (OCV) and -

0.77 V (vs. RHE) cathodic potential with CO₂ atmosphere respectively, in GDE cell using KOH with different concentrations. Those Nyquist plots are analogous either in OCV or -0.77 V with two arcs. The arc in the low-frequency range is attributed to the electrochemical reaction as phenomenally its diameter strongly decreased with applying reaction potential. Figure 4-13 b displays the enlarged views of OCV and -0.77 V Nyquist plots sorted by KOH concentration. The arc in the high-frequency range is independent of the reaction potential, which is probably related to the gas adsorption in porous GDE¹⁵⁷⁻¹⁵⁸. The equivalent circuit could be simplified as $-R_s-(R_{ct}-(R_{ad}C_{ad}))C_{dl}$ ¹⁵⁶, where R_s stands for the uncompensated internal resistance including the electrolyte, the parallel connected $(R_{ad}C_{ad})$ is related to the gas adsorption in the high-frequency domain, independent of the reaction potential. The R_{ct} and C_{dl} represents the charge transfer resistance and the double layer capacitance respectively in the low-frequency range. Table 4-4 summarized the electrical conductivities and the fitted R_s , R_{ad} , and R_{ct} values at -0.77 V varied by KOH concentration. All the three resistances decreased with the increasing KOH concentration, with the R_s decreased more dramatically due to the more electrical conductivity of concentrated KOH. R_{ct} also decreased due to faster reaction kinetics in more alkaline catholyte.

Table 4-4 The electrical conductivities¹⁵⁹ at 20°C and ambient pressure, and the fitted R_s , R_{ad} and R_{ct} values of eCO₂RR at -0.77 V(RHE) cathodic potential varied by KOH catholyte concentration

	0.1 M KOH	0.5 M KOH	1.0 M KOH	2.0 M KOH
Conductivity (S/cm)	0.0226	0.1074	0.2013	0.3494
R_s (Ω)	19.25	5.622	3.536	0.984
R_{ad} (Ω)	8.369	1.968	1.457	1.260
R_{ct} (Ω)	2.796	1.400	0.974	0.793

KOH with higher concentration has smaller resistances of solution and charge transfer. The charge transfer resistance decreased with $[\text{OH}^-]$, corresponding to the increasing exchange current density j_0 shown in Table 4-3. -234 mA cm^{-2} current density was achieved at -1.17 V in 2.0 M KOH , with 40% FE of C_2 . The production rate of ethylene and ethanol was respectively $0.105 \text{ mg min}^{-1}$ and $0.035 \text{ mg min}^{-1}$ on 2 cm^2 electrode with CO_2 flow rate 15 ml min^{-1} , implying the industrialisation potential for C_2 production.

The catholyte with higher alkalinity showing improved eCO_2RR kinetics and C_2 selectivity could be due to the altered local environment by OH groups from the catholyte. Zhang et al.¹³⁵ compared eCO_2RRs on three different local oxygen-induced surfaces: 1. fully oxidized Cu_2O surface, 2. partially oxidized $\text{Cu}(110)\text{-(}2\times\text{1)O}$ surface, 3. presence of OH spectators. The existence of OH groups as spectators on Cu^0 surface could flip the selectivity between CH_4 and CH_3OH , playing the similar role with the oxidized Cu surface. It has been widely accepted that oxide-derived electrocatalysts applied in eCO_2RR can reduce the energy barrier of CO_2 activation through enhancing the adsorption strength¹⁴¹ and stability of the active species CO^* on reaction sites^{24, 100, 140}. The CO^* dimerization is the rate determining step of C_2 products formation¹⁶⁰⁻¹⁶⁴, which occurs at high local $\text{pH}(\geq 12)$ ¹⁶⁵, and easier to take place on an oxygen-induced Cu surface than bare metallic Cu^{139, 142}. XRD and XPS were applied to investigate the status of catalyst and reaction interfaces, as shown in Figure 4-14.

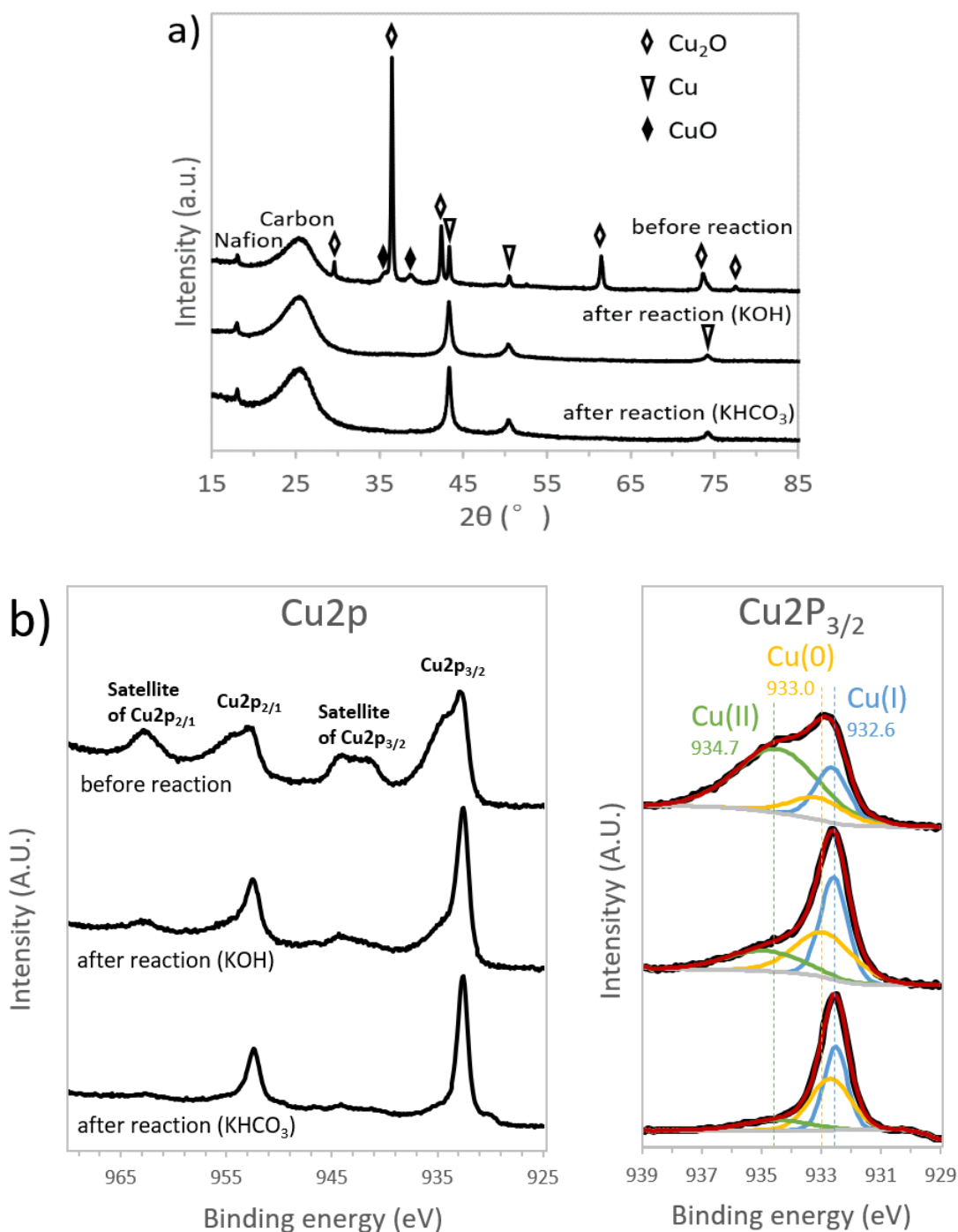


Figure 4-14 a) XRD patterns and b) XPS spectra of Cu₂P and the peak-differentiating of Cu₂P_{3/2} for the Cu_xO-GDE before eCO₂RR and after 3 hours eCO₂RR in 1.0 M KOH and 1.0 M KHCO₃.

The self.Cu_xO applied as the catalyst in this study is a mixture of Cu₂O (main), CuO and Cu as observed in its XRD pattern (Figure 4-14 a). The reduction of Cu_xO to Cu⁰ has less-negative potential than eCO₂RR as found in the CV results in Figure 4-5 and 4-9. Thus, under the reaction potential of eCO₂RR, the Cu_xO catalyst should be reduced to Cu⁰ rapidly. The XRD patterns of

the two “after reaction” samples indicate the main component in the bulk catalyst after reaction either in 1.0 M KHCO₃ or 1.0 M KOH was metallic Cu. However, even though the bulk Cu_xO catalyst reduced to Cu⁰, the catalytic activity maintained over 4 hours with stable C₂ FE between 30-40%, as shown in Figure 4-15. One possibility is the stably-existed grain boundaries on oxide-derived catalyst which could largely get rid of the effect of the reduction potential¹²². The stable catalytic performance also suggests the unaffected Cu-based active sites with favourable carbonaceous products formation, probably from the combination of Cu⁰ and OH or from the remained oxide-derived feature. XPS which was used to characterize the catalyst surface further proved this. Figure 4-14 b displays the XPS spectra of self.Cu_xO-GDE before eCO₂RR and after 3h eCO₂RR in GDE cell with 1.0 M KOH and 1.0 M KHCO₃. The reduction of the catalyst after reaction is also observed since the satellite peaks of Cu 2p_{3/2} and Cu 2p_{1/2} on the fresh catalyst are both largely attenuated after reaction¹⁶⁶. These peaks are stronger mitigated in the “after reaction (KHCO₃)” catalyst than those of “after reaction (KOH)”, indicating the catalyst surface after reaction remains higher oxidation degree in KOH than in KHCO₃. The Cu2P_{3/2} photoelectric peak was fitted to quantitatively analysis Cu species¹⁶⁷⁻¹⁶⁸. The fresh catalyst surface contains 14.65 % Cu(0), 21.99 % Cu(I), and 63.36 % Cu(II). After eCO₂RR, the catalyst surface of “after reaction (KOH)” contains 37.82% Cu(0), 39.92% Cu(I) and 22.26% Cu(II), showing higher oxidation degree than that of “after reaction (KHCO₃)” containing 44.31% Cu(0), 41.15% Cu(I) and 14.54% Cu(II). Although the bulk Cu_xO catalyst was substantially reduced to metallic Cu after eCO₂RR, oxidized Cu partially remained on the catalyst surface. Most probably, the OH groups from alkaline catholyte adsorbed on the catalyst surface and partially prevented the oxidized Cu surface from being reduced. KOH supplying more adsorbed OH groups retained more oxide-derived Cu than KHCO₃. High population of OH on catalyst surface was in favor of C-C coupling leading to enhanced selectivity for C₂ products.

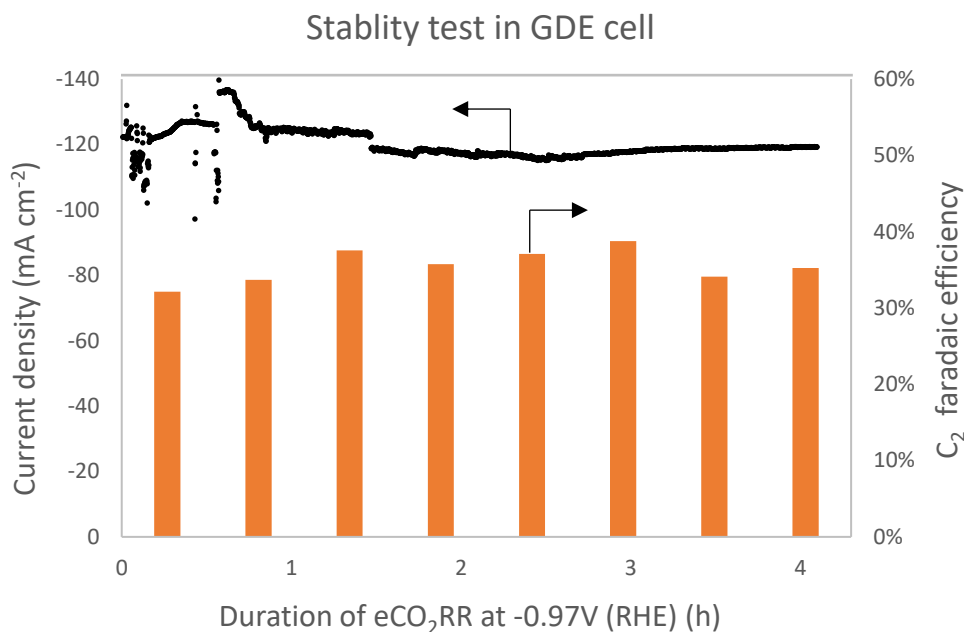


Figure 4-15 Stability test of eCO₂RR at -0.97 V (vs. RHE) using self.Cu_xO catalyst and 1 M KOH catholyte in GDE cell

4.4 Chapter summary

In this study, the feasibility of applying gas diffusion electrode (GDE) in CO₂ electro-reduction was successfully tested. The effects of CO₂ supply method and alkalinity on the selectivity of carbonaceous products, and C₂ products were investigated in aqueous electrolyte using Cu_xO catalyst. The results suggested that GDE cell with CO₂ supplied through gas diffusion has higher selectivity for carbonaceous products and suppression of hydrogen evolution compared to two-chamber cell with CO₂ purging into electrolyte. Faradaic efficiency (FE) of carbonaceous products increased from <10% in 2C cell to 55% in GDE cell at -1.17 V in 1.0 M KHCO₃. This was primarily due to different reactants for CO₂ electrochemical reduction in GDE and in reaction solution, being CO₂ (g)* and hydrated CO₂(aq)*, respectively. The alkalinity of catholyte also had a significant influence on the selectivity of carbonaceous products leading to higher FE from KOH than KHCO₃. Higher FE of C₂ products, ethanol and ethylene, were observed from KOH with higher concentration (≥ 0.5 M) and at higher overpotentials (-0.97 and -1.17 V), suggesting C-C coupling process occurring with high

concentration of OH at catalyst interface with high energy input. XRD and XPS proved the effect of OH groups on the catalysts surface could be favourable to carbonaceous products formation. At -1.17 V with 2 M KOH, C₂ FE achieved at 40% with current density -234 mA cm⁻², producing 0.105 mg min⁻¹ ethylene and 0.035 mg min⁻¹ ethanol on 2 cm² electrode with CO₂ flow rate 15 ml min⁻¹. This is promising for further development and scale-up.

Chapter 5 A Scalable Process for Cu-In Catalyst Synthesis for Highly Selective CO and Tunable Syngas Production from CO₂ Electrochemical Reduction

5.1 Introduction

CO is a promising product from eCO₂RR for its high market price and the industrial utilization for the production of fuels and chemicals⁷⁸⁻⁷⁹. As stated in Section 2.3.2 of Chapter 2, the electrocatalysts for CO₂ reduction to CO are mostly reported to be noble metals or their oxides such as Au^{80, 169}, Ag^{89, 170}, Pd¹⁷¹⁻¹⁷² species. Some metal-free carbon materials were also presented to perform high CO selectivity from eCO₂RR, such as carbon nanotubes¹⁷³⁻¹⁷⁴ and graphene quantum dots³³ with doping nitrogen to modify the active sites. Those catalytic materials all bring their own cost and sustainable issues. Aiming at the practical use, the combination of multiple non-noble metals in the form of homogeneous alloy or heterogeneous composite should be a cost-effective approach for the design of catalytic materials. Rasul et al.¹⁰⁰ combined two non-noble metals Cu and In for catalysing eCO₂RR, because indium presents higher overpotential towards the competitive HER¹⁷⁵. The In-deposited oxide-derived Cu electrode showed improved CO Faradaic efficiency (FE) at moderate potentials (e.g. ~90% FE at -0.6 V), which was comparable with the catalytic performance of noble metals.

Although electrocatalysts with > 90% CO FE from eCO₂RR have been widely reported, the general reaction rate is low with current density (j) <10 mA cm⁻² at moderate potentials. Our previous work^{36, 176} (also the content in Chapter 4) illustrated the slow reaction rate was caused by the limitation of CO₂ mass transfer in a traditional two-chambers reactor with CO₂-saturated catholyte, and the low current density to a large extent was resulted from using dilute carbonate/bicarbonate catholyte. A combination between gas diffusion electrode (GDE) and strong alkaline catholyte can achieve high current density of the reduction reaction³¹, due to the developed CO₂ mass transfer of GDE and faster reaction kinetics when using strong alkali.

To combine the non-noble CuIn catalyst and GDE system, herein, we firstly developed two spontaneous precipitation methods, which are simple to fabricate GDE-coated CuIn catalyst for CO₂ electro-reduction. The different mechanisms of these two methods, spontaneous precipitation (SP) and electrochemical spontaneous precipitation (ESP), were discussed based on the material characterisation. CuIn-ESP showed better Cu-In interaction enabled higher CO selectivity from eCO₂RR than CuIn-SP. Free from the alloy active centre formed by conventional electro-deposition, the material presents a heterostructure of Cu-In combination that amorphous In(OH)₃ nanolayer (3~10 nm thickness) tightly capping on polycrystalline Cu_xO. The key factors of CuIn catalyst on the CO selectivity has been studied. With the GDE cell, ~ 200 mA cm⁻² current density was reached at -1.17 V. CO yield achieves 3.05 mg min⁻¹ with CO₂ supplying at 15 ml min⁻¹ on 2 cm² electrode. Interestingly, Syngas with tunable ratio of CO/H₂ could be also produced by changing the ESP conditions. The cost-efficient strategy of synthesizing GDE-loaded electro-catalyst is easy to scale up and of general applicability, which may open a new avenue for high-efficient CO₂ reduction catalysis.

5.2 Experimental

5.2.1 Preparation of Cu-In catalysts on gas diffusion electrode by two spontaneous precipitation methods

As stated in Section 3.3.3 of Chapter 3, the Cu-In catalysts coated gas diffusion electrode (GDE) was prepared by precipitation of indium species on the com.Cu₂O-GDE. Preparation process of com.Cu₂O-GDE was given in Section 3.3.1, with Nafion/catalyst = 20 wt.%. The two spontaneous precipitation processes both started from placing an In foil and the com.Cu₂O-GDE in a 20 ml container filled with the acidified In³⁺ solution (0.05 M In₂(SO₄)₃ and 0.4 M citric acid, pH = 2.5). Differently, the electrochemical spontaneous precipitation (ESP) included an external cable (2 Ω) connected between Com.Cu₂O-GDE and In foil to facilitate the redox reaction whereas the spontaneous precipitation (SP) did not. Figure 5-1 shows the schematic of

experiment set-up and process observation for 1 hour of these two spontaneous precipitation processes.

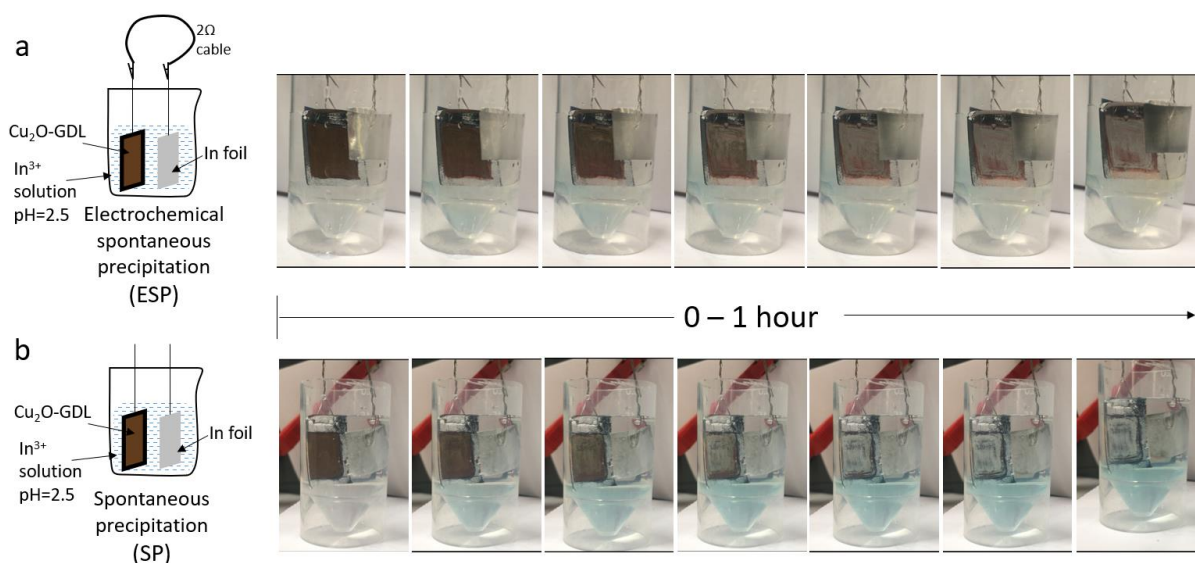


Figure 5-1 Experiment set-up schematic and process observation for 1 hour of a) electrochemical spontaneous precipitation (ESP) and b) spontaneous precipitation (SP).

To find out the reaction mechanism of ESP, the open circuit voltage (OCV) was individually monitored by the potentiostat (Metrohm Autolab PGSTAT128N). In another current-monitoring experiment, an amperemeter ($1.4\ \Omega$ internal resistance) was connected between the In foil and com. Cu_2O -GDE to record the current change over the ESP time. The charge over ESP duration was also calculated by integrating the current-time curve.

5.2.2 Catalyst characterisations

X-ray diffraction (XRD), X-ray photoelectron spectroscopy (XPS), scanning electron microscopy (SEM), and transmission electron microscope (TEM) were applied to analyse catalyst properties, which have been stated in Section 3.5.2 of Chapter 3.

5.2.3 Catalyst evaluation by CO_2 electro-reduction

A 3D printed GDE reactor mentioned in Section 3.2.2 of Chapter 3 was used to perform the

mass transfer developed eCO₂RR. The synthesized CuIn-GDE was the cathode with the geometric surface area 2 cm² and the anode was Platinum plated Titanium mesh with a dimension of 4 cm². Ag/AgCl with a luggin capillary was used as the reference electrode. 1 M KOH and 5 M KOH were used as the catholyte and anolyte respectively separated by a cation exchange membrane. ECO₂RR was carried out by chronoamperometry (CA) recording the current at a particular applied potential for 30 minutes ranging from -0.17 to -1.17 V (vs. RHE). The potentials stated in this study are referred to RHE unless otherwise stated. The CO₂ flow rate and catholyte flow rate were controlled the same with the stated in Section 3.4.1 of Chapter 3. The products of eCO₂RR were analysed by gas chromatography (GC) and ion chromatography (IC) as expounded in Section 3.5.1.

5.3 Results and discussion

5.3.1 Cu-In prepared by spontaneous precipitation (SP)

5.3.1.1 Catalyst characterisation and synthesis mechanism

The spontaneous precipitation (SP) of In species on Cu started from immersing com.Cu₂O-GDE and In foil into acidified In³⁺ solution (pH = 2.5), with controlled SP time by discharging the solution. The photographic images of CuIn-SP varied by SP time are shown in Figure 5-2.

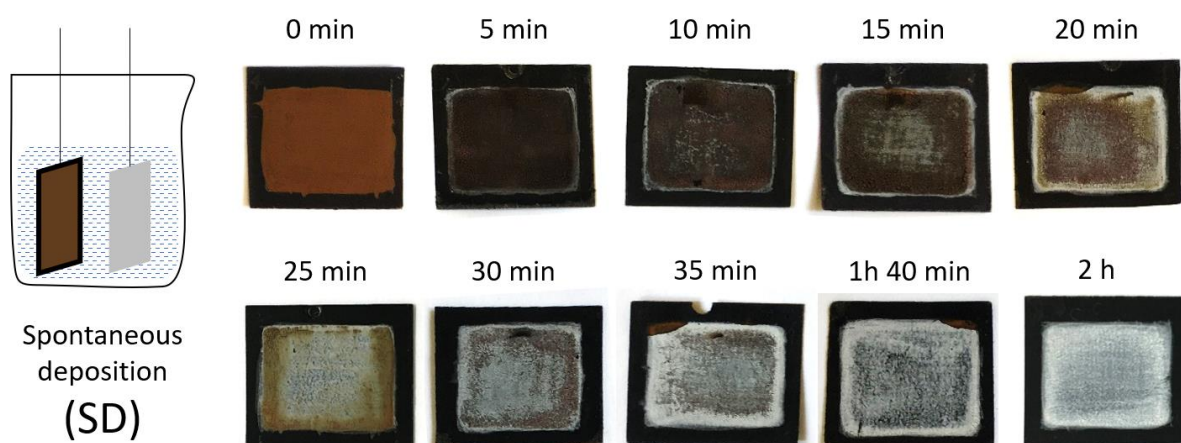
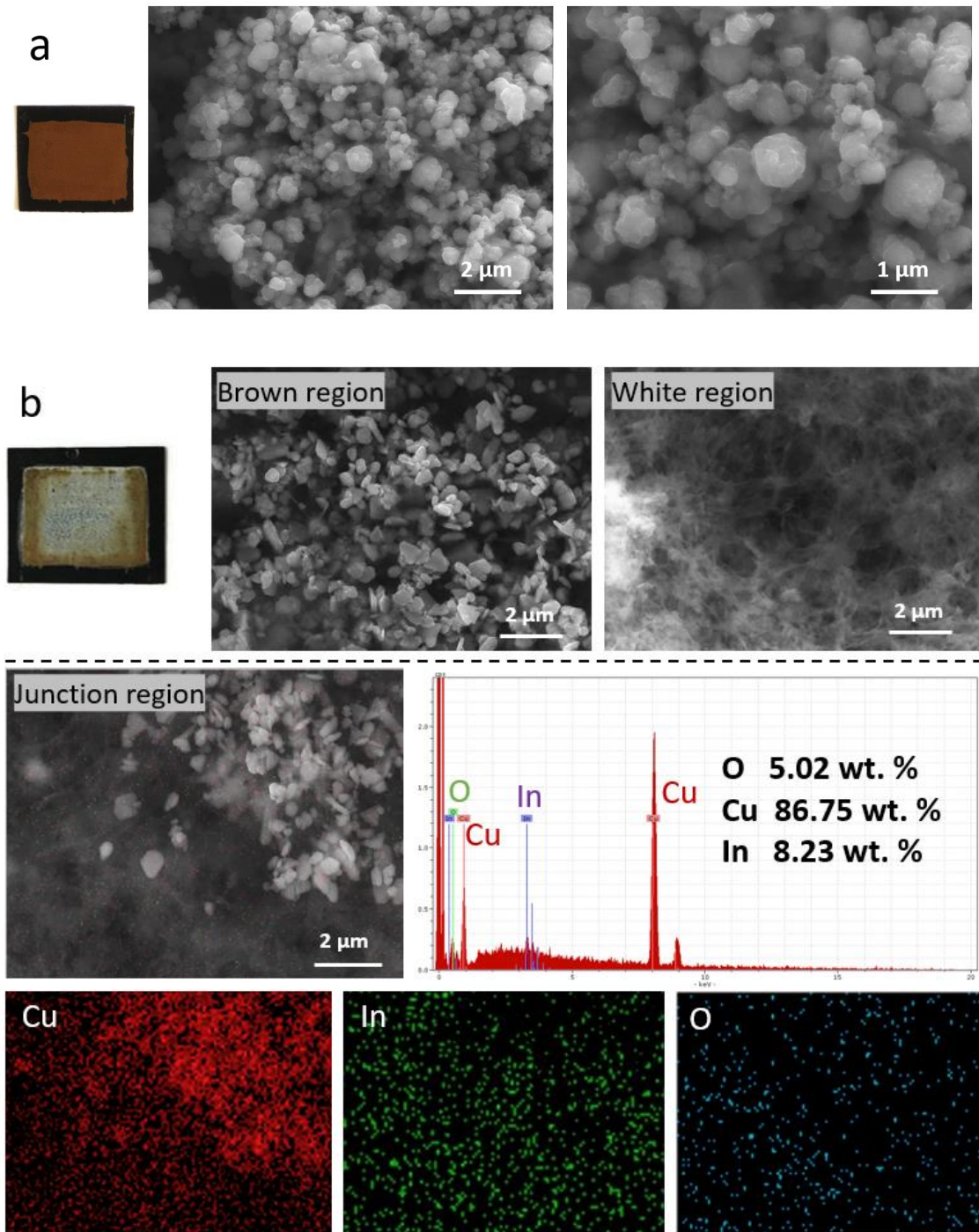


Figure 5-2 Photographic images of com.Cu₂O-GDE (0 min) and CuIn-SP by 5 min to 2 h SP time.

From the photographic images in Figure 5-2, com.Cu₂O-GDE (SP 0min) shows the brown Cu₂O layer bond on the black GDL. As the precipitation time prolonged, a white layer gradually appeared upon the brown layer. The electrode with SP 2h only shows the white layer with the disappearing brown base. The SEM technology was used to study the morphology of com.Cu₂O, CuIn-SP25min, and CuIn-SP2h, as presented in Figure 5-3.



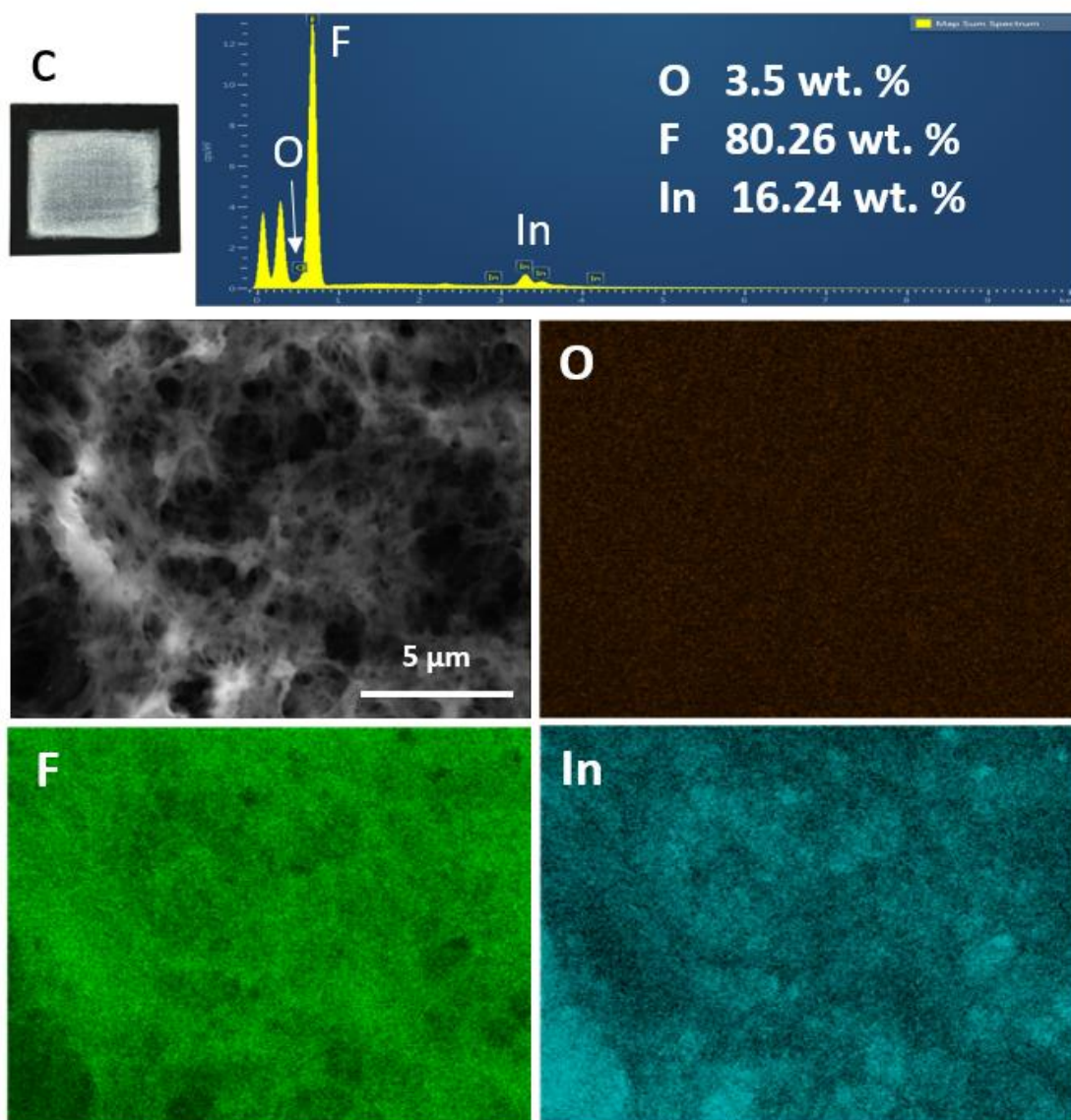
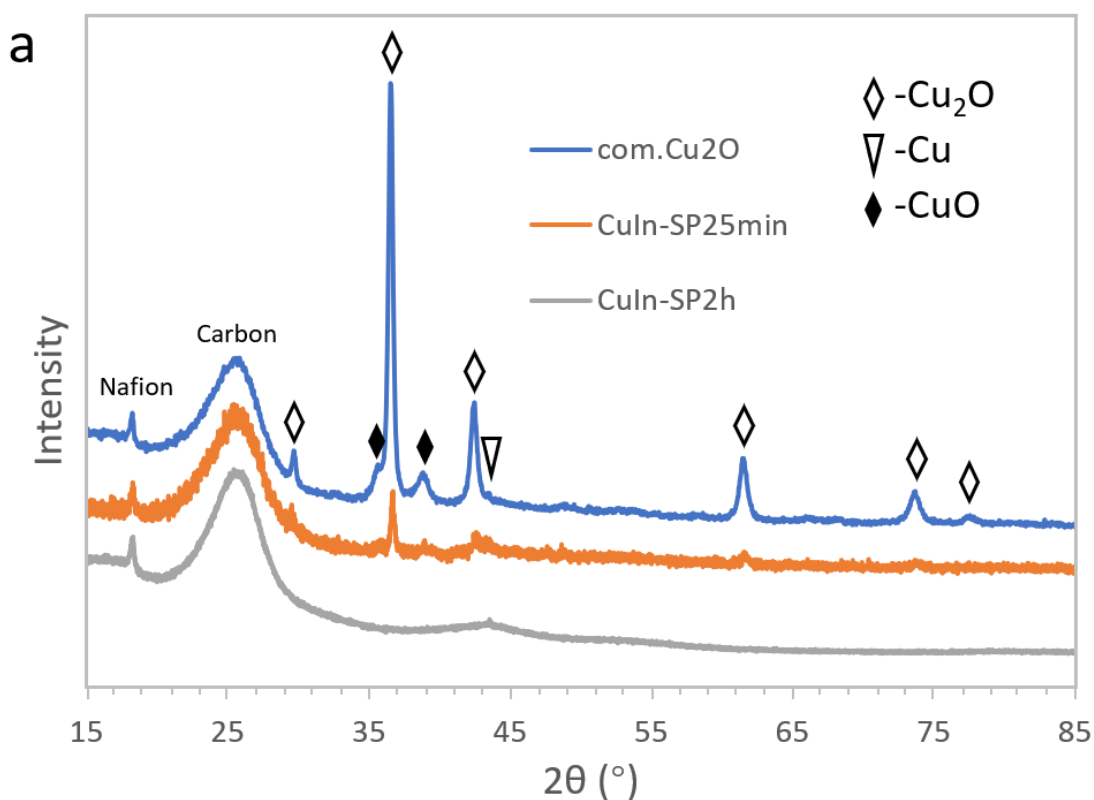


Figure 5-3 a) SEM images of com.Cu₂O. SEM images, elemental mapping, and quantitative EDX analysis of b) CuIn-SP25min and c) CuIn-SP2h.

The fresh Cu₂O (Figure 5-3 a) contains uniformly distributed polygon particles with the size ranging from 100 to 1000 nm. After SP 25min, two different morphologies are presented as shown in Figure 5-3 b - crystalline particles and cloudy reticular structure, respectively corresponds to the brown and white regions on the electrode surface. The shape of particles in the brown region is evenly in the form of triangular prism with the edge length around 0.5 μm while the reticular material in the white region presents disordered structure. Elemental mapping and EDX were applied to analyse the junction region, which certificate the existence

of Cu and In and further indicate the triangular particles are Cu species while In species are mostly distributed on the cloudy reticular structure. On the CuIn-SP2h, the crystalline triangular particles completely vanish but the reticular disordered material existed as displayed in Figure 5-3 c. The EDX result in Figure 5-3 c also proves the disappearing of Cu species that F and In are the main elements on the surface of CuIn-SP2h, linked to the Nafion binder and indium precipitation layer respectively. The elemental mapping indicates Nafion constitutes the framework of the reticular material while the indium species primarily occupies the pores. The generation of the pores on Nafion framework should be most probably resulted from the disappearing Cu particles where the indium precipitation took place. XRD and XPS were applied to analyse the phase composition of those electrodes with the results shown in Figure 5-4.



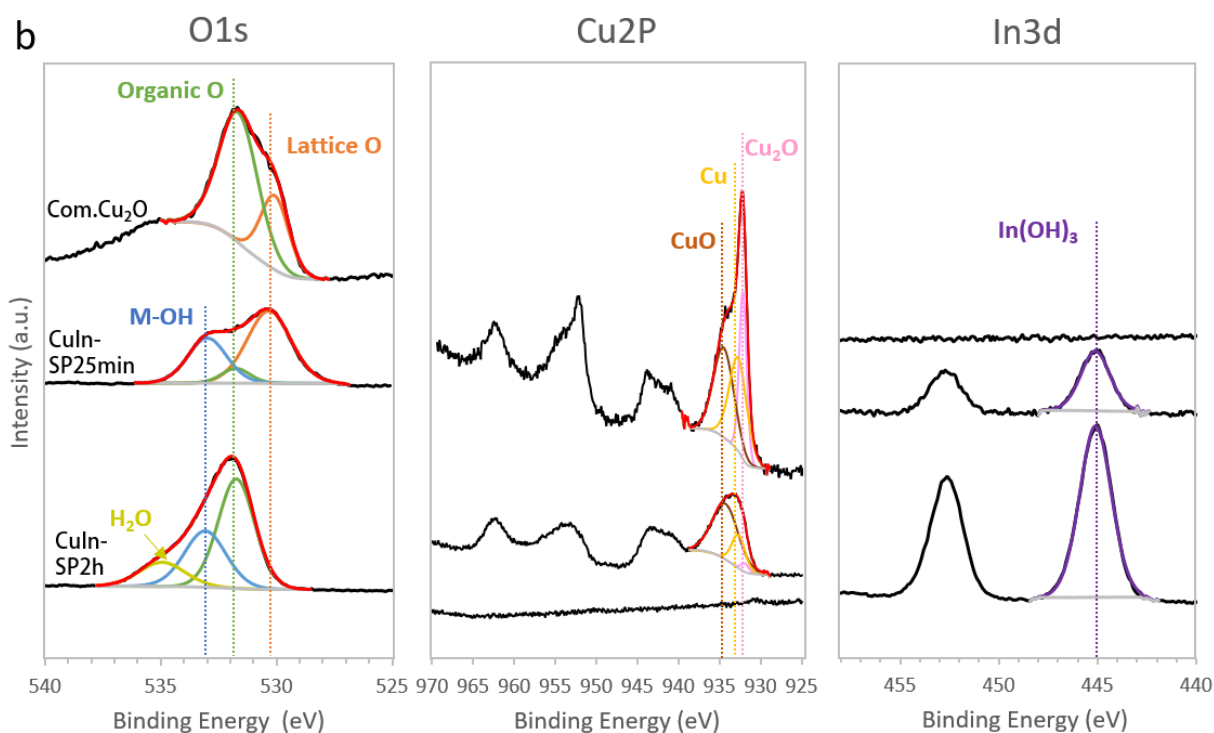


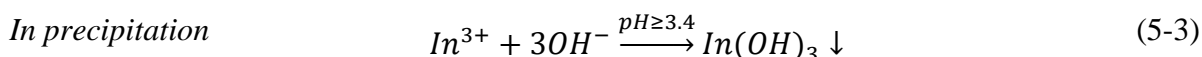
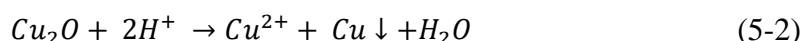
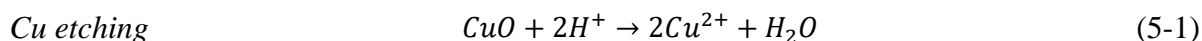
Figure 5-4 a) XRD profiles of com.Cu₂O, CuIn-SP25min and CuIn-SP2h. b) High-resolution XPS spectrum of O1s, Cu2p, and In3d of com.Cu₂O (top), CuIn-SP25min (middle), and CuIn-SP2h (bottom).

In Figure 5-4 a, the XRD pattern of com.Cu₂O confirms Cu₂O is the major phase with a small amount of CuO and Cu. Its Cu2p spectra in XPS analysis (Figure 5-4 b) also presents the mixture of oxidized and metallic Cu, with showing the CuO (934.8 eV), Cu (933.0 eV), and Cu₂O (932.6 eV) peaks differentiated from the Cu2P_{3/2} photoelectric peak^{167-168, 177}. The O1s spectra can be de-convoluted into two distinct peaks at 530.3 eV and 531.5 eV, attributed to the lattice oxygen from copper oxides and organic oxygen from Nafion binder respectively¹⁷⁸⁻¹⁸⁰.

XRD patterns of CuIn-SP in Figure 5-4 a indicate the gradual vanish of Cu species, since all the Cu-related peaks attenuated in CuIn-SP25min and disappeared in CuIn-SP2h. No In-related peaks can be found in the XRD patterns of either CuIn-SP25min or CuIn-SP2h, however, the XPS spectrum (Figure 5-4 b) certificate the existence of indium species on the electrode surface. The prominent photoelectronic peaks in In 3d spectra are symmetrical, at 445.0 eV and 452.5 eV assigned as In 3d_{5/2} and In 3d_{3/2} of In(OH)₃¹⁸¹⁻¹⁸². Compared to the XPS O1s result of

com.Cu₂O, a new peak can be differentiated at ~532.8 eV in either CuIn-SP25min or CuIn-SP2h, attributed to the formation of In(OH)₃¹⁸²⁻¹⁸³. The absence of lattice oxygen in the O 1s region as well as the disappearing Cu2p signal of “CuIn-SP2h” indicate the vanish of Cu species during SP process, in accordance with the XRD results. From the above analysis, Cu oxides and In(OH)₃ were both presented on the surface of CuIn-SP25min but only In(OH)₃ was shown on CuIn-SP2h.

The mechanism of SP could be speculated based on the above analysis. Cu oxides were firstly etched by the acidified In³⁺ solution (pH = 2.5), protons were consumed which raised the local pH, as Equation (5-1) and (5-2) described. The initial colourless solution changed to light blue from experimental observation in Figure 5-1 b also indicated the formation of Cu²⁺ ions. Indium precipitation took place locally where pH growth over 3.4¹⁸⁴ by proton consumption, as shown in Equation (5-3). In summary, during SP process, In(OH)₃ was in-situ precipitated on the sites of Cu oxides etching on Nafion framework. The SP process terminated by the complete Cu etching.



5.3.1.2 eCO₂RR activities of CuIn-SP

Com.Cu₂O and CuIn-SP with different precipitation time were evaluated by eCO₂RR at -0.77 V (vs. RHE) in a GDE cell with 1 M KOH as the catholyte. A blank GDL without catalyst coating was also tested as the control. Results of the normalized Faradaic efficiencies (FE) and current density (*j*) are displayed in Figure 5-5.

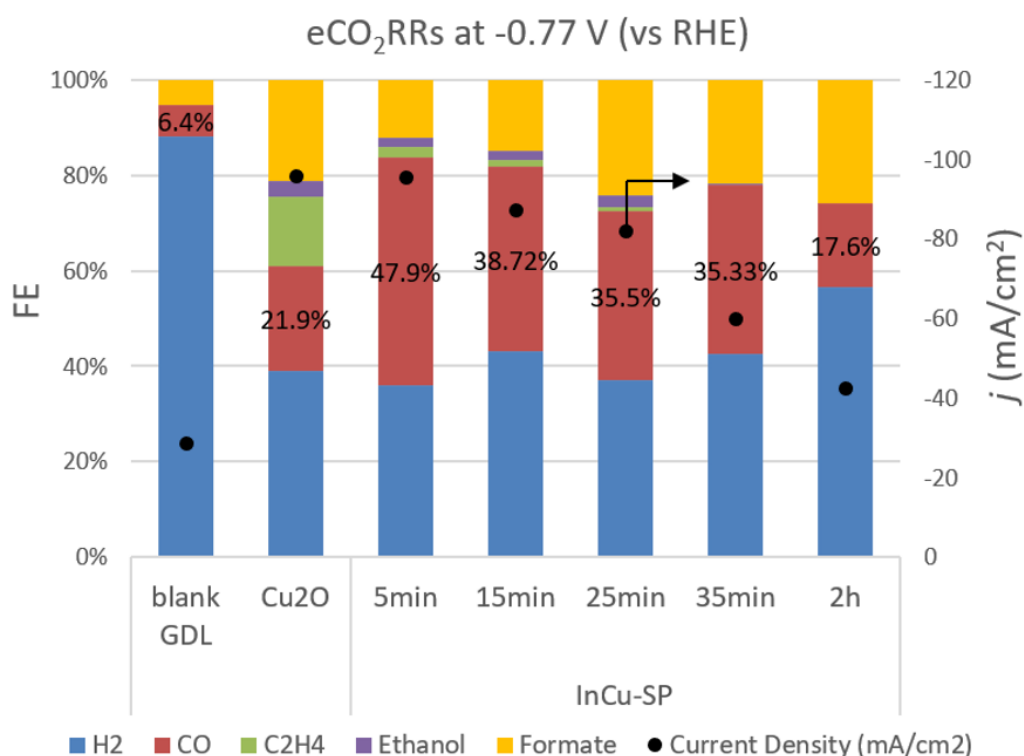


Figure 5-5 Normalized FE of all the products and current density (j) of eCO₂RRs at -0.77 V (vs. RHE) catalysed by blank GDL, com.Cu₂O, and CuIn prepared by SP with different precipitation time.

As shown in Figure 5-5, the blank GDL which contained mainly carbon black on the electrode surface shows the catalytic ability of eCO₂RR to produce CO and formate, but more than 90% of the current was contributed to the hydrogen evolution reaction (HER). With using com.Cu₂O catalyst, HER was strongly suppressed, C₁ (CO and formate) and C₂ (ethylene and ethanol) with the total FE > 60% were produced. The current density of com.Cu₂O reached 96.1 mA cm⁻².

The SP treatment on com.Cu₂O weakened the capability of C₂ production, only 4.0% C₂ could be produced by CuIn-SP5min and no C₂ produced by CuIn-SP2h. This is in accordance with the vanishing Cu observed by XRD and XPS, as Cu is the only metal centre that can form deep reduction products (i.e., C_{≥1} hydrocarbons and alcohols)^{32, 185}. As the SP time prolonged, the CO FE increased to 47.9% by CuIn-SP5min but dropped to 17.6% by CuIn-SP2h. The slight growth of CO production by applying short-time SP implies the evolved interaction between

Cu and In, since the Cu-In combination forms the active sites for CO production with suppressed HER⁹⁹⁻¹⁰⁰. However, the formate FE presents a slow-growth trend over the precipitation time, which is an indication of the increasing indium content on the surface as indium is known for the preference of formate production from eCO₂RR, either in the form of In metal¹⁸¹ or In(OH)₃¹⁸⁶. The CuIn-SP2h which contains mainly In(OH)₃ without Cu species shows highest formate FE of 25.7%. The current density decreased over the SP time, probably owing to the declined electrode surface area and conductivity during the complete etching of Cu.

5.3.2 Cu-In prepared by electrochemical spontaneous precipitation (ESP)

5.3.2.1 Catalyst characterisation and synthesis mechanism

Similar with the SP process, the electrochemical spontaneous precipitation (ESP) started from immersing com.Cu₂O-GDE and In foil into acidified In³⁺ solution (pH = 2.5) with controlled ESP time by discharging the solution. Differently, a conductive cable was connected between com.Cu₂O-GDE and In foil so that an electrochemical process was carried out spontaneously. The photographic images of CuIn-ESP GDEs prepared by different ESP time are shown in Figure 5-6.

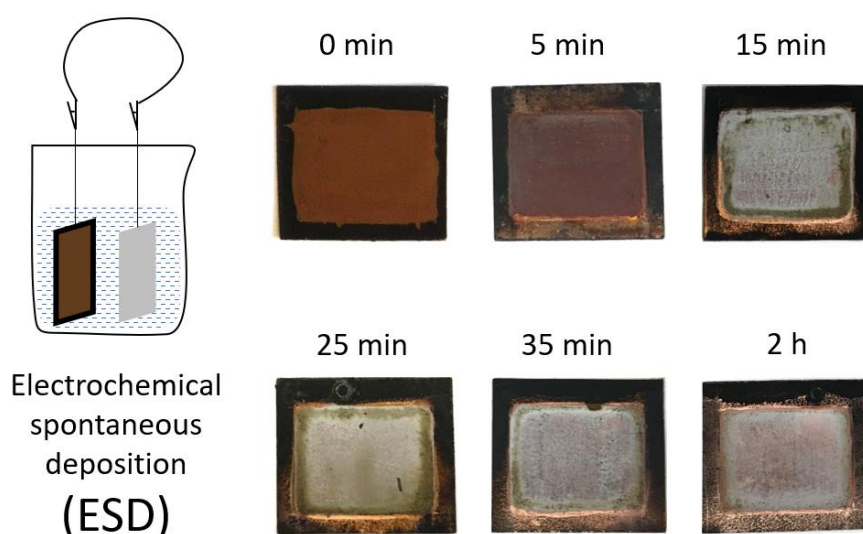
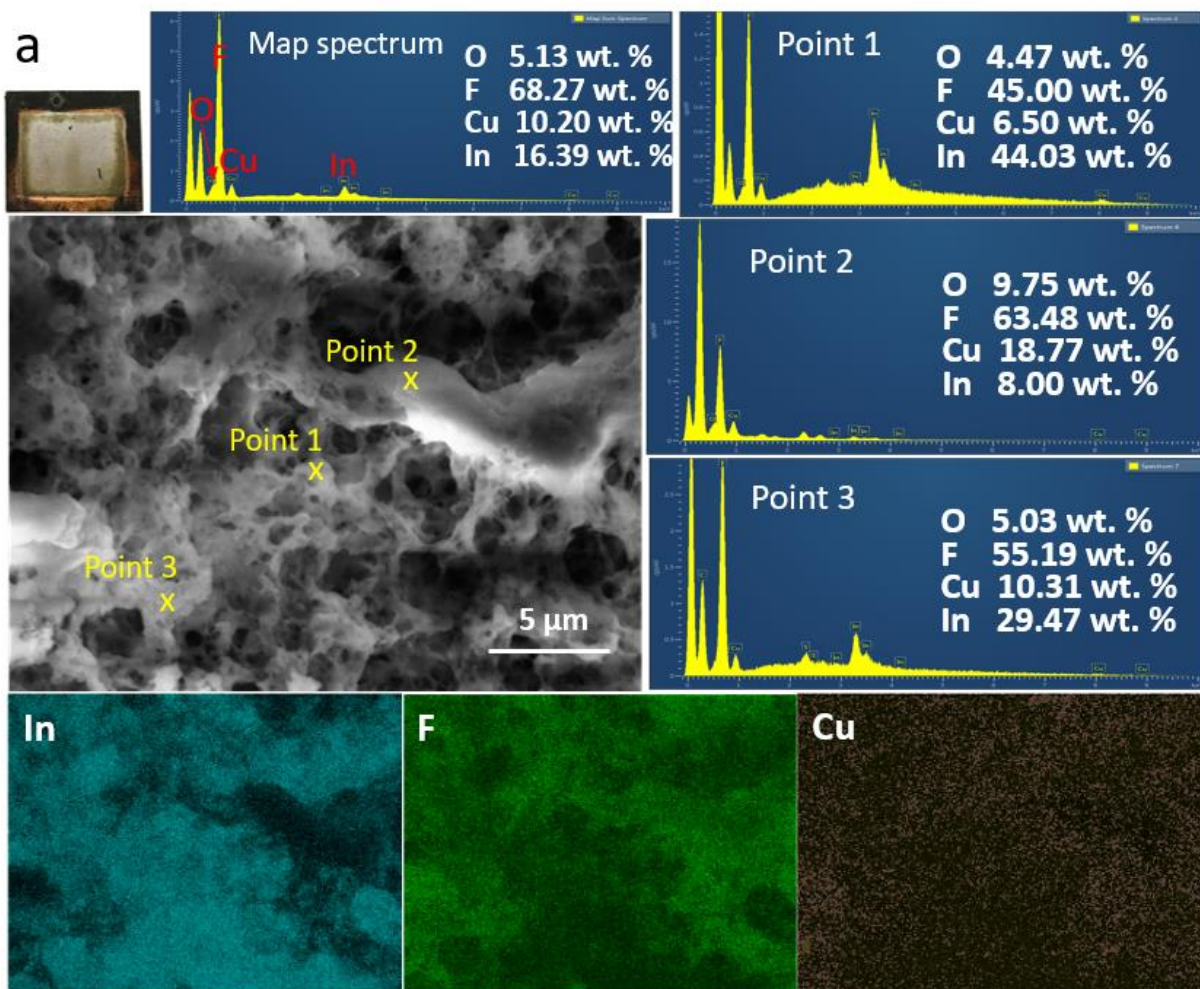


Figure 5-6 Photographic images of com.Cu₂O-GDE (0 min) and CuIn-ESP GDEs with 5 min

to 2 h precipitation time.

From the photographic images in Figure 5-6, the appearance of the white layer indicates the successful precipitation of indium species. Different from the CuIn-SP illustrated in the last section, CuIn-ESP shows the coverage of the white layer on the brown Cu_2O substrate rather than a replacement, the brown substrate still existed even with long time (2h) ESP. The complete coverage of white layer took place by 15min ESP. SEM and EDX technologies were used to study the morphology of CuIn-ESP25min, and CuIn-ESP2h, as presented in Figure 5-7.



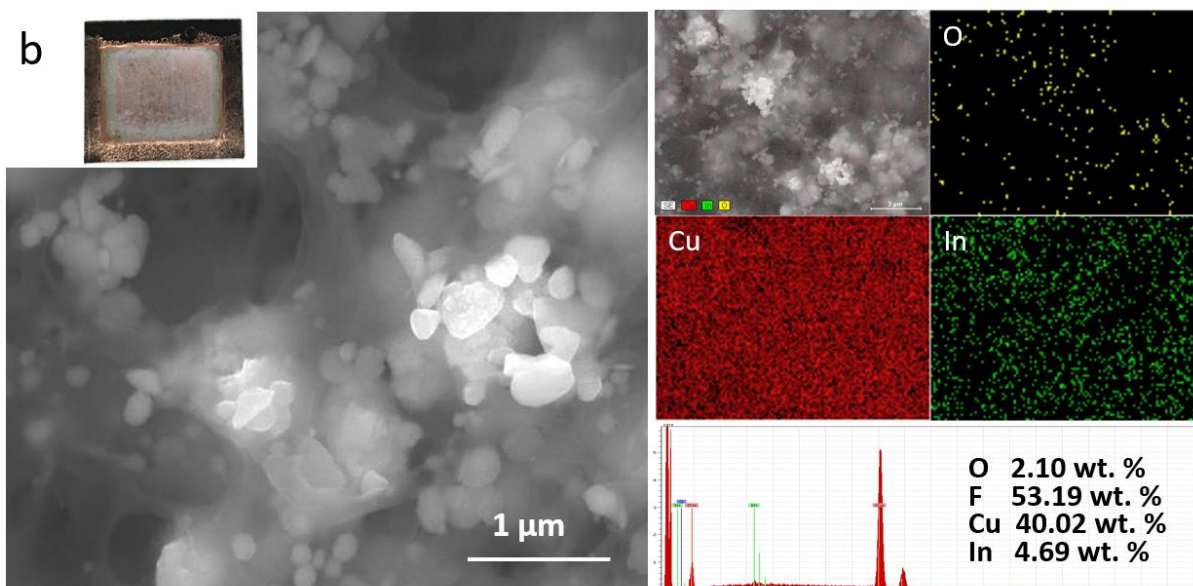


Figure 5-7 SEM images, elemental mapping, and quantitative EDX analysis of a) CuIn-ESP25min and b) CuIn-ESP2h.

The surface of CuIn-ESP25min in Figure 5-7 a presents disordered reticular structure which is similar to the CuIn-SP2h in Figure 5-3 c, but differently with attaching irregular protrusions (point 1 and 3) in micro-scale. From the elemental mapping analysis, Cu distributes almost the whole selected area but the distribution areas of In and F are mostly non-overlapping, implying the indium precipitation was majorly taken place on Cu species rather than on Nafion. The EDX result of map spectrum shows the mass ratio of In/Cu in the selected area is 1.6, while the point scan result of In/Cu mass ratio is 6.7, 0.4, and 2.9 for point 1, 2, and 3 respectively. The micro-scale irregular protrusions (point 1 and 3) show higher amount of In precipitation, indicating different kinetics of In precipitation on different sites. The morphology of CuIn-ESP2h in Figure 5-7 b also shows the reticular framework. Different from CuIn-ESP25min, the particles surrounding the framework show more regular crystal structure which are mostly thin triangle prisms (~0.5 mm edge length), similar with the morphology of the brown region on CuIn-SP25min (Figure 5-3 b). The Elemental mapping and EDX result indicate Cu and F to be the major elements on electrode surface, with very small amount of In and O. XRD and XPS were applied to analyse the phase composition of CuIn-ESP25min and CuIn-ESP2h with the results

shown in Figure 5-8.

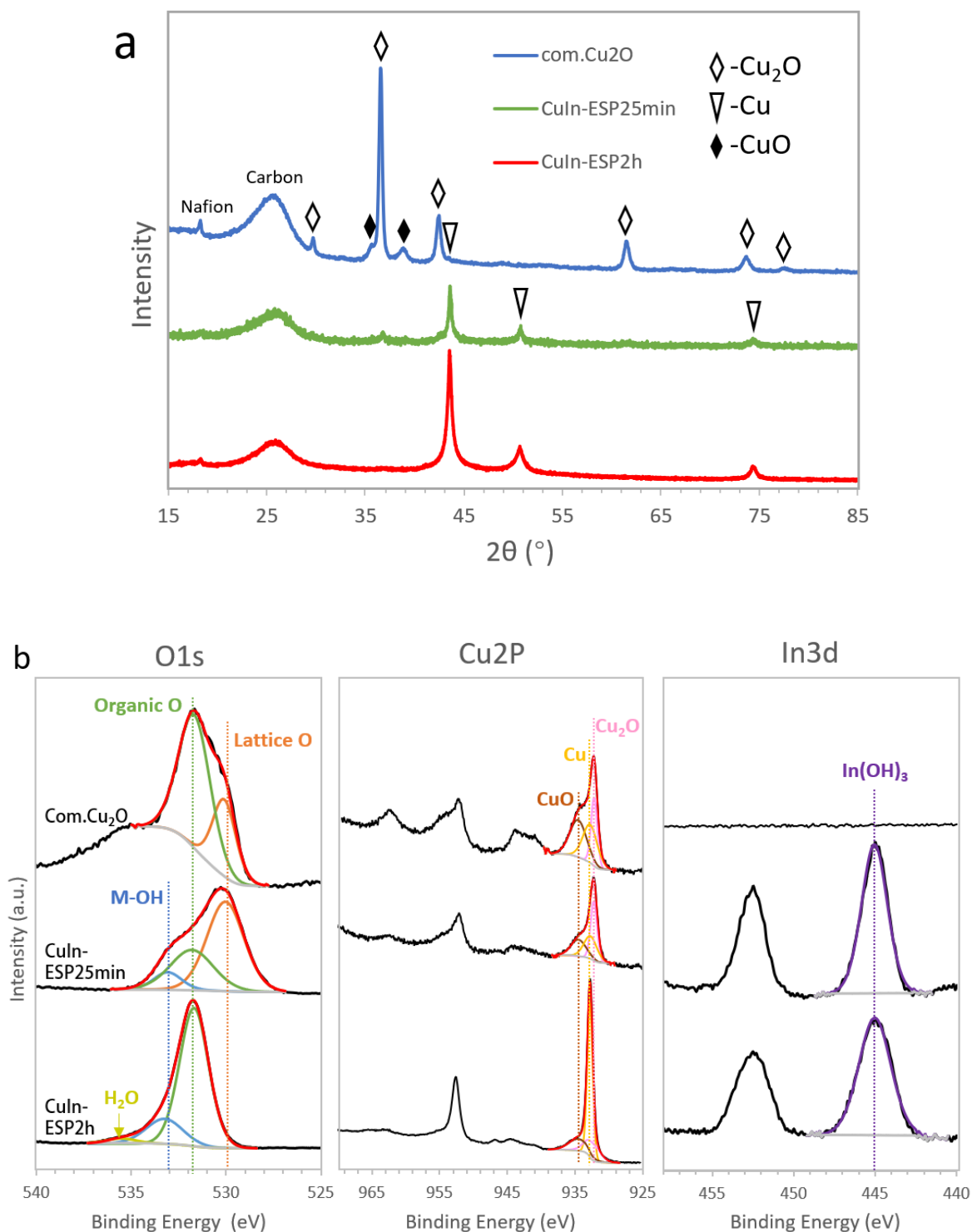


Figure 5-8 a) XRD profiles of com.Cu₂O, CuIn-ESP25min and CuIn-ESP2h. b) High-resolution XPS spectrum of O1s, Cu2p, and In3d of com.Cu₂O (top), CuIn-ESP25min (middle), and CuIn-ESP2h (bottom). c) Quantification analysis on XPS survey spectrum of CuIn-ESP15min, CuIn-ESP25min, and CuIn-ESP2h.

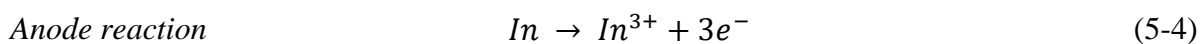
XRD pattern of CuIn-ESP25min in Figure 5-8 a rises three strong peaks of metallic Cu with the greatly declined Cu₂O peaks compared to com.Cu₂O. Those metallic Cu peaks get intensified with the absence of Cu oxides in the spectrum of CuIn-ESP2h. This indicates the reduction of Cu oxides during ESP process, and CuIn-ESP with longer precipitation time get higher reduction degree of Cu oxides. Indium species is still difficult to be found by XRD, probably implying its amorphous characteristics or an ultrathin surface layer.

The XPS results in Figure 5-8 b further indicate the reduction of Cu oxides. Compared to the Cu2P spectrum of com.Cu₂O, the CuO peak of CuIn-ESP25min at 934.5 eV in the Cu2p_{3/2} region^{167-168, 177} reduced and Cu₂O (932.2 eV) constituted the major Cu species on the electrode surface. With the ESP prolonged to 2h, the Cu species on the electrode surface was mostly metallic Cu with the largest Cu peak at 932.7 eV. Even though no In-related signal was found on the XRD, the existence of indium can be observed from the XPS In3d spectra in the form of In(OH)₃¹⁸¹⁻¹⁸², same to the CuIn-SP catalysts shown in Figure 5-4 b. The O1s spectra also indicates the reduction of Cu oxides and formation of In(OH)₃ during ESP process, since the lattice O peak (529.5 eV)¹⁷⁸⁻¹⁸⁰ which linked to the crystallized Cu oxides no longer exists in CuIn-ESP2h and the existence of M-OH peak (532.5 eV)¹⁸²⁻¹⁸³ which linked to the In(OH)₃ in both CuIn-ESP25min and CuIn-ESP2h.

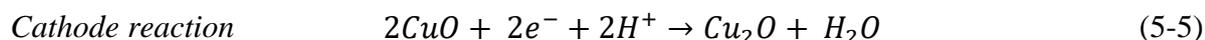
The multi-point quantification analysis by the XPS survey spectra of CuIn-ESP15min, CuIn-ESP25min, and CuIn-ESP2h are given in Figure AIV-1 of Appendix IV. The In/Cu population ratios of three points on any CuIn-ESP electrode are close, indicating the uniform In precipitation. The average surface In/Cu atom ratio of CuIn-ESP15min, CuIn-ESP25min, and CuIn-ESP2h is 0.12, 0.44, and 0.03 respectively. In/Cu was increased over the first 25 minutes but decreased afterwards, in accordance with the EDX results presented in Figure 5-7. In brief, CuIn-ESP25min had uniform In(OH)₃ precipitation on Cu oxides with a high surface In/Cu atom ratio of 0.44. However, the In(OH)₃ precipitation in CuIn-ESP2h was on metallic Cu with

a small In/Cu atom ratio of 0.03.

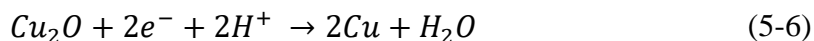
Based on the above analysis, the mechanism of ESP process could be determined. Similar with the SP process at the beginning, the outer layer of Cu oxides etched by the acidic In^{3+} solution which allowed an initial precipitation of $\text{In}(\text{OH})_3$. This assumption could be supported by the experimental observation in Figure 5-1 a that the colourless solution around the catalyst surface zone turned into very light blue. Differently, the electroreduction reactions of the bottomed Cu oxides were carried out simultaneously (Equation (5-5) and (5-6)), driven by electrons generated from the spontaneous anode reaction (Equation (5-4)). Their standard Half-cell reduction potentials E^0 are also presented below, which were calculated as displayed in Table AIV-2 of Appendix VI.



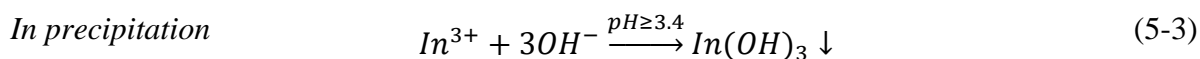
$$E^0 = -0.233 \text{ V vs. SHE, } \Delta G_r^\ominus = -67.27 \text{ kJ mol}^{-1}$$



$$E^0 = +0.668 \text{ V vs. SHE, } \Delta G_r^\ominus = -128.83 \text{ kJ mol}^{-1}$$



$$E^0 = +0.463 \text{ V vs. SHE, } \Delta G_r^\ominus = -89.30 \text{ kJ mol}^{-1}$$



The thermodynamic cell potential of (-)In|CuO(+) and (-)In|Cu₂O(+) under reaction conditions in this work is respectively 0.901 and 0.696 V, confirming the measured initial OCV value of 0.68 V (indicated in Figure 5-9 a) to be reasonable. CuO reduction to Cu₂O with more positive potential should be carried out firstly. The recorded current over ESP time is shown in Figure 5-9 b, which was increased within the first 13 min and decreased in the next 20 min before maintaining around 7.2 mA after 35min ESP. The CuO/Cu₂O reduction should mostly contribute to the initial current growth while the gradual precipitation of $\text{In}(\text{OH})_3$ was possibly

the main reason for the current drop. ESP process was probably terminated around 35 min as indicated by the constant current. The charge on each 1 cm² cathode over ESP time is plotted in Figure 5-9 c by integrating the current-time curve. The slope change at 1500 s indicates declined electro-reaction rate.

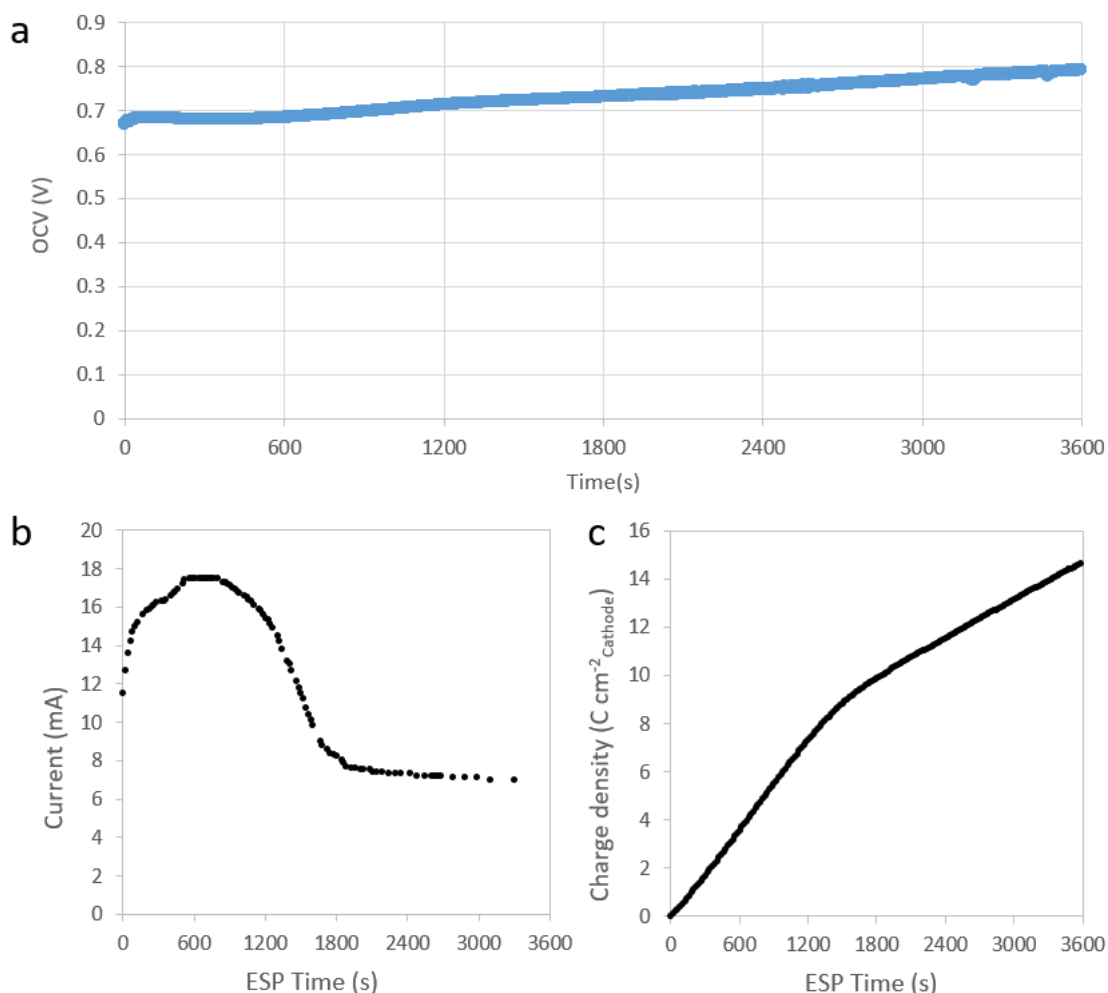


Figure 5-9 a) Open circuit voltage (OCV) between fresh In foil and Cu₂O-GDL immersed in 0.4 M citric acid mixed 0.05 M In₂(SO₄)₃ solution (pH = 2.5), measured for an hour. b) Current recording during ESP process. c) The calculated charge density over ESP time.

Same as the SP process, indium was precipitated in the form of In(OH)₃ due to higher local pH. The cathode potential (ca. 0.68 V vs. SHE) was much more positive than In³⁺ (-0.233 V vs. SHE), therefore In³⁺ reduction unlikely occurred on the cathode. There are two types of In(OH)₃ precipitation sites in ESP process, as drawn in Figure 5-10, the etching site of the surface Cu

oxides and the reduction site of the subsurface Cu oxides. Different from the SP process, Cu species still existed after 2h ESP, since the bottomed Cu oxides had been reduced to metallic Cu which was stable in the acidic solution at the reduction potential. After about 25 min, the amount of $\text{In}(\text{OH})_3$ reduced over the ESP time. This is possibly due to the shrunken particles of Cu species during the reduction process, which were gradually free from the bond of Nafion binder and collaterally took away the precipitated In species. With more exposed subsurface Cu metal which unlikely to be the indium precipitation site, the surface In/Cu ratio declined.

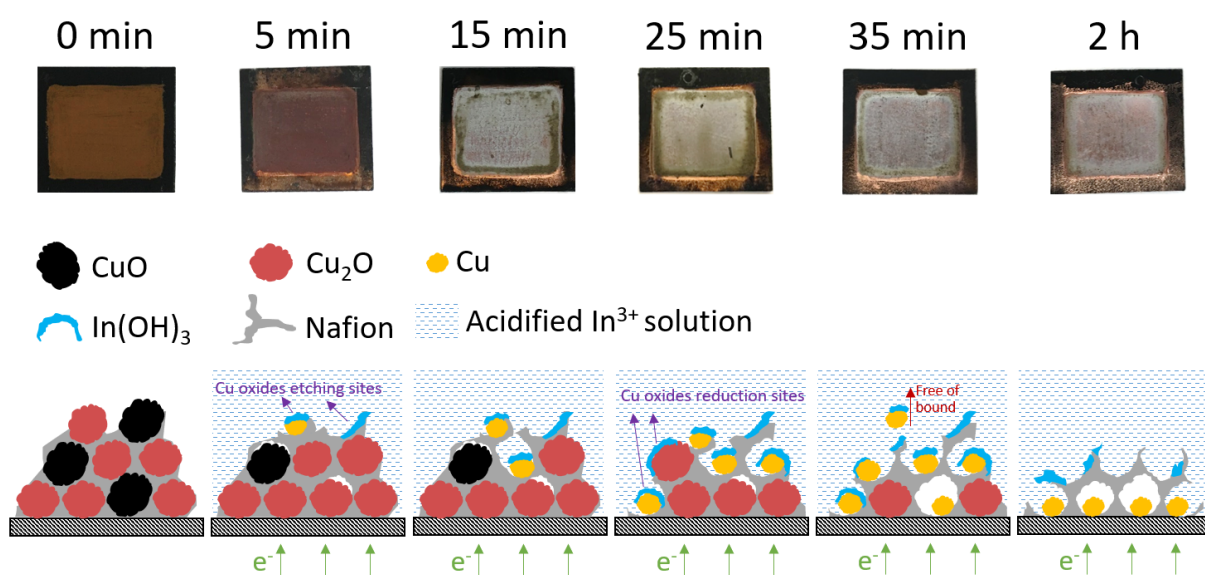


Figure 5-10 Photographic images and schematic illustration of the electrode surface reconstruction over ESP time from 0 to 2 hours. Within 5 min: the bottomed $\text{CuO}/\text{Cu}_2\text{O}$ were firstly reduced, with the outmost Cu oxides etching simultaneously. The initial $\text{In}(\text{OH})_3$ precipitation site was where the Cu oxides etched. From 5~25 min: with reduction of $\text{CuO}/\text{Cu}_2\text{O}$ on going, protons consumed causing local pH increasing, resulting in $\text{In}(\text{OH})_3$ precipitation. The surface mass ratio of In/Cu increased during this period as more $\text{In}(\text{OH})_3$ precipitated. After 25min: particle size of $\text{CuO}/\text{Cu}_2\text{O}$ shrank after reduction so that outer Cu particles were gradually free of the bond of Nafion and collaterally took away the precipitated $\text{In}(\text{OH})_3$. With the exposure of the nether Cu without precipitated indium, the surface In/Cu ratio decreased.

5.3.2.2 eCO₂RR activities of CuIn-ESP

The CuIn-ESP catalysts by different precipitation time: 5min, 15min, 25min, 35min, and 2h were compared by eCO₂RR in GDE cell at various applied potentials. 1 M KOH and 5 M KOH were used as the catholyte and anolyte respectively separated by a CEM. Results of the normalized Faradaic efficiencies (FE) and current density (*j*) are displayed in Figure 5-11.

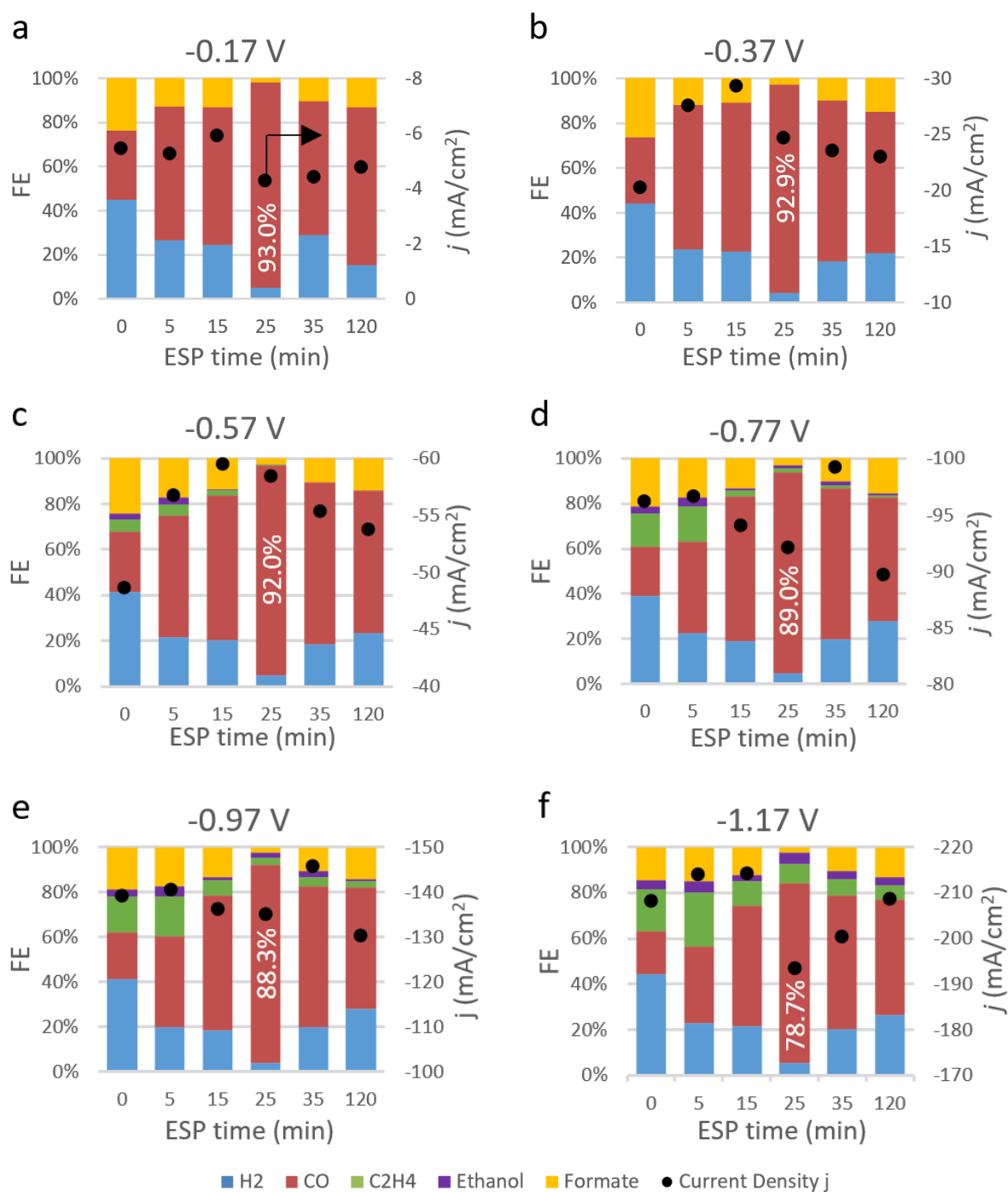


Figure 5-11 eCO₂RR activities of CuIn-ESP catalysts with different precipitation time at a) -0.17 V, b) -0.37 V, c) -0.57 V, d) -0.77 V, e) -0.97 V, f) -1.17 V (vs. RHE).

At any potential in Figure 5-11, CuIn-ESP with any precipitation time shows developed CO FE (>50 %) compared to the Cu₂O (ESP 0 min). With the increasing ESP time, CO FE enhances and reaches the maximum value of around 90% with CuIn-ESP25min before decreasing to around 50% with CuIn-ESP2h. On the contrary, FEs of H₂ and formate decrease with the increasing ESP time, reaching their minimal values with CuIn-ESP25min. The difference of product distribution between CuIn-ESP35min and CuIn-ESP2h is small, probably implying the ESP process was terminated a little while after 35 min, the assumption could be supported by the current recoding in Figure 5-9 b. When applying more negative potential, the current density (*j*) and C₂ selectivity increased. Although the CO FE decreased with more negative potential, the FE sum of CO and C₂ does not change much over the potential: ~93% was maintained in the tested potential range using CuIn-ESP25min. This probably because of the key intermediate CO*: the CO* dimerization is the rate-determine step of C₂ production¹⁶⁰⁻¹⁶⁴ promoted by high overpotential while the CO* desorption is crucial for CO production which is a potential-independent step⁸⁰.

CO formation is favoured in the contact points of In and Cu species^{99, 187}, so a moderate population ratio of In/Cu is necessary. The CuIn-ESP25min reached the highest CO FE, suggesting a suitable In/Cu atom ratio to be about 0.44 (XPS survey analysis in Figure AIV-1 b of Appendix IV) on the surface. Apart from a suitable In/Cu population ratio, the incompletely-reduced Cu oxides in CuIn-ESP25min should be another key factor for CO production. The proper structural-interaction of Cu-In combination should also play an important role of high CO selectivity, which was analysed in the next sub-section.

5.3.2.3 The structural Cu-In interaction

Material characterizations by TEM technology was carried out on CuIn-ESP25min to further investigate the Cu-In interaction, as shown in Figure 5-12.

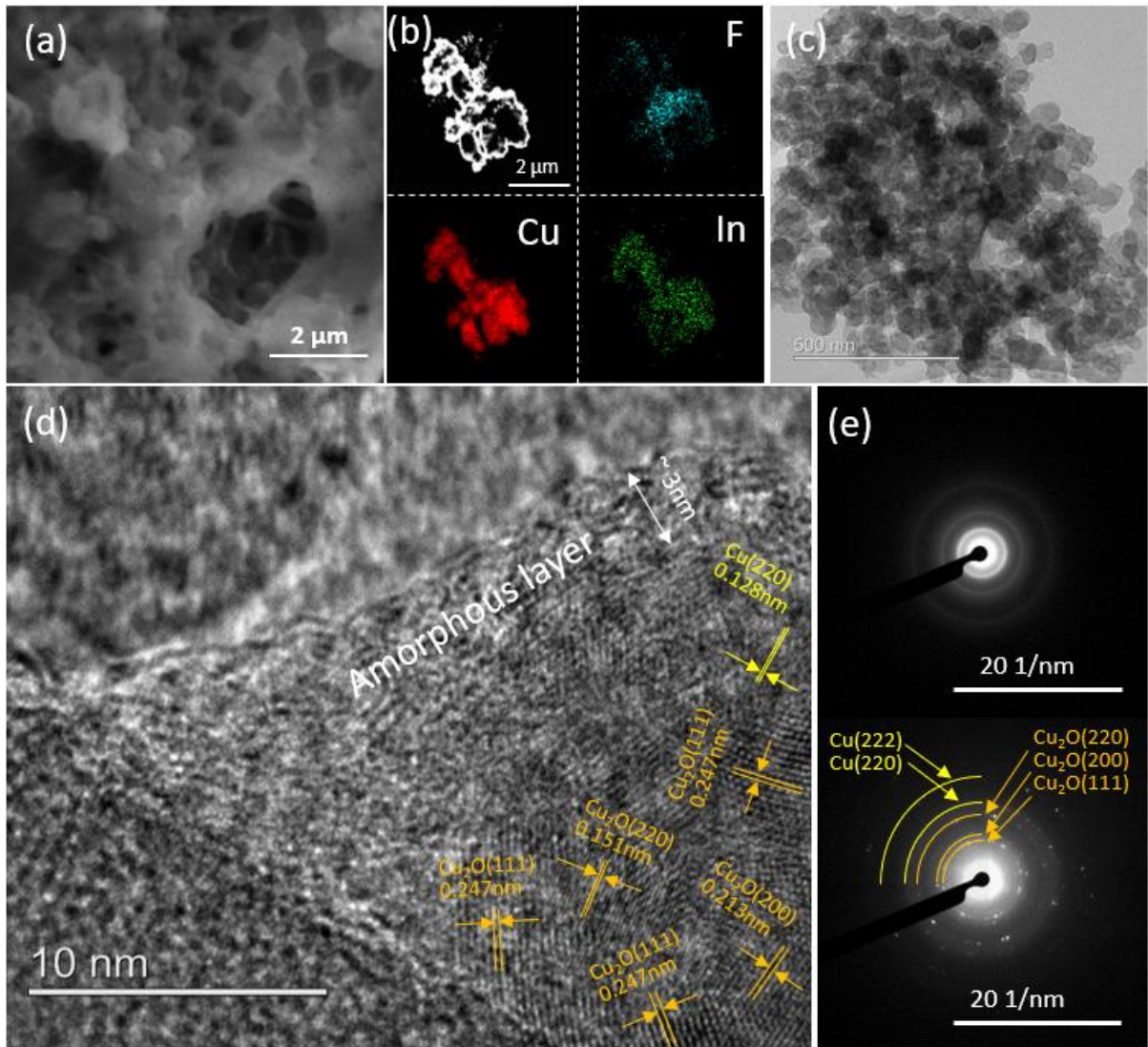


Figure 5-12 a) SEM, b) HAADF STEM image and element mapping, c) TEM, d) HRTEM, and e) SAED of CuIn-ESP25min.

The SEM image in Figure 5-12 a shows the morphology of CuIn-ESP25min that irregular protrusions with about 0.5 - 2 μm dimension attaching on the reticular Nafion framework. The high-angle annular dark-field (HAADF) STEM image in Figure 5-12 b displays a typical protrusion in micro-scale which is actually an assembly of microparticles bonded by Nafion since F mostly distributes in-between the micro-particles from the elemental mapping results. Cu is the leading element which mostly distributed in the center of microparticles while In covers more evenly on the whole particle. The TEM image in Figure 5-12 c indicates the microparticle is an aggregate of nanoparticles with the average diameter 50 nm. Atomic-scale

high-resolution TEM (HRTEM) analysis in Figure 5-12 d presents both crystalline and amorphous characteristics of the nanoparticle. The bottom right region shows various crystal fringes with distances of 0.128, 0.151, 0.213, 0.247 nm represents Cu (220), Cu₂O (220), Cu₂O (200), and Cu₂O (111) respectively based on the ICDD database with PDF file No. 03-065-9743 and 01-078-2076. The featureless area without showing obvious crystal fringes shaped like a shell with 3~10 nm thickness that tightly capping on the polycrystalline Cu phase corresponds to the amorphous In(OH)₃ layer. The SAED images in Figure 5-12 e show both amorphous and crystalline characteristics, and the crystalline phase consists of polycrystalline Cu and Cu₂O mixture (denoted as Cu_xO) in accordance with the lattice fringes in the HRTEM image. The above analysis indicates the amorphous/crystalline hybrid structure of CuIn-ESP25min: the nanolayer of amorphous In(OH)₃ capping on the polycrystalline Cu_xO.

The Cu-In interaction plays a key role in high CO selectivity, this interaction was reported to be the Cu-In alloy by Rasul et al.^{100, 148}. After introducing indium as a second metal center to Cu, the binding energy of H* was remarkably weakened while CO adsorption energy was substantially unchanged. The stability of COOH* was improved resulting in less formate releasing. However, Larrazábal et al.⁹⁹ stated the Cu-In alloy was not the main active species for CO evolution, since during eCO₂RR process the Cu-In composite was evolved with a transition from homogeneous alloy to heterogeneous bimetal, along with the development of CO selectivity. They also found In(OH)₃ played a crucial role in favouring the production of CO over Cu-In electrocatalysts. The results from this study confirmed their observation that the hybrid structure of amorphous In(OH)₃ nanolayer capping on polycrystalline Cu_xO facilitates the Cu-In interaction of CO formation from eCO₂RR.

In summary, the key factors that enable CuIn-ESP25min to be a high-selective catalyst for CO production from eCO₂RR are: 1. A moderate In/Cu population ratio which is suggested to be around 0.44 atom ratio with the reaction conditions in this work. 2. The existence form of Cu

species should be oxide-derived Cu rather than Cu metal. 3. A proper Cu-In interaction which is, structurally, amorphous $\text{In}(\text{OH})_3$ nanolayer (3~10 nm thickness) tightly capping on the polycrystalline Cu_xO .

5.3.2.4 Production of highly selective CO and tunable Syngas using Cu-In catalyst

Combined with the GDE reactor and strong alkali catholyte, the CuIn-ESP25min achieved both high current density and efficiency towards CO production. The yields of all the gas and liquid products from eCO₂RR catalysed by Cu₂O and CuIn-ESPs with different precipitation time were presented in Table AIV-3 of Appendix IV. CuIn-ESP25min with the highest CO selectivity presents high CO yield and CO₂ conversion rate, which are steadily enhancing with the overpotential as displayed in Figure 5-13 a, showing the controllability by the energy input. With the highest energy input of -1.17 V, CO₂ conversion and CO yield reaches the maximum value at 18.2% and 3.05 mg min⁻¹ respectively, with CO₂ supplying at 15 ml min⁻¹ on 2 cm² working electrode (WE). The potential-dependent CO yield of this work is compared with some related studies in Figure 5-13 b, this work shows improvement than the best documented using noble Ag-GDE so far in the literature^{99-103, 171, 188}. Interestingly, Syngas could be also produced by CuIn-ESP. Changing the ESP time, or applying different ESP charge density in a more general condition, the CO/H₂ producing ratio is tunable as shown in Figure 5-13 c. The CO/H₂ mole ratio was ranging from 1.49 to 14.77 when using CuIn-ESP catalysts with different ESP time from 5 min to 2 h.

The stability test of CuIn-ESP25min was carried out at -0.77 V as shown in Figure 5-14, the CO FE maintained around 90% for more than 5 hours.

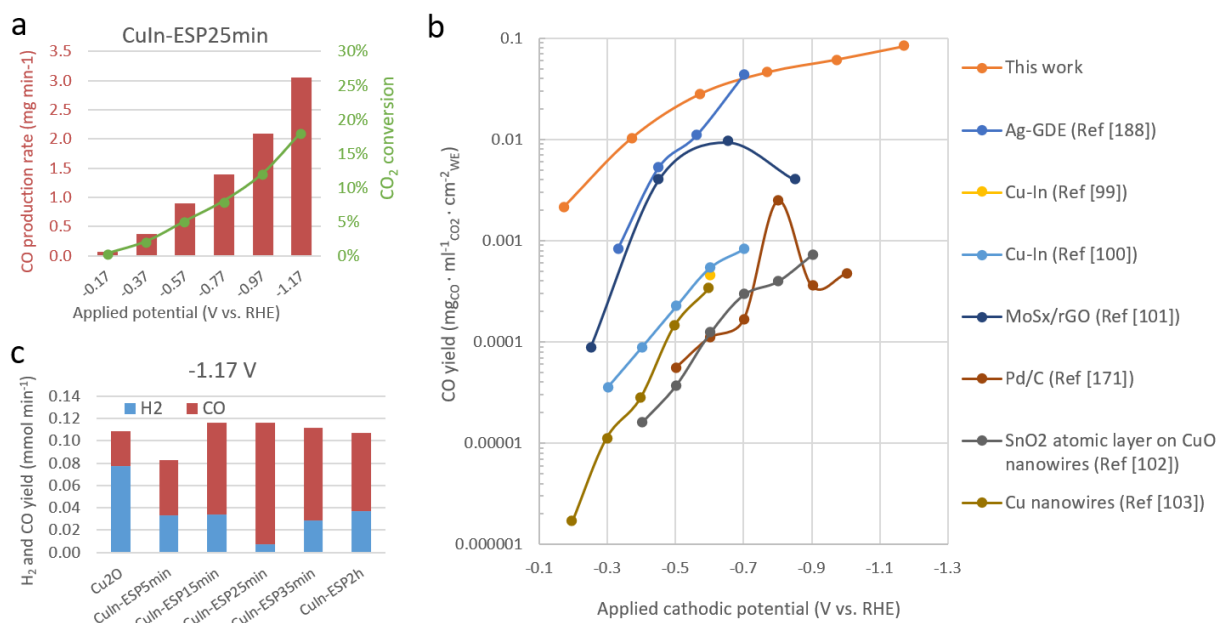


Figure 5-13 a) CO yield and CO₂ conversion of eCO₂RR catalysed by CuIn-ESP25min at a wide range of applied potentials. b) A comparison of CO yield from eCO₂RR between this work and other published related studies in recent years. c) Syngas production at -1.17 V from eCO₂RR catalysed by Cu₂O, CuIn-ESP5min, CuIn-ESP15min, CuIn-ESP25min, CuIn-ESP35min and CuIn-ESP2h.

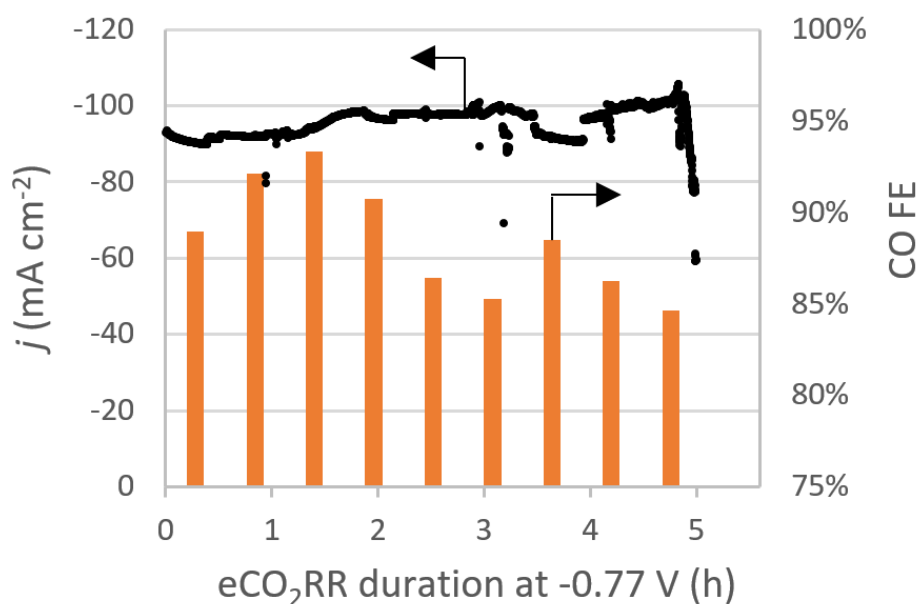


Figure 5-14 Stability test of CuIn-ESP25min catalysed eCO₂RR at -0.77 V (vs. RHE).

5.4 Chapter summary

A facile electrochemical spontaneous precipitation (ESP) method was developed to synthesis binary Cu-In catalyst on the gas diffusion electrode (GDE). It shows a hybrid structure that amorphous $\text{In}(\text{OH})_3$ nanolayer (3 ~10 nm thickness) tightly capping on the polycrystalline Cu_xO . The proper Cu-In interaction of this heterostructure enables ~90% FE of CO production from eCO_2RR . An appropriate population ratio of In/Cu around 0.44 atom ratio, and the presence of lattice oxygen in the polycrystalline Cu_xO which enabled the oxide-derived feature, were assumed to play crucial roles in the development of CO selectivity. With the synergy of GDE reactor and 1 M KOH catholyte, high current density ~ 200 mA cm^{-1} at -1.17 V and high CO FE ~ 90% were both achieved by using CuIn-ESP25min. This enabled CO_2 conversion rate and CO yield of 18.2 % and 3.05 mg min^{-1} respectively with CO_2 supplying at 15 ml min^{-1} on 2 cm^2 electrodes. This CO yield was higher than the reported CO production from eCO_2RR in literature. Syngas could be also produced with tunable CO/ H_2 ratio by applying different ESP time when preparing Cu-In catalyst. The potential of scaling up from this bench-scale reaction was revealed. As a more general conclusion, the present study provides a method to simply construct a catalytic surface with joint active centres, which may bring new ideas to the development of novel catalysts.

Chapter 6 Production of Formate from CO₂ Reduction and Its Application in Energy Storage

6.1 Introduction

The carbonaceous products from eCO₂RR can be from a wide range, both gases such as CO, CH₄, and C₂H₄, which can be formed at current efficiencies greater than 70%^{52, 100, 189}, and liquid products, such as formate, methanol and ethanol¹⁹⁰ produced with Faradaic efficiencies greater than 90%^{176, 191}, 40%¹²⁸, and 40%¹⁹² respectively. Liquid products have advantages in terms of transportation, storage, as well as handling. In terms of electric energy generation, formate is superior to alcohols as it is non-flammable and non-toxic. The thermodynamic cell voltage of a formate fuel cell is of 1.48 V¹⁰⁶, which is higher than methanol (1.21V), ethanol (1.14V) and hydrogen (1.23V).

Vo et al.¹⁹³ firstly demonstrated the concept of electricity storage and release by formate produced from CO₂ electro-reduction and investigated the possibility of this close-loop energy conversion. However, electric energy generation from formate produced from CO₂ has not been realized due to low concentration of the products. In a normal direct formate fuel cell (DFFC), a high concentration formate (≥ 1 M) is used¹⁹⁴. Table AI-3 and AI-4 summarize related studies of selective formate production from eCO₂RR published in recent years, with their corresponding formate yields and its concentration in the residual electrolyte - which were rarely mentioned in the original publications. The formate concentrations are characteristically below 0.1 M after 1-hour electrolysis, far less than the level required for energy generation and storage. The reasons for the low formate concentration could be poor CO₂ mass transfer efficiency in aqueous medium and low current density by using electrolyte with low alkalinity. Lee et al.⁵⁰ developed a catholyte-free electrolyzer using vapor stream on the cathode, with 25 cm² electrode area. Formate concentration of 0.9 M was produced at 70 °C but decreased to 0.5 M at 30 °C without mentioning the time scale. However, providing vapour would increase

energy and cost of such a process.

In this study, we developed a cost-effective and high-efficient gas diffusion system to achieve a controllable formate production from eCO₂RR in aqueous medium. 0.5 M formate could be produced directly in alkaline media within 1 hour under ambient conditions. This formate product was then directly utilized as the fuel for a DFFC without pre-treatment.

6.2 Experimental

6.2.1 Fabricating SnO₂/C bonded gas diffusion electrode (GDE)

The C-supported SnO₂ catalyst (SnO₂/C) catalyst was prepared by physical mixing SnO₂ particles and Vulcan XC 72R carbon black particles with the desired mass ratio of 0.5, 1, and 3.5. The individual SnO₂ and C were also used for comparison. Section 3.3.4 of Chapter 3 has given the detailed information on applying ~ 4 mg cm⁻² SnO₂/C catalyst to the gas diffusion layer (GDL) to fabricate SnO₂/C-GDE with the mass ratio of Nafion binder/catalyst = 10 %.

6.2.2 Catalyst characterization

X-ray diffraction (XRD) and scanning electron microscopy (SEM) were applied to respectively evaluate the catalyst crystal structure and morphology in micro-scale, as stated in Section 3.5.2.

6.2.3 CO₂ reduction system and electrochemical analysis

A GDE reactor illustrated in Section 3.2.2 was used to carry out the mass transfer developed eCO₂RR. The SnO₂/GDE was the cathode with the geometric surface area 2 cm² and the anode was a coiled Platinum wire. An alkaline reference electrode (RE-61AP, 0.117 V vs. SHE, ALS CO., Ltd) was used as the reference electrode. The applied potentials (vs. RE-61AP) in the three-electrode system were all converted to the reversible hydrogen electrode (RHE) according to Equation (3-2) unless otherwise stated.

All the electrochemical reactions and measurements were carried out at ambient temperature and pressure using a potentiostat (Metrohm Autolab PGSTAT128N). The flow rate of CO₂ was maintained at 15.8 ml min⁻¹. 1 M KOH and 5 M KOH solutions were used as catholyte and anolyte respectively, separated by a cation exchange membrane. In the catholyte flow mode, a peristaltic pump was used to supply fresh catholyte at a flow rate of 1.0 ml min⁻¹ to maintain the local pH and to remove liquid products for reaction equilibrium. In the catholyte fixed mode, about 13 ml catholyte was maintained without circulating and flowing. All the information of reagents and apparatus can be found in Section 3.4.1.

Cyclic voltammetry (CV) was carried out in triplicate between -1.46 to 0.84 V (vs. RHE) with the scan rate 10 mV s⁻¹ to initially explore the cathode electrochemical behavior. eCO₂RR was measured chronoamperometrically (CA) by recording the current at a particular applied potential over reaction time. The current density (j) was calculated based on the geometric surface area 2 cm² of the working electrode.

6.2.4 Analysis of products from CO₂ reduction

As stated in Section 3.5.1, A gas chromatography (GC) equipped with the ShinCarbon ST micropacked column and the Zebron ZB-WAXplus capillary column was used to quantitatively analyze permanent gases, light hydrocarbons, and alcoholic liquids. An ion chromatography (IC) was used for quantifying volatile fatty acids (VFA) including formic acid. The Faradaic efficiency (FE) and half-cell energy efficiency (EE) for each product was calculated as reported by Zhu et al.²⁴.

6.2.5 Test of direct formate fuel cell (DFFC)

The fuel cell was based on a membrane electrode assembly (MEA) as previously reported, using nickel foam supported Pd/C-CeO₂ as anode, Tokuyama A201 anion exchange membrane, and carbon cloth coated FeCo/C as the cathode¹⁹⁵. A model fuel consisting of 0.5 M HCOOK

(Merck, Germany) in 1.0 M KOH (Merck, Germany) solution was compared as the control. The fuel solution was supplied to the anodic chamber at a flow rate of 1 ml min⁻¹ and a temperature of either 25 °C or 60 °C, while the oxygen flow on the cathodic side was held at 0.1 L min⁻¹. Fuel cell polarization curves were run at a scan rate of 10 mV s⁻¹ from the open circuit voltage (OCV) to 0.5 V cell voltage and monitored by an ARBIN BT-2000 5A 4 channels instrument (Arbin Instruments, College Station, TX, USA). Galvanostatic experiments were undertaken at the constant current density of 25 mA cm⁻² with circulating 25 ml fuel solution. The cell potential was monitored, and the tests were stopped when the potential reached 0 V. The delivered energy for a single cell load, the Faradaic efficiency for the fuel utilization and energy efficiency for the complete oxidation of formate to carbonate were calculated according to a related study¹⁹⁶.

6.3 Results and discussion

6.3.1 Catalyst Characterization

SEM was employed to characterize the morphology of Vulcan XC-72 carbon black and SnO₂/C catalyst with the mass ratio of SnO₂/C=3.5. The carbon black particles, as shown in Figure 6-1 a, are in regular spherical shape with the size about 50 nm. The fresh SnO₂/C catalyst (Figure 6-1 b) shows a uniform mixture of SnO₂ (~ 100 nm irregular particles) and carbon black support. Clusters (> 300 nm) of irregular SnO₂ particles are also present. The catalyst morphology was changed after eCO₂RR as shown in Figure 6-1 c, with the size of Sn-based crystal now 200~500 nm. However, the shape and size of carbon spherical particles remained unchanged. The XRD spectra in Figure 6-2 show the crystal structure of SnO₂/C(3.5) catalyst before and after eCO₂RR respectively, and that their compositions changing from polycrystalline SnO₂ to polycrystalline Sn due to electrochemical reduction. Thus, the SnO₂ in the catalyst underwent reduction to metallic Sn resulting in changes in morphology during eCO₂RR.

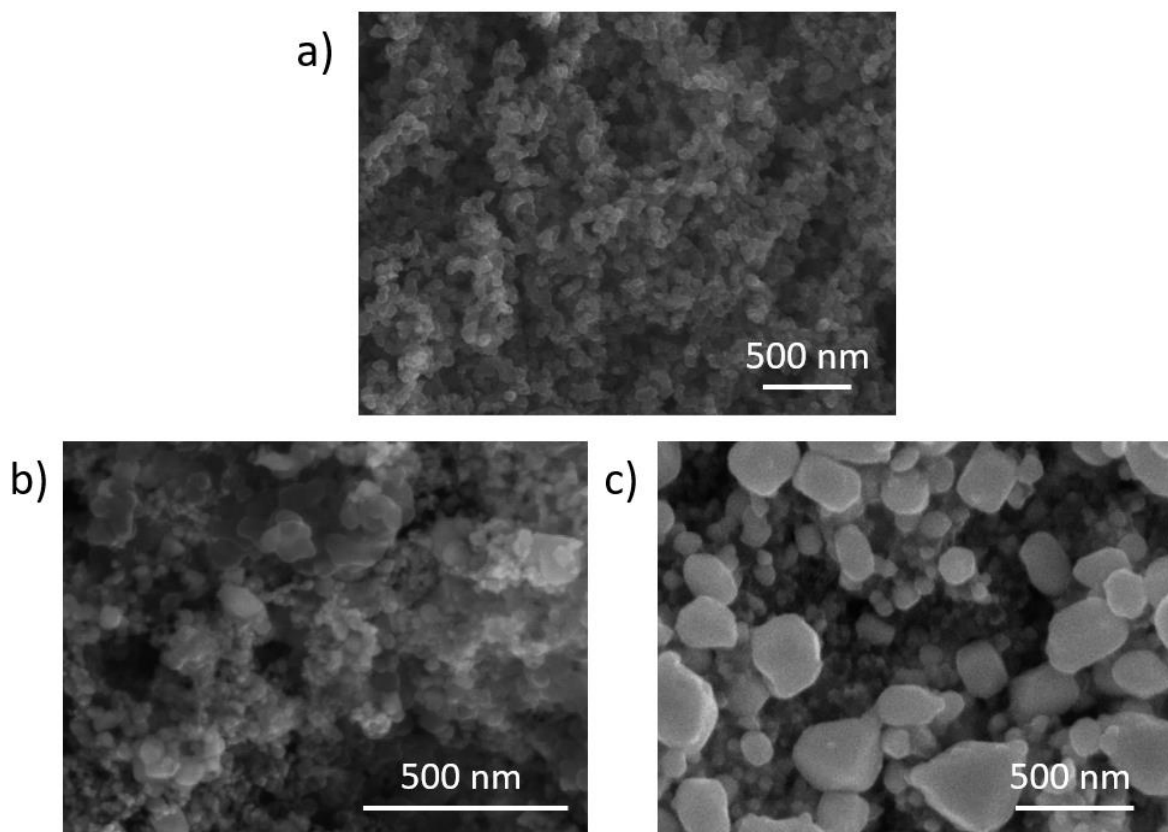


Figure 6-1 SEM images of a) Vulcan XC-72 carbon black, b) SnO₂/C(3.5) catalyst before eCO₂RR, c) SnO₂/C(3.5) catalyst after 6 hours' eCO₂RR at -1.43 V.

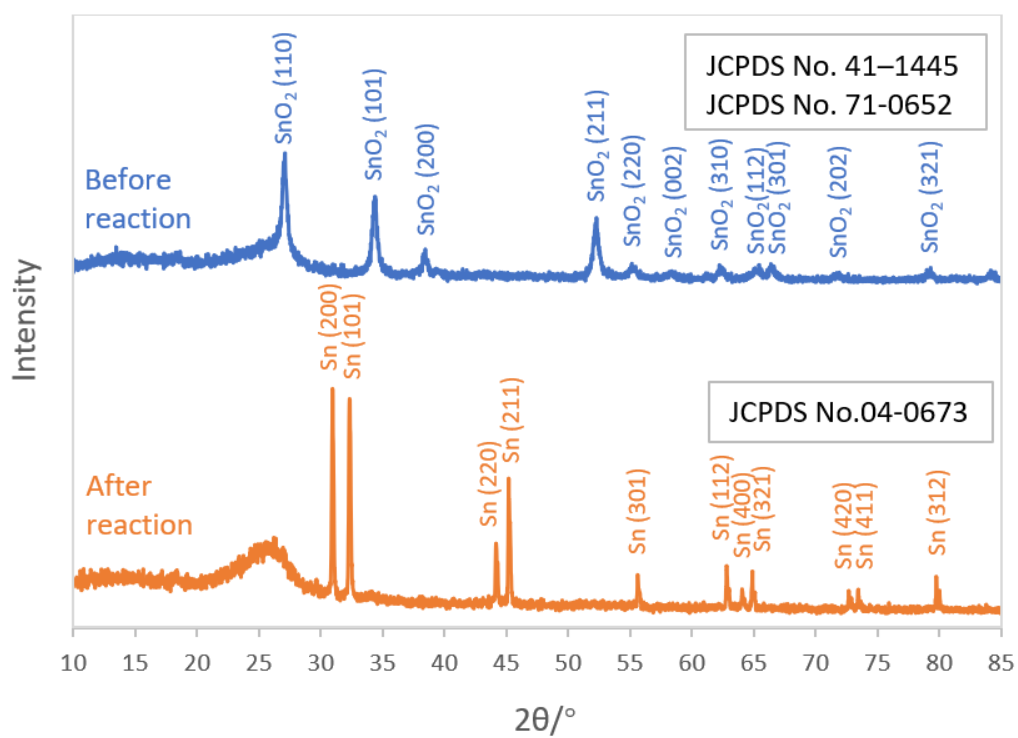


Figure 6-2 XRD spectra of SnO₂/C(3.5) catalyst before eCO₂RR (blue) and after 6 hours' eCO₂RR at -1.43 V (orange).

The CV measurements displayed in Figure 6-3 also prove the reduction of SnO₂ during eCO₂RR. The reduction potential of SnO₂ to Sn under N₂ atmosphere is about -1.2 V (vs. RE-61AP) which is even less-negative than the onset potential of HER at -1.6 V. The CV curve at CO₂ atmosphere (orange) also shows the same conclusion: reduction of SnO₂ to Sn is at -0.8 V while the reduction reaction occurs more negatively at -1.2 V, in accordance with the results from Yu et al.¹⁹⁷.

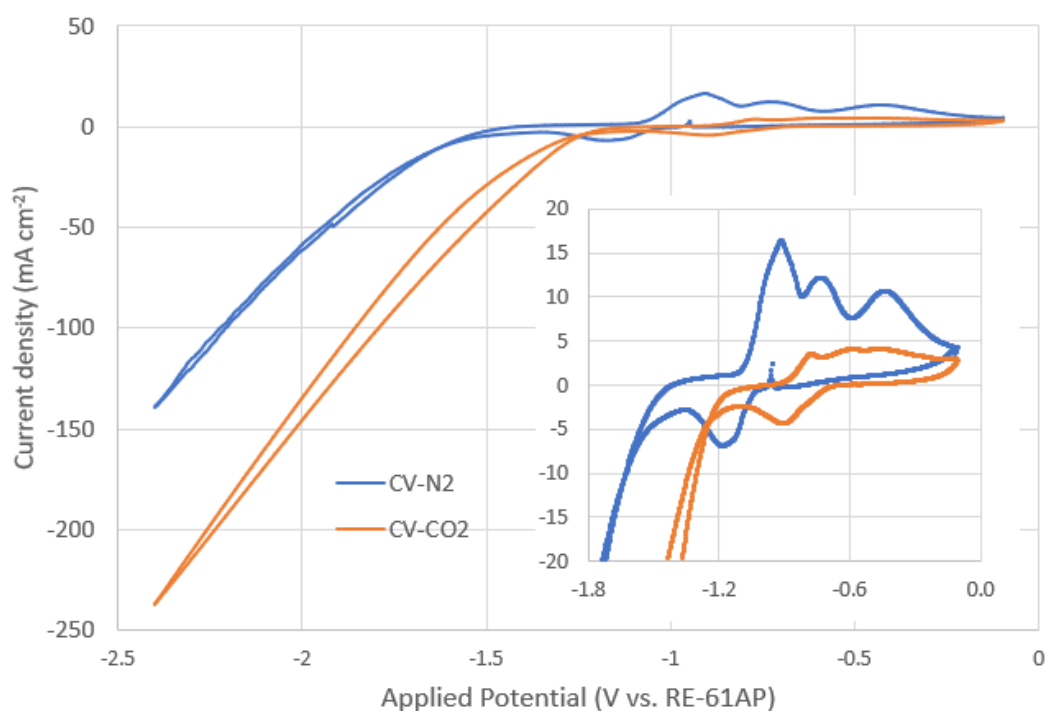


Figure 6-3 Cyclic voltammetry (CV) measurements under N₂ (blue) and CO₂ (orange) atmosphere using SnO₂/C(3.5) catalyst. Scan rate: 10 mV s⁻¹, scan circles: 3, both diagrams were taken from the 3rd cycle of scan.

6.3.2 Catalyst performance on electrochemical CO₂ reduction reaction

6.3.2.1 Effect of carbon support

The eCO₂RR catalytic performances of SnO₂/C mixtures (with mass ratios of 0.5, 1, and 3.5), individual SnO₂ and carbon were examined at a wide range of potential from -0.63 ~ -1.43 V

(vs. RHE), with a flowing catholyte. The normalized Faradaic efficiency (FE) of all the products (H_2 , CO, and formate) and overall current density (j) are displayed in Table AIV-4 of Appendix IV and summarized in Figure 6-4. The partial current densities for H_2 , CO, and formate as a function of the applied potential for each catalyst are presented in Figure AIV-2 of Appendix IV.

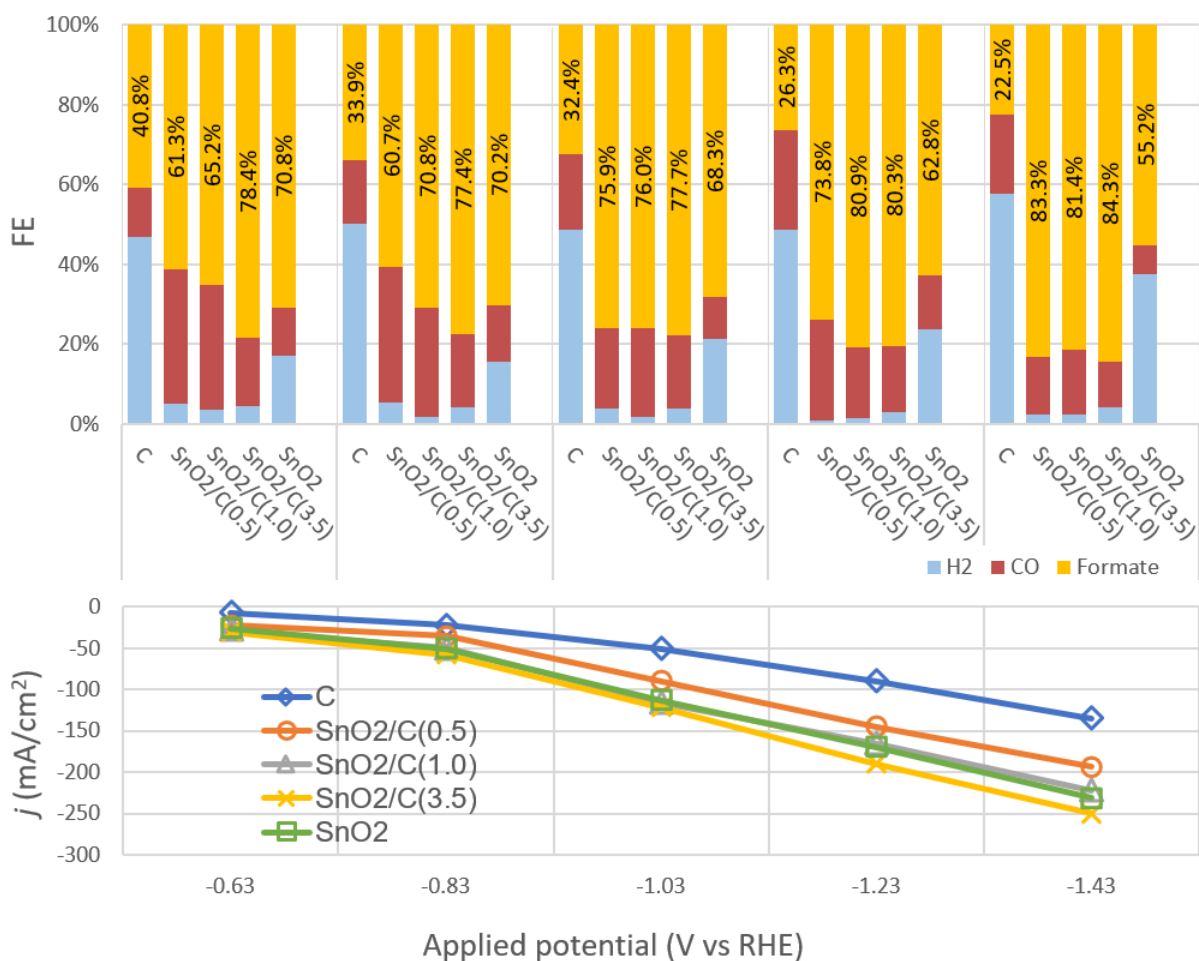


Figure 6-4 Results of eCO₂RRs catalysed by SnO₂/C mixtures and individual SnO₂ and carbon at a wide range of applied potentials.

As shown in Figure 6-4, carbon black and SnO₂ both show catalytic activity for eCO₂RR, producing H₂, CO, and formate as the major products. It is interesting to see that carbon black itself was active for eCO₂RR with 50% FE for C1 product (40% formate and 10% CO) at low overpotential of -0.63 V, but the FE for C1 decreased at

higher overpotentials. At the same applied potential, SnO₂ achieved much higher current densities and formate FE than carbon alone suggesting SnO₂ possessing higher activity and faster kinetics. SnO₂ showed similar trend as carbon in terms of FE for C1 products, decreasing as overpotential increasing. The SnO₂/C composites show enhancement in both formate FE and current density compared to carbon alone at any applied potential. However, in contrast to SnO₂ alone, the SnO₂/C composites generally need high overpotential (i.e., applied potential more negative than -1.03 V) to achieve higher formate FE. Only SnO₂/C(3.5) shows higher formate FE and current density than the SnO₂ alone at any potential.

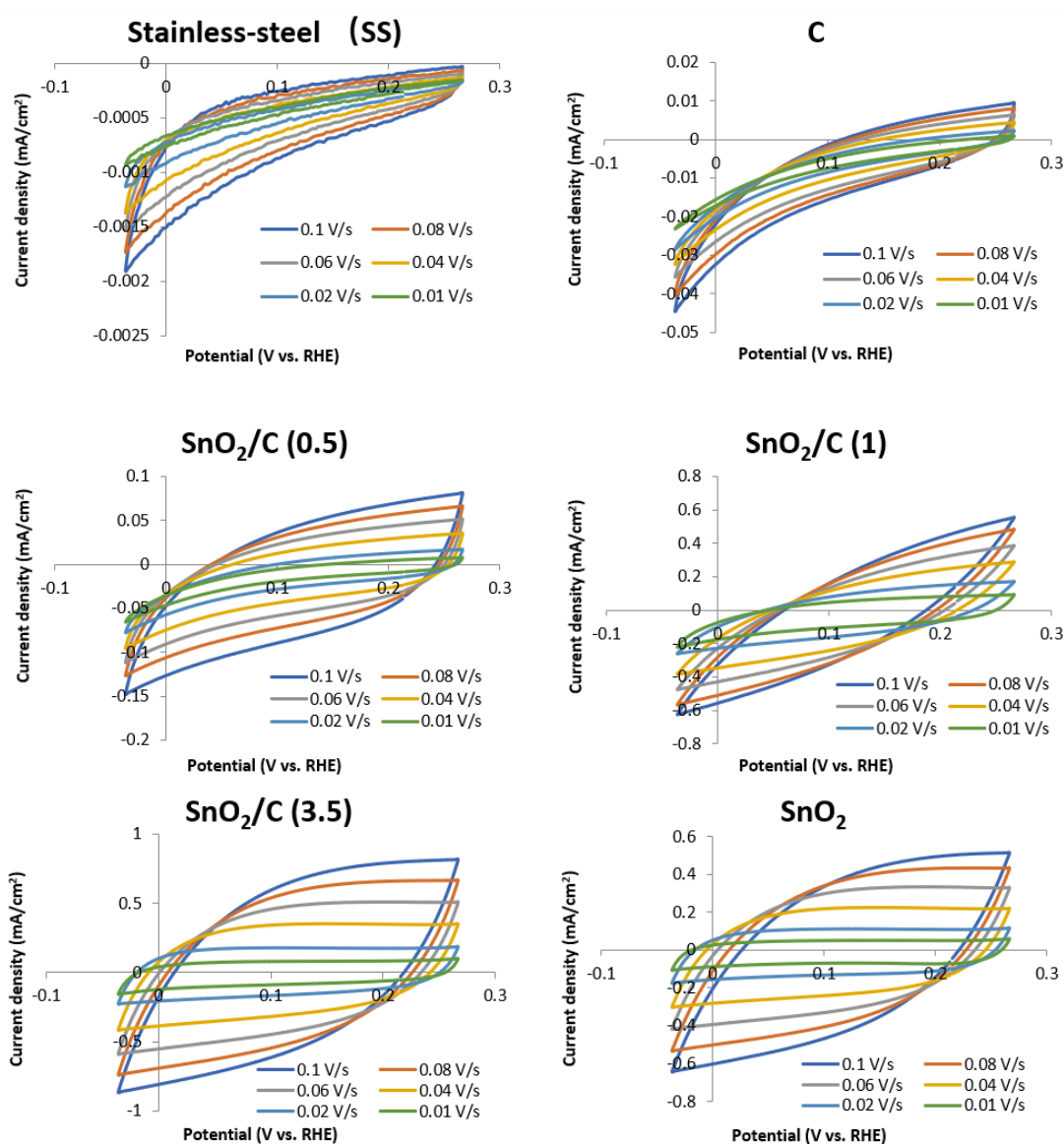
Sn and SnO₂ are known for their catalytic activity for formate production from eCO₂RR^{72, 108-109}, which is also reflected in the result of this study. However, the formate FE showed a decreasing trend with the increasing overpotential when using SnO₂ alone, whereas it was maintained or even increased with the increasing overpotential if using SnO₂/C composites. One reason could be improved electric conductivity of carbon facilitated the electron/charge transfer of the catalyst. For the catalytically-optimum SnO₂/C(3.5), the molar ratio of SnO₂:C on the reaction interface should be 1 : 3.6 (mol/mol). Carbon-composition could provide efficient bridges for charge transfer between SnO₂ particles.

Another function of carbon support could be adapting the SnO₂ catalyst pore structure to build a more effective reaction interface. Generally, inside the catalyst layer of GDE, there are three pore conditions: flooded pore, wetted pore, and dry pore as illustrated by Weng et al.¹⁹⁸ and reproduced in Figure AIV-3. The dry pores are gas transport channels, but they are inactive for eCO₂RR due to the lack of aqueous electrolyte and ion transfer. The flooded pores completely eliminate gas channels so that possessing big mass-transport resistance for gaseous CO₂ reactant. Thus, an ideal gas-liquid-solid three-phase

interface that maximizing gas, liquid, and charge transfer was assumed to be facilitated by partially wetted pores.

Measuring the double-layer capacitances of the porous electrode in aqueous solution is normally used to evaluate the electrode-electrolyte phase boundary and to investigate the pore conditions¹⁹⁹⁻²⁰⁰. The double-layer capacitances of those 5 electrodes were measured in HClO₄ solution by the method reported¹²¹, a smooth stainless-steel (SS) foil was also tested as a reference with the relative area of electrode/electrolyte interface regarding as 1, presented in Figure 6-5 and Table 6-1.

a



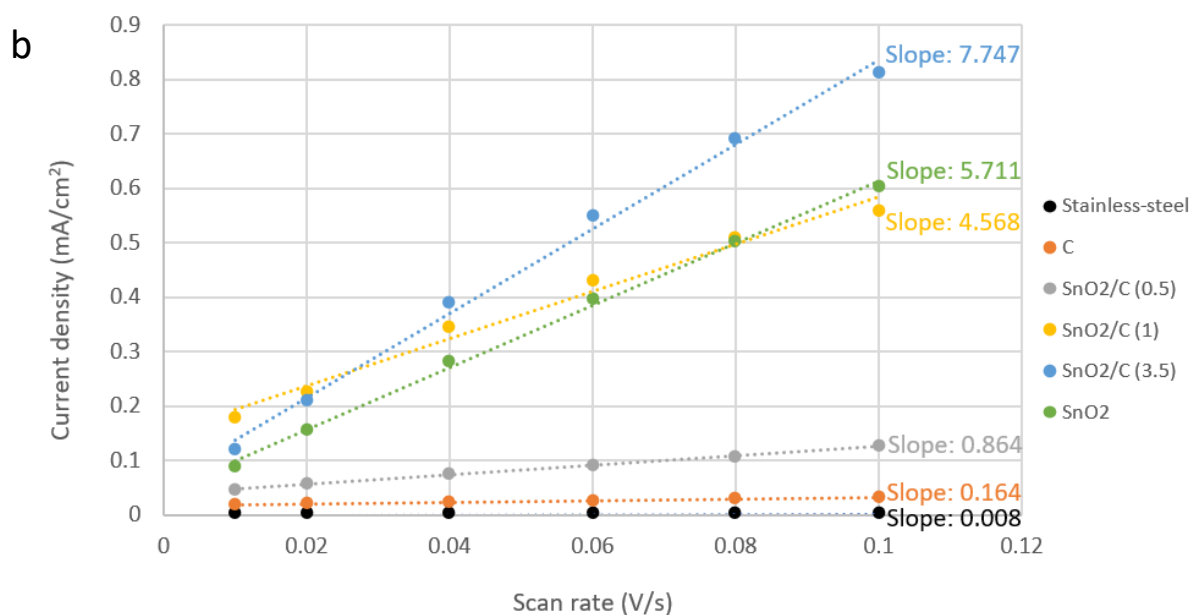


Figure 6-5 Determination of double-layer capacitance for a smooth stainless-steel sheet and the SnO₂/C-GDEs with various SnO₂/C mass ratio. a) CVs taken over a range of scan rates in a potential window where only double-layer charging and discharging is relevant for stainless-steel and SnO₂/C-GDEs. b) Current due to double-layer charge/discharge plotted against CV scan rate for stainless-steel and SnO₂/C-GDEs.

Table 6-1 Double layer capacitances and relative area of electrode/electrolyte interface of SnO₂/C-GDEs with various SnO₂/C mass ratio, C-GDE, and SnO₂-GDE in contrast with a smooth stainless-steel (SS) foil.

Sample	SS foil	C	SnO ₂ /C (0.5)	SnO ₂ /C (1.0)	SnO ₂ /C (3.5)	SnO ₂
Molar ratio of SnO ₂ /C (mol/mol)	--	--	0.04	0.08	0.28	--
Double-layer capacitance (mF)	0.008	0.164	0.864	4.568	7.747	5.711
Relative area of electrode/electrolyte interface	1	20.7	109.3	578.2	980.6	722.9

As shown in Table 6-1, the capacitance of carbon alone is 0.164 mF, nearly as small as the smooth SS foil (0.008 mF), although Vulcan carbon black is well-known for its large specific surface area $> 200 \text{ m}^2 \text{ g}^{-1}$ ²⁰¹⁻²⁰². This indicates hydrophobic carbon alone

resulting in mostly “dry pores” situation. Ahn et al.²⁰³ measured the contact angle of Nafion-binded Vulcan XC72 to water was ca. 150°, implying strong hydrophobicity. The SnO₂ alone shows much larger double-layer capacitance of 5.711 mF, indicating good electrolyte intrusion and large active area at the electrode/electrolyte interface. Whereas the contact angle of bare SnO₂ to water was 98°²⁰⁴, relatively more hydrophilic than carbon. When mixing SnO₂ and carbon with different ratios, the electrode capacitances were different. For SnO₂/C(0.5) with the smallest SnO₂/C molar ratio of 0.04 (mol/mol), the electrode/electrolyte interface area developed about 5-folds compared to carbon alone, showing the effect from more hydrophilic SnO₂ in SnO₂/C composite. With the increasing SnO₂ molar ratio, the electrolyte intrusion of the porous electrode developed. SnO₂/C(3.5) obtained the largest electrode/electrolyte interface area, more than SnO₂ alone, which also shows the optimum eCO₂RR performance in Figure 6-4. This is probably a sign that SnO₂/C(3.5) mostly contains partially wetted pores that favor eCO₂RR. Moreover, since the size of Sn-based grains grew during eCO₂RR as indicated in the SEM result (Figure 6-1), the appropriate amount of carbon that unaffected by electrolysis should be beneficial to maintain the pore structure in SnO₂/C composites.

Since the overall current density was almost linearly going up with the overpotential and the formate FE maintained in the selected potential range by using SnO₂/C composites (especially the SnO₂/C(3.5)), the partial current density of formate production approximately follows a linear relationship with the applied potential as indicated in Figure AIV-2 d, which means the formate production could be feasibly controlled by the energy input.

6.3.2.2 Controllable formate production

Figure 6-6 a shows the relationship of the overall CO₂ conversion and the formate yield (mg min⁻¹) vs applied potential when SnO₂/C(3.5) was used as the catalyst. The formate yield and CO₂ conversion follow a linear-increasing trend with increased overpotential, reaching about 3.03 mg min⁻¹ cm⁻²_{working electrode} and 22.9% respectively at -1.43 V. The formate yield per millilitre CO₂ on each 1 cm² working electrode (WE) was calculated and compared to related studies published in recent 5 years (Figure 6-6 b). This work shows at least 10-fold improvement than the best documented so far in the literature^{72, 107, 109, 113-116}.

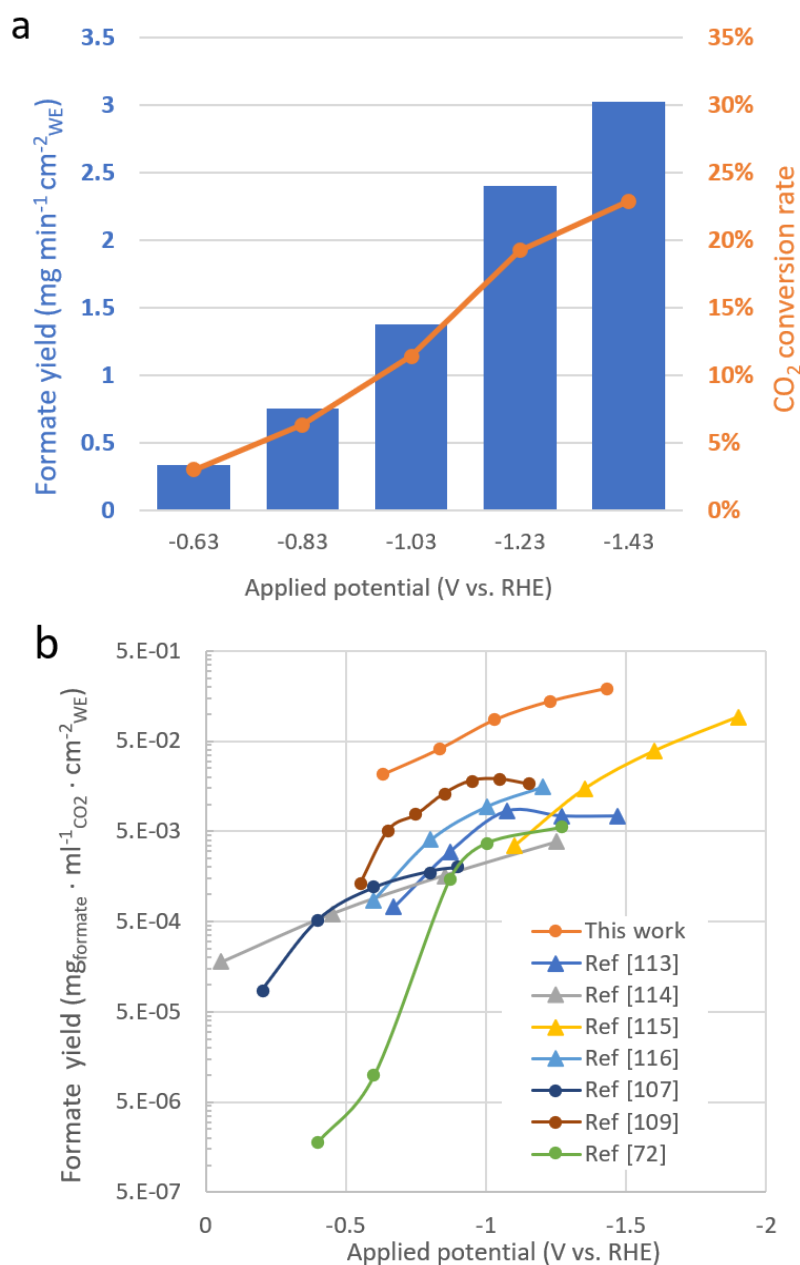
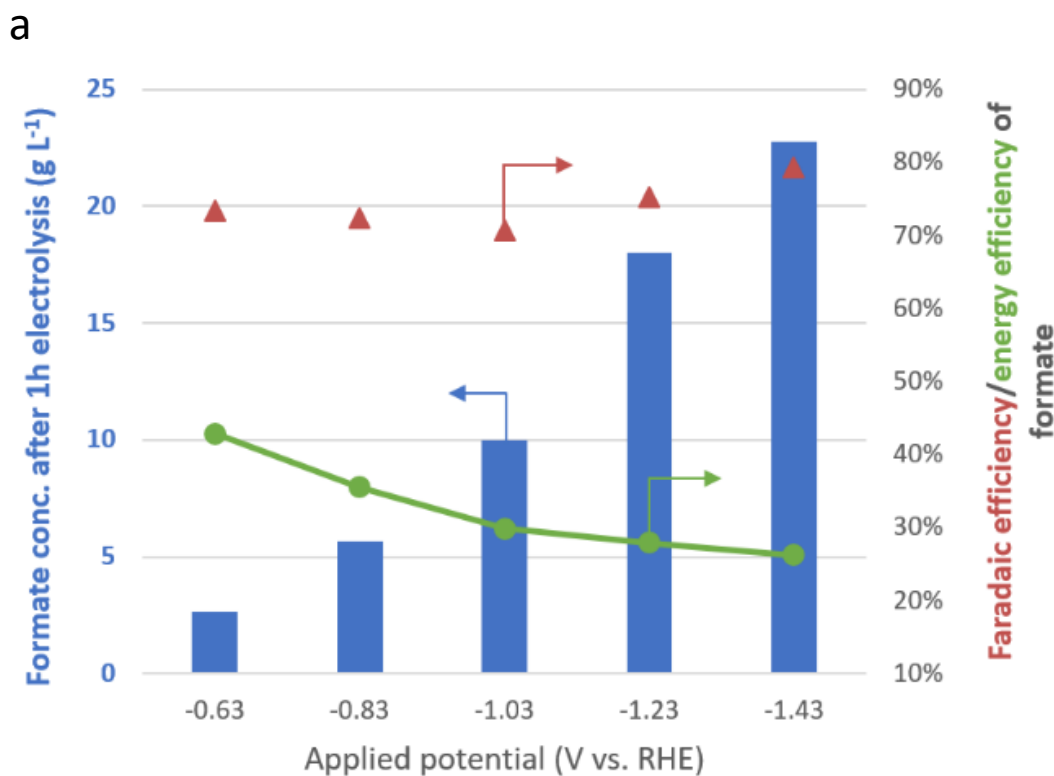


Figure 6-6 a) The yield of formate and overall CO₂ conversion rate of eCO₂RRs catalysed by SnO₂/C(3.5) at specific applied potentials. b) A comparison with related studies published in recent 5 years in terms of formate yield per milliliter CO₂ feedstock on every 1 cm² working electrode (WE).

To produce formate with higher concentration, a batch reactor with static catholyte was used. Figure 6-7 a shows the average FE and energy efficiency (EE) of formate production using the optimum SnO₂/C ratio (3.5) and operating the cell for one hour at various specific potentials. The formate FE at any potential is maintained around 73% which is lower than the results (~80%) with flowing catholyte mode in Figure 6-4, most probably due to the accumulated formate products affecting the reaction equilibrium and hindering the forward reaction. With the increasing overpotential, formate concentration in 1h electrolysis increased with the declined EE. A concentration of 0.5 M formate could be produced at -1.43 V within 1-hour electrolysis with about 26.3% energy efficiency. The EE could be developed to higher than 42.9% when applying lower overpotential -0.63 V to produce 0.5 M formate solution, but much longer electrolysis time (9 h) would be needed as suggested in Figure 6-7 b.



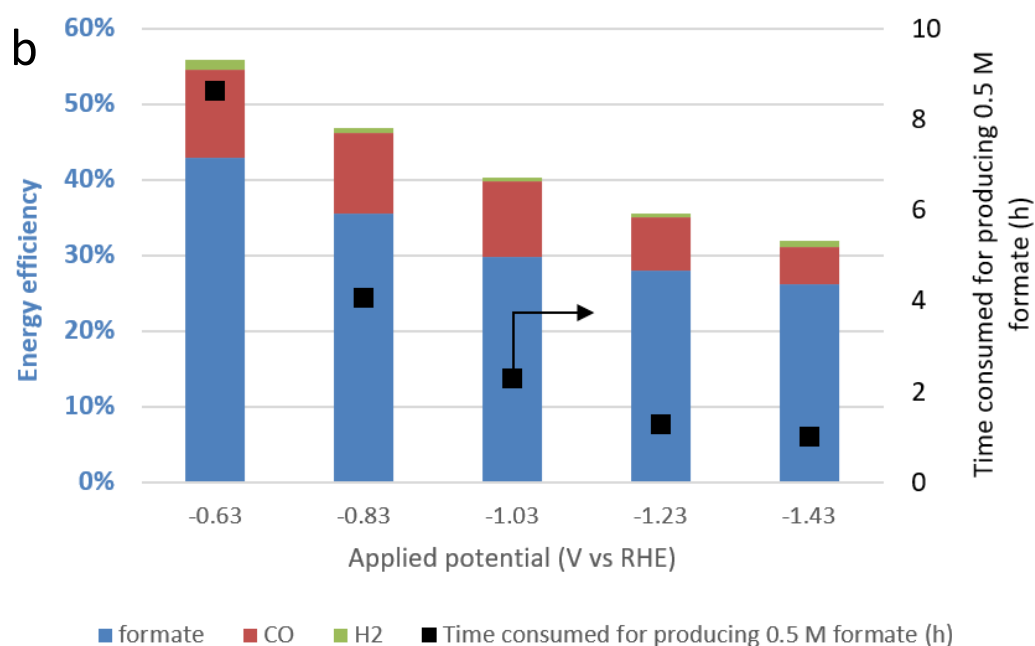


Figure 6-7 a) Formate concentration, average Faradaic efficiency (FE) and energy efficiency (EE) with 1-hour electrolysis at specific applied potentials -0.63 ~ -1.43 V. b) Energy efficiencies of all the products from eCO₂RR and the time consumed for producing 0.5 M formate at specific applied potentials -0.63 ~ -1.43 V with static catholyte

6.3.3 Performance with direct formate fuel cell (DFFC) using formate from eCO₂RR

The 0.5 M formate solution produced by eCO₂RR, denoted as “renewable fuel”, was then filtered by PTFE membrane with 0.2 μm pore size and directly utilized as the fuel of DFFC. A model fuel of 0.5 M HCOOK dissolved in 1 M KOH prepared by commercial reagents was also tested by this DFFC as a control. Table 6-2 summarizes the cation and anion concentrations of the fuel determined by IC and ICP measurement.

Table 6-2 Fuel composition

	Ion concentration (mol L ⁻¹)				pH
	COOH ⁻	K ⁺	CO ₃ ²⁻ /HCO ₃ ⁻	Sn ⁴⁺ / Sn ²⁺	
Model fuel	0.50	1.50	—	—	13.8
Renewable fuel	0.50	2.82	0.62	1.66 × 10 ⁻⁵	> 14

The potentiodynamic (VI curves) results of these two fuels at 25 °C and 60 °C are given in Figure 6-8 a. Power densities were calculated based on the VI curves and plotted in Figure 6-8 b. The galvanostatic experiments for both fuels were carried out at 25 mA cm⁻² by circulating 25 ml fuel (60 °C), with results illustrated in Figure 6-8 c. Figure 6-8 d shows the discharge energy, by integrating the galvanostatic curves over time until the cell voltage reaching 0 V. The parameters of DFFC performance by using those two fuels are concluded in Table 6-3.

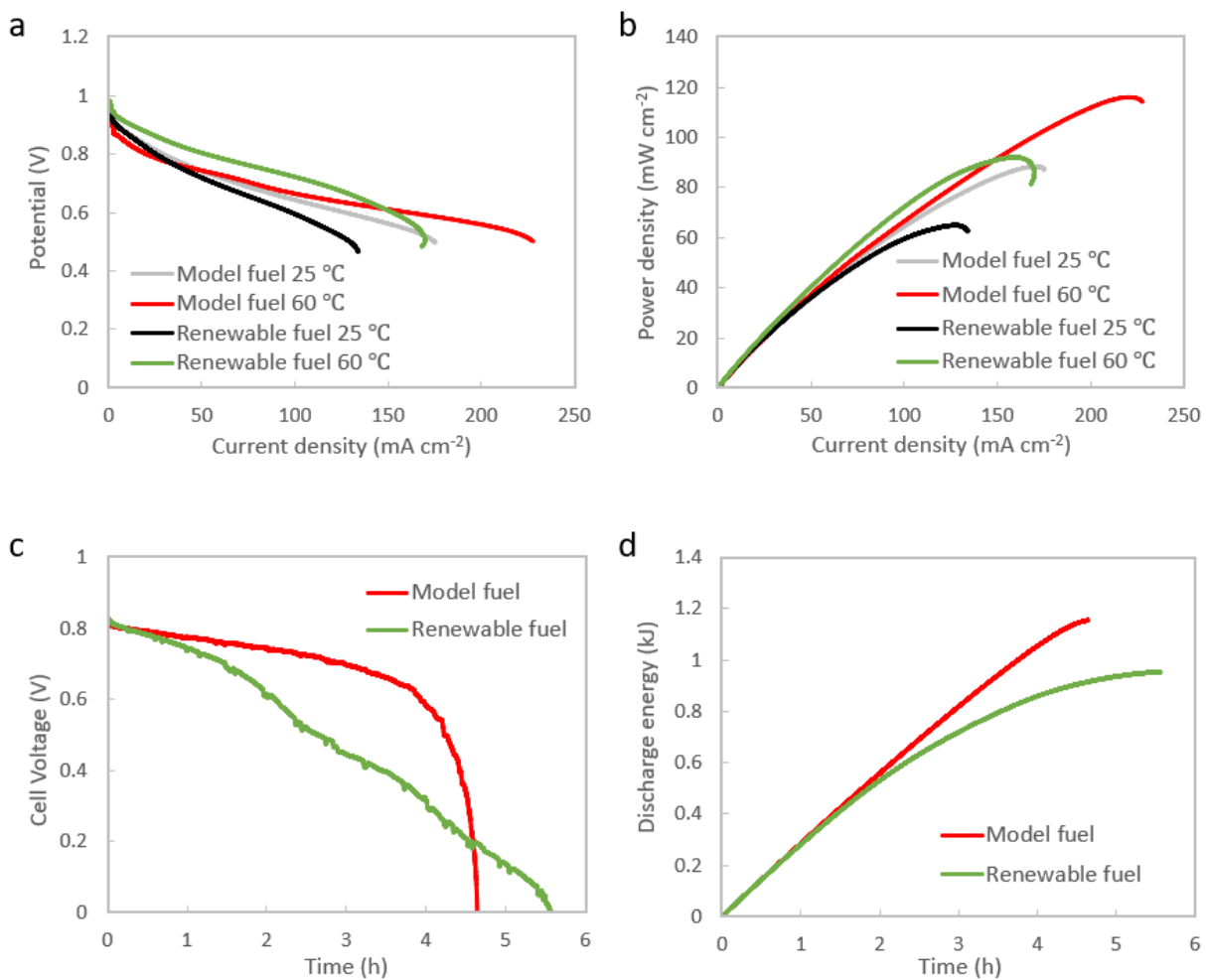
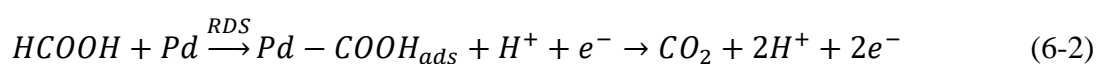
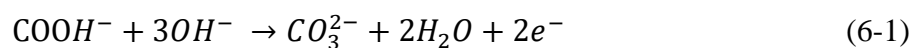


Figure 6-8 The performances of DFFC using the model fuel and renewable fuel: a) polarization curves at 25 °C and 60 °C, b) power density curves at 25 °C and 60 °C, c) galvanostatic curves at 25 mA cm⁻² (60 °C) by circulating 25 ml fuel, and d) discharge energy curves at 25 mA cm⁻² (60 °C) by circulating 25 ml fuel.

Table 6-3 Parameters of DFFC performance using the model fuel and renewable fuel at 60 °C.

	Model fuel	Renewable fuel
OCV (V)	0.98	0.99
Cell resistance (mΩ)	72	84
Peak power density (mW cm ⁻²)	118	92
Discharge Current Density (mA cm ⁻²)	25	25
Discharge energy (kJ)	1.15 (25 ml)	0.95 (25 ml)
Faradaic efficiency (%)	69	84
Energy efficiency (%)	36	30

As shown in Table 6-3, the OCV of DFFC using the renewable fuel reached almost 1 V and was relatively close to the theoretical potential 1.356 V of the formate fuel cell operated under 60 °C with formate concentration 0.5 M and pH = 14. This theoretical potential was calculated by Gibbs–Helmholtz equation and Nernst equation as shown in Table AIV-5 of Appendix IV. The renewable fuel achieved its peak power density, discharging energy, and energy efficiency at 92 mW cm⁻², 0.95 kJ, and 30% respectively, but all were slightly lower than the model fuel. From the componential analysis in Table 6-2, even though the formate concentrations in both fuels are the same, the renewable fuel from CO₂ reduction contained a high concentration of carbonate (0.62 M) and small quantity of Sn (~2 ppm), due to the reaction with dissolved CO₂ and etching of Sn catalyst during eCO₂RR. The existence of carbonate ions can shift the equilibrium of DFFC anodic reaction (Equation 6-1) and hinder the forward reaction to some extent. From the view of catalysis, the adsorption of COOH_{ads} is the rate determining step (RDS) for electrooxidation of formate over Pd (Equation 6-2)²⁰⁵. The high coverage of carbonate/bicarbonate ions leads to the chemisorption of carbonate/bicarbonate groups which reported to be a potential-independent process on Pd surface²⁰⁶, the adsorption of COOH_{ads} can be competed accordingly. Thus, the lower cell voltage when using the renewable fuel should be most-probably caused by the large concentration of CO₃²⁻/HCO₃⁻.



However, the Faradaic efficiency of the renewable fuel reached 84% which is 15% higher than the model fuel. This is probably attributed to the higher alkalinity of the renewable fuel, as higher alkaline formate fuel enabled higher Faradaic efficiency of DFFC¹⁹⁵⁻¹⁹⁶. Although it was not possible to measure the pH value of the renewable fuel as it outranged 14, the concentration of hydroxyl ion could be roughly calculated as presented in Table 6-4. The calculated concentration of OH⁻ is 1.22 M, showing higher alkalinity than the model fuel.

Table 6-4 Calculations of OH⁻ concentration in the residual catholyte after eCO₂RR producing 0.5 M formate.

	Reactions	Calculation	C _{OH⁻} (M)
Original OH ⁻	---	---	1.0
Produced OH ⁻	$\text{CO}_2 + 2\text{H}_2\text{O} + 2e^- \rightarrow \text{HCOOH} + 2\text{OH}^-$ (6-3) $\text{CO}_2 + \text{H}_2\text{O} + 2e^- \rightarrow \text{CO} \uparrow + 2\text{OH}^-$ (6-4) $2\text{H}_2\text{O} + 2e^- \rightarrow \text{H}_2 \uparrow + 2\text{OH}^-$ (6-5)	$n_{\text{OH}^-} = n_{e^-}$ $Q = It \approx 0.502 \times 3622 = 1817 \text{ C}$ $n_{e^-} = \frac{Q}{F} = \frac{1817}{96485} = 0.019 \text{ mol}$ $C_{\text{OH}^-} = \frac{n_{\text{OH}^-}}{V_{\text{catholyte}}} = \frac{0.019}{0.013} = 1.46 \text{ mol L}^{-1}$	1.46
Consumed OH ⁻	$\text{CO}_2 + 2\text{OH}^- \rightarrow \text{CO}_3^{2-} + \text{H}_2\text{O}$ (6-6)	$C_{\text{OH}^-} = 2C_{\text{CO}_3^{2-}} = 2 \times 0.62 = 1.24 \text{ M}$	-1.24
			Net. 1.22

C: molar concentration (M or mol L⁻¹)

n: molar mass (mol)

Q: Quantity of electric charge (C)

I: current (A)

t: time (s)

F: Faradaic constant (96485 C mol⁻¹)

V: volume (L)

When circulating 25 ml renewable fuel to achieve a more adequate fuel utilization, the overall chemical to electricity energy efficiency of the single cell reached 30%, which is

comparable to those using higher-concentrated formate fuel ($C_{\text{COOH}^-} \geq 1 \text{ M}$) in stronger alkaline media ($C_{\text{OH}^-} \geq 2 \text{ M}$)¹⁹⁵⁻¹⁹⁶. From the DFFC, a close loop of “electricity-formate-electricity” has been achieved. With high overpotential -1.43 V , the overall EE was 26.3% leading to the efficiency of 8% for “electricity-formate-electricity”. However, it proves the concept of converting CO_2 to fuels as energy storage for renewable energy. Further overall efficiency can be improved by using lower overpotentials (showing in Figure 6-7 a) and enhancing the anodic Oxygen evolution reaction (OER), which is currently not optimised.

6.4 Chapter summary

The work in this chapter utilized carbon black supported SnO_2 catalyst to efficiently convert CO_2 to formate, in a gas diffusion cell with an alkaline catholyte (1 M KOH) at high current densities. An “optimum” SnO_2/C mass ratio was reached suggesting the interaction of SnO_2 and carbon at this ratio built an appropriate three-phase reaction interface with efficient charge and mass transfer leading to higher selectivity of formate production. The Faradaic efficiency of formate production under the optimized condition could be maintained at around 80% in the potential range of $-0.63 \sim -1.43 \text{ V}$ (vs. RHE), with the overall current densities from $30 \sim 250 \text{ mA cm}^{-2}$. This enabled a high formate yield which is, about $3 \text{ mg min}^{-1} \text{ cm}^{-2}_{\text{WE}}$ formate could be produced when applying -1.43 V cathodic potential. 0.5 M formate which was produced within 1 hour with the energy efficiency 26.3% was directly used as the fuel for direct formate fuel cell (DFFC). A fuel cell with a Pd- CeO_2/C anode and FeCo/C cathode achieved a peak power density of 92 mW cm^{-2} and an energy efficiency of 30%. A close loop of “electricity-formate-electricity” was achieved signifying the promising future for electrochemical CO_2 reduction to fuels for energy storage.

Chapter 7 Conclusions and future directions

7.1 Conclusions

The electrochemical CO₂ reduction reaction (eCO₂RR) to fuels which only consumes electricity and water as the inputs has great potential to alleviate environmental and energy crisis caused by excessive CO₂ emission and the shortage of fossil fuels. Even though there has been a huge upsurge in publications of related studies in recent decades, eCO₂RR research is still at its early-stage and far from industrialization. To realize the scale-up of the present bench-scale reaction, an economically-feasible system, high reaction rate of eCO₂RR, exclusive selectivity towards a value-added product, high energy efficiency, and long-term stability are simultaneously required.

This thesis firstly worked on the development of CO₂ mass transfer and ion transfer through the studies on reactor configuration and electrolyte engineering, achieved a great enhancement on overall reaction rate of eCO₂RR, and provided insights into mass transfer mechanism on the three-phase reaction interface and the role of alkaline electrolyte. Targeting different gaseous and liquid products, highly-active catalysts were afterwards designed and synthesized which achieved dual-enhancement in product selectivity and production rate. The catalytic mechanism was highlighted in terms of the synergetic effect of binary active components and multi-functions of catalyst support. Finally, to explore the sustainability of eCO₂RR, the produced formate solution was reutilised as an energy storage media. In details, the following issues were addressed in this study.

1) Enhanced selectivity of carbonaceous products from electrochemical reduction of CO₂ in aqueous media. The effects of CO₂ supply method and alkalinity on the selectivity of carbonaceous products (especially C₂) were investigated in aqueous electrolyte using Cu_xO catalyst, which had great impact on CO₂ mass transfer and further affected the overall reaction rate. The results suggested that gas diffusion electrode (GDE) cell with CO₂

supplied through gas diffusion enabled higher selectivity for carbonaceous products and stronger suppression of hydrogen evolution reaction (HER), compared to a two-chamber (2C) cell with CO₂ purging into electrolyte. Faradaic efficiency (FE) of carbonaceous products increased from <10% in 2C cell to 55% in GDE cell at -1.17 V when using 1.0 M KHCO₃ catholyte. This was primarily due to different reactants for CO₂ electrochemical reduction in GDE and in CO₂-saturated solution, being CO₂* and hydrated H₂CO₃*, respectively. The alkalinity of catholyte also showed significant influence on the selectivity of carbonaceous products leading to higher FE from KOH than KHCO₃. Higher FE of C₂ products, ethanol and ethylene, were observed from KOH with higher concentration (\geq 0.5 M) and at higher overpotentials (-0.97 and -1.17 V), suggesting C-C coupling process occurring with a high concentration of OH at catalyst interface with high energy input. XRD and XPS proved the effect of OH groups from alkaline catholyte on the catalyst surface could be favourable to carbonaceous products formation. At -1.17 V with 2 M KOH, C₂ FE achieved at 40% with current density -234 mA cm⁻², producing 0.105 mg min⁻¹ ethylene and 0.035 mg min⁻¹ ethanol on 2 cm² electrode with CO₂ flow rate 15 ml min⁻¹. Those results presented a promising reaction system for further development and scale-up.

- 2) **A scalable process for Cu-In catalyst synthesis for highly selective CO and tunable Syngas production from CO₂ electrochemical reduction.** A facile electrochemical spontaneous precipitation (ESP) method with zero energy consumption was developed to synthesis binary Cu-In catalyst on GDE. It shows a hybrid structure that amorphous In(OH)₃ nanolayer (3 ~10 nm thickness) tightly capping on the polycrystalline Cu_xO. The proper Cu-In interaction of this heterostructure enables ~90% FE of CO production from eCO₂RR. An appropriate population ratio of In/Cu (around 0.44 atom ratio) and the presence of lattice oxygen in the polycrystalline Cu_xO which enabled the oxide-derived feature, were also assumed to play crucial roles in the development of CO selectivity. With the synergy of GDE reactor and 1 M KOH catholyte, high current density ~ 200 mA cm⁻¹ at -1.17 V and

high CO FE ~ 90% were both achieved by using CuIn-ESP25min. This enabled CO₂ conversion rate and CO yield of 18.2 % and 3.05 mg min⁻¹ respectively with CO₂ supplying at 15 ml min⁻¹ on 2 cm² electrodes. Syngas could be also produced with tunable CO/H₂ ratio by applying different ESP time when preparing Cu-In catalyst. The potential of scaling up from this bench-scale reaction was revealed. As a more general conclusion, the present study provides a method to simply construct a catalytic surface with joint active centres, which may bring new ideas to the development of novel catalysts.

- 3) **Production of formate from CO₂ reduction and its application in energy storage.** This work utilized carbon black supported SnO₂ catalyst to efficiently convert CO₂ to formate, in a gas diffusion cell with an alkaline catholyte (1 M KOH) at relatively high current densities. An “optimum” SnO₂/C mass ratio was achieved and the effect of C support on performance was shown. The Faradaic efficiency of formate production under the optimized condition could be achieved at around 80% in the potential range of -0.63 ~ -1.43 V (vs. RHE), and with overall current densities from 30 ~ 250 mA cm⁻². This enabled a high formate yield which is, about 6 mg min⁻¹ formate could be produced when applying -1.43 V cathodic potential on a 2 cm² working electrode. 0.5 M formate which was produced within 1 hour with the energy efficiency 26.3% was directly used as the fuel for direct formate fuel cell (DFFC). A fuel cell with a Pd-CeO₂/C anode and FeCo/C cathode achieved a peak power density of 92 mW cm⁻² and an energy efficiency of 30%. A close loop of “electricity-formate-electricity” was realized which establishing the significant potential of formate in energy storage.

7.2 Future Directions

Electrochemical conversion of CO₂ into fuels has attracted increasing attention and research interests. However, the development of this technology is still challenging as lots of problems

need to be addressed, such as the lack of fundamental understanding into the reaction mechanism, the further development of catalyst activity and GDE stability, and so on. Stemmed from the results of this work, future studies can be carried out in the following directions:

- 1) **Gaining further understanding into reaction mechanism, especially for the generation of multi-carbon products.** Producing multi-carbon products with higher power density is attractive but challenging as more than 10 pairs of proton and electron transfer are involved in the reaction pathway. The in-situ study is necessary to find out the key intermediates with rate-determining function in order to provide guidance for the design of targeted catalysts. Apart from the catalyst material, other reaction elements such as the catholyte and applied potential also play crucial roles in reaction rate and product distribution. Thus, systematic study which meanwhile considering CO₂ mass transfer, the competitive HER, catalyst, catholyte, and applied potential is necessary.
- 2) **Stability enhancement.** The reactor equipped with gas diffusion electrode (GDE) has been examined to be an efficient reaction system with developed CO₂ mass transfer, but commonly suffers the flooding problem when using liquid electrolyte leading to a poor stability. This issue calls for studies on GDE engineering with robust hydrophobic layer which can tolerate the corrosion by the applied negative potentials and aqueous electrolyte.
- 3) **Developing the sustainability.** The sustainability of eCO₂RR can be developed by two ways: using renewable electricity (probably by photovoltaic cell or a direct photoanode for oxygen evolution reaction) as the power input and exploring the usage of downstream products.

Appendix I Literature Research in Terms of Different Heterogeneous Catalysts Used for Electrochemical CO₂ Reduction

The heterogeneous catalysts for electrochemical CO₂ reduction reaction (eCO₂RR) in literatures published in recent years were listed in this appendix.

Classified by the different target products and different reaction conditions, Table AI-1, Table AI-2, Table AI-3, Table AI-4, and Table AI-5 respectively summarise CO-selective catalysts in two-chamber (2C) cell, CO-selective catalysts in GDE cell, formate-selective catalysts in 2C cell, formate-selective catalysts in GDE cell, and Cu-based catalysts for (oxygenated) hydrocarbon production.

Most of the numerical value were obtained by analysing original figures from literature using Engauge Digitizer Software.

Table AI-1 An overview of heterogeneous catalysts for selective CO production from eCO₂RR in two-chamber (2C) cell system

Catalyst/cathode material	Reaction conditions (reactor/membrane/catholyte/CO ₂ flow rate/Cathode geometric area)	Cathodic potential (V vs. RHE)	Current density (mA cm ⁻²)		CO Faradaic efficiency
			Overall	CO partial	
Ref [81] Polycrystalline Au foil	2C cell, AEM CO ₂ -saturated 0.1 M KHCO ₃ CO ₂ flow 20 ml min ⁻¹ S _{geo} : 5.8 cm ²	-0.4	-0.2		78%
		-0.55	-1.9		82%
		-0.68	-3.7		97%
		-0.83	-4.8		76%
		-0.96	-5.9		68%
		-1.00	-8.0		58%
Ref [80] Ultrathin Au nanowires (500nm long)	2C cell, AEM CO ₂ -saturated 0.5 M KHCO ₃ , CO ₂ flow 40 ml min ⁻¹ . S _{geo} : 0.49 cm ²	-0.20	-2.04		37%
		-0.25	-4.08		69%
		-0.30	-6.122		82%
		-0.35	-8.16		94%
		-0.40	-12.245		90.5%
		-0.45	-20.408		90%
		-0.50	-32.65		90.5
-0.55	-44.90		90%		
Ref [82] Oxide-derived Au nano- particles (electro-deposited)	2C cell, AEM CO ₂ -saturated 0.5 M NaHCO ₃ CO ₂ flow 5 ml min ⁻¹ S _{geo} : 0.5 cm ²	-0.25	-0.35		68%
		-0.35	-2.2		93%
		-0.40	-8		94%
Ref [83] Pillar-like Au layer with nanostructure on Ti	Single-compartment cell CO ₂ -saturated 0.2 M KHCO ₃ (With KCl added to maintain ionic strength) S _{geo} : 0.5 cm ²	-1.00056		-5.4861	73.419%
		-0.90147		-4.9722	79.352%
		-0.80083		-5.2222	92.669%
		-0.59305		-2.6111	96.731%
		-0.49366		-1.0556	96.546%

			-0.38862		-0.3333	78.218%
			-0.34891		-0.0833	36.668%
Ref [84] 260 nm porous Au film	2C cell, CO ₂ -saturated 0.5 M KHCO ₃ CO ₂ flow 20 ml min ⁻¹ S _{geo} : 3.17 cm ²		-1.29	-40		74%
			-1.49	-52		66%
			-1.64	-60		63%
Ref [85] Au inverse opal (Au-IO) thin films 1.6μm thick	2C cell, AEM CO ₂ -saturated 0.1 M KHCO ₃ CO ₂ flow 10 ml min ⁻¹		-0.35	-0.004		35%
			-0.4	-0.025		73%
			-0.45	-0.06		90%
			-0.5	-0.11		97%
			-0.53	-0.2		99%
Ref [86] acid etched nano-porous Au film (~664 nm thickness)	2C cell, AEM CO ₂ -saturated 0.05M K ₂ CO ₃ CO ₂ flow 5 ml min ⁻¹		-1.1		-5.4394	24%
			-0.9		-7.7647	66%
			-0.7		-8.0969	89%
			-0.5		-6.2284	99%
			-0.3		-1.2042	82%
Ref [87] Anodized-reduced Ag foil (An-red-Ag) with high unoccupied density of states (DOS)	2C cell, AEM CO ₂ -saturated 0.5 M KHCO ₃ CO ₂ flow 5 ml min ⁻¹		-0.3		-0.004	4.2%
			-0.4		-0.0046	20.4%
			-0.5		-0.0522	35.4%
			-0.6		-0.195	45.9%
			-0.7		-0.5565	65.8%
			-0.8		-0.896	90.2%
Ref [88]	Ag cube	2C cell, PEM	-0.95		-4	62%
	Ag octahedra	CO ₂ -saturated 0.5 M KHCO ₃	-0.95		-1.6	47.5%
	Ag₂O cube	CO ₂ flow 10 ml min ⁻¹	-0.95		-3.2	57.5%
	Ag₂O octahedra	3h reaction	-0.95		-2.2	55%
Ref [89] Nano-porous Ag	2C cell, PEM CO ₂ -saturated 0.5 M KHCO ₃		-0.3	-0.603		17.8%
			-0.4	-3.34		81%
			-0.5	-8.97		89.2%
			-0.6	-17.6		92.1%

		-0.7	-29.8		92.3%
		-0.8	-37.3		93.1%
Ref [⁹⁰] Highly porous Ag film (16 μm thickness)	2C cell, PEM CO ₂ -saturated 0.5 M KHCO ₃ S _{geo} : 0.5 cm ²	-0.5	-13.6		85%
		-0.6	-25		88%
Ref [⁹¹] Ag nano-corals	2C cell, CO ₂ -saturated 0.1 M KHCO ₃	-0.4	-0.55		74%
		-0.49	-2.3		95%
		-0.57	-5.5		95%
		-0.65	-10		95%
		-0.72	-15		95%
Ref [⁹²] Air-annealed Ag on carbon fiber paper	2C cell, PEM CO ₂ -saturated 0.1 M KHCO ₃ CO ₂ flow 20 ml min ⁻¹ S _{geo} : 1 cm ²	-0.972	-21.068		92.093%
		-0.9368	-11.595		85.116%
		-0.9048	-8.329		82.326%
		-0.8536	-4.899		74.419%
		-0.7928	-3.266		63.256%
		-0.7224	-1.796		44.186%
		-0.6392	-0.817		29.302%
Ref [⁹³] Triangular Ag nanoplates on glassy carbon electrode	2C cell, PEM CO ₂ -saturated 0.1 M KHCO ₃ CO ₂ flow 20 ml min ⁻¹ S _{geo} : 0.785 cm ²	-1.25681		-2.72426	54.493%
		-1.15774		-2.85809	73.751%
		-1.05866		-2.29412	82.418%
		-0.95958		-1.72059	89.838%
		-0.86051		-1.21397	96.636%
		-0.75889		-0.60221	85.986%
		-0.65982		-0.24853	67.239%
		-0.56074		-0.06691	44.753%
Ref [⁹⁴] 5 nm Ag nanoparticles immobilized on carbon	2C cell, PEM CO ₂ -saturated 0.5 M KHCO ₃ CO ₂ flow 120 ml min ⁻¹	-0.93977		-7.9459	53.841%
		-0.87764		-8.0676	74.785%
		-0.81203		-6	79.314%

support glass carbon	S_{geo} : 0.5 cm ²	-0.74643		-3.6892	84.45%
		-0.66863		-1.5405	81.07%
		-0.57875		-0.4459	73.429%
Ref [⁹⁵] PdTe deposited on few-layer graphene bonded on carbon fibre paper	2C cell, PEM CO ₂ -saturated 0.1 M KHCO ₃ S_{geo} : 1 cm ²	-0.6	-0.6		64%
		-0.8	-1.8		89%
		-1.0	-3.75		70%
		-1.2	-5.6		15%
Ref [⁹⁶] Au₇₅Pd₂₅ Alloy	2C cell, PEM CO ₂ -saturated 0.1 M KHCO ₃	-0.6086	-0.87565		96.581%
		-0.55892	-0.43126		85.47%
		-0.47922	-0.18851		74.359%
		-0.39849	-0.02357		17.094%
		-0.34881	-0.00433		2.564%
Ref [⁹⁷] Pd Octahedra nano-particles	2C cell, PEM CO ₂ -saturated 0.5 M NaHCO ₃	-1.10334	-39.612		43.676%
		-0.99988	-40.475		72.845%
		-0.90251	-39.988		85.98%
		-0.80107	-26.704		90.308%
		-0.7037	-16.385		94.324%
		-0.59821	-6.872		92.673%
		-0.50084	-1.268		88.199%
		-0.40143	-0.648		28.691%
Ref [⁹⁸] Cu (0.1 wt%) anchored Pd₁₀Te₃ nanowires	2C cell, PEM CO ₂ -saturated 0.2 M NaHCO ₃ CO ₂ flow 20 ml min ⁻¹	-0.98108		-13.7234	72.751%
		-0.8693		-10.8967	80.423%
		-0.78017		-8.5714	92.063%
		-0.65916		-2.234	64.021%
Ref [⁹⁹] Evolved Cu-In catalyst	2C cell, PEM CO ₂ -saturated 0.1 M KHCO ₃ CO ₂ flow 20 ml min ⁻¹ S_{geo} : 2.25 cm ²	-0.6		-1.9	55%
Ref [¹⁰⁰] Cu-In Alloy	2C cell, CEM CO ₂ -saturated 0.1 M KHCO ₃	-0.3	-0.1		65%
		-0.4	-0.2		80%

	S_{geo} : 1 cm ²	-0.5	-0.5		80%
		-0.6	-1.1		88%
		-0.7	-1.7		87%
Ref [101] MoS _x /PEI-modified rGO	2C cell, Glass frit CO ₂ -saturated 0.5 M NaHCO ₃ S_{geo} : 0.6 cm ²	-0.25	-1		4%
		-0.45	-4		45%
		-0.65	-5		85%
		-0.85	-6		30%
Ref [102] SnO ₂ atomic layer deposited on CuO nanowire	2C cell, PEM CO ₂ -saturated 0.1 M NaHCO ₃ (treated with an ion exchange Resin) CO ₂ flow 10 ml min ⁻¹ S_{geo} : 1.6~2 cm ²	-0.4		-0.0578	63.48%
		-0.5		-0.1334	79.33%
		-0.6		-0.4366	89.59%
		-0.7		-1.0568	88.09%
		-0.8		-1.4294	83.81%
Ref [103] Highly Dense Cu Nanowires	2C cell, AEM CO ₂ -saturated 0.1 M KHCO ₃ CO ₂ flow 20 ml min ⁻¹	-0.9		-2.5941	78.6%
		-0.195		-0.03	29.5%
		-0.295		-0.2	61.19%
		-0.395		-0.5	61.78%
		-0.495		-2.59	53.25%
		-0.595		-5.98	15.99%
		-0.695		-10.7	4.97%

Table AI-2 An overview of heterogeneous catalysts for selective CO production from eCO₂RR in GDE cell system

Catalyst/cathode material	Reaction conditions (reactor/membrane/catholyte/CO ₂ flow rate/Cathode geometric area)	Potential (V)		Current density (mA cm ⁻²)		CO Faradaic efficiency
		Cathodic (V vs RHE)	Cell (V)	Overall	CO partial	
Ref [104] Ag-GDL	GDE cell, PEM 1M KOH CO ₂ flow 17 ml min ⁻¹ S _{geo} : 10 cm ²	-0.78		-135.7		94.8%
		-0.9		-193.1		99.5%
Ref [105] Ag-GDL	GDE cell, PEM 1M KOH CO ₂ flow 7 ml min ⁻¹ S _{geo} : 1.13 cm ²	-0.42			-24.86	N.G.
		-0.57			-68.93	N.G.
		-0.72			-117	N.G.
		-0.87			-163	N.G.
		-1.02			-220	N.G.
Ref [174] Nitrogen-Doped Carbon Nanotube-GDL	GDE cell, Pt-GDL anode 0.1 M KHCO ₃ S _{geo} : 3.8 cm ²		-2.26		-3.7568	36.847%
			-1.88		-4.1835	45.8%
			-1.51		-4.2975	53.526%
			-1.34		-4.3727	64.902%
			-1.17		-3.9142	73.823%
			-1.09		-3.3626	79.357%
			-0.95		-1.5972	74.165%
			-0.86		-0.7329	60.374%
Ref [188] Ag-GDL	GDE cell, 1 M KOH CO ₂ flow 25 ml min ⁻¹ S _{geo} : 1 cm ²	-0.33			-3	N.G.
		-0.45			-19	N.G.
		-0.56			-39	N.G.
		-0.7			-77.36	96.7%

Table AI-3 An overview of heterogeneous catalysts for selective formate/formic acid production from eCO₂RR in 2C cell system

Catalyst/cathode material	Reaction conditions (catholyte/CO ₂ flow rate/Cathode geometric area)	Cathodic potential (V vs. RHE)	Current density <i>j</i> (mA cm ⁻²)	Formate FE	Formate production	
					Yield per hour (mg/h)	Conc. Per hour (mM/h)
Ref [107] Hierarchical Cu pillar electrode	10ml CO ₂ -saturated 0.1 M KHCO ₃ , CO ₂ flow 6 ml/min. S _{geo} : 1 cm ²	-0.2	Ap. -0.4	Ap.9.5%	Cal. 0.03	Cal. 0.07
		-0.4	Ap. -0.9	Ap. 24%	Cal. 0.19	Cal. 0.40
		-0.6	Ap. -1.9	Ap. 26%	Cal. 0.42	Cal. 0.92
		-0.8	Ap. -3.4	Ap. 22%	Cal. 0.64	Cal. 1.40
		-1.0	Ap. -4.6	Ap. 18%	Cal. 0.71	Cal. 1.55
Ref [108] Hierarchical Mesoporous SnO ₂ Nanosheets on Carbon Cloth	10ml CO ₂ -saturated 0.5 M NaHCO ₃ (pH 7.2), No CO ₂ flow during eCO ₂ RR S _{geo} : 2 cm ²	-0.38	Ap. -2	Ap. 28%	Cal. 0.96	Cal. 2.09
		-0.58	Ap. -7	Ap. 35%	Cal. 4.21	Cal. 9.14
		-0.78	Ap. -24	Ap. 46%	Cal. 18.96	Cal. 41.21
		-0.98	Ap. -50	Ap. 90%	Cal. 77.27	Cal. 80
		-1.18	Ap. -70	Ap. 50%	Cal. 60.10	Cal. 130.64
Ref [109] SnO ₂ /carbon Aerogels	30ml CO ₂ -saturated 1.0 M KHCO ₃ , CO ₂ flow 20 ml/min S _{geo} : 2 cm ²	-0.55	Ap. -5	Ap. 37%	Ap. 12.14	Ap. 8.80
		-0.65	Ap. -10	Ap. 72%	Ap. 25.39	Ap. 18.40
		-0.75	Ap. -15	Ap. 71%	Ap. 25.39	Ap. 18.40
		-0.85	Ap. -25	Ap. 73%	Ap. 26.50	Ap. 19.20
		-0.95	Ap. -34	Ap. 75%	Ap. 27.05	Ap. 19.60
		-1.05	Ap. -44	Ap. 60%	Ap. 20.42	Ap. 14.80
		-1.15	Ap. -53	Ap. 44%	Ap. 15.46	Ap. 11.20
Ref [110] SnPb alloy	65 ml CO ₂ -saturated 0.5 M KHCO ₃ CO ₂ flow 30 ml/min S _{geo} : 1 cm ²	-1.38	-57.3	79.8%	Cal. 39.26	Ap. 13
Ref [111] Cu-CDots nanocorals	75 ml CO ₂ -saturated 0.5 M KHCO ₃ , No CO ₂ flow during eCO ₂ RR S _{geo} : 0.49 cm ²	-0.5	Ap. -1	Ap. 25%	Cal. 0.11	Cal. 0.03
		-0.6	Ap. -3.4	Ap. 50%	Cal. 0.72	Cal. 0.21
		-0.7	Ap. -6	Ap. 68%	Cal. 1.72	Cal. 0.50

		-0.8	Ap. -9.5	Ap. 58%	Cal. 2.32	Cal. 0.67
Ref [112] Pt _x Pd _(100-x) /C nanoparticles	Ap. 30 ml CO ₂ -saturated 0.1 M K ₂ HPO ₄ / 0.1 KH ₂ PO ₄ electrolyte (pH 6.7), No CO ₂ flow during eCO ₂ RR. S _{geo} : 0.49 cm ²	-0.1	Ap. -1.4	Ap. 20%	Cal. 0.19	Cal. 0.14
		-0.2	Ap. -1.6	Ap. 20%	Cal. 0.22	Cal. 0.16
		-0.3	Ap. -1.8	Ap. 70%	Cal. 0.85	Cal. 0.62
		-0.4	Ap. -2	Ap. 84%	Cal. 1.13	Cal. 0.82
		-0.5	Ap. -4	Ap. 60%	Cal. 1.62	Cal. 1.17
Ref [72] Sn foil	8 ml CO ₂ -saturated 0.1 M KHCO ₃ , CO ₂ flow 20 ml/min. S _{geo} : 4.5 cm ²	-0.4	Ap. -0.0195	Ap. 13%	Cal. 0.01	Cal. 0.03
		-0.6	Ap. -0.1365	Ap. 10%	Cal. 0.05	Cal. 0.14
		-0.87	Ap. -3	Ap. 67%	Cal. 7.77	Cal. 21.10
		-1.0	Ap. -7.3	Ap. 70%	Cal. 19.74	Cal. 53.64
		-1.27	Ap. 14.3	Ap. 54%	Cal. 29.83	Cal. 81.07

S_{geo}: electrode geometric surface area,

Ap.: Approximate value as seen directly from the given diagrams in literature,

Cal.: Calculated value based on the given and approximate values.

For the calculation method:

Hypothesis the current density j and formate production rate held constant within 1 hour,

$$\text{formate yield per hour (mg/h)} = \frac{FE_{\text{formate}} \times Q \times M_r(\text{formate})}{F \times 2} = \frac{FE_{\text{formate}} \times j \times S_{\text{geo}} \times 3600 \times 46}{96500 \times 2}$$

$$\text{formate conc. per hour (mM/h)} = \frac{\text{formate yield per hour}}{M_r(\text{formate}) \times \text{Vol. catholyte}}$$

Table AI-4 An overview of heterogeneous catalysts for selective formate/formic acid production from eCO₂RR in GDE cell system

Catalyst/cathode material	Reaction conditions (catholyte/CO ₂ flow rate/Cathode geometric area)	Potential		Current density j (mA cm ⁻²)	Formate FE	Formate production	
		Cell (V)	Cathodic (V vs. RHE)			Yield per hour (mg/h)	Conc. Per hour (mM/h)
Ref [113] GDL attaching on Sn-loading Cu mesh (rolling press)	0.5M KHCO ₃ , CO ₂ flow 30ml/min. S _{geo} : 7 cm ²	—	-0.67	Ap. -3.49	Ap. 43%	Cal. 9.01	Catholyte vol. N.G.
		—	-0.87	Ap. -13.48	Ap. 46%	Cal. 37.26	
		—	-1.07	Ap. -22.44	Ap. 78%	Cal. 105.17	
		—	-1.27	Ap. -23.85	Ap. 65%	Cal. 93.15	
		—	-1.47	Ap. -36.05	Ap. 43%	Cal. 93.15	
Ref [114] Sn-GDE with thin SnOx nanolayer	7ml/min 0.1M KHCO ₃ , CO ₂ flow 45ml/min S _{geo} : 4 cm ²	-0.8	Ap. -0.05	Ap. -1	Ap. 55%	Cal. 1.89	Cal. 0.10
		-1.2	Ap. -0.45	Ap. -3	Ap. 64%	Cal. 6.60	Cal. 0.34
		-1.6	Ap. -0.85	Ap. -7	Ap. 73%	Cal. 17.55	Cal. 0.91
		-2.0	Ap. -1.25	Ap. -15	Ap. 80%	Cal. 41.21	Cal. 2.13
Ref [115] Pb/PtRu-GDL	0.5 ml/min Catholyte(pH = 2) CO ₂ flow 50 mL/min S _{geo} : 0.1 cm ²	2.5	Ap. -1.1	Ap. -20	Ap. 60%	Cal. 1.03	Cal. 0.75
		3	Ap. -1.35	Ap. -55	Ap. 93%	Cal. 4.39	Cal. 3.18
		3.5	Ap. -1.6	Ap. -150	Ap. 90%	Cal. 11.59	Cal. 8.40
		4	Ap. -1.9	Ap. -350	Ap. 92%	Cal. 27.64	Cal. 20.03
Ref [116] Sn-GDE	10ml/min 0.5M NaHCO ₃ CO ₂ flow 10ml/min S _{geo} : 10.2 cm ²	—	-0.6	Ap. -3	Ap. 20%	Cal. 5.25	Cal. 0.19
		—	-0.8	Ap. -5	Ap. 55%	Cal. 24.08	Cal. 0.87
		—	-1.0	Ap. -10	Ap. 65%	Cal. 56.92	Cal. 2.06
		—	-1.2	Ap. -18	Ap. 60%	Cal. 94.57	Cal. 3.43
Ref [117] In/C-GDL	130 ml 0.1M Na ₂ SO ₄ , CO ₂ flow 10ml/min S _{geo} : 0.95 cm ²	—	Ap. -1.2	-7.5	38%	Cal. 2.32	Cal. 0.38

Table AI-5 An overview of modified Cu-based catalysts for (oxygenated) hydrocarbon production from eCO₂RR

Catalyst/cathode material	Electrolyte	Applied potential	Faradaic efficiencies (%)							C ₂ H ₄ /CH ₄
			C ₂ H ₄	C ₂ H ₅ OH	C ₂ H ₆	CO	CH ₄	formate	Other C ₂ ⁺	
Polycrystalline Cu ³⁷	0.1 M KHCO ₃	-1.41V vs NHE	30.1	6.9	N.G.	2.0	29.4	9.7	3.0	1.0
Polycrystalline Cu ¹¹⁸	0.1 M KHCO ₃	-1.05 V vs RHE	26.0	9.8	N.G.	1.1	24.4	2.1	4.8	1.1
Cu(100) ⁷⁶	0.1 M KHCO ₃	-1.39 V vs SHE	40.7	12.8	N.G.	1.9	19.8	11.7	61.5	2.1
Cu(111) ⁷⁶	0.1 M KHCO ₃	-1.52 V vs SHE	8.8	5.3	N.G.	4.9	50.5	16.6	20.4	0.2
Cu(S)-[4(100)×(111)] ²⁰⁷	0.1 M KHCO ₃	-1.34V vs SHE	51.6	7.4	N.G.	1.1	3.8	4.6	14.1	13.5
Cu(111) ¹⁴⁷	0.01 M KH ₂ PO ₄ / 0.1 M K ₂ HPO ₄	-1.9 V vs Ag/AgCl	3	N.G.	N.G.	N.G.	24	N.G.	N.G.	0.125
Electro-deposited Cu ¹¹⁹	0.1 M KClO ₄	-1.1V vs RHE	36	N.G.	0	34	1	N.G.	N.G.	36
Argon Sputtered Cu ⁶¹	0.1 M KClO ₄	-1.1V vs RHE	26	N.G.	1	23	8	N.G.	N.G.	3.25
Electro-deposited Cu ⁶²	0.1 M KHCO ₃	-1.9V vs. Ag/AgCl	33.3	N.G.	0	2	3.6	N.G.	N.G.	9.25
Ex situ electro-	0.1 M KHCO ₃	-1.9V vs.	11	N.G.	6	0.2	0	N.G.	N.G.	∞

deposited Cu ¹²³		Ag/AgCl								
Cu nanofoam ²⁰⁸	0.1 M KHCO ₃	-1.7V vs. Ag/AgCl	1.4	N.G.	1.2	8	0.2	24	N.G.	7
Cu ₂ O-derived Cu ¹³⁴	0.1 M KHCO ₃	-1.1V vs RHE	12-33	N.G.	0-9	1-3	0-4	22	N.G.	8-12
Oxygen-evacuated Cu ₂ O ¹⁴⁰	0.5 M KHCO ₃	-1.82 V vs Ag/AgCl	26.0	N.G.	N.R	6	1	8	N.G.	26
0.9 μm Cu ₂ O film ¹³⁹	0.1 M KHCO ₃	-0.99V vs RHE	40.25	8.66	0.04	0.66	2.48	8.34	N.G.	16.2
thick Cu ₂ O film ¹²¹	0.1 M KHCO ₃	-0.95 V vs RHE	5	N.G.	8	5	N.G.	10	N.G.	-
15nm CuNPs ¹²⁴	0.1 M KHCO ₃	-1.1V vs RHE	3	N.G.	N.G.	23	12	N.G.	N.G.	0.25
Cu _x O nano-sphere ²⁰⁹	0.5 M KHCO ₃	-0.55 V vs SHE	N.G.	N.G.	N.G.	N.G.	N.G.	59.36	N.G.	—
Cu nano-flower ¹²⁵	0.1 M KHCO ₃	-1.3 V vs RHE	19	N.G.	N.G.	N.G.	3	30	N.G.	6.3
44nm Cu nano-cube ¹²⁶	0.1 M KHCO ₃	-1.1 V vs RHE	41	4	8	1.5	20.2	3	~22	2.03
Cu nano-wire ¹²⁷	0.1 M KHCO ₃	-1.9 V vs Ag/AgCl	5	N.G.	11	N.G.	N.G.	N.G.	1	—

N.G.: Not given

Appendix II Product Analysis and The Calculation of Faradaic Efficiency

All the products from eCO₂RR were analysed by chromatography. The internal standard method and external standard method were used for quantifying gas and liquid products respectively.

1. Gas analysis

A customized standard mixed gas (BOC) with the components of H₂ (1.000%), CO (1.000%), CH₄ (0.500%), CO₂ (96.000%), C₂H₄ (0.500%), C₂H₆ (0.500%), and C₃H₆ (0.500%) was used as the reference standard for the GC to analyse gas. The detecting conditions of the GC were set as Table AII-1.

Table AII-1 Detecting conditions of GC for analysing gas

Injector	Injector Temperature	150 °C		
	Split/direct	direct		
	Carrier gas	Helium		
	Flow control mode	Pressure 36.3 psi		
	Total flow	51.3 ml min ⁻¹		
	Purge flow	3.0 ml min ⁻¹		
Column	ShinCarbon ST micropacked column (Restek), 3 m length, 0.53 mm inner diameter.			
	Temperature programming			
		Rate (°C min ⁻¹)	Temperature (°C)	Hold time (min)
		--	40	2.5
		20	250	0
	15	255	2.7	
BID detector	Temperature	280 °C		
	Discharge gas flow	70 ml min ⁻¹		

The data acquisition of a standard gas is showing in Figure AII-1 a, with the peak order H₂, O₂, N₂, CO, CH₄, CO₂, C₂H₄, C₂H₆. According to this, the product gases could be determined by the retention time of each component. Figure AII-1 b displays the data acquisition of a typical sample gas, indicating H₂, CO, and C₂H₄ to be the products. The peak area value of each component is given in Table AII-2.

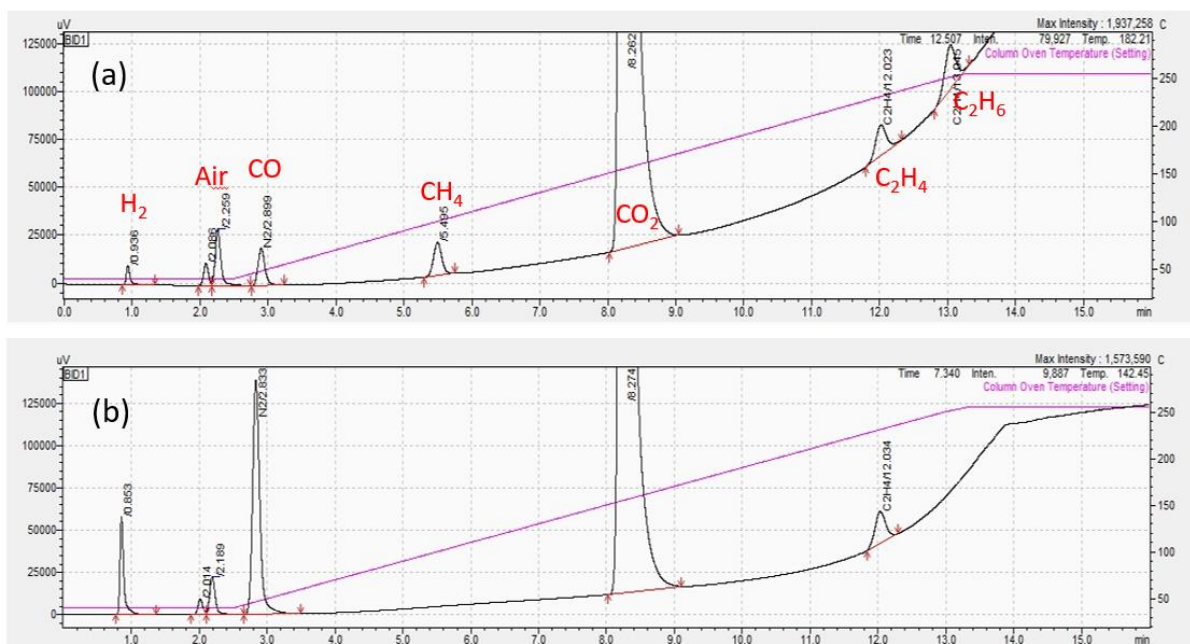


Figure AII-1 GC data acquisition in gas mode of a) the standard gas and b) a sample gas.

Table AII-2 Peak areas of the standard gas and sample gas

	H ₂	CO	CH ₄	CO ₂	C ₂ H ₄	C ₂ H ₆
Standard gas	23390	98038	96099	12380279	113629	179140
Sample gas	32642	641877	0	16780163	16685	0

Area normalization method was used to calculate the concentration of each component in the sample gas, as shown in Equation (AII-1)

$$C_i = \frac{f_i A_i}{\sum_{i=1}^n f_i A_i} \quad (\text{AII-1})$$

Where: C_i is the concentration of the component i in mix gas, f_i is the relative correction factor of i , and A_i is the peak area of i .

The ratio of relative correction factor between component i and j could be calculated by Equation (AII-2) based on the standard gas.

$$\frac{f_i}{f_j} = \frac{C_i A_j}{C_j A_i} \quad (\text{AII-2})$$

Hypothesize $f(\text{H}_2) = x$, then:

$$f(\text{CO}) = \frac{C_{\text{CO}} A_{\text{H}_2}}{C_{\text{H}_2} A_{\text{CO}}} \times f(\text{H}_2) = \frac{1\% \times 23390}{1\% \times 98038} \times x = 0.239x$$

Likewise, $f(\text{CH}_4) = 0.122x$, $f(\text{CO}_2) = 0.181x$, $f(\text{C}_2\text{H}_4) = 0.103x$, $f(\text{C}_2\text{H}_6) = 0.065x$.

Regarding the sample gas,

$$\begin{aligned} \sum_{i=1}^n f_i A_i &= f_{\text{H}_2} A_{\text{H}_2} + f_{\text{CO}} A_{\text{CO}} + f_{\text{CH}_4} A_{\text{CH}_4} + f_{\text{CO}_2} A_{\text{CO}_2} + f_{\text{C}_2\text{H}_4} A_{\text{C}_2\text{H}_4} + f_{\text{C}_2\text{H}_6} A_{\text{C}_2\text{H}_6} \\ &= 32642x + 641877 \times 0.239x + 0 \times 0.122x + 16780163 \times 0.181x + \\ &\quad 16685 \times 0.103x + 0 \times 0.065x = 3224978.661x \end{aligned}$$

Then, the concentration of H_2 is:

$$C_{\text{H}_2} = \frac{f_{\text{H}_2} A_{\text{H}_2}}{\sum_{i=1}^n f_i A_i} = \frac{32642x}{3224978.661x} = 0.01012$$

Likewise, $C_{\text{CO}} = 0.04757$, $C_{\text{CO}_2} = 0.94178$, $C_{\text{C}_2\text{H}_4} = 0.00053$.

Regarding the calculation of Faradaic efficiency (FE), the current value has been acquired from the chronoamperometry measurement, here is 137 mA when taken this sample gas. Hypothesize the sample gas was collected for t seconds with the outlet flow rate 15 ml min^{-1} , then the total volume of collected gas is $\frac{15t}{60}$ ml.

$$\text{The moles of H}_2 \quad n(\text{H}_2) = \frac{\frac{15t}{60} \times C(\text{H}_2)}{24.465} \text{ (mmol)} = 0.000103413t \text{ mmol}$$

(at room temperature and pressure, gas molar volume is 24.465 l/mol)

$$\begin{aligned} \text{FE of H}_2 \text{ is: } \quad \text{FE}(\text{H}_2) &= \frac{n(\text{H}_2)}{\text{moles of electrons} / \text{number of transferred electrons}} \\ &= \frac{0.000103413t}{\frac{It}{96485} / 2} = \frac{0.000103413t \times 2}{137t/96485} = 14.57\% \end{aligned}$$

Likewise, $\text{FE}(\text{CO}) = 68.47\%$, $\text{FE}(\text{C}_2\text{H}_4) = 4.58\%$.

2. Liquid analysis

The common liquid products from eCO₂RR can be classified as alcohols and fatty acids, which were determined by GC and IC respectively. Liquid standards were prepared with concentration gradients for qualifying and quantifying the liquid products by drawing the calibration curves. The detecting conditions of the GC and IC were set as Table AII-3 and Table AII-4 respectively.

Table AII-3 Detecting conditions of GC for analysing alcoholic liquid

Auto-sampler	Injection volume	1.0 μl	
Injector	Injector Temperature	250 $^{\circ}\text{C}$	
	Split/direct	Split, ratio 5	
	Carrier gas	Helium	
	Flow control mode	Linear velocity	
	Pressure	24.6 psi	
	Total flow	18 ml min^{-1}	
	Column flow	2.5 ml min^{-1}	
	Linear velocity	46.1 cm sec^{-1}	
	Purge flow	3.0 ml min^{-1}	
Column	Zebron ZB-WAXplus capillary column (Phenomenex), 30 m length, 0.25 mm inner diameter.		
	Temperature programming		
	Rate ($^{\circ}\text{C min}^{-1}$)	Temperature ($^{\circ}\text{C}$)	Hold time (min)
	--	50	1
30	230	5	
BID detector	Temperature	280 $^{\circ}\text{C}$	
	Discharge gas flow	50 ml min^{-1}	

Table AII-4 Detecting conditions of IC for analysing fatty acid

Auto-sampler	Injection volume	25 μ l
Columns	Metrosep Organic Acids Guard/4.6 (guard column)	
	Metrosep Organic Acids - 100/7.8	
	Eluent	0.5 mmol L ⁻¹ H ₂ SO ₄
	Flow	0.5 ml min ⁻¹
	Pressure	2.37 MPa
Peristaltic Pump	Peristaltic Metrohm Suppressor Module (MSM)	
	Solution	0.5 mmol L ⁻¹ LiCl
Detector	Conductivity detector	
	Thermostat	40 °C

3. Faradaic efficiency normalization

Since the gas sample was taken at the last few seconds before reaction termination while the liquid sample was accumulated during the whole reaction process, FEs of gas products were instantaneous values while FEs of liquid products were the average. The FE sum always fluctuated in the range of 100% \pm 20% as illustrated in Table AII-5. To achieve a more comparable and close-to-ideal dataset, the FE sum was normalized to 100% with fixing the liquid FEs and proportionally adjusting the gas FEs. Sample calculations are shown below:

Table AII-5 An example of the actual calculated FE values of all the products from eCO₂RR.

H ₂	CO	C ₂ H ₄	Formate	Ethanol	FE sum
14.57%	68.47%	4.58%	15.76%	2.29%	105.67%

Subtract the average FE of all the liquid products, the desired overall FE of gas products is $100\% - FE_{Formate} - FE_{ethanol} = 81.95\%$.

The FE ratio of H₂ among all the gas products is $\frac{FE_{H_2}}{FE_{H_2} + FE_{CO} + FE_{C_2H_4}} = 0.1663$

Thus, the normalized FE of H₂ is $81.95\% \times 0.1663 = 13.63\%$

Likewise, the normalized FE of CO and C₂H₄ are 64.04% and 4.28% respectively.

Appendix III Design of the compact cell

A compact gas diffusion electrode (GDE) cell composed of five 3D printouts, including a gas chamber, two GDE window plates, a cathode chamber, and an anode chamber as illustrated in Figure AIII-1. The design drawings of all the compartments with detailed dimensions are shown in Figure AIII-2, AIII-3, AIII-4, and AIII-5.

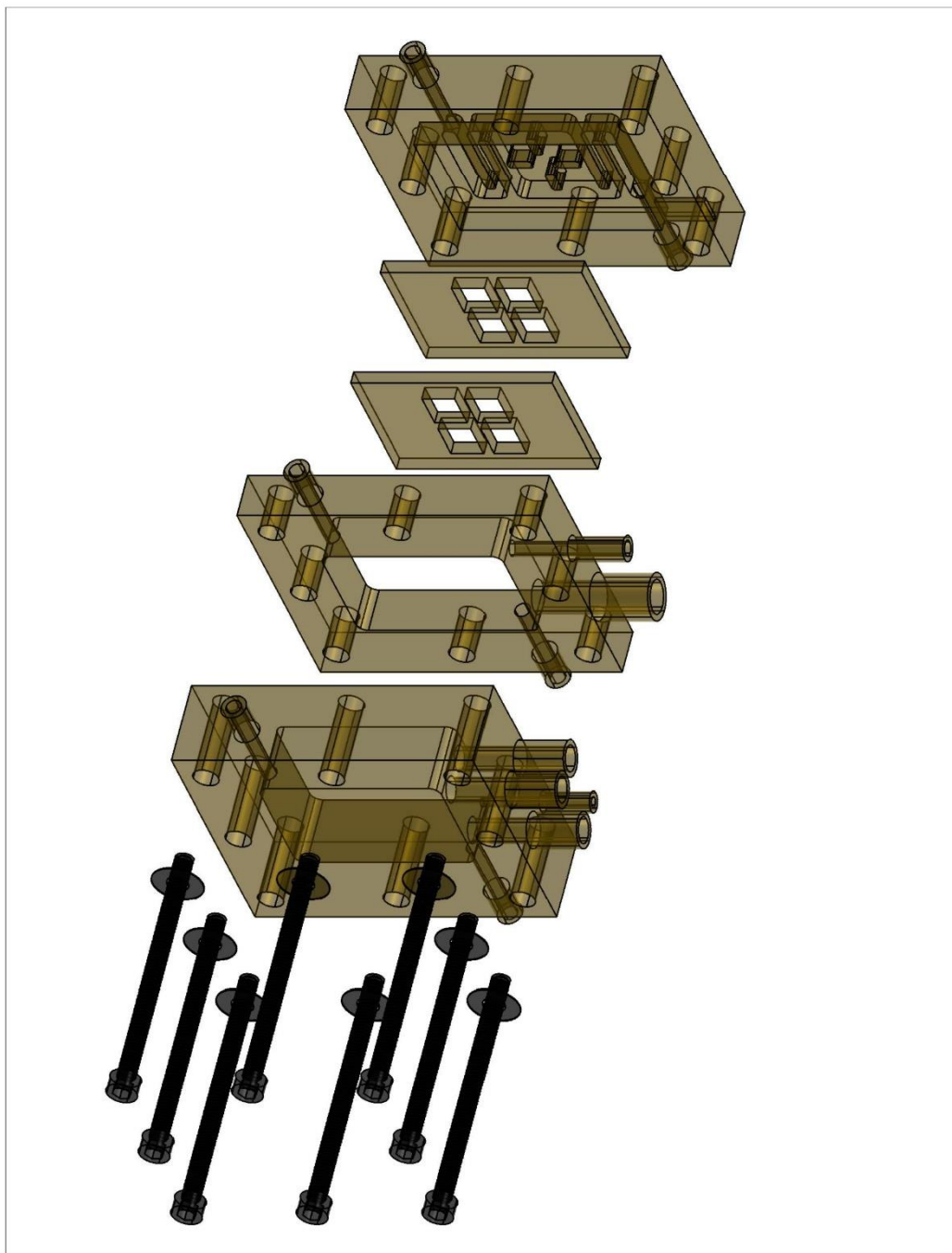


Figure AIII-1 3D drawing of all the 3D printouts (yellow) to constitute a GDE cell.

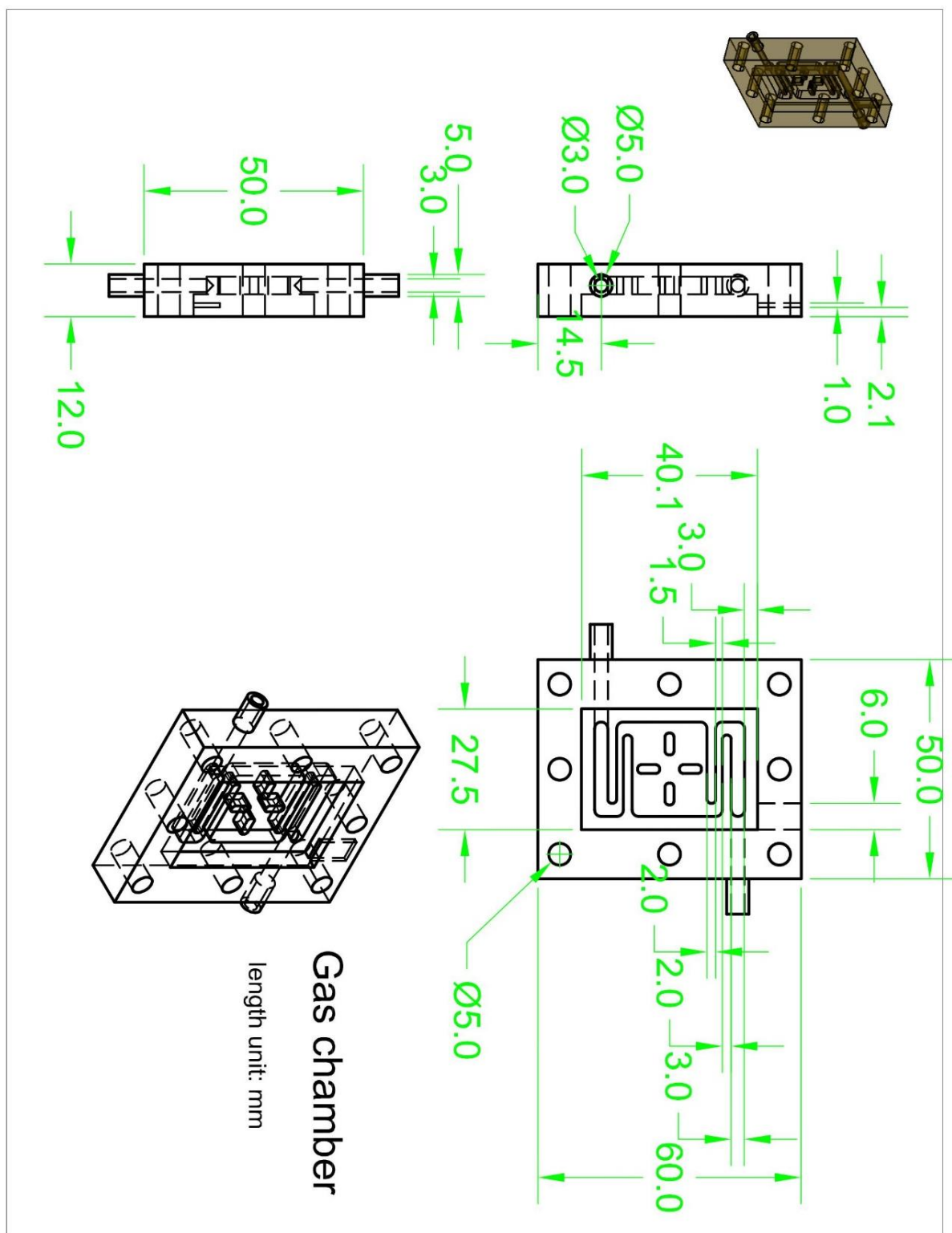


Figure AIII-2 The design drawing of the gas chamber with dimensions.

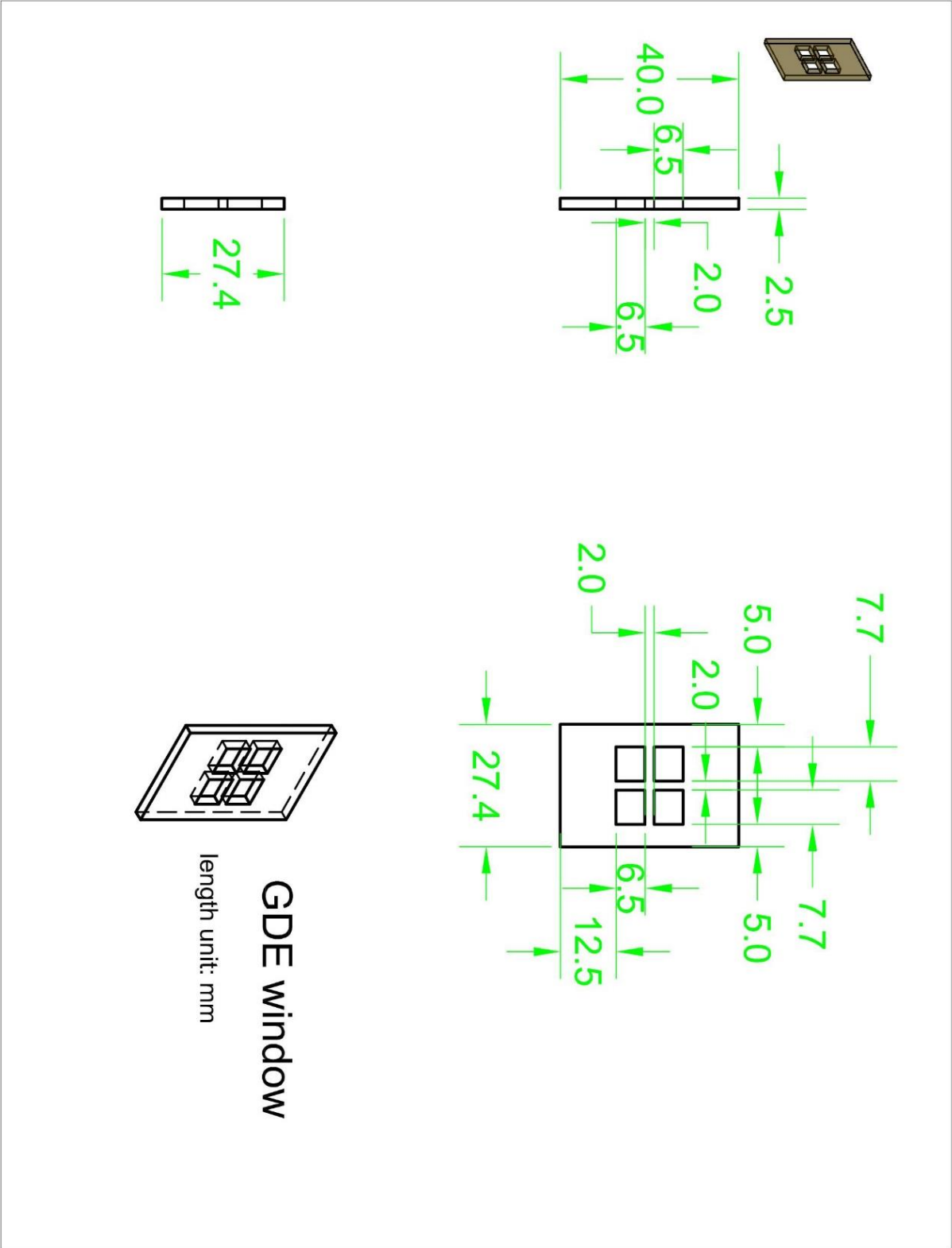


Figure AIII-3 The design drawing of the GDE-window plate with dimensions.

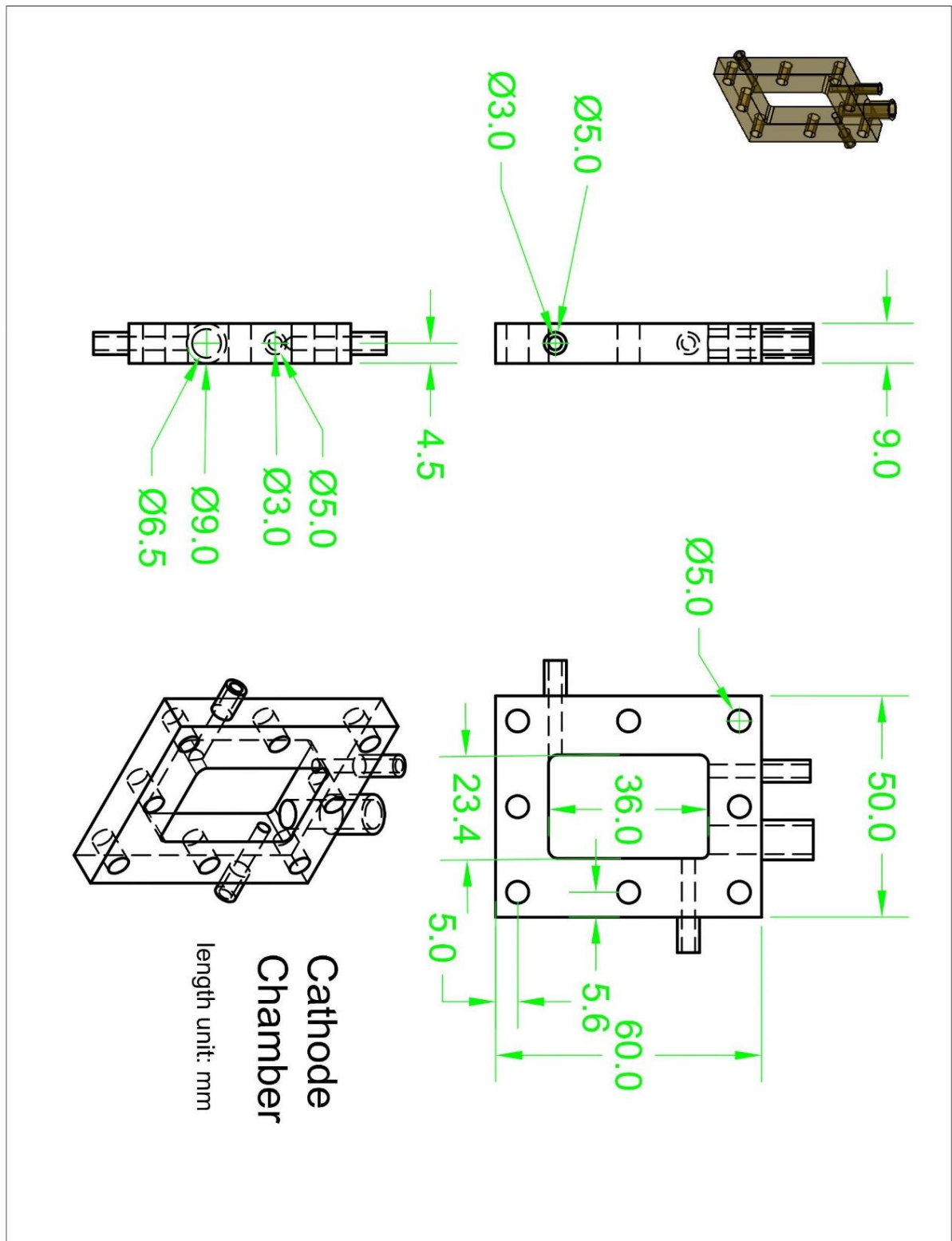


Figure AIII-4 The design drawing of the cathode chamber with dimensions.

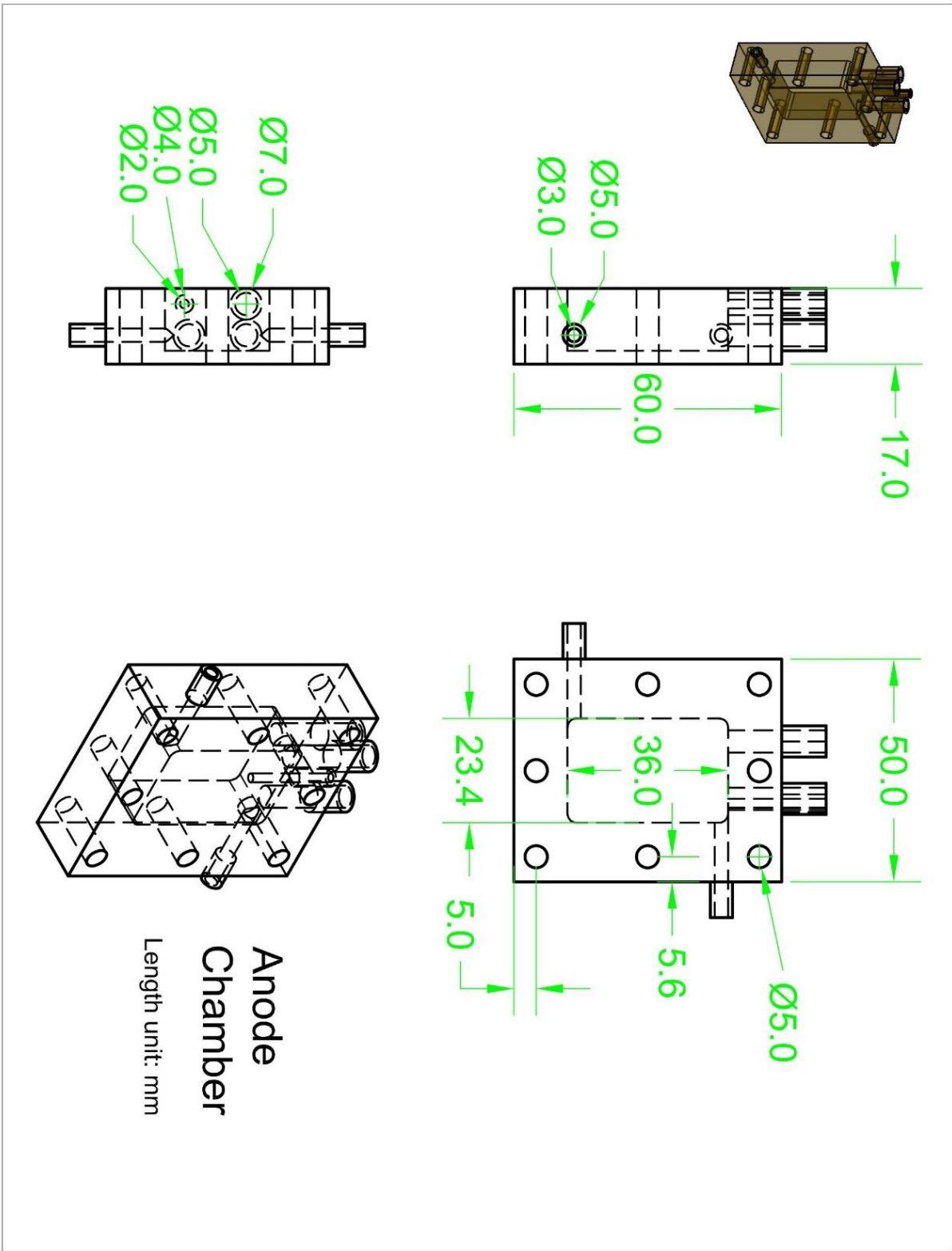


Figure AIII-5 The design drawing of the anode chamber with dimensions.

Appendix IV Supplementary Information of Chapter 4, 5, and 6

Table AIV-1 The a) absolute Faradaic efficiencies (FEs) and b) normalized FEs of all the products and average current density (j) of eCO₂RRs in two-chamber (2C) cell and gas diffusion electrode (GDE) cell with various catholytes, at wide range of cathodic potentials (V vs. RHE). Random error is shown in brackets.

a)	Cathodic potential	Catholyte conc.	Absolute FE (random error)					j (mA cm ⁻²) (random error)
			H ₂	CO	HCOO ⁻	C ₂ H ₄	Ethanol	
2C cell KHCO ₃	-0.17 V	0.1 M	9.84%	0.00%	0.00%	0.00%	0.00%	-0.47
		0.5 M	4.77%	0.00%	0.00%	0.00%	0.00%	-0.50
		1.0 M	11.26%	0.00%	0.00%	0.00%	0.00%	-0.74
	-0.37 V	0.1 M	38.03% (0.00%)	0.00% (0.00%)	0.00% (0.00%)	0.00% (0.00%)	0.00% (0.00%)	-1.17 (0.00)
		0.5 M	35.67% (0.00%)	0.00% (0.00%)	0.00% (0.00%)	0.00% (0.00%)	0.00% (0.00%)	-1.16 (0.00)
		1.0 M	28.00% (0.00%)	0.00% (0.00%)	0.00% (0.00%)	0.00% (0.00%)	0.00% (0.00%)	-1.18 (0.00)
	-0.57 V	0.1 M	89.44% (1.19%)	1.74% (1.37%)	5.45% (0.18%)	0.00% (0.00%)	0.00% (0.00%)	-3.08 (0.24)
		0.5 M	93.05% (0.62%)	0.70% (0.20%)	2.25% (0.42%)	0.00% (0.00%)	0.00% (0.00%)	-6.53 (0.21)
		1.0 M	99.09% (0.54%)	0.25% (0.04%)	1.87% (0.50%)	0.00% (0.00%)	0.00% (0.00%)	-8.65 (0.15)
	-0.77 V	0.1 M	89.58% (0.30%)	1.38% (1.02%)	5.32% (0.72%)	0.00% (0.00%)	0.00% (0.00%)	-4.71 (0.30)
		0.5 M	95.23% (0.66%)	0.50% (0.08%)	2.27% (0.58%)	0.00% (0.00%)	0.00% (0.00%)	-15.22 (0.50)
		1.0 M	94.94% (0.21%)	0.20% (0.02%)	1.33% (0.19%)	0.00% (0.00%)	0.00% (0.00%)	-25.30 (1.82)
	-0.97 V	0.1 M	89.65% (0.32%)	0.30% (0.23%)	4.87% (0.55%)	0.00% (0.00%)	0.00% (0.00%)	-7.22 (0.01)
		0.5 M	95.48% (0.66%)	0.43% (0.33%)	2.09% (0.24%)	0.00% (0.00%)	0.00% (0.00%)	-22.30 (0.83)
		1.0 M	108.64% (0.51%)	0.22% (0.17%)	1.04% (0.68%)	0.00% (0.00%)	0.00% (0.00%)	-38.60 (1.43)
	-1.17 V	0.1 M	99.12% (1.70%)	0.14% (0.06%)	4.90% (1.65%)	0.00% (0.00%)	0.00% (0.00%)	-11.38 (0.57)
		0.5 M	99.84% (0.70%)	0.35% (0.21%)	1.80% (0.49%)	0.00% (0.00%)	0.00% (0.00%)	-38.80 (1.71)
		1.0 M	106.32% (0.14%)	0.00% (0.00%)	0.97% (0.14%)	0.00% (0.00%)	0.00% (0.00%)	-52.30 (3.10)

GDE cell KHCO_3	-0.17 V	0.1 M	7.67% (0.86%)	0.33% (0.85%)	0.00% (0.00%)	0.00% (0.00%)	0.00% (0.00%)	-0.19 (0.03)
		0.5 M	10.78%	0.50%	0.00%	0.00%	0.00%	-0.48
		1.0 M	11.43% (0.41%)	0.65% (0.41%)	0.00% (0.00%)	0.00% (0.00%)	0.00% (0.00%)	-0.67 (0.04)
	-0.37 V	0.1 M	21.13% (1.02%)	1.66% (1.02%)	0.00% (0.00%)	0.00% (0.00%)	0.00% (0.00%)	-0.85 (0.07)
		0.5 M	80.77%	16.94%	2.52%	0.00%	0.00%	-2.52
		1.0 M	75.25% (3.38%)	10.68% (3.05%)	9.10% (0.28%)	0.00% (0.00%)	0.00% (0.00%)	-4.60 (0.17)
	-0.57 V	0.1 M	62.59% (2.77%)	26.11% (2.77%)	0.00% (0.00%)	0.00% (0.00%)	0.00% (0.00%)	-2.33 (0.01)
		0.5 M	67.25%	21.41%	7.32%	0.00%	0.00%	-7.33
		1.0 M	70.59% (0.10%)	16.96% (0.22%)	9.45% (0.31%)	0.00% (0.00%)	0.00% (0.00%)	-9.92 (0.12)
	-0.77 V	0.1 M	71.81% (3.57%)	11.62% (0.91%)	13.57% (2.66%)	0.00% (0.00%)	0.00% (0.00%)	-5.36 (0.09)
		0.5 M	70.15%	19.30%	9.48%	0.00%	0.00%	-16.30
		1.0 M	74.17% (0.40%)	23.09% (0.82%)	9.74% (0.43%)	0.00% (0.00%)	0.00% (0.00%)	-24.79 (1.12)
	-0.97 V	0.1 M	66.57% (0.27%)	20.55% (0.96%)	13.58% (0.68%)	0.00% (0.00%)	0.00% (0.00%)	-11.35 (0.36)
		0.5 M	56.57%	29.44%	18.91%	0.00%	0.00%	-30.08
		1.0 M	54.42% (1.43%)	32.05% (3.25%)	17.52% (1.83%)	0.00% (0.00%)	0.00% (0.00%)	-41.95 (1.11)
	-1.17 V	0.1 M	60.49% (2.52%)	24.21% (1.52%)	16.23% (1.01%)	0.00% (0.00%)	0.00% (0.00%)	-16.20 (1.07)
		0.5 M	47.12%	34.91%	19.59%	0.00%	0.00%	-45.50
		1.0 M	50.36% (0.31%)	38.64% (1.14%)	17.40% (1.34%)	3.21% (0.50%)	0.00% (0.00%)	-64.03 (5.65)
GDE cell KOH	-0.17 V	0.1 M	38.68%	10.75%	0.00%	0.00%	0.00%	-1.07
		0.5 M	48.53%	12.14%	16.50%	0.00%	0.00%	-3.47
		1.0 M	46.68% (0.04%)	12.89% (2.93%)	20.43% (2.97%)	0.00% (0.00%)	0.00% (0.00%)	-6.65 (0.38)
		2.0 M	34.47% (2.76%)	30.20% (2.17%)	15.51% (0.58%)	0.00% (0.00%)	0.00% (0.00%)	-6.74 (0.15)
	-0.37 V	0.1 M	58.77%	18.15%	9.99%	0.00%	0.00%	-2.80
		0.5 M	60.15%	21.02%	13.83%	0.00%	0.00%	-11.67
		1.0 M	49.27% (3.83%)	21.73% (3.06%)	19.00% (0.77%)	0.00% (0.00%)	0.00% (0.00%)	-23.60 (0.74)
		2.0 M	43.38% (3.18%)	39.87% (4.34%)	7.66% (1.16%)	0.00% (0.00%)	0.00% (0.00%)	-33.54 (0.10)

	-0.57 V	0.1 M	64.20%	21.50%	10.30%	0.00%	0.00%	-5.28
		0.5 M	54.72%	23.94%	14.57%	0.00%	0.00%	-23.65
		1.0 M	42.70% (1.35%)	36.66% (2.07%)	14.86% (0.72%)	0.00% (0.00%)	0.00% (0.00%)	-48.95 (0.32)
		2.0 M	43.11% (3.60%)	48.31% (0.16%)	12.90% (2.11%)	15.32% (2.28%)	2.37% (0.95%)	-77.30 (2.46)
	-0.77 V	0.1 M	64.05%	24.13%	9.82%	0.00%	0.00%	-8.39
		0.5 M	53.05%	27.36%	16.58%	0.00%	0.00%	-37.75
		1.0 M	34.22% (1.21%)	31.38% (1.61%)	17.16% (0.23%)	3.82% (1.18%)	8.32% (0.54%)	-80.92 (7.78)
		2.0 M	50.30% (2.84%)	25.53% (4.19%)	12.99% (3.90%)	32.55% (2.80%)	8.63% (0.34%)	-128.43 (2.25)
	-0.97 V	0.1 M	54.45%	37.51%	14.04%	0.00%	0.00%	-12.17
		0.5 M	33.27%	43.02%	17.78%	4.94%	0.23%	-53.73
		1.0 M	37.39% (1.39%)	32.10% (0.88%)	11.45% (0.82%)	27.25% (1.26%)	9.82% (0.95%)	-120.31 (3.92)
		2.0 M	33.72% (4.66%)	19.67% (1.56%)	7.58% (2.54%)	22.92% (1.45%)	5.41% (2.22%)	-185.88 (2.74)
	-1.17 V	0.1 M	49.24%	38.57%	16.20%	0.00%	0.00%	-15.40
		0.5 M	38.60%	54.50%	17.75%	8.89%	1.25%	-66.53
		1.0 M	35.51% (3.06%)	24.27% (4.04%)	10.52% (3.17%)	22.28% (4.34%)	9.13% (0.20%)	-152.37 (3.44)
		2.0 M	51.69% (1.94%)	15.80% (3.05%)	4.12% (2.02%)	38.63% (1.65%)	6.26% (1.48%)	-234.05 (16.70)

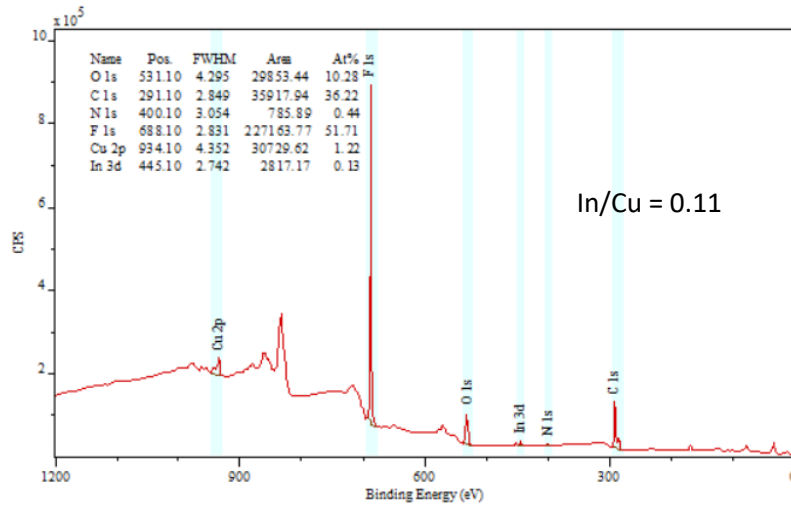
b)	Cathodic potential	Catholyte conc.	Normalised FE (random error)					j (mA cm ⁻²) (random error)
			H ₂	CO	HCOO ⁻	C ₂ H ₄	Ethanol	
2C cell KHCO ₃	-0.37 V	0.1 M	100.00% (0.00%)	0.00% (0.00%)	0.00% (0.00%)	0.00% (0.00%)	0.00% (0.00%)	-1.17 (0.00)
		0.5 M	100.00% (0.00%)	0.00% (0.00%)	0.00% (0.00%)	0.00% (0.00%)	0.00% (0.00%)	-1.16 (0.00)
		1.0 M	100.00% (0.00%)	0.00% (0.00%)	0.00% (0.00%)	0.00% (0.00%)	0.00% (0.00%)	-1.18 (0.00)
	-0.57 V	0.1 M	92.75% (1.19%)	1.80% (1.37%)	5.45% (0.18%)	0.00% (0.00%)	0.00% (0.00%)	-3.08 (0.24)
		0.5 M	97.02% (0.62%)	0.73% (0.20%)	2.25% (0.42%)	0.00% (0.00%)	0.00% (0.00%)	-6.53 (0.21)
		1.0 M	97.88% (0.54%)	0.25% (0.04%)	1.87% (0.50%)	0.00% (0.00%)	0.00% (0.00%)	-8.65 (0.15)
	-0.77 V	0.1 M	93.24%	1.44%	5.32%	0.00%	0.00%	-4.71

			(0.30%)	(1.02%)	(0.72%)	(0.00%)	(0.00%)	(0.30)	
		0.5 M	97.22% (0.66%)	0.51% (0.08%)	2.27% (0.58%)	0.00% (0.00%)	0.00% (0.00%)	-15.22 (0.50)	
		1.0 M	98.46% (0.21%)	0.21% (0.02%)	1.33% (0.19%)	0.00% (0.00%)	0.00% (0.00%)	-25.30 (1.82)	
	-0.97 V	0.1 M	94.82% (0.32%)	0.31% (0.23%)	4.87% (0.55%)	0.00% (0.00%)	0.00% (0.00%)	-7.22 (0.01)	
		0.5 M	97.56% (0.66%)	0.44% (0.33%)	2.09% (0.24%)	0.00% (0.00%)	0.00% (0.00%)	-22.30 (0.83)	
		1.0 M	98.76% (0.51%)	0.20% (0.17%)	1.04% (0.68%)	0.00% (0.00%)	0.00% (0.00%)	-38.60 (1.43)	
	-1.17 V	0.1 M	94.96% (1.70%)	0.13% (0.06%)	4.90% (1.65%)	0.00% (0.00%)	0.00% (0.00%)	-11.38 (0.57)	
		0.5 M	97.85% (0.70%)	0.35% (0.21%)	1.80% (0.49%)	0.00% (0.00%)	0.00% (0.00%)	-38.80 (1.71)	
		1.0 M	99.03% (0.14%)	0.00% (0.00%)	0.97% (0.14%)	0.00% (0.00%)	0.00% (0.00%)	-52.30 (3.10)	
	GDE cell KHCO ₃	-0.17 V	0.1 M	95.88% (0.86%)	4.12% (0.85%)	0.00% (0.00%)	0.00% (0.00%)	0.00% (0.00%)	-0.19 (0.03)
			0.5 M	95.59%	4.41%	0.00%	0.00%	0.00%	-0.48
			1.0 M	94.62% (0.41%)	5.38% (0.41%)	0.00% (0.00%)	0.00% (0.00%)	0.00% (0.00%)	-0.67 (0.04)
-0.37 V		0.1 M	92.70% (1.02%)	7.30% (1.02%)	0.00% (0.00%)	0.00% (0.00%)	0.00% (0.00%)	-0.85 (0.07)	
		0.5 M	80.58%	16.90%	2.52%	0.00%	0.00%	-2.52	
		1.0 M	79.60% (3.38%)	11.29% (3.05%)	9.10% (0.28%)	0.00% (0.00%)	0.00% (0.00%)	-4.60 (0.17)	
-0.57 V		0.1 M	70.57% (2.77%)	29.43% (2.77%)	0.00% (0.00%)	0.00% (0.00%)	0.00% (0.00%)	-2.33 (0.01)	
		0.5 M	70.30%	22.38%	7.32%	0.00%	0.00%	-7.33	
		1.0 M	73.01% (0.10%)	17.54% (0.22%)	9.45% (0.31%)	0.00% (0.00%)	0.00% (0.00%)	-9.92 (0.12)	
-0.77 V		0.1 M	74.39% (3.57%)	12.04% (0.91%)	13.57% (2.66%)	0.00% (0.00%)	0.00% (0.00%)	-5.36 (0.09)	
		0.5 M	70.99%	19.53%	9.48%	0.00%	0.00%	-16.30	
		1.0 M	68.83% (0.40%)	21.43% (0.82%)	9.74% (0.43%)	0.00% (0.00%)	0.00% (0.00%)	-24.79 (1.12)	
-0.97 V	0.1 M	66.03% (0.27%)	20.39% (0.96%)	13.58% (0.68%)	0.00% (0.00%)	0.00% (0.00%)	-11.35 (0.36)		
	0.5 M	59.33%	27.76%	18.91%	0.00%	0.00%	-30.08		
	1.0 M	54.90% (1.43%)	27.57% (3.25%)	17.52% (1.83%)	0.00% (0.00%)	0.00% (0.00%)	-41.95 (1.11)		

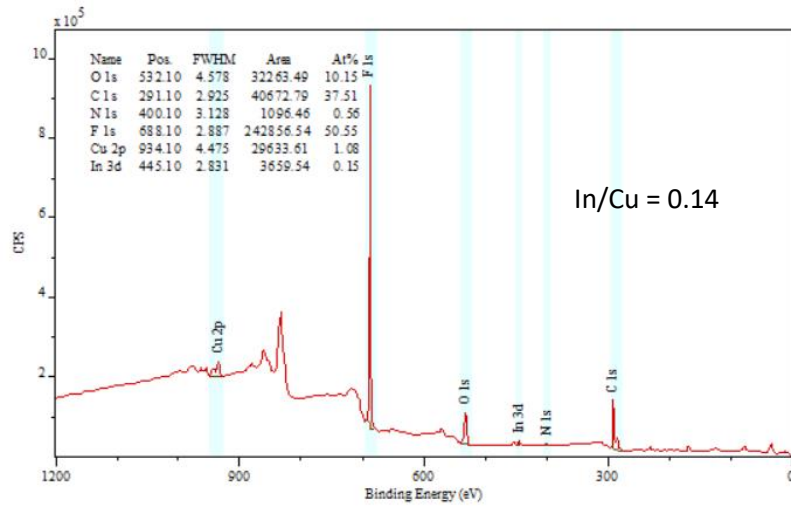
GDE cell KOH	-1.17 V	0.1 M	59.82% (2.52%)	23.94% (1.52%)	16.23% (1.01%)	0.00% (0.00%)	0.00% (0.00%)	-16.20 (1.07)	
		0.5 M	46.19%	34.22%	19.59%	0.00%	0.00%	-45.50	
		1.0 M	46.92% (0.31%)	32.46% (1.14%)	17.40% (1.34%)	3.21% (0.50%)	0.00% (0.00%)	-64.03 (5.65)	
	-0.17 V	0.1 M	78.25%	21.75%	0.00%	0.00%	0.00%	-1.07	
		0.5 M	66.79%	16.71%	16.50%	0.00%	0.00%	-3.47	
		1.0 M	62.35% (0.04%)	17.22% (2.93%)	20.43% (2.97%)	0.00% (0.00%)	0.00% (0.00%)	-6.65 (0.38)	
		2.0 M	45.03% (2.76%)	39.45% (2.17%)	15.51% (0.58%)	0.00% (0.00%)	0.00% (0.00%)	-6.74 (0.15)	
	-0.37 V	0.1 M	68.77%	21.24%	9.99%	0.00%	0.00%	-2.80	
		0.5 M	63.85%	22.31%	13.83%	0.00%	0.00%	-11.67	
		1.0 M	56.21% (3.83%)	24.79% (3.06%)	19.00% (0.77%)	0.00% (0.00%)	0.00% (0.00%)	-23.60 (0.74)	
		2.0 M	48.12% (3.18%)	44.22% (4.34%)	7.66% (1.16%)	0.00% (0.00%)	0.00% (0.00%)	-33.54 (0.10)	
	-0.57 V	0.1 M	67.20%	22.50%	10.30%	0.00%	0.00%	-5.28	
0.5 M		59.43%	26.00%	14.57%	0.00%	0.00%	-23.65		
1.0 M		45.81% (1.35%)	39.33% (2.07%)	14.86% (0.72%)	0.00% (0.00%)	0.00% (0.00%)	-48.95 (0.32)		
2.0 M		34.22% (3.60%)	38.35% (0.16%)	12.90% (2.11%)	12.16% (2.28%)	2.37% (0.95%)	-77.30 (2.46)		
-0.77 V	0.1 M	65.50%	24.68%	9.82%	0.00%	0.00%	-8.39		
	0.5 M	55.03%	28.38%	16.58%	0.00%	0.00%	-37.75		
	1.0 M	36.73% (1.21%)	33.68% (1.61%)	17.16% (0.23%)	4.10% (1.18%)	8.32% (0.54%)	-80.92 (7.78)		
	2.0 M	36.38% (2.84%)	18.47% (4.19%)	12.99% (3.90%)	23.54% (2.80%)	8.63% (0.34%)	-128.43 (2.25)		
-0.97 V	0.1 M	50.90%	35.06%	14.04%	0.00%	0.00%	-12.17		
	0.5 M	33.58%	43.42%	17.78%	4.98%	0.23%	-53.73		
	1.0 M	30.43% (1.39%)	26.12% (0.88%)	11.45% (0.82%)	22.18% (1.26%)	9.82% (0.95%)	-120.31 (3.92)		
	2.0 M	38.45% (4.66%)	22.43% (1.56%)	7.58% (2.54%)	26.14% (1.45%)	5.41% (2.22%)	-185.88 (2.74)		
-1.17 V	0.1 M	46.99%	36.81%	16.20%	0.00%	0.00%	-15.40		
	0.5 M	30.66%	43.28%	17.75%	7.06%	1.25%	-66.53		
	1.0 M	34.77% (3.06%)	23.77% (4.04%)	10.52% (3.17%)	21.82% (4.34%)	9.13% (0.20%)	-152.37 (3.44)		
	2.0 M	43.65% (1.94%)	13.34% (3.05%)	4.12% (2.02%)	32.63% (1.65%)	6.26% (1.48%)	-234.05 (16.70)		

(a) **CuIn-ESP15min Average In/Cu atom ratio = 0.12**

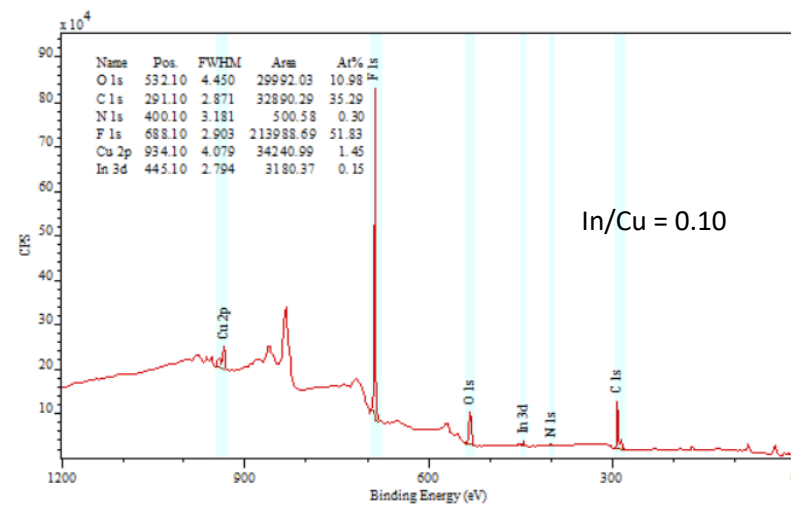
Point 1



Point 2

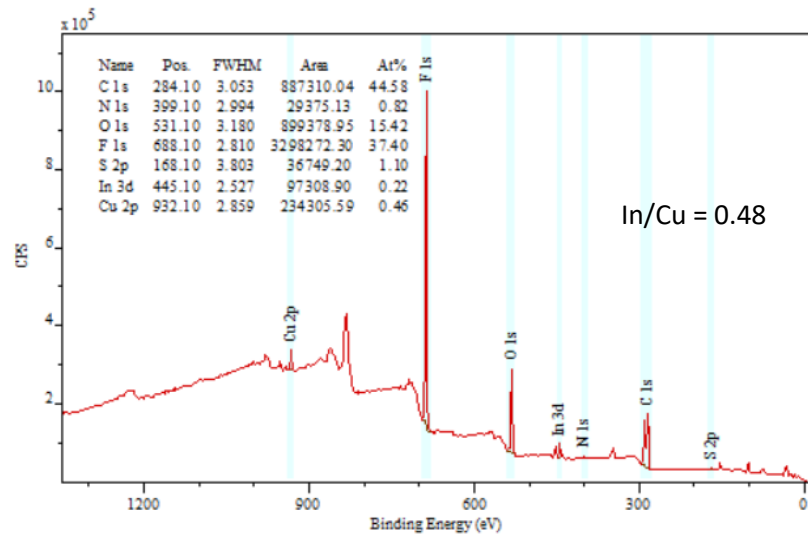


Point 3

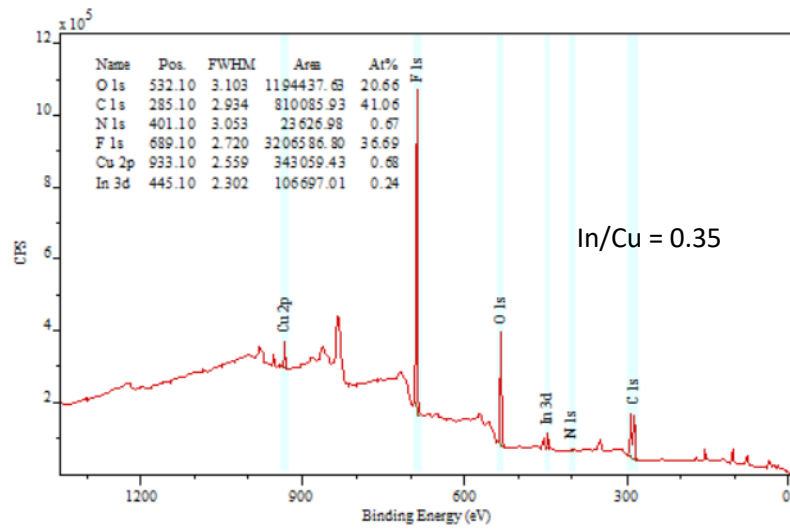


(b) **CuIn-ESP25min Average In/Cu atom ratio = 0.44**

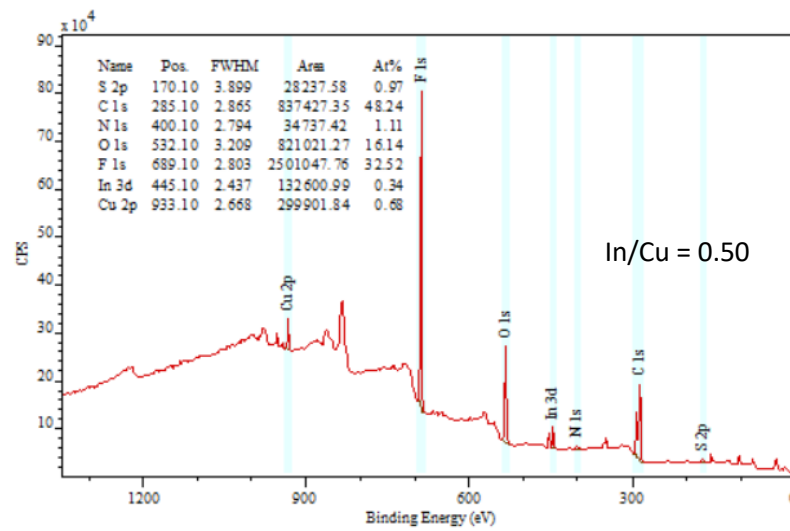
Point 1



Point 2

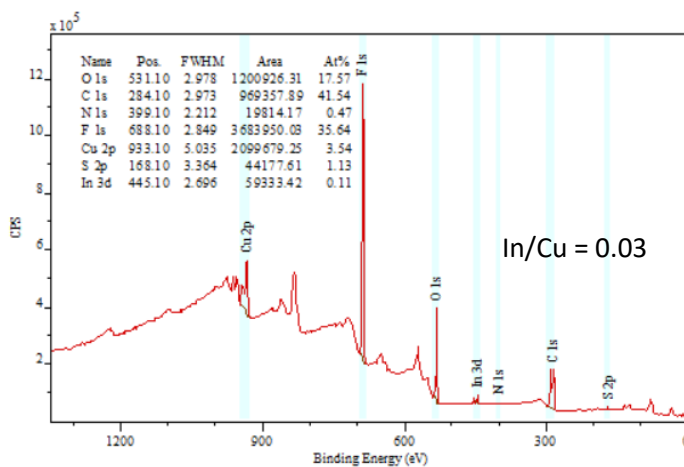


Point 3

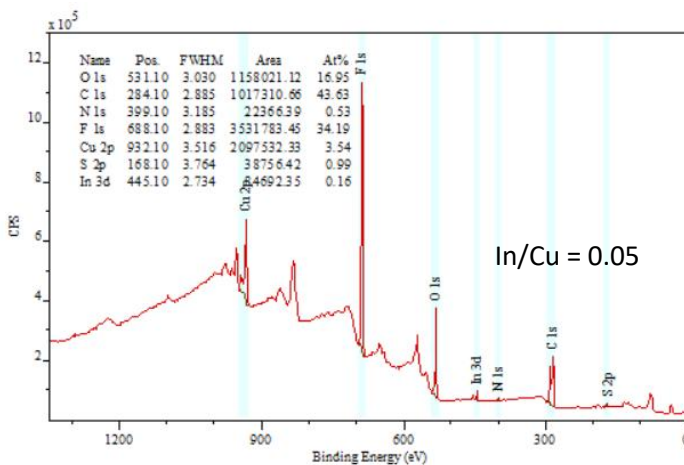


(c) **CuIn-ESP2h Average In/Cu atom ratio = 0.03**

Point 1



Point 2



Point 3

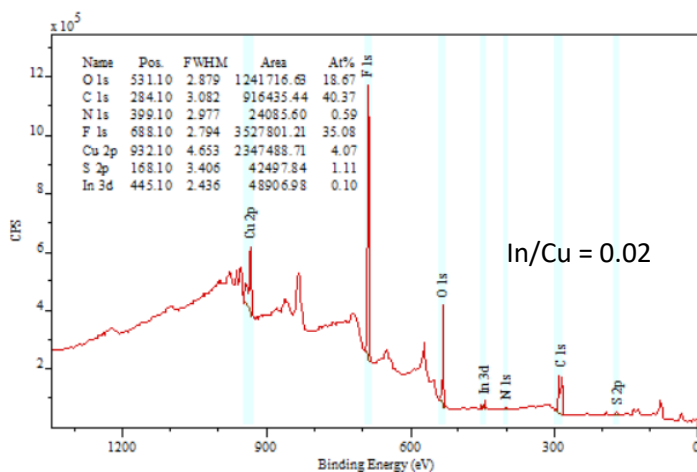


Figure AIV-1 Multi-point quantification analysis on XPS survey spectrum of a) CuIn-ESP15min, b) CuIn-ESP25min, and c) CuIn-ESP2h.

Table AIV-2 Calculations on half-cell reduction potentials (in reduction form) involved in ESP process at standard state. Gibbs–Helmholtz equation, Nernst equation were used based on the database from Outokumpu HSC Chemistry 6.0 software.

Half-cell Reactions	ΔH_r^\ominus (KJ)	ΔS_r^\ominus (J K ⁻¹)	ΔG_r^\ominus (KJ)	E^0 (V vs. SHE)
$In^{3+} + 3e^- \rightarrow In$	104.60	125.2	67.265	-0.233
$2CuO + 2e^- + 2H^+ \rightarrow Cu_2O + H_2O$	-144.83	-53.66	-128.83	0.668
$Cu_2O + 2e^- + 2H^+ \rightarrow 2Cu + H_2O$	-115.23	-86.98	-89.297	0.463
$\Delta G_r^\ominus = \Delta H_r^\ominus - T\Delta S_r^\ominus$ $E^0 = -\frac{\Delta G_r^\ominus}{zF}$	ΔH_r^\ominus : change in enthalpy at standard state ΔS_r^\ominus : change in entropy at standard state ΔG_r^\ominus : change in the Gibbs free energy at standard state E^0 : standard half-cell reduction potential z : the number of electrons transferred in the half-cell reaction F : Faradaic constant, 96485 C mol ⁻¹ . T : temperature, here is 298.15 K			

Table AIV-3 The practical production amounts of all the gas and liquid products of eCO₂RR catalysed by Cu₂O, CuIn-ESP5min, CuIn-ESP15min, CuIn-ESP25min, CuIn-ESP35min and CuIn-ESP2h.

	Cathode potential (V vs RHE)	Current density (mA/cm ²)	Percentages of gas products in tail gas				Yields of liquid products (mg/min)	
			H ₂ %	CO %	C ₂ H ₄ %	CO ₂ %	Formate	Ethanol
Cu ₂ O	-0.17	-5.43	0.19	0.13	0.00	99.68	0.0366	0.000
	-0.37	-20.20	0.70	0.47	0.00	98.84	0.1525	0.000
	-0.57	-48.60	1.91	1.24	0.04	96.80	0.3387	0.005
	-0.77	-96.1	3.58	2.01	0.22	94.19	0.5853	0.015
	-0.97	-139	5.75	2.95	0.36	90.95	0.7446	0.023
	-1.17	-208	11.06	4.58	0.77	83.58	0.8558	0.040
CuIn-ESP5min	-0.17	-5.25	0.10	0.24	0.00	99.66	0.0190	0.000
	-0.37	-27.56	0.65	1.77	0.00	97.58	0.0937	0.000
	-0.57	-56.72	1.26	3.12	0.05	95.58	0.2782	0.009
	-0.77	-96.63	1.86	3.36	0.21	94.56	0.4781	0.019
	-0.97	-140.28	3.14	6.36	0.47	90.03	0.7035	0.029
	-1.17	-213.75	5.12	7.62	0.89	86.36	0.9102	0.051
CuIn-ESP15min	-0.17	-5.92	0.15	0.37	0.00	99.48	0.0221	0.000
	-0.37	-29.23	0.61	1.78	0.00	97.62	0.0922	0.000
	-0.57	-59.40	1.04	3.22	0.02	95.73	0.2338	0.001
	-0.77	-94	1.53	5.10	0.04	93.33	0.3528	0.004
	-0.97	-135.99	2.56	8.25	0.15	89.04	0.5125	0.010
	-1.17	-214.12	5.13	12.50	0.43	81.94	0.7436	0.028
CuIn-ESP25min	-0.17	-4.25	0.02	0.35	0.00	99.64	0.0024	0.000
	-0.37	-24.68	0.10	2.06	0.00	97.85	0.0197	0.000
	-0.57	-58.40	0.27	4.92	0.00	94.81	0.0512	0.000
	-0.77	-92.00	0.43	7.73	0.02	91.82	0.0750	0.007
	-0.97	-134.84	0.53	11.54	0.07	87.86	0.1026	0.013
	-1.17	-193.45	1.14	16.85	0.30	81.70	0.1218	0.049
CuIn-ESP35min	-0.17	-4.40	0.14	0.29	0.00	99.58	0.0132	0.000
	-0.37	-23.48	0.41	1.61	0.00	97.98	0.0665	0.000
	-0.57	-55.23	0.85	3.23	0.00	95.92	0.1655	0.000
	-0.77	-99.175	2.00	6.63	0.02	91.35	0.2848	0.009
	-0.97	-145.7	2.76	8.62	0.10	88.52	0.4427	0.018
	-1.17	-200.125	4.41	12.60	0.27	82.73	0.5946	0.033

CuIn-ESP2h	-0.17	-4.74	0.07	0.30	0.00	99.63	0.0178	0.000
	-0.37	-22.98	0.50	1.43	0.00	98.06	0.0980	0.000
	-0.57	-53.71	1.20	3.16	0.00	95.64	0.2171	0.000
	-0.77	-89.6	2.72	5.27	0.02	91.99	0.3949	0.003
	-0.97	-130.205	3.68	7.00	0.06	89.26	0.5303	0.006
	-1.17	-208.39	5.59	10.61	0.23	83.57	0.7960	0.033

Table AIV-4 Normalized Faradaic efficiencies (FEs) of all the products and current density (j) of eCO₂RRs using different catalysts in gas diffusion electrode (GDE) cell with 1 M KOH catholyte, at wide range of cathodic potentials (V vs. RHE). Random error is shown in brackets.

Cathodic potential	Catalyst	FE (random error)			j (mA cm ⁻²) (random error)
		H ₂	CO	HCOO ⁻	
-0.63 V	C	46.77% (3.95%)	12.39% (6.24%)	40.84% (10.19%)	-7.36 (1.97)
	SnO ₂ /C(0.5)	4.96% (0.97%)	33.77% (6.57%)	61.27% (7.54%)	-13.84 (6.23)
	SnO ₂ /C(1.0)	3.44% (1.27%)	31.38% (2.71%)	65.18% (1.44%)	-22.30 (3.68)
	SnO ₂ /C(3.5)	4.47% (2.24%)	17.11% (7.93%)	78.42% (5.69%)	-31.72 (2.10)
	SnO ₂	17.09% (6.35%)	12.08% (10.05%)	70.83% (16.40%)	-28.20 (1.94)
-0.83 V	C	50.29% (3.62%)	15.82% (2.49%)	33.89% (1.13%)	-25.93 (2.16)
	SnO ₂ /C(0.5)	5.28% (1.09%)	34.03% (3.04%)	60.69% (4.13%)	-36.58 (0.30)
	SnO ₂ /C(1.0)	1.76% (4.08%)	27.42% (7.22%)	70.82% (3.14%)	-40.80 (10.08)
	SnO ₂ /C(3.5)	4.26% (0.87%)	18.35% (8.10%)	77.39% (7.23%)	-68.12 (0.28)
	SnO ₂	15.54% (2.10%)	14.29% (10.32%)	70.17% (12.42%)	-44.56 (8.18)
-1.03 V	C	48.58% (1.13%)	18.99% (3.00%)	32.43% (4.13%)	-59.83 (9.20)
	SnO ₂ /C(0.5)	3.83% (1.06%)	20.28% (3.99%)	75.89% (2.93%)	-72.35 (2.62)
	SnO ₂ /C(1.0)	1.72% (2.67%)	22.25% (4.52%)	76.03% (1.85%)	-126.95 (6.64)
	SnO ₂ /C(3.5)	3.83% (2.67%)	18.44% (4.52%)	77.72% (1.85%)	-123.74 (6.64)

		(1.17%)	(1.92%)	(0.74%)	(4.08)
	SnO ₂	21.40% (2.91%)	10.34% (5.59%)	68.26% (2.68%)	-106.63 (15.76)
-1.23 V	C	48.56% (6.71%)	25.19% (6.24%)	26.25% (0.47%)	-85.60 (3.11)
	SnO ₂ /C(0.5)	1.00% (1.29%)	25.18% (2.72%)	73.82% (1.43%)	-125.48 (24.15)
	SnO ₂ /C(1.0)	1.60% (2.44%)	17.51% (2.11%)	80.89% (4.55%)	-195.00 (5.73)
	SnO ₂ /C(3.5)	2.95% (1.02%)	16.71% (1.13%)	80.34% (2.15%)	-209.05 (13.11)
	SnO ₂	23.81% (0.82%)	13.42% (1.13%)	62.77% (1.95%)	-174.05 (18.41)
-1.43 V	C	57.66% (1.51%)	19.87% (0.55%)	22.47% (2.06%)	-119.04 (6.85)
	SnO ₂ /C(0.5)	2.44% (0.59%)	14.29% (6.29%)	83.27% (6.88%)	-156.78 (23.64)
	SnO ₂ /C(1.0)	2.47% (1.41%)	16.18% (2.68%)	81.35% (4.09%)	-247.00 (8.94)
	SnO ₂ /C(3.5)	4.16% (0.04%)	11.51% (4.22%)	84.33% (4.18%)	-251.00 (8.43)
	SnO ₂	37.55% (0.78%)	7.21% (1.18%)	55.24% (1.96%)	-235.11 (5.62)

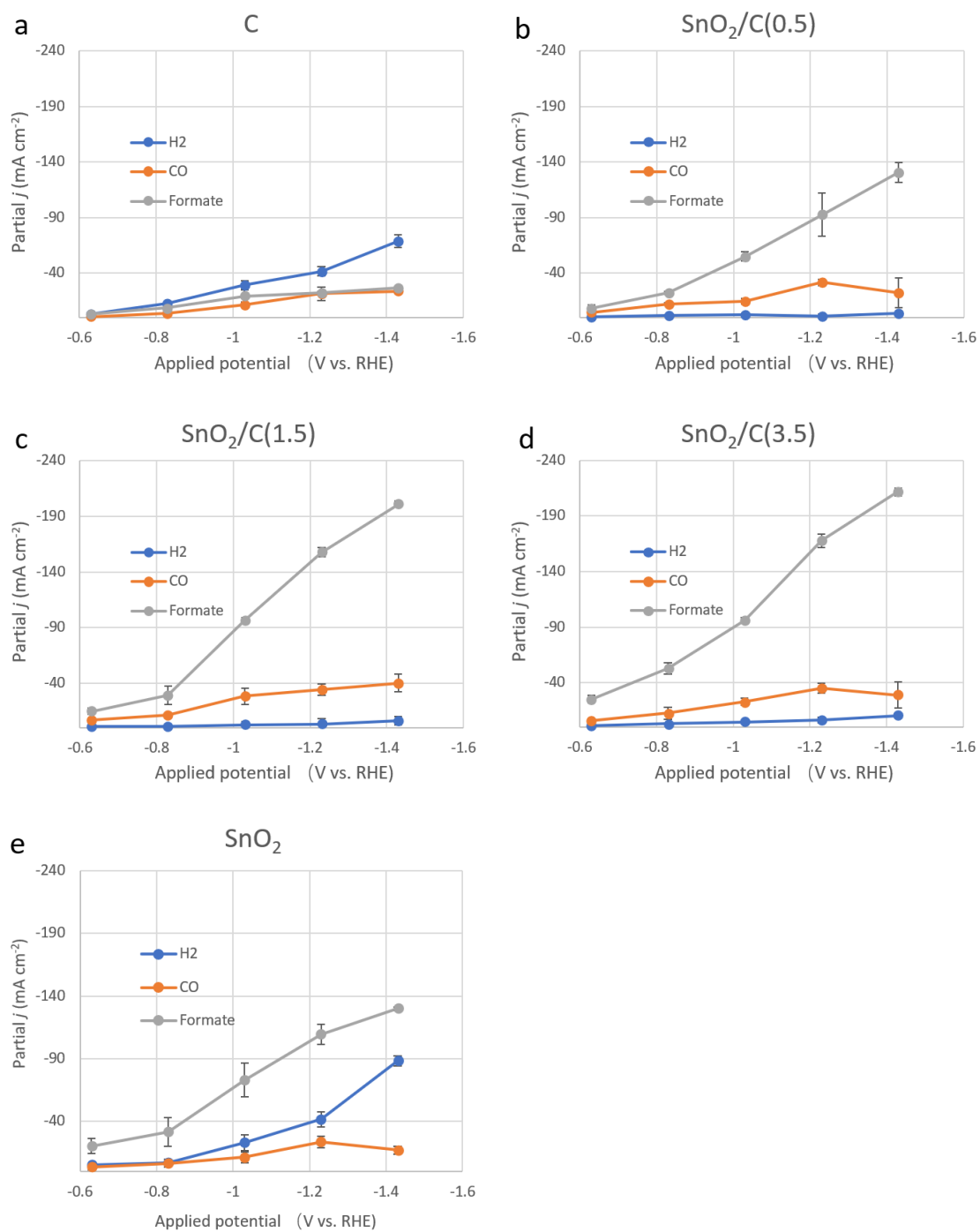


Figure AIV-2 Partial current densities to produce H₂, CO, and format from eCO₂RR as a function of the applied potential for different catalysts: a) C, b) SnO₂/C(0.5), c) SnO₂/C(1.5), d) SnO₂/C(3.5), e) SnO₂.

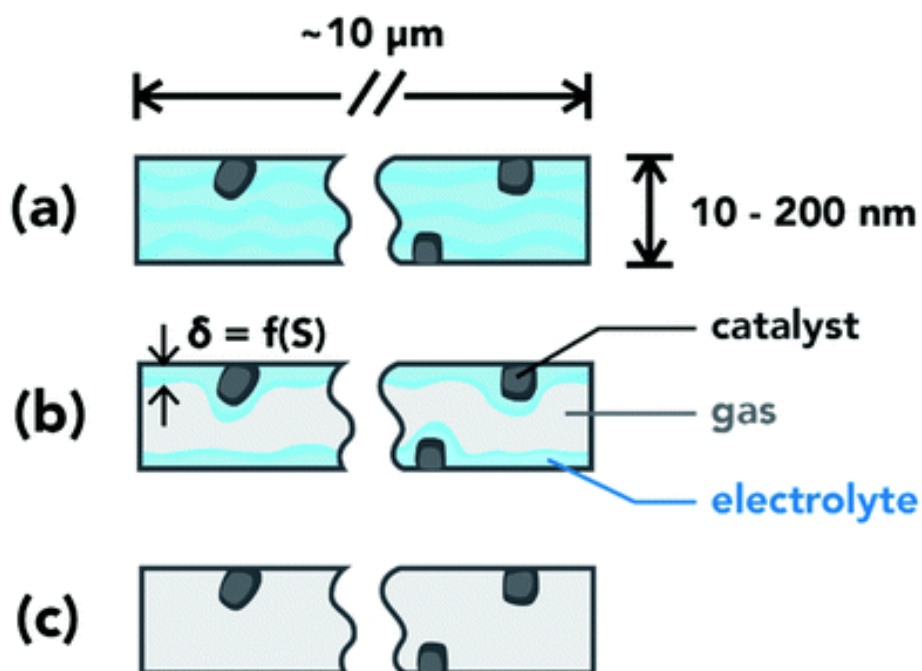


Figure AIV-3 Schematic of pore conditions in the catalyst layer. (a) Flooded pore: pore volume filled with electrolyte. (b) Wetted pore: a thin layer of electrolyte covers the pore walls. (c) Dry pore: catalyst inactive due to lack of an ionic pathway. Reproduced from Ref. ¹⁹⁸ with permission from the PCCP Owner Societies.

Table AIV-5 Calculations on half-cell reduction potentials (in reduction form) involved in formate fuel cell when formate concentration is 0.5 M at pH=14, 60 °C. Gibbs–Helmholtz equation, Nernst equation were used based on the database from Outokumpu HSC Chemistry 6.0 software.

Redox reactions	ΔH_r^\ominus (KJ)	ΔS_r^\ominus (J K ⁻¹)	ΔG_r^\ominus (KJ)	E ⁰ (V vs SHE)	E (V vs SHE)
Anode half-cell: $CO_2 + 2H_2O + 2e^- \rightarrow HCOOH + 2OH^-$	79.689	-343.01	181.96	-0.944	-0.954
Cathode half-cell $\frac{1}{2}O_2 + H_2O + 2e^- \rightarrow 2OH^-$	-174.22	-324.63	-77.43	+0.402	+0.402
Full-cell $HCOOH + \frac{1}{2}O_2 \rightarrow CO_2 + H_2O$	-253.91	18.39	-259.39	_____	1.356
$\Delta G_r^\ominus = \Delta H_r^\ominus - T\Delta S_r^\ominus$ $E^0 = -\frac{\Delta G_r^\ominus}{zF}$ $E = E^0 + \frac{RT}{zF} \ln \frac{a_{Ox}}{a_{Red}}$	<p>ΔH_r^\ominus: change in enthalpy at standard state ΔS_r^\ominus: change in entropy at standard state ΔG_r^\ominus: change in the Gibbs free energy at standard state E^0: standard half-cell reduction potential E: half-cell reduction potential z: the number of electrons transferred in the half-cell reaction F: Faradaic constant, 96485 C mol⁻¹. R: gas constant, 8.413 T: temperature, here is 298.15 K a_{Ox}/a_{Red}: chemical activity of the oxidized/reduced form, for solid or pure phase, $a=1$; for ions in solution, a can be related to ion concentration.</p>				

References

1. NASA's Jet Propulsion Laboratory Global Temperature Anomaly. <https://climate.nasa.gov/vital-signs/global-temperature/>.
2. Earth, , C. Atmospheric CO2 Growth. <https://www.co2.earth/co2-acceleration>.
3. Dimitrov, R. S., The Paris agreement on climate change: Behind closed doors. *Global Environmental Politics* **2016**, *16* (3), 1-11.
4. Hoekstra, A.; Vijayashankar, A.; Sundrani, V. L. In *Modelling the Total Cost of Ownership of Electric Vehicles in the Netherlands*, 30th International Electric Vehicle Symposium and Exhibition, EVS 2017, 2017.
5. Lund, P. D., Implications of Finland's plan to ban coal and cutting oil use. *Energy Policy* **2017**, *108*, 78-80.
6. Shell Sky Scenario https://www.shell.com/promos/business-customers-promos/download-latest-scenario-sky/_jcr_content.stream/1530643931055/eca19f7fc0d20adbe830d3b0b27bcc9ef72198f5/shell-scenario-sky.pdf.
7. Roberts, D. Shell's vision of a zero carbon world by 2070, explained. <https://www.vox.com/energy-and-environment/2018/3/30/17171370/shell-oil-climate-change-carbon-2070>.
8. Boffey, D. Empty North Sea gas fields to be used to bury 10m tonnes of CO2. <https://www.theguardian.com/environment/2019/may/09/empty-north-sea-gas-fields-bury-10m-tonnes-co2-eu-ports>.
9. Song, C., CO2 conversion and utilization: an overview. ACS Publications: 2002.
10. Pérez-Fortes, M.; Tzimas, E., Techno-economic and environmental evaluation of CO2 utilisation for fuel production. *JRC Science Hub: ZG Petten, The Netherlands* **2016**.
11. Metcalf, G. E.; Weisbach, D., The design of a carbon tax. *Harv. Envtl. L. Rev.* **2009**, *33*, 499.
12. Ma, J.; Sun, N.; Zhang, X.; Zhao, N.; Xiao, F.; Wei, W.; Sun, Y., A short review of catalysis for CO2 conversion. *Catalysis Today* **2009**, *148* (3-4), 221-231.
13. Hu, B.; Guild, C.; Suib, S. L., Thermal, electrochemical, and photochemical conversion of CO2 to fuels and value-added products. *J. CO2 Util.* **2013**, *1*, 18-27.

14. Yang, Z.-Z.; He, L.-N.; Gao, J.; Liu, A.-H.; Yu, B., Carbon dioxide utilization with C–N bond formation: carbon dioxide capture and subsequent conversion. *Energy Environ. Sci.* **2012**, *5* (5), 6602-6639.
15. Saeidi, S.; Amin, N. A. S.; Rahimpour, M. R., Hydrogenation of CO₂ to value-added products—A review and potential future developments. *J. CO₂ Util.* **2014**, *5*, 66-81.
16. Cole, A.; Dinburg, Y.; Haynes, B. S.; He, Y.; Herskowitz, M.; Jazrawi, C.; Landau, M.; Liang, X.; Magnusson, M.; Maschmeyer, T., From macroalgae to liquid fuel via wastewater remediation, hydrothermal upgrading, carbon dioxide hydrogenation and hydrotreating. *Energy Environ. Sci.* **2016**, *9* (5), 1828-1840.
17. Qiao, J.; Liu, Y.; Zhang, J., *Electrochemical reduction of carbon dioxide: fundamentals and technologies*. CRC Press: 2016.
18. Song, J. T.; Song, H.; Kim, B.; Oh, J., Towards Higher Rate Electrochemical CO₂ Conversion: From Liquid-Phase to Gas-Phase Systems. *Catalysts* **2019**, *9* (3), 224.
19. Sun, Z.; Ma, T.; Tao, H.; Fan, Q.; Han, B., Fundamentals and challenges of electrochemical CO₂ reduction using two-dimensional materials. *Chem* **2017**, *3* (4), 560-587.
20. Nahar, S.; Zain, M.; Kadhum, A.; Hasan, H.; Hasan, M., Advances in photocatalytic CO₂ reduction with water: a review. *Materials* **2017**, *10* (6), 629.
21. Halmann, M., Photoelectrochemical reduction of aqueous carbon dioxide on p-type gallium phosphide in liquid junction solar cells. *Nature* **1978**, *275* (5676), 115.
22. Li, K.; An, X.; Park, K. H.; Khraisheh, M.; Tang, J., A critical review of CO₂ photoconversion: Catalysts and reactors. *Catalysis Today* **2014**, *224*, 3-12.
23. Martín, A. J.; Larrazábal, G. O.; Pérez-Ramírez, J., Towards sustainable fuels and chemicals through the electrochemical reduction of CO₂: lessons from water electrolysis. *Green Chem.* **2015**, *17* (12), 5114-5130.
24. Zhu, D. D.; Liu, J. L.; Qiao, S. Z., Recent advances in inorganic heterogeneous electrocatalysts for reduction of carbon dioxide. *Adv. Mater.* **2016**, *28* (18), 3423-3452.
25. Qiao, J.; Liu, Y.; Zhang, J., *Electrochemical Reduction of Carbon Dioxide: Fundamentals and Technologies*. CRC Press: 2016; Vol. 11.
26. Sullivan, B. P.; Krist, K.; Guard, H., *Electrochemical and electrocatalytic reactions of carbon dioxide*. Elsevier: 2012.

27. Armand, J.; Bellec, C.; Boulares, L.; Pinson, J., Electrochemical reductive carboxylation: reduction of unsaturated compounds in the presence of methyl chloroformate. *The Journal of Organic Chemistry* **1983**, *48* (17), 2847-2853.
28. Bard, A. J.; Faulkner, L. R.; Leddy, J.; Zoski, C. G., *Electrochemical methods: fundamentals and applications*. Wiley New York: 1980; Vol. 2.
29. Nørskov, J. K.; Bligaard, T.; Logadottir, A.; Kitchin, J.; Chen, J. G.; Pandelov, S.; Stimming, U., Trends in the exchange current for hydrogen evolution. *J. Electrochem. Soc.* **2005**, *152* (3), J23-J26.
30. Seh, Z. W.; Kibsgaard, J.; Dickens, C. F.; Chorkendorff, I.; Nørskov, J. K.; Jaramillo, T. F., Combining theory and experiment in electrocatalysis: Insights into materials design. *Science* **2017**, *355* (6321), eaad4998.
31. Endrődi, B.; Bencsik, G.; Darvas, F.; Jones, R.; Rajeshwar, K.; Janáky, C., Continuous-flow electroreduction of carbon dioxide. *Prog. Energy Combust. Sci.* **2017**, *62*, 133-154.
32. Zhang, L.; Zhao, Z. J.; Gong, J., Nanostructured materials for heterogeneous electrocatalytic CO₂ reduction and their related reaction mechanisms. *Angew. Chem., Int. Ed.* **2017**, *56* (38), 11326-11353.
33. Wu, J.; Ma, S.; Sun, J.; Gold, J. I.; Tiwary, C.; Kim, B.; Zhu, L.; Chopra, N.; Odeh, I. N.; Vajtai, R., A metal-free electrocatalyst for carbon dioxide reduction to multi-carbon hydrocarbons and oxygenates. *Nat. Commun.* **2016**, *7*, 13869.
34. Lu, X.; Leung, D. Y.; Wang, H.; Xuan, J., A high performance dual electrolyte microfluidic reactor for the utilization of CO₂. *Applied Energy* **2017**, *194*, 549-559.
35. Ma, S.; Sadakiyo, M.; Luo, R.; Heima, M.; Yamauchi, M.; Kenis, P. J., One-step electrosynthesis of ethylene and ethanol from CO₂ in an alkaline electrolyzer. *Journal of Power Sources* **2016**, *301*, 219-228.
36. Xiang, H.; Rasul, S.; Scott, K.; Portoles, J.; Cumpson, P.; Eileen, H. Y., Enhanced selectivity of carbonaceous products from electrochemical reduction of CO₂ in aqueous media. *J. CO₂ Util.* **2019**, *30*, 214-221.
37. Hori, Y.; Murata, A.; Takahashi, R., Formation of hydrocarbons in the electrochemical reduction of carbon dioxide at a copper electrode in aqueous solution. *Journal of the Chemical Society, Faraday Transactions 1: Physical Chemistry in Condensed Phases* **1989**, *85* (8), 2309-2326.

38. Kumar, B.; Llorente, M.; Froehlich, J.; Dang, T.; Sathrum, A.; Kubiak, C. P., Photochemical and photoelectrochemical reduction of CO₂. *Annual review of physical chemistry* **2012**, *63*, 541-569.
39. Zhong, H.; Fujii, K.; Nakano, Y.; Jin, F., Effect of CO₂ Bubbling into Aqueous Solutions Used for Electrochemical Reduction of CO₂ for Energy Conversion and Storage. *The Journal of Physical Chemistry C* **2014**, *119* (1), 55-61.
40. Hori, Y.; Murata, A.; Kikuchi, K.; Suzuki, S., Electrochemical reduction of carbon dioxides to carbon monoxide at a gold electrode in aqueous potassium hydrogen carbonate. *Journal of the Chemical Society, Chemical Communications* **1987**, (10), 728-729.
41. Lobaccaro, P.; Singh, M. R.; Clark, E. L.; Kwon, Y.; Bell, A. T.; Ager, J. W., Effects of temperature and gas–liquid mass transfer on the operation of small electrochemical cells for the quantitative evaluation of CO₂ reduction electrocatalysts. *Phys. Chem. Chem. Phys.* **2016**, *18* (38), 26777-26785.
42. Ogura, K.; Yano, H.; Tanaka, T., Selective formation of ethylene from CO₂ by catalytic electrolysis at a three-phase interface. *Catalysis today* **2004**, *98* (4), 515-521.
43. Lyu, L.; Jin, F.; Zhong, H.; Chen, H.; Yao, G., A novel approach to reduction of CO₂ into methanol by water splitting with aluminum over a copper catalyst. *RSC Adv.* **2015**, *5* (40), 31450-31453.
44. Zarghami, S.; Boukadi, F.; Al-Wahaibi, Y., Diffusion of carbon dioxide in formation water as a result of CO₂ enhanced oil recovery and CO₂ sequestration. *Journal of Petroleum Exploration and Production Technology* **2017**, *7* (1), 161-168.
45. Resasco, J.; Chen, L. D.; Clark, E.; Tsai, C.; Hahn, C.; Jaramillo, T. F.; Chan, K.; Bell, A. T., Promoter effects of alkali metal cations on the electrochemical reduction of carbon dioxide. *J. Am. Chem. Soc.* **2017**, *139* (32), 11277-11287.
46. Park, S.; Lee, J.-W.; Popov, B. N., A review of gas diffusion layer in PEM fuel cells: Materials and designs. *International Journal of Hydrogen Energy* **2012**, *37* (7), 5850-5865.
47. Bultel, Y.; Ozil, P.; Durand, R., Modelling of mass transfer within the PEM fuel cell active layer: limitations at the particle level. *Journal of applied electrochemistry* **1999**, *29* (9), 1025-1033.

48. Dumitrescu, I.; Crooks, R. M., Effect of mass transfer on the oxygen reduction reaction catalyzed by platinum dendrimer encapsulated nanoparticles. *Proceedings of the National Academy of Sciences* **2012**, *109* (29), 11493-11497.
49. Zhang, J., *PEM fuel cell electrocatalysts and catalyst layers: fundamentals and applications*. Springer Science & Business Media: 2008.
50. Lee, W.; Kim, Y. E.; Youn, M. H.; Jeong, S. K.; Park, K. T., Catholyte-Free Electrocatalytic CO₂ Reduction to Formate. *Angew. Chem., Int. Ed.* **2018**, *57* (23), 6883-6887.
51. Pătru, A.; Binninger, T.; Pribyl, B.; Schmidt, T. J., Design principles of bipolar electrochemical co-electrolysis cells for efficient reduction of carbon dioxide from gas phase at low temperature. *J. Electrochem. Soc.* **2019**, *166* (2), F34-F43.
52. Dinh, C.-T.; Burdyny, T.; Kibria, M. G.; Seifitokaldani, A.; Gabardo, C. M.; de Arquer, F. P. G.; Kiani, A.; Edwards, J. P.; De Luna, P.; Bushuyev, O. S., CO₂ electroreduction to ethylene via hydroxide-mediated copper catalysis at an abrupt interface. *Science* **2018**, *360* (6390), 783-787.
53. Gabardo, C. M.; Seifitokaldani, A.; Edwards, J. P.; Dinh, C.-T.; Burdyny, T.; Kibria, M. G.; O'Brien, C. P.; Sargent, E. H.; Sinton, D., Combined high alkalinity and pressurization enable efficient CO₂ electroreduction to CO. *Energy Environ. Sci.* **2018**, *11* (9), 2531-2539.
54. Dufek, E. J.; Lister, T. E.; Stone, S. G.; McIlwain, M. E., Operation of a pressurized system for continuous reduction of CO₂. *J. Electrochem. Soc.* **2012**, *159* (9), F514-F517.
55. Dufek, E. J.; Lister, T. E.; Stone, S. G., Sampling dynamics for pressurized electrochemical cells. *Journal of Applied Electrochemistry* **2014**, *44* (7), 849-855.
56. Mignard, D.; Barik, R. C.; Bharadwaj, A. S.; Pritchard, C. L.; Ragnoli, M.; Cecconi, F.; Miller, H.; Yellowlees, L. J., Revisiting strontium-doped lanthanum cuprate perovskite for the electrochemical reduction of CO₂. *J. CO₂ Util.* **2014**, *5*, 53-59.
57. Del Castillo, A.; Alvarez-Guerra, M.; Solla-Gullón, J.; Sáez, A.; Montiel, V.; Irabien, A., Sn nanoparticles on gas diffusion electrodes: Synthesis, characterization and use for continuous CO₂ electroreduction to formate. *J. CO₂ Util.* **2017**, *18*, 222-228.
58. Wang, G.; Pan, J.; Jiang, S. P.; Yang, H., Gas phase electrochemical conversion of humidified CO₂ to CO and H₂ on proton-exchange and alkaline anion-exchange

- membrane fuel cell reactors. *J. CO2 Util.* **2018**, *23*, 152-158.
59. Kutz, R. B.; Chen, Q.; Yang, H.; Sajjad, S. D.; Liu, Z.; Masel, I. R., Sustainion Imidazolium-Functionalized Polymers for Carbon Dioxide Electrolysis. *Energy Technology* **2017**, *5* (6), 929-936.
60. Yu, C.-H.; Huang, C.-H.; Tan, C.-S., A review of CO₂ capture by absorption and adsorption. *Aerosol Air Qual. Res* **2012**, *12* (5), 745-769.
61. Tang, W.; Peterson, A. A.; Varela, A. S.; Jovanov, Z. P.; Bech, L.; Durand, W. J.; Dahl, S.; Nørskov, J. K.; Chorkendorff, I., The importance of surface morphology in controlling the selectivity of polycrystalline copper for CO₂ electroreduction. *Phys. Chem. Chem. Phys.* **2012**, *14* (1), 76-81.
62. Gonçalves, M.; Gomes, A.; Condeço, J.; Fernandes, R.; Pardal, T.; Sequeira, C.; Branco, J., Selective electrochemical conversion of CO₂ to C₂ hydrocarbons. *Energy Conversion and Management* **2010**, *51* (1), 30-32.
63. Pérez-Cadenas, A. F.; Ros, C. H.; Morales-Torres, S.; Pérez-Cadenas, M.; Kooyman, P. J.; Moreno-Castilla, C.; Kapteijn, F., Metal-doped carbon xerogels for the electrocatalytic conversion of CO₂ to hydrocarbons. *Carbon* **2013**, *56*, 324-331.
64. Savéant, J.-M., Molecular catalysis of electrochemical reactions. Mechanistic aspects. *Chemical Reviews* **2008**, *108* (7), 2348-2378.
65. Francke, R.; Schille, B.; Roemelt, M., Homogeneously catalyzed electroreduction of carbon dioxide—methods, mechanisms, and catalysts. *Chemical reviews* **2018**, *118* (9), 4631-4701.
66. Hori, Y.; Kikuchi, K.; Murata, A.; Suzuki, S., Production of methane and ethylene in electrochemical reduction of carbon dioxide at copper electrode in aqueous hydrogencarbonate solution. *Chemistry Letters* **1986**, *15* (6), 897-898.
67. Hori, Y.; Kikuchi, K.; Suzuki, S., Production of CO and CH₄ in electrochemical reduction of CO₂ at metal electrodes in aqueous hydrogencarbonate solution. *Chemistry Letters* **1985**, *14* (11), 1695-1698.
68. Hori, Y.; Murata, A.; Takahashi, R.; Suzuki, S., Electrochemical Reduction of Carbon Monoxide to Hydrocarbons at Various Metal Electrodes in Aqueous Solution. *Chemistry Letters* **1987**, *16* (8), 1665-1668.
69. Fan, Q.; Zhang, M.; Jia, M.; Liu, S.; Qiu, J.; Sun, Z., Electrochemical CO₂ reduction to

- C2+ species: Heterogeneous electrocatalysts, reaction pathways, and optimization strategies. *Materials today energy* **2018**, *10*, 280-301.
70. Kortlever, R.; Shen, J.; Schouten, K. J. P.; Calle-Vallejo, F.; Koper, M. T., Catalysts and reaction pathways for the electrochemical reduction of carbon dioxide. *The journal of physical chemistry letters* **2015**, *6* (20), 4073-4082.
 71. Sabatier, P., Hydrogénations et déshydrogénations par catalyse. *Berichte der deutschen chemischen Gesellschaft* **1911**, *44* (3), 1984-2001.
 72. Feaster, J. T.; Shi, C.; Cave, E. R.; Hatsukade, T.; Abram, D. N.; Kuhl, K. P.; Hahn, C.; Nørskov, J. K.; Jaramillo, T. F., Understanding selectivity for the electrochemical reduction of carbon dioxide to formic acid and carbon monoxide on metal electrodes. *ACS Catal.* **2017**, *7* (7), 4822-4827.
 73. Peterson, A. A.; Nørskov, J. K., Activity descriptors for CO₂ electroreduction to methane on transition-metal catalysts. *The Journal of Physical Chemistry Letters* **2012**, *3* (2), 251-258.
 74. Duan, X.; Xu, J.; Wei, Z.; Ma, J.; Guo, S.; Wang, S.; Liu, H.; Dou, S., Metal-free carbon materials for CO₂ electrochemical reduction. *Adv. Mater.* **2017**, *29* (41), 1701784.
 75. Liu, X.; Dai, L., Carbon-based metal-free catalysts. *Nature Reviews Materials* **2016**, *1* (11), 16064.
 76. Hori, Y.; Takahashi, I.; Koga, O.; Hoshi, N., Selective formation of C₂ compounds from electrochemical reduction of CO₂ at a series of copper single crystal electrodes. *The Journal of Physical Chemistry B* **2002**, *106* (1), 15-17.
 77. Liu, S. P.; Zhao, M.; Gao, W.; Jiang, Q., Mechanistic insights into the unique role of copper in CO₂ electroreduction reactions. *ChemSusChem* **2017**, *10* (2), 387-393.
 78. Yang, J.; Ma, W.; Chen, D.; Holmen, A.; Davis, B. H., Fischer–Tropsch synthesis: A review of the effect of CO conversion on methane selectivity. *Appl. Catal., A* **2014**, *470*, 250-260.
 79. Jahangiri, H.; Bennett, J.; Mahjoubi, P.; Wilson, K.; Gu, S., A review of advanced catalyst development for Fischer–Tropsch synthesis of hydrocarbons from biomass derived syn-gas. *Catal. Sci. Technol.* **2014**, *4* (8), 2210-2229.
 80. Zhu, W.; Zhang, Y.-J.; Zhang, H.; Lv, H.; Li, Q.; Michalsky, R.; Peterson, A. A.; Sun, S., Active and selective conversion of CO₂ to CO on ultrathin Au nanowires. *J. Am.*

- Chem. Soc.* **2014**, *136* (46), 16132-16135.
81. Cave, E. R.; Montoya, J. H.; Kuhl, K. P.; Abram, D. N.; Hatsukade, T.; Shi, C.; Hahn, C.; Nørskov, J. K.; Jaramillo, T. F., Electrochemical CO₂ reduction on Au surfaces: mechanistic aspects regarding the formation of major and minor products. *Phys. Chem. Chem. Phys.* **2017**, *19* (24), 15856-15863.
 82. Chen, Y.; Li, C. W.; Kanan, M. W., Aqueous CO₂ reduction at very low overpotential on oxide-derived Au nanoparticles. *J. Am. Chem. Soc.* **2012**, *134* (49), 19969-19972.
 83. Kim, J.; Song, J. T.; Ryoo, H.; Kim, J.-G.; Chung, S.-Y.; Oh, J., Morphology-controlled Au nanostructures for efficient and selective electrochemical CO₂ reduction. *J. Mater. Chem. A* **2018**, *6* (12), 5119-5128.
 84. Stevens, G. B.; Reda, T.; Raguse, B., Energy storage by the electrochemical reduction of CO₂ to CO at a porous Au film. *Journal of Electroanalytical Chemistry* **2002**, *526* (1-2), 125-133.
 85. Hall, A. S.; Yoon, Y.; Wuttig, A.; Surendranath, Y., Mesostructure-induced selectivity in CO₂ reduction catalysis. *J. Am. Chem. Soc.* **2015**, *137* (47), 14834-14837.
 86. Welch, A. J.; DuChene, J. S.; Tagliabue, G.; Davoyan, A.; Cheng, W.-H.; Atwater, H. A., Nanoporous Gold as a Highly Selective and Active Carbon Dioxide Reduction Catalyst. *ACS Applied Energy Materials* **2018**, *2* (1), 164-170.
 87. Sun, K.; Wu, L.; Qin, W.; Zhou, J.; Hu, Y.; Jiang, Z.; Shen, B.; Wang, Z., Enhanced electrochemical reduction of CO₂ to CO on Ag electrocatalysts with increased unoccupied density of states. *J. Mater. Chem. A* **2016**, *4* (32), 12616-12623.
 88. Yang, M.; Zhang, J.; Cao, Y.; Wu, M.; Qian, K.; Zhang, Z.; Liu, H.; Wang, J.; Chen, W.; Huang, W., Facet Sensitivity of Capping Ligand-Free Ag Crystals in CO₂ Electrochemical Reduction to CO. *ChemCatChem* **2018**, *10* (22), 5128-5134.
 89. Lu, Q.; Rosen, J.; Zhou, Y.; Hutchings, G. S.; Kimmel, Y. C.; Chen, J. G.; Jiao, F., A selective and efficient electrocatalyst for carbon dioxide reduction. *Nat. Commun.* **2014**, *5*, 3242.
 90. Zhang, L.; Wang, Z.; Mehio, N.; Jin, X.; Dai, S., Thickness-and Particle-Size-Dependent Electrochemical Reduction of Carbon Dioxide on Thin-Layer Porous Silver Electrodes. *ChemSusChem* **2016**, *9* (5), 428-432.
 91. Hsieh, Y.-C.; Senanayake, S. D.; Zhang, Y.; Xu, W.; Polyansky, D. E., Effect of

chloride anions on the synthesis and enhanced catalytic activity of silver nanocoral electrodes for CO₂ electroreduction. *ACS Catal.* **2015**, *5* (9), 5349-5356.

92. Jiang, K.; Kharel, P.; Peng, Y.; Gangishetty, M. K.; Lin, H.-Y. G.; Stavitski, E.; Attenkofer, K.; Wang, H., Silver nanoparticles with surface-bonded oxygen for highly selective CO₂ reduction. *ACS Sustainable Chemistry & Engineering* **2017**, *5* (10), 8529-8534.
93. Liu, S.; Tao, H.; Zeng, L.; Liu, Q.; Xu, Z.; Liu, Q.; Luo, J.-L., Shape-dependent electrocatalytic reduction of CO₂ to CO on triangular silver nanoplates. *J. Am. Chem. Soc.* **2017**, *139* (6), 2160-2163.
94. Kim, C.; Jeon, H. S.; Eom, T.; Jee, M. S.; Kim, H.; Friend, C. M.; Min, B. K.; Hwang, Y. J., Achieving selective and efficient electrocatalytic activity for CO₂ reduction using immobilized silver nanoparticles. *J. Am. Chem. Soc.* **2015**, *137* (43), 13844-13850.
95. Tao, H.; Sun, X.; Back, S.; Han, Z.; Zhu, Q.; Robertson, A. W.; Ma, T.; Fan, Q.; Han, B.; Jung, Y., Doping palladium with tellurium for the highly selective electrocatalytic reduction of aqueous CO₂ to CO. *Chem. Sci.* **2018**, *9* (2), 483-487.
96. Valenti, M.; Prasad, N. P.; Kas, R.; Bohra, D.; Ma, M.; Balasubramanian, V.; Chu, L.; Gimenez, S.; Bisquert, J.; Dam, B., Suppressing H₂ Evolution and Promoting Selective CO₂ Electroreduction to CO at Low Overpotentials by Alloying Au with Pd.
97. Zhu, W.; Kattel, S.; Jiao, F.; Chen, J. G., Shape-Controlled CO₂ Electrochemical Reduction on Nanosized Pd Hydride Cubes and Octahedra. *Advanced Energy Materials* **2019**, *9* (9), 1802840.
98. Jiao, J.; Lin, R.; Liu, S.; Cheong, W.-C.; Zhang, C.; Chen, Z.; Pan, Y.; Tang, J.; Wu, K.; Hung, S.-F., Copper atom-pair catalyst anchored on alloy nanowires for selective and efficient electrochemical reduction of CO₂. *Nature chemistry* **2019**, *11* (3), 222.
99. Larrazábal, G. n. O.; Martín, A. J.; Mitchell, S.; Hauert, R.; Pérez-Ramírez, J., Enhanced Reduction of CO₂ to CO over Cu–In Electrocatalysts: Catalyst Evolution Is the Key. *ACS Catal.* **2016**, *6* (9), 6265-6274.
100. Rasul, S.; Anjum, D. H.; Jedidi, A.; Minenkov, Y.; Cavallo, L.; Takanebe, K., A highly selective copper–indium bimetallic electrocatalyst for the electrochemical reduction of aqueous CO₂ to CO. *Angew. Chem.* **2015**, *127* (7), 2174-2178.
101. Li, F.; Zhao, S.-F.; Chen, L.; Khan, A.; MacFarlane, D. R.; Zhang, J., Polyethylenimine

- promoted electrocatalytic reduction of CO₂ to CO in aqueous medium by graphene-supported amorphous molybdenum sulphide. *Energy Environ. Sci.* **2016**, *9* (1), 216-223.
102. Schreier, M.; Héroguel, F.; Steier, L.; Ahmad, S.; Luterbacher, J. S.; Mayer, M. T.; Luo, J.; Grätzel, M., Solar conversion of CO₂ to CO using Earth-abundant electrocatalysts prepared by atomic layer modification of CuO. *Nat. Energy* **2017**, *2* (7), 17087.
103. Raciti, D.; Livi, K. J.; Wang, C., Highly dense Cu nanowires for low-overpotential CO₂ reduction. *Nano letters* **2015**, *15* (10), 6829-6835.
104. Verma, S.; Lu, X.; Ma, S.; Masel, R. I.; Kenis, P. J., The effect of electrolyte composition on the electroreduction of CO₂ to CO on Ag based gas diffusion electrodes. *Phys. Chem. Chem. Phys.* **2016**, *18* (10), 7075-7084.
105. Kim, B.; Hillman, F.; Ariyoshi, M.; Fujikawa, S.; Kenis, P. J., Effects of composition of the micro porous layer and the substrate on performance in the electrochemical reduction of CO₂ to CO. *Journal of Power Sources* **2016**, *312*, 192-198.
106. Fukuzumi, S., Production of liquid solar fuels and their use in fuel cells. *Joule* **2017**, *1* (4), 689-738.
107. Chung, J.; Koh, J.; Kim, E.-H.; Woo, S. I., Hierarchical Cu pillar electrodes for electrochemical CO₂ reduction to formic acid with low overpotential. *Phys. Chem. Chem. Phys.* **2016**, *18* (8), 6252-6258.
108. Li, F.; Chen, L.; Knowles, G. P.; MacFarlane, D. R.; Zhang, J., Hierarchical mesoporous SnO₂ nanosheets on carbon cloth: a robust and flexible electrocatalyst for CO₂ reduction with high efficiency and selectivity. *Angew. Chem., Int. Ed.* **2017**, *56* (2), 505-509.
109. Yu, J.; Liu, H.; Song, S.; Wang, Y.; Tsiakaras, P., Electrochemical reduction of carbon dioxide at nanostructured SnO₂/carbon aerogels: The effect of tin oxide content on the catalytic activity and formate selectivity. *Appl. Catal., A* **2017**, *545*, 159-166.
110. Choi, S. Y.; Jeong, S. K.; Kim, H. J.; Baek, I.-H.; Park, K. T., Electrochemical reduction of carbon dioxide to formate on tin-lead alloys. *ACS Sustainable Chemistry & Engineering* **2016**, *4* (3), 1311-1318.
111. Guo, S.; Zhao, S.; Gao, J.; Zhu, C.; Wu, X.; Fu, Y.; Huang, H.; Liu, Y.; Kang, Z., Cu-CDots nanocorals as electrocatalyst for highly efficient CO₂ reduction to formate. *Nanoscale* **2017**, *9* (1), 298-304.

112. Kortlever, R.; Peters, I.; Koper, S.; Koper, M. T., Electrochemical CO₂ reduction to formic acid at low overpotential and with high faradaic efficiency on carbon-supported bimetallic Pd–Pt nanoparticles. *ACS Catal.* **2015**, *5* (7), 3916-3923.
113. Wang, Q.; Dong, H.; Yu, H., Development of rolling tin gas diffusion electrode for carbon dioxide electrochemical reduction to produce formate in aqueous electrolyte. *Journal of Power Sources* **2014**, *271*, 278-284.
114. Wu, J.; Risalvato, F. G.; Ma, S.; Zhou, X.-D., Electrochemical reduction of carbon dioxide III. The role of oxide layer thickness on the performance of Sn electrode in a full electrochemical cell. *J. Mater. Chem. A* **2014**, *2* (6), 1647-1651.
115. Lu, X.; Leung, D. Y.; Wang, H.; Xuan, J., A high performance dual electrolyte microfluidic reactor for the utilization of CO₂. *Applied energy* **2017**, *194*, 549-559.
116. Irtem, E.; Andreu, T.; Parra, A.; Hernández-Alonso, M.; García-Rodríguez, S.; Riesco-García, J.; Penelas-Pérez, G.; Morante, J., Low-energy formate production from CO₂ electroreduction using electrodeposited tin on GDE. *J. Mater. Chem. A* **2016**, *4* (35), 13582-13588.
117. Bitar, Z.; Fecant, A.; Trela-Baudot, E.; Chardon-Noblat, S.; Pasquier, D., Electrocatalytic reduction of carbon dioxide on indium coated gas diffusion electrodes—Comparison with indium foil. *Applied Catalysis B: Environmental* **2016**, *189*, 172-180.
118. Kuhl, K. P.; Cave, E. R.; Abram, D. N.; Jaramillo, T. F., New insights into the electrochemical reduction of carbon dioxide on metallic copper surfaces. *Energy Environ. Sci.* **2012**, *5* (5), 7050-7059.
119. Li, H.; Li, Y.; Koper, M. T.; Calle-Vallejo, F., Bond-making and breaking between carbon, nitrogen, and oxygen in electrocatalysis. *J. Am. Chem. Soc.* **2014**, *136* (44), 15694-15701.
120. Hori, Y.; Takahashi, I.; Koga, O.; Hoshi, N., Electrochemical reduction of carbon dioxide at various series of copper single crystal electrodes. *Journal of Molecular Catalysis A: Chemical* **2003**, *199* (1-2), 39-47.
121. Li, C. W.; Kanan, M. W., CO₂ reduction at low overpotential on Cu electrodes resulting from the reduction of thick Cu₂O films. *J. Am. Chem. Soc.* **2012**, *134* (17), 7231-7234.
122. Mariano, R. G.; McKelvey, K.; White, H. S.; Kanan, M. W., Selective increase in CO₂

- electroreduction activity at grain-boundary surface terminations. *Science* **2017**, 358 (6367), 1187-1192.
123. Goncalves, M.; Gomes, A.; Condeço, J.; Fernandes, T.; Pardal, T.; Sequeira, C.; Branco, J., Electrochemical conversion of CO₂ to C₂ hydrocarbons using different ex situ copper electrodeposits. *Electrochim. Acta* **2013**, 102, 388-392.
 124. Reske, R.; Mistry, H.; Behafarid, F.; Roldan Cuenya, B.; Strasser, P., Particle size effects in the catalytic electroreduction of CO₂ on Cu nanoparticles. *J. Am. Chem. Soc.* **2014**, 136 (19), 6978-6986.
 125. Xie, J.-F.; Huang, Y.-X.; Li, W.-W.; Song, X.-N.; Xiong, L.; Yu, H.-Q., Efficient electrochemical CO₂ reduction on a unique chrysanthemum-like Cu nanoflower electrode and direct observation of carbon deposite. *Electrochim. Acta* **2014**, 139, 137-144.
 126. Loiudice, A.; Lobaccaro, P.; Kamali, E. A.; Thao, T.; Huang, B. H.; Ager, J. W.; Buonsanti, R., Tailoring copper nanocrystals towards C₂ products in electrochemical CO₂ reduction. *Angew. Chem., Int. Ed.* **2016**, 55 (19), 5789-5792.
 127. Xie, M. S.; Xia, B. Y.; Li, Y.; Yan, Y.; Yang, Y.; Sun, Q.; Chan, S. H.; Fisher, A.; Wang, X., Amino acid modified copper electrodes for the enhanced selective electroreduction of carbon dioxide towards hydrocarbons. *Energy Environ. Sci.* **2016**, 9 (5), 1687-1695.
 128. Albo, J.; Irabien, A., Cu₂O-loaded gas diffusion electrodes for the continuous electrochemical reduction of CO₂ to methanol. *J. Catal.* **2016**, 343, 232-239.
 129. Nie, X.; Griffin, G. L.; Janik, M. J.; Asthagiri, A., Surface phases of Cu₂O (111) under CO₂ electrochemical reduction conditions. *Catalysis Communications* **2014**, 52, 88-91.
 130. Bugayong, J.; Griffin, G. L., Electrochemical Reduction of CO₂ Using Supported Cu₂O Nanoparticles. *ECS Transactions* **2013**, 58 (2), 81-89.
 131. Terunuma, Y.; Saitoh, A.; Momose, Y., Relationship between hydrocarbon production in the electrochemical reduction of CO₂ and the characteristics of the Cu electrode. *Journal of Electroanalytical Chemistry* **1997**, 434 (1-2), 69-75.
 132. Dubé, P.; Brisard, G., Influence of adsorption processes on the CO₂ electroreduction: An electrochemical mass spectrometry study. *Journal of Electroanalytical Chemistry* **2005**, 582 (1-2), 230-240.
 133. Frese, K. W., Electrochemical reduction of CO₂ at intentionally oxidized copper

- electrodes. *J. Electrochem. Soc.* **1991**, *138* (11), 3338-3344.
134. Kas, R.; Kortlever, R.; Milbrat, A.; Koper, M. T.; Mul, G.; Baltrusaitis, J., Electrochemical CO₂ reduction on Cu₂O-derived copper nanoparticles: controlling the catalytic selectivity of hydrocarbons. *Phys. Chem. Chem. Phys.* **2014**, *16* (24), 12194-12201.
135. Zhang, Y.-J.; Peterson, A. A., Oxygen-induced changes to selectivity-determining steps in electrocatalytic CO₂ reduction. *Phys. Chem. Chem. Phys.* **2015**, *17* (6), 4505-4515.
136. Gattrell, M.; Gupta, N.; Co, A., A review of the aqueous electrochemical reduction of CO₂ to hydrocarbons at copper. *Journal of electroanalytical Chemistry* **2006**, *594* (1), 1-19.
137. Hori, Y.; Konishi, H.; Futamura, T.; Murata, A.; Koga, O.; Sakurai, H.; Oguma, K., "Deactivation of copper electrode" in electrochemical reduction of CO₂. *Electrochim. Acta* **2005**, *50* (27), 5354-5369.
138. Sirkiä, P.; Saario, T.; Maekelae, K.; Laitinen, T.; Bojinov, M. *Electric and electrochemical properties of surface films formed on copper in the presence of bicarbonate anions*; Radiation and Nuclear Safety Authority: 1999.
139. Ren, D.; Deng, Y.; Handoko, A. D.; Chen, C. S.; Malkhandi, S.; Yeo, B. S., Selective electrochemical reduction of carbon dioxide to ethylene and ethanol on copper (I) oxide catalysts. *ACS Catal.* **2015**, *5* (5), 2814-2821.
140. Kim, D.; Lee, S.; Ocon, J. D.; Jeong, B.; Lee, J. K.; Lee, J., Insights into an autonomously formed oxygen-evacuated Cu₂O electrode for the selective production of C₂H₄ from CO₂. *Phys. Chem. Chem. Phys.* **2015**, *17* (2), 824-830.
141. Liu, C.; Lourenço, M. P.; Hedström, S.; Cavalca, F.; Diaz-Morales, O.; Duarte, H. A.; Nilsson, A.; Pettersson, L. G., Stability and Effects of Subsurface Oxygen in Oxide-Derived Cu Catalyst for CO₂ Reduction. *The Journal of Physical Chemistry C* **2017**, *121* (45), 25010-25017.
142. Lum, Y.; Ager, J. W., Stability of Residual Oxides in Oxide-Derived Copper Catalysts for Electrochemical CO₂ Reduction Investigated with ¹⁸O Labeling. *Angew. Chem., Int. Ed.* **2018**, *57* (2), 551-554.
143. Watanabe, M.; Shibata, M.; Kato, A.; Azuma, M.; Sakata, T., Design of alloy electrocatalysts for CO₂ reduction III. The selective and reversible reduction of on Cu

- alloy electrodes. *J. Electrochem. Soc.* **1991**, *138* (11), 3382-3389.
144. Hirunsit, P., Electroreduction of carbon dioxide to methane on copper, copper–silver, and copper–gold catalysts: a DFT study. *The Journal of Physical Chemistry C* **2013**, *117* (16), 8262-8268.
 145. Reske, R.; Duca, M.; Oezaslan, M.; Schouten, K. J. P.; Koper, M. T.; Strasser, P., Controlling catalytic selectivities during CO₂ electroreduction on thin Cu metal overlayers. *The Journal of Physical Chemistry Letters* **2013**, *4* (15), 2410-2413.
 146. Varela, A. S.; Schlaup, C.; Jovanov, Z. P.; Malacrida, P.; Horch, S.; Stephens, I. E.; Chorkendorff, I., CO₂ electroreduction on well-defined bimetallic surfaces: Cu overlayers on Pt (111) and Pt (211). *The Journal of Physical Chemistry C* **2013**, *117* (40), 20500-20508.
 147. Christophe, J.; Doneux, T.; Buess-Herman, C., Electroreduction of carbon dioxide on copper-based electrodes: activity of copper single crystals and copper–gold alloys. *Electrocatalysis* **2012**, *3* (2), 139-146.
 148. Jedidi, A.; Rasul, S.; Masih, D.; Cavallo, L.; Takanebe, K., Generation of Cu–In alloy surfaces from CuInO₂ as selective catalytic sites for CO₂ electroreduction. *J. Mater. Chem. A* **2015**, *3* (37), 19085-19092.
 149. Marini, S.; Salvi, P.; Nelli, P.; Pesenti, R.; Villa, M.; Berrettoni, M.; Zangari, G.; Kiros, Y., Advanced alkaline water electrolysis. *Electrochim. Acta* **2012**, *82*, 384-391.
 150. Zhang, Z.; Che, H.; Gao, J.; Wang, Y.; She, X.; Sun, J.; Gunawan, P.; Zhong, Z.; Su, F., Shape-controlled synthesis of Cu₂O microparticles and their catalytic performances in the Rochow reaction. *Catal. Sci. Technol.* **2012**, *2* (6), 1207-1212.
 151. Cindrella, L.; Kannan, A. M.; Lin, J.; Saminathan, K.; Ho, Y.; Lin, C.; Wertz, J., Gas diffusion layer for proton exchange membrane fuel cells—A review. *Journal of Power sources* **2009**, *194* (1), 146-160.
 152. Lockett, V.; Horne, M.; Sedev, R.; Rodopoulos, T.; Ralston, J., Differential capacitance of the double layer at the electrode/ionic liquids interface. *Phys. Chem. Chem. Phys.* **2010**, *12* (39), 12499-12512.
 153. Kaluzhina, S.; Sieber, I., Copper passivity and its breakdown in sodium bicarbonate solutions: A scanning electron microscopy and x-ray photoelectron and auger spectroscopy study. *Russian Journal of Electrochemistry* **2006**, *42* (12), 1352-1357.

154. Beverskog, B.; Puigdomenech, I., Revised Pourbaix diagrams for copper at 25 to 300 C. *J. Electrochem. Soc.* **1997**, *144* (10), 3476-3483.
155. Giner, J.; Hunter, C., The Mechanism of Operation of the Teflon-Bonded Gas Diffusion Electrode: A Mathematical Model. *J. Electrochem. Soc.* **1969**, *116* (8), 1124-1130.
156. Hernandez, D.; Cabrera, C. R.; Mendez, L.; Diaz-Serrano, M.; Vega, O.; Weiner, B. R.; Rosa, L. G., Oxidized SWCNT chemically attached to a modified copper substrate. *Applied Surface Science* **2015**, *346*, 415-422.
157. Yu, E.; Scott, K.; Reeve, R., Electrochemical reduction of oxygen on carbon supported Pt and Pt/Ru fuel cell electrodes in alkaline solutions. *Fuel Cells* **2003**, *3* (4), 169-176.
158. Alcaide, F.; Brillas, E.; Cabot, P.-L. s., EIS analysis of hydroperoxide ion generation in an uncatalyzed oxygen-diffusion cathode. *Journal of Electroanalytical Chemistry* **2003**, *547* (1), 61-73.
159. Gilliam, R.; Graydon, J.; Kirk, D.; Thorpe, S., A review of specific conductivities of potassium hydroxide solutions for various concentrations and temperatures. *International Journal of Hydrogen Energy* **2007**, *32* (3), 359-364.
160. Calle-Vallejo, F.; Koper, M., Theoretical considerations on the electroreduction of CO to C2 species on Cu (100) electrodes. *Angew. Chem.* **2013**, *125* (28), 7423-7426.
161. Montoya, J. H.; Shi, C.; Chan, K.; Nørskov, J. K., Theoretical insights into a CO dimerization mechanism in CO2 electroreduction. *The journal of physical chemistry letters* **2015**, *6* (11), 2032-2037.
162. Nie, X.; Esopi, M. R.; Janik, M. J.; Asthagiri, A., Selectivity of CO2 reduction on copper electrodes: the role of the kinetics of elementary steps. *Angew. Chem., Int. Ed.* **2013**, *52* (9), 2459-2462.
163. DeWulf, D. W.; Jin, T.; Bard, A. J., Electrochemical and surface studies of carbon dioxide reduction to methane and ethylene at copper electrodes in aqueous solutions. *J. Electrochem. Soc.* **1989**, *136* (6), 1686-1691.
164. Schouten, K.; Kwon, Y.; Van der Ham, C.; Qin, Z.; Koper, M., A new mechanism for the selectivity to C 1 and C 2 species in the electrochemical reduction of carbon dioxide on copper electrodes. *Chem. Sci.* **2011**, *2* (10), 1902-1909.
165. Xiao, H.; Cheng, T.; Goddard III, W. A., Atomistic mechanisms underlying selectivities in C1 and C2 products from electrochemical reduction of CO on Cu (111). *J. Am. Chem.*

- Soc.* **2016**, *139* (1), 130-136.
166. Severino, F.; Brito, J. L.; Laine, J.; Fierro, J.; Agudo, A. L., Nature of Copper Active Sites in the Carbon Monoxide Oxidation on CuAl₂O₄ and CuCr₂O₄ Spinel Type Catalysts. *J. Catal.* **1998**, *177* (1), 82-95.
 167. Karthik, T. V. K.; Olvera, M. d. I. L.; Maldonado, A.; Gómez Pozos, H., CO Gas sensing properties of pure and Cu-incorporated SnO₂ nanoparticles: A study of Cu-induced modifications. *Sensors* **2016**, *16* (8), 1283.
 168. Deutsch, K. L.; Shanks, B. H., Active species of copper chromite catalyst in C–O hydrogenolysis of 5-methylfurfuryl alcohol. *J. Catal.* **2012**, *285* (1), 235-241.
 169. Hori, Y.; Wakebe, H.; Tsukamoto, T.; Koga, O., Electrocatalytic process of CO selectivity in electrochemical reduction of CO₂ at metal electrodes in aqueous media. *Electrochim. Acta* **1994**, *39* (11-12), 1833-1839.
 170. Hatsukade, T.; Kuhl, K. P.; Cave, E. R.; Abram, D. N.; Jaramillo, T. F., Insights into the electrocatalytic reduction of CO₂ on metallic silver surfaces. *Phys. Chem. Chem. Phys.* **2014**, *16* (27), 13814-13819.
 171. Sheng, W.; Kattel, S.; Yao, S.; Yan, B.; Liang, Z.; Hawxhurst, C. J.; Wu, Q.; Chen, J. G., Electrochemical reduction of CO₂ to synthesis gas with controlled CO/H₂ ratios. *Energy Environ. Sci.* **2017**, *10* (5), 1180-1185.
 172. Gao, D.; Zhou, H.; Wang, J.; Miao, S.; Yang, F.; Wang, G.; Wang, J.; Bao, X., Size-dependent electrocatalytic reduction of CO₂ over Pd nanoparticles. *J. Am. Chem. Soc.* **2015**, *137* (13), 4288-4291.
 173. Wu, J.; Yadav, R. M.; Liu, M.; Sharma, P. P.; Tiwary, C. S.; Ma, L.; Zou, X.; Zhou, X.-D.; Yakobson, B. I.; Lou, J., Achieving highly efficient, selective, and stable CO₂ reduction on nitrogen-doped carbon nanotubes. *ACS Nano* **2015**, *9* (5), 5364-5371.
 174. Sharma, P. P.; Wu, J.; Yadav, R. M.; Liu, M.; Wright, C. J.; Tiwary, C. S.; Yakobson, B. I.; Lou, J.; Ajayan, P. M.; Zhou, X. D., Nitrogen-doped carbon nanotube arrays for high-efficiency electrochemical reduction of CO₂: on the understanding of defects, defect density, and selectivity. *Angew. Chem., Int. Ed.* **2015**, *54* (46), 13701-13705.
 175. Conway, B.; Jerkiewicz, G., Relation of energies and coverages of underpotential and overpotential deposited H at Pt and other metals to the ‘volcano curve’ for cathodic H₂ evolution kinetics. *Electrochim. Acta* **2000**, *45* (25-26), 4075-4083.

176. Rasul, S.; Pugniant, A.; Xiang, H.; Fontmorin, J.-M.; Eileen, H. Y., Low cost and efficient alloy electrocatalysts for CO₂ reduction to formate. *J. CO₂ Util.* **2019**, *32*, 1-10.
177. Liu, P.; Hensen, E. J., Highly efficient and robust Au/MgCuCr₂O₄ catalyst for gas-phase oxidation of ethanol to acetaldehyde. *J. Am. Chem. Soc.* **2013**, *135* (38), 14032-14035.
178. Akhavan, O.; Azimirad, R.; Safa, S.; Hasani, E., CuO/Cu (OH)₂ hierarchical nanostructures as bactericidal photocatalysts. *J. Mater. Chem.* **2011**, *21* (26), 9634-9640.
179. Liu, P.; Li, Z.; Cai, W.; Fang, M.; Luo, X., Fabrication of cuprous oxide nanoparticles by laser ablation in PVP aqueous solution. *RSC Adv.* **2011**, *1* (5), 847-851.
180. Yu, Y.-H.; Lin, Y.-Y.; Lin, C.-H.; Chan, C.-C.; Huang, Y.-C., High-performance polystyrene/graphene-based nanocomposites with excellent anti-corrosion properties. *Polym. Chem.* **2014**, *5* (2), 535-550.
181. Detweiler, Z. M.; White, J. L.; Bernasek, S. L.; Bocarsly, A. B., Anodized indium metal electrodes for enhanced carbon dioxide reduction in aqueous electrolyte. *Langmuir* **2014**, *30* (25), 7593-7600.
182. Hoch, L. B.; Wood, T. E.; O'Brien, P. G.; Liao, K.; Reyes, L. M.; Mims, C. A.; Ozin, G. A., The Rational Design of a Single-Component Photocatalyst for Gas-Phase CO₂ Reduction Using Both UV and Visible Light. *Adv. Sci.* **2014**, *1* (1), 1400013.
183. Ge, Y.; Kan, K.; Yang, Y.; Zhou, L.; Jing, L.; Shen, P.; Li, L.; Shi, K., Highly mesoporous hierarchical nickel and cobalt double hydroxide composite: fabrication, characterization and ultrafast NO_x gas sensors at room temperature. *J. Mater. Chem. A* **2014**, *2* (14), 4961-4969.
184. Busev, A. I., *The analytical chemistry of indium: international series of monographs on analytical chemistry*. Elsevier: 2013.
185. Vasileff, A.; Xu, C.; Jiao, Y.; Zheng, Y.; Qiao, S.-Z., Surface and interface engineering in copper-based bimetallic materials for selective CO₂ electroreduction. *Chem* **2018**.
186. Rabiee, A.; Nematollahi, D., Electrochemical reduction of CO₂ to formate ion using nanocubic mesoporous In (OH)₃/carbon black system. *Mater. Chem. Phys.* **2017**, *193*, 109-116.
187. Larrazábal, G. O.; Shinagawa, T.; Martín, A. J.; Pérez-Ramírez, J., Microfabricated

- electrodes unravel the role of interfaces in multicomponent copper-based CO₂ reduction catalysts. *Nat. Commun.* **2018**, 9 (1), 1477.
188. Thorson, M. R.; Siil, K. I.; Kenis, P. J., Effect of Cations on the Electrochemical Conversion of CO₂ to CO. *J. Electrochem. Soc.* **2013**, 160 (1), F69-F74.
189. Kaneco, S.; Katsumata, H.; Suzuki, T.; Ohta, K., Electrochemical reduction of CO₂ to methane at the Cu electrode in methanol with sodium supporting salts and its comparison with other alkaline salts. *Energy & fuels* **2006**, 20 (1), 409-414.
190. Singh, A. K.; Singh, S.; Kumar, A., Hydrogen energy future with formic acid: a renewable chemical hydrogen storage system. *Catal. Sci. Technol.* **2016**, 6 (1), 12-40.
191. Rasul, S.; Pugnant, A.; Yu, E., Electrochemical Reduction of CO₂ at Multi-Metallic Interfaces. *ECS Transactions* **2018**, 85 (10), 57-66.
192. Theaker, N.; Strain, J. M.; Kumar, B.; Brian, J. P.; Kumari, S.; Spurgeon, J. M., Heterogeneously catalyzed two-step cascade electrochemical reduction of CO₂ to ethanol. *Electrochim. Acta* **2018**, 274, 1-8.
193. Vo, T.; Purohit, K.; Nguyen, C.; Biggs, B.; Mayoral, S.; Haan, J. L., Formate: an energy storage and transport bridge between carbon dioxide and a formate fuel cell in a single device. *ChemSusChem* **2015**, 8 (22), 3853-3858.
194. An, L.; Chen, R., Direct formate fuel cells: a review. *Journal of power sources* **2016**, 320, 127-139.
195. Miller, H.; Ruggeri, J.; Marchionni, A.; Bellini, M.; Pagliaro, M.; Bartoli, C.; Pucci, A.; Passaglia, E.; Vizza, F., Improving the energy efficiency of direct formate fuel cells with a Pd/C-CeO₂ anode catalyst and anion exchange ionomer in the catalyst layer. *Energies* **2018**, 11 (2), 369.
196. Wang, L.; Bellini, M.; Filippi, J.; Folliero, M.; Lavacchi, A.; Innocenti, M.; Marchionni, A.; Miller, H.; Vizza, F., Energy efficiency of platinum-free alkaline direct formate fuel cells. *Applied Energy* **2016**, 175, 479-487.
197. Fu, Y.; Li, Y.; Zhang, X.; Liu, Y.; Qiao, J.; Zhang, J.; Wilkinson, D. P., Novel hierarchical SnO₂ microsphere catalyst coated on gas diffusion electrode for enhancing energy efficiency of CO₂ reduction to formate fuel. *Applied energy* **2016**, 175, 536-544.
198. Weng, L.-C.; Bell, A. T.; Weber, A. Z., Modeling gas-diffusion electrodes for CO₂ reduction. *Phys. Chem. Chem. Phys.* **2018**, 20 (25), 16973-16984.

199. Kamat, A.; Huth, A.; Klein, O.; Scholl, S., Chronoamperometric investigations of the electrode–electrolyte interface of a commercial high temperature PEM fuel cell. *Fuel Cells* **2010**, *10* (6), 983-992.
200. Sow, P. K.; Lu, Z.; Talebian, H.; Damron, L.; Mérida, W., Double layer capacitance measurements to characterize the water intrusion into porous materials. *The Journal of Physical Chemistry C* **2016**, *120* (43), 24794-24802.
201. Lázaro, M.; Calvillo, L.; Celorrio, V.; Pardo, J.; Perathoner, S.; Moliner, R., Study and application of carbon black Vulcan XC-72R in polymeric electrolyte fuel cells. *Carbon black: production, properties and uses* **2011**, 41.
202. Bevilacqua, M.; Bianchini, C.; Marchionni, A.; Filippi, J.; Lavacchi, A.; Miller, H.; Oberhauser, W.; Vizza, F.; Granozzi, G.; Artiglia, L., Improvement in the efficiency of an OrganoMetallic Fuel Cell by tuning the molecular architecture of the anode electrocatalyst and the nature of the carbon support. *Energy Environ. Sci.* **2012**, *5* (9), 8608-8620.
203. Ahn, M.; Cho, Y.-H.; Cho, Y.-H.; Kim, J.; Jung, N.; Sung, Y.-E., Influence of hydrophilicity in micro-porous layer for polymer electrolyte membrane fuel cells. *Electrochim. Acta* **2011**, *56* (5), 2450-2457.
204. Kumar, A.; Sanger, A.; Kumar, A.; Chandra, R., Highly sensitive and selective CO gas sensor based on a hydrophobic SnO₂/CuO bilayer. *RSC Adv.* **2016**, *6* (52), 47178-47184.
205. Gunji, T.; Matsumoto, F., Electrocatalytic Activities towards the Electrochemical Oxidation of Formic Acid and Oxygen Reduction Reactions over Bimetallic, Trimetallic and Core–Shell-Structured Pd-Based Materials. *Inorganics* **2019**, *7* (3), 36.
206. Berná, A.; Rodes, A.; Feliu, J. M.; Illas, F.; Gil, A.; Clotet, A.; Ricart, J. M., Structural and spectroelectrochemical study of carbonate and bicarbonate adsorbed on Pt (111) and Pd/Pt (111) electrodes. *The Journal of Physical Chemistry B* **2004**, *108* (46), 17928-17939.
207. Hori, Y.; Takahashi, I.; Koga, O.; Hoshi, N., Electrochemical reduction of carbon dioxide at various series of copper single crystal electrodes. *Journal of Molecular Catalysis A: Chemical* **2003**, *199* (1), 39-47.
208. Sen, S.; Liu, D.; Palmore, G. T. R., Electrochemical reduction of CO₂ at copper

nanofoms. *ACS Catal.* **2014**, *4* (9), 3091-3095.

209. Fan, M.; Bai, Z.; Zhang, Q.; Ma, C.; Zhou, X.-D.; Qiao, J., Aqueous CO₂ reduction on morphology controlled Cu_xO nanocatalysts at low overpotential. *RSC Adv.* **2014**, *4* (84), 44583-44591.